Quantum Technology using Cold Diatomic Molecular Ions: Interferometry and Cooling

Jan Martin Berglund

kassel university press

Jan Martin Berglund

Quantum Technology using Cold Diatomic Molecular Ions:

Interferometry and Cooling

kassel university press

This work has been accepted by the Faculty of Mathematics and Natural Sciences of the University of Kassel as a thesis for acquiring the academic degree of Doktor der Naturwissenschaften (Dr. rer. nat.).

Supervisor: Prof. Dr. Christiane P. Koch, FU Berlin
Co-Supervisor: Prof. Dr. Stefan Yoshi Buhmann, University of Kassel

Defense day: 30. June 2023

Bibliographic information published by Deutsche Nationalbibliothek
The Deutsche Nationalbibliothek lists this publication in the Deutsche Nationalbibliografie; detailed bibliographic data is available in the Internet at http://dnb.dnb.de.

Zugl.: Kassel, Univ., Diss. 2023
ISBN 978-3-7376-1137-4
DOI: https://doi.org/10.17170/kobra-202308088587

https://kup.uni-kassel.de

Printing Shop: Print Management Logistik Service, Kassel
Printed in Germany

Abstract

Atoms and atomic ions have proved to be useful as quantum technological systems, where atomic clocks are one of the more famous implementations. Molecules, with more degrees of freedom (vibrations and rotations) are considered as natural extensions to atomic systems. In particular, we study cold molecular diatomic ions as systems for implementation in quantum technology and in particular the rotational degree of freedom of such molecular ions. Quantum effects manifest themselves at very cold temperatures. To reach such low temperatures, Doppler cooling via resonant coupling to external laser fields can be used for atoms and atomic ions. Molecules are in general more difficult to cool down due to their more complex internal structure and generally require other cooling methods. One such strategy uses pre cooled atomic ions as coolants for the molecular ions, mediated via repeated collisions between the two ionic species. This method, known as sympathetic cooling, is independent on the internal structure of the molecular ions.

It may however, lead to unwanted excitations of the internal degrees of freedom of the molecular ions, and in particular rotational excitations are to be expected. We investigate the rotational population excitation in a cooling process and its relation to the molecular parameters such as the rotational constant and the relevant molecular coupling constants. Based on the separate energy scales of the associated with the translational and rotational degrees of freedom we propose a model that separates the translational energy transfer and the rotational transfer. Polar molecular ions, which possess a permanent dipole moment interact linearly with the field originating from the coolant ion, and due to the gradual change of the field the interaction tends to lead to high field, but near adiabatic dynamics of the rotational states. Apolar molecular ions, on the other hand, lack a permanent dipole moment, due to symmetry, and interact via higher order moments and they therefore couple weakly to the field and the rotational dynamics can be studied using perturbation theory.

In addition, we propose to use sympathetically cooled MgH^+-ions, forming a Coulomb crystal in a linear Paul trap, to implement a Ramsey-like interferometric setup which can be utilized for sensitive measurments of molecular parameters, such as the polarizability anisotropy. Two time delayed femtosecond laser pulses are used to excite rotational population of the ion. The delay dependent final rotational population defines the interferogram. The ionic spacing in the crystal is typically of the order of μm and allows for single ion addressability and long storage times (up to hours) in a typical experimental setup. Our simulations indicate that the interferometer can be used to measure the average polarizability of the molecular ion to within errors of the errors of the population measurement.

Zusammenfassung

Atome und Atomionen als quantentechnologische Systeme haben sich als nützlich erwiesen. Atomuhren sind eine der bekanntesten Anwendungen. Moleküle mit mehr Freiheitsgraden (Schwingungen und Rotationen) gelten als natürliche Erweiterungen atomarer Systeme. In meiner Doktorarbeit untersuchen wir kalte molekulare zweiatomige Ionen als Systeme zur Implementierung in der Quantentechnologie, insbesondere den Rotationsfreiheitsgrad solcher molekularer Ionen. Quanteneffekte manifestieren sich bei sehr kalten Temperaturen. Um solch niedrige Temperaturen zu erreichen, kann die Doppler-Kühlung durch Resonanzkopplung an externe Laserfelder für Atome und Atomionen verwendet werden. Moleküle sind im Allgemeinen aufgrund ihrer komplexeren inneren Struktur schwieriger abzukühlen und erfordern deswegen andere Kühlmethoden. Eine solche Strategie ist die Verwendung vorgekühlte Atomionen, die die Molekühlionen mittels wiederholter Kollisionen abkühlen. Diese, als sympathetische Kühlung bekannte Methode, ist unabhängig von der inneren Struktur der Molekülionen.

Es kann jedoch zu unerwünschten Anregungen der inneren Freiheitsgrade der Molekülionen kommen, insbesondere sind Rotationsanregungen zu erwarten. Wir untersuchen die Anregung der Rotationspopulation in einem Abkühlungsprozess und ihre Beziehung zu den molekularen Parametern wie der Rotationskonstante und den relevanten molekularen Kopplungskonstanten. Basierend auf den getrennten Energieskalen, die mit den Translations- und Rotationsfreiheitsgraden verbundenen sind, schlagen wir ein Modell vor, das den translatorischen Energietransfer und den Rotationstransfer trennt. Polare Molekülionen, die ein permanentes Dipolmoment besitzen, interagieren linear mit dem Feld des vorgekühlten Atomions, der tendenziell zu einem hochen Wechselwirkung führt. Aufgrund der allmählichen Änderung des Feldes, entsteht allerdings einer fast adiabatischen Dynamik der Rotationszustände. Apolare Molekülionen hingegen haben aufgrund ihrer Symmetrie kein permanentes Dipolmoment und interagieren über Momente höherer Ordnung. Sie koppeln daher schwach an das Feld und die Rotationsdynamik kann mithilfe der Störungstheorie untersucht werden.

Zusätzlich schlagen wir vor, sympathetisch gekühlte MgH^+-Ionen zu verwenden, die einen Coulomb-Kristall in einer linearen Paul-Falle bilden, um einen Ramsey-ähnlichen interferometrischen Aufbau zu implementieren, der angewennt werden kann um molekülare Parametern sensitiv zu Messen, z.B. die Polarizationsanisotropie. Zwei zeitverzögerte Femtosekundenlaserpulse werden verwendet, um die Rotationspopulation des Ions anzuregen. Die verzögerungsabhängige endgültige Rotationspopulation definiert das Interferogramm. Der Ionenabstand im Kristall liegt typischerweise in der Größenordnung von μm und ermöglicht die Adressierbarkeit einzelner Ionen und lange Lagerzeiten (bis zu Stunden) in einem typischen Versuchsaufbau. Meine Simulationen zeigen, dass das Interferometer ver-

wendet werden kann, um die durchschnittliche Polarisierbarkeit des Molekülions innerhalb von Fehlern der Fehler der Populationsmessung zu messen.

Contents

1

Introduction and motivation

The wave-particle duality states that, at the fundamental level all objects, light as well as matter, have wave- and particle manifestations. The wave like behavior of matter can consequently be characterized by a wave function. The wavelength of the matter-wave, λ, is connected to its momentum p via the de-Broglie relation, $\lambda = \frac{h}{p}$, where h is Planck's constant. One of the fundamental characteristics of wave behavior, classical or quantum, is the interference effect, where two (or several) waves impinging on each other can enhance or suppress the amplitude of the outgoing wave. As an example we can consider two interfering waves with amplitudes a_1 and a_2 respectively. The resulting intensity I is given by $I = |a_1|^2 + |a_2|^2 + 2a_1a_2\cos(\theta)$, where θ is the phase difference of the two waves. When $\theta = 0 \quad mod(2\pi)$ the interference term adds constructively to the total intensity and we talk about constructive interference. Correspondingly for $\theta = \pi \quad mod(2\pi)$ the interference term adds destructively and we talk about destructive interference. When $|a_1| = |a_2|$ the interference effect is most pronounced, we obtain full constructive and destructive interference. The intensity then takes values in the interval $I \in \left[0, 4|a_1|^2\right]$. This result illustrates the power of the high discernibility inherent in the interference effect, both for classical and quantum waves.

Indeed, the classical interference effect has been successfully applied in the development of high precision measurement devices, known as interferometers. An historically important interferometry measurement is the famous experiment of Michelson and Morley [1] to measure the difference of the speed of light through different directions in the so called ether. The absence of such difference contradicted the directional dependence of the speed of light and led to the conclusion that light propagates at constant speed through vacuum regardless of the relative motion of the observer.

Typically, beam-splitters are used to split a wave into two components which are allowed to traverse different optical path-lengths. Then, a second beam splitter is used to rejoin

the two waves and direct them towards a detector. The difference in optical path-length translates into a phase difference between the two components which in turn gives rise to an interference pattern. In a similar way, the wave nature of a material object allows for interference to occur between the different components of its wavefunction. Whenever two or more paths are open for evolution between two quantum states, interference sets in between these paths. The famous two-slit experiment, where each slit opens up a possible path of evolution, is a well-known example of this phenomenon, see e.g. [2].

The wave particle duality enables the interference effect to manifest itself in massive objects, e.g. atoms and molecules. The method of Ramsey interferometry has been particularly successful in this respect [3]. The method is a development from Rabi oscillations [4,5] and it too involves two-level objects. Instead of one pulse it utilizes two $\frac{\pi}{2}$-pulses (pulses that create a $50-50\%$ coherent superposition of ground and excited states from the ground state) [6]. Ramsey interferometry can be implemented on e.g. trapped atoms interacting with two pulses with a controllable time delay [5]. The relative phase between the two states depends on the time delay between the two interactions as each phase evolves according to its own characteristic speed set by its eigenvalue. If the phases combine constructively the two pulses combine to an effective π-pulse, i.e., complete population inversion is achieved with 100% population in the excited state, whereas if the phases combine destructively the effect of the first pulse is completely countered and the final population is found completely in the ground state. The resulting interferogram defined by the population in either of the states is a periodic function of the time delay [5]. The pulses take the role of beam splitters and the time-delay that of the optical path length in interferometer experiments of light.

The interference effect relies on maintaining a well defined and predictable phase relation between the interference waves in order to manifest itself. When such a relation exists the state (light or matter) is coherent. A system can extend its coherence in both space (spatial coherence) and time (temporal coherence). The evolution of coherent quantum systems can be steered, or controlled, by the means of external coherent light sources, such as laser pulses. It is possible to engineer pulses to drive quantum systems to a desired final state while suppressing other, unwanted states by manipulating constructive and destructive interferences in the different quantum channels (pathways). The process of controlling the dynamics of a quantum system by manipulating interfering pathways is known as *Coherent Control* and was developed in the eighties and nineties. The theory was pioneered by the works of Tannor, Kosloff and Rice [7,8], Brumer and Shapiro [9,10], as well as Pierce et. al. [11]. Tannor, Kosloff and Rice proposed a strategy based on the time delay between the pulses, whereas Brumer and Shapiro introduced a strategy based on varying the relative phase and amplitude of two simultaneous pulses.

Pulses (e.g. lasers, radio fields and micro wave) are versatile tools that can coherently steer, or control, the dynamics of a quantum system [7–10,12–14]. It is nowadays possible to

theoretically design, using a method is known as *quantum optimal control theory* (QOCT), and tailor pulses to this end in the lab [15].

Preparing and controlling quantum objects have made it possible to utilize quantum effects in technological applications with improved sensitivity compared to technology based on classical components. This quickly emerging field is known as *quantum technology* and an overview of the interests in the field can be found in e.g. [16,17]. As an example, the atomic clock is used to define the second and is used as the standard time reference [18], making use of the Ramsey method [5,19]. Portable atomic clocks are envisaged as systems that can be utilized in applications in science as well as in industry [20] and geodesy [21,22]. In addition, ultracold atomic systems are used in some of the most precise measurements of natural constants [5]. Here, the quantum interference effect is utilized to create a sensitive measurement device. Quantum technological applications are not limited to matter interference, but other quantum properties of matter, such as quantum superposition, tunneling, entanglement and teleportation can be utilized in a controlled fashion in technological components that can significantly outperform their classical counterparts. Examples are found in quantum information, including quantum cryptography and quantum computation [16,17]. Additionally, squeezed states and entanglement are effects that are utilized in quantum metrology, or sensing [23].

As an extension to atomic systems, molecules can be utilized as more flexible experimental systems due to their extra degrees of freedom. However, the extra degree of freedom comes at a cost, since the increasing complexity of the system makes it more difficult to cool and control. Therefore, small molecular systems, such as diatomics are of special interest. The rovibrational levels of ultracold molecules can be utilized as sensitive probes in fundamental physics experiments including tests of quantum electrodynamics (QED), measurement of and search for a space-time variability of the proton-to-electron mass ratio [24,25]. High resolution experiments with high accuracy requirements benefit from highly stable and long-lived systems on which to perform the measurement. The lifetime of the rovibrational states of molecules can be on the order of hours [26], or even as long as days, [27] and they are therefore strong candidates for such experiments. Another important addition to the repertoire provided by dipolar molecular systems is the dipole moment. As an example, the long range and anisotropic dipole interaction is important for the properties of e.g. quantum gases [28].

An other example of flexibility that molecular systems offer on account of their extra degrees of freedom is molecular wave packet interferometry (MWPI) based on the internal degrees of freedom of the molecule, e.g. the vibrational degree of freedom [29–31]. Since molecular vibrational periods are typically on the order of 10 fs to $\sim$ ps, femtosecond pulses have enough bandwidth to coherently excite several molecular vibrational eigenstates, with the central frequency of the laser on resonance with the ground and some wanted target

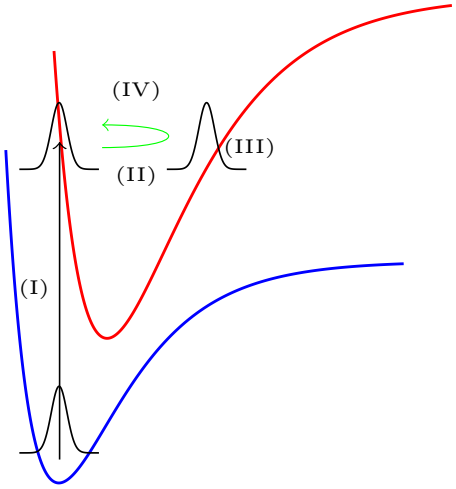

Figure 1.1: Schematics of the principle of vibrational molecular wave packet interferometry (MWPI). A fs pulse generates a vibrational wave packet on an excited state potential (red) from the initial state on the ground electronic potential (blue) (I). The excited wave packet starts evolving outwards under the influence of the excited state potential (II). The wave packet stops when reaching the outer classical turning point (III) and subsequently moves inwards (IV). This cycle repeats itself after reaching the classical inner turning point. A second, identical replica of the excited wave packet is created by an identical, but time-delayed, fs pulse, step (I) repeated. The two wave packet interferes with each other in a manner dependent on the time delay.

excited vibrational state [29]. Consequently, femtosecond lasers are suitable tools to create coherent superpositions of vibrational wave packets (WP's) in molecules. Indeed, two time delayed femtosecond pulses with a definite optical phase angle were used to create two identical, but time delayed, wave packets (e.g. vibrational wave packets in molecules) on an excited electronic potential curve from the ground electronic curve, see Figure 1.1 for a schematic illustration of the process. Constructive and destructive interference between the two wave packets can be selectively induced by the delay of the second pulse [32, 33]. Due to the larger number of degrees of freedom of the molecules (vibrations and rotations), molecular WPI is a much larger experimental challenge than atomic WPI. In molecular setups the thermal rotational distribution and the different rotational constants of the two electronic curves are found to be the major source of decoherence [32, 33].

Rather than vibrational wave packets, rotational wave packets have recently been proposed as a means for quantum information processing [34, 35]. The rotational degree of freedom is also an important part of several applications in molecular physics, e.g. chemical reaction dynamics [36–38] and implementation of quantum information, e.g. as qubits using polar molecules as integrated part of a hybrid quantum processor [35,39]. We must therefore find a way to control the rotational degree of freedom. In e.g. chemical reaction dynamics, where a reaction channel is activated not only if enough energy to overcome the activation barrier is provided, but also if the reactants are oriented/aligned in such a way that the

relevant chemical bounds meet in the collision process [40]. Here, it is in order to distinguish between two closely related quantities that relate to the angular confinement along a given spatial direction, e.g. a laboratory axis or a polarization vector of an external field are orientation and alignment [41]. Orientation distinguishes between parallel and anti parallel confinement along the given axis, whereas alignment does not. Mathematically orientation is given by $\langle \cos\theta \rangle$ and alignment by $\langle \cos^2\theta \rangle$. In order to achieve orientation / alignment at field-free conditions pulses, short temporal profiles (usually fs pulses) significantly shorter than $T_{rot} = (2B)^{-1}$, with B the rotational constant, can be utilized [41–43]. Both resonant and non-resonant pulses are used to this end [42]. In both cases a coherent wave packet is achieved, in the resonant case by the dipole interaction [42] and in the off-resonance case due to the polarizability anisotropy of the molecule [42].

1.1 Molecular Ions in Quantum Technology

Molecular ions are in many applications an appealing alternative to neutral species, which can capitalize particularly well on the long lifetimes of the rovibrational states since ion traps provide long storage times, minutes [44] or even hours, and a pure experimental environment [45, 46]. The ion traps can provide internally, as well as translationally, cold molecular ions [47–50]. Many applications which are implemented by neutral molecules can also utilize ionic species. In some cases, such as the simplest molecular system H_2^+, a system of particular interest in theoretical quantum chemical theoretical studies due to its simplicity, is inherently ionic. Rovibrational spectroscopy of the HD^+-ion is proposed and demonstrated as a sensitive spectroscopic method to measure the fundamental ratio of the electron to proton (or neutron) masses and an improved limit on its (their) time variation(s) [51, 52].

In addition to high precision spectroscopy, molecular ions can also be utilized as information carriers in quantum information applications, where they can also benefit from the long storage time provided by ionic traps [53–58]. Both polar and apolar molecular ions are considered as systems in which to implement the information processing [55, 57, 58]. Typically, the molecular state is destroyed in the information read-out process [48, 50, 59–61].

One method that avoids destroying the molecular state is quantum logical spectroscopy (QLS) [62]. Here the quantum state to be retrieved from one ion is coherently mapped via the common translational motion to a co-trapped atomic ion, the logical ion, on which the read-out is performed. This method is particularly of interest when reading out information of molecular states, since, due to their more complex internal structure, they are typically more difficult to retrieve than atomic states. An additional advantage is that measurement on the atomic ion leaves the state of the molecular ion unaltered and is therefore non-

destructive, a fact that makes the method interesting in quantum information processing. Several methods make use of laser systems to drive the transitions [61,63,64]. These setups can transfer the information efficiently, but the coherent lasers make them system specific. One way to achieve a general experimental setup is to replace the lasers with microwaves [55].

The permanent dipole moment of polar molecular ions is an effective tool implementing quantum technologies, and has been utilized in various applications [53,55,65,66]. One issue with polar molecular ions is that they interact with the surrounding black body radiation, which induces rotational redistribution. Apolar molecular ions on the other hand do not interact with the black body radiation due to their vanishing permanent dipole moment [57]. Therefore analogous implementation of QLS has been proposed and demonstrated, by utilizing the spin-rovibrational states of an apolar molecular ion (N_2^+) [57]. The decoupling from the black body radiation makes the method particularly sensitive, and the long storage time afforded by the decoupling makes the method suitable for implementation of molecular qubits [57].

Quantum technology relies on precise manipulation of the quantum system of interest, which in turn requires accurate spectroscopic knowledge of the relevant molecular parameters, such as e.g. dipole moments. In the previous paragraphs we have discussed quantum spectroscopic methods that can provide us with this information. Another prerequisite to be able to coherently manipulate a quantum state is a precise coherent relation between the relative phases and amplitudes. In a thermal ensemble the precise relation is gradually lost, i.e. incoherence is built up, with increasing temperature. In contrast, the colder the ensemble, the fewer number of states are populated. One usually refers to cold when temperatures are lower than 1 K and down to mK and ultracold at temperatures lower than mK [67]. At ultracold temperatures, the thermal ensemble approaches a pure state. Therefore, a lot of effort has been devoted into preparing cold polar molecular ions, where Drewsen et. al were the first to produce translationally and internally cold molecular ions [44, 50, 68, 69]. Since then many more groups have been able to produce a wide range of cold molecular ions [59, 60, 66, 70]. We will now shortly discuss how cold molecular ions, which can be utilized for quantum technological applications, can be achieved.

1.2 Methods for creating and storing cold molecules and molecular ions

Cold atoms are routinely achieved in the lab by laser cooling, and with subsequent evaporative cooling ultracold atoms can be achieved [5]. The monochromatic laser exerts a decelerating force on the atom when the frequency of the laser matches a resonance within the atom [5]. Laser cooling is however not generally applicable to molecules due to their

more complex internal structure. Notwithstanding, certain molecules have been successfully laser cooled [71, 72]. To date, alternative methods need to be devised for cooling molecules. Frequently these methods rely on pre-cooled atoms as the initiator. So called direct methods, which is a cooling strategy where formation of the molecules or molecular ions precedes the cooling step. One such method, which will be of relevance in this work, is called *Sympathetic cooling*, a cooling method where one type of particle is used to cool another type of particle, is particularly useful when cooling ions using preccoled atomic ions. The molecular ions lose kinetic energy by collisions with the coolants mediated by way of their mutual Coulomb interaction. The molecules are cooled down by successive collisions with the atomic ions, which are kept cold by Doppler cooling, allowing for the mixed ensemble to reach ultracold temperatures, reducing both energy and entropy. Cooling is efficient due to the strong coupling provided by the Coulomb interaction [27]. The efficiency of the method is only dependent on the masses and charges of the two types of particles, and in particular, independent on the details of their internal structures, which makes the method generally applicable, and can therefore be utilized to cool a wide range of molecular species [44, 45, 47, 60, 73, 74]. This is in contrast to the assembly methods, which rely on knowledge about the internal structure of the species, i.e. knowledge of the potential surfaces, coupling constants, about the internal structure of the species, i.e. knowledge of e.g. the potential surfaces, coupling constants, and Franck-Condon factors.

In practice, the so called Penning traps [75–77] in which a combination of electric and magnetic fields provide the trapping potential, Paul traps [78] which utilizes a combination of static and radio frequency electric fields are frequently used traps for ions. The Paul traps do not cause any Zeeman-splitting of the trapped ions due to the absence of magnetic field [27]. Optical traps are usually used for trapping neutral atoms and molecules [79], and so called hybrid methods, combining rf and optical fields have been used to trap ionic species [80,81]. In addition, pure optical traps are used to trap ions [82–84], with the benefit that the absence of rf-fields mitigates micromotion [83]. Paul traps come in quadrupole and linear variants. One advantage of the linear Paul trap is that the rf-field vanishes aling the long, linear axis, which allows it to store a large number of ions with little micromotion [27]. When temperatures of typically $T \sim 10$ mK or lower has been reached in the traps the trapped ions condense into a quasi-crystalline phase due to their mutual Coulomb repulsion, called a *Coulomb crystal* [85].

1.3 Motivation for the present work

Cold and ultracold molecular ions are systems that are candidates for extending the already successful role played by the corresponding atomic systems in e.g. quantum sensing [86]. The natural first extension to atomic systems are diatomic molecular ions. In the present work,

we study diatomic molecular ions in the confinement of a linear Paul trap with the aim at quantum technologies. All practical applications of the molecular ions in this context require very well defined initial states, i.e. cold species, both translationally and internally [46]. In this respect cold and ultracold trapped ions have another appealing feature, namely their condensation into a Coulomb crystal, which have some characteristics that make them excellent experimental tools for quantum technology applications such as e.g. high-precision spectroscopy [87, 88, 88, 89]:

1. The ions are translationally cold, corresponding to temperatures at the mK range or even lower.
2. The ions are strongly localized ($\sim \mu$m), allowing for single ion manipulation and observation.
3. The trap is immersed in a ultra-high vacuum environment, minimizing external perturbations, providing an ideal environment for precision measurements.
4. The trap provides for hours of storage times or even longer, allowing for experiments of long interaction and observation times.
5. The trapping potential is decoupled from the internal states.

Drewsen and coworkers were the first to demonstrate a method for producing and cooling MgH^+ and MgD^+-ions in which the molecular ions were created by a photo-chemical reaction between Mg^+-ions and neutral H_2 (D_2) which was leaked into the chamber [44]. After sympathetic cooling of the molecular ions by Mg^+-ions, the authors estimate the translational temperature to be below 100 mK, i.e., cold enough for crystallization. The resulting ion crystal was reported to contain more than 1000 ions with 95% being molecular [44]. Due to the long storage time the internal degrees of freedom are expected to be in equilibrium with the surrounding black body radiation at 300 K [44]. Other molecular ions have been produced and studied by various groups, e.g., various hydrogen molecular ions by the group of Schiller (e.g. H_2^+, HD^+ and D_2^+) [90–95]. Sympathetically cooled molecular ions can also be obtained by first creating the molecular ion using a technique based on state selective threshold-photoionization to produce molecular ions and subsequently sympathetically cool. The technique was demonstrated by Willitsch and coworkers on the N_2^+-ion [60], but the method is applicable to a wide range of molecular ions.

Sympathetic cooling of ions is effective for cooling the translational degrees of freedom due to the strong Coulomb interaction. But, as a consequence of the strong repulsive interaction, the scattering pair is normally prevented from ever being close enough to each other during a collision and the coupling of the internal states of the molecular ion to the electric field arising from the coolant ions is weak [46]. The internal degrees of freedom are therefore

more difficult to cool and it is required to produce cold internal states from different methods than sympathetic cooling [96]. Polar molecular ions may relax to the vibrational ground state via spontaneous emission given enough time [97]. Fortunately ion traps generally provide significant storage times to allow relaxation and e.g. MgH^+ ions can be found with 99.9% of the vibrational population in the vibrational ground state via equilibrium with the surrounding black body radiation at 300 K [26]. Once the vibrational ground state is attained, one can think of cooling the rotational degree of freedom. Extensive work on cooling the rotational degree of freedom of e.g. the MgH^+-ion has been performed [26,50,68,98,99]. It has been demonstrated that MgH^+-ions can be produced with a ground state population of more than 80 % corresponding to a thermal ensemble of 8.5 K after about 100 s of cooling [47]. These molecular ions have been used in applications, such as microwave quantum logic spectroscopy [55]. Rotational cooling of polar molecular ions has also been achieved by the group of Schiller, using the HD^+-ion as a model system [59]. Here rovibrational cooling was achieved by applying two cw-lasers for optical pumping and subsequent spontaneous decay to the ground state. Examples of applications are rotational spectroscopy [100], test of quantum electrodynamics and precise determination of fundamental constants [52], test of time variation of the electron and nuclear masses [51].

Alternatively, molecular ions can be produced in a rovibrationally state-selective way by resonantly enhanced photon threshold photo-ionization [60, 96] from neutral precursor molecules. Internally ($> 90\%$ population in the rovibrational ground state) and translationally cold N_2^+-ions were produced with this method and subsequent sympathetic cooling of the translational degree of freedom by co-trapped Ca^+-ions [60]. The method works as long as a state-selective photo-ionization method is applicable, which is the case for a number of polar and apolar diatomic molecules as well as polyatomic molecules e.g. H_2, O_2, CO, H_2O and more [60, 101]. These ions have been demonstrated to work as systems for e.g., charge transfer in reactions between ion-molecule reactions [102], millikelvin reactive collisions between atomic and molecular ions [103]. An overview of molecular ions in quantum technology can be found in [104].

1.3.1 Rotational state excitations when cooling molecular ions

The state specifically prepared ions are susceptible to rotational state redistribution from various sources. Polar molecules and molecular ions admit dipole allowed transitions between rotational states driven by interactions with the surrounding black body radiation (BBR). The coupling to the background field can potentially reduce the lifetimes of the internal states of molecules and molecular ions [105, 106].

Apolar molecular ions are unaffected by rotational redistribution from the BBR since, by symmetry, they lack dipole allowed transitions. They are, however, not completely

protected from rotational redistribution. A source of rotational redistribution is the neutral gas present in the chamber, which can affect the rotational distribution within the molecular ions via inelastic collisions. An alternative strategy, equally viable for both polar and apolar molecular ions, is one where the production and experimental regions are separated from each other by means of two separate traps, each in their separate chamber [107]. In the two-trap scenario, the molecular ions which are introduced to the second trap are already prepared in an internally state selective manner, whether polar or apolar. This strategy automatically separates the ions of experimental interest and the reactants, and in the case of polar molecular ions, the experimental chamber can be coated with a shielding material from the background radiation, thus mitigating the problem of rotational heating from BBR excitation [107].

The Coulomb field arising from the coolant atomic ions, which leads to the cooling of the molecular ions, can also couple to the internal degrees of freedom of the molecular ions, and in particular to the rotational degree of freedom. The initially well prepared internal state (we consider only a pure ground state in our work) can then undergo a rotational state redistribution. We present a study of rotational excitations in sympathetic cooling of polar and apolar diatomic molecular ions.

1.3.2 Prospects of using diatomic molecular ions for Ramsey like rotational interferometry

The wave-particle duality allows us to take advantage of the interference effect to use massive particles to implement sensitive spectroscopic devices, as done in e.g. Ramsey interferometry [3]. In this context, the rotational states of molecular ions have been proposed and used as a quantum system for the implementation of high-precision spectroscopy and quantum information processing.

As we have discussed above, a Coulomb crystal formed by cold molecular ions within a linear Paul trap would provide an ideal environment in which to implement a highly sensitive interferometer, due mainly to long storage times, low enviromental effects and single ion addressability. Here translationally and vibrationally cold MgH^+ ions can be readily achieved [26, 97] with a narrow rotational state distribution [47].

Furthermore, rather than using resonant fs-laser pulses, coherent rotational state transitions can be achieved without altering the vibronic state of the molecule by applying off-resonance fs-pulses to the molecular ion. The off resonance pulse will not excite vibrational states if the molecule is stiff enough such that rovibrational coupling is weak. Therefore, the choice of off-resonant pulses reduces rotational decoherence, offering a great advantage over vibrational wave packet interferometry. Moreover, since off-resonance pulses interact

with the molecular ions via (the square of) the electric field envelope instead of the instantaneous value of the field, which is the case for resonant pulses, no phase-locking between pulses is required, thus providing another major experimental simplification. Additionally, with off-resonance fs pulses the method is generally applicable and can be extended to other species as long as the pulses remain off-resonance and as long as the vibrational degree of freedom remains decoupled from the rotational motion, i.e. as long as the molecular ion is stiff enough.

Considering all these advantages, in this work, we propose the implementation of a Ramsey-type interferometric scheme based on the rotational levels of a trapped and sympathetically cooled MgH^+ molecular ion in the confinment of a linear Paul trap [108], using off-resonance fs laser pulses to drive the rotational wave packet dynamics.

1.4 Thesis structure

This thesis is organized as follows: The relevant theoretical background for describing molecular rotation and methods we used are presented in Chapter 2. The calculations are performed by numerically integrating the Schrödinger equation using a FORTRAN based library, called QDYN [109]. A computational implementation for the study of the quantum dynamics of molecular rotations has been developed as an extension of an existing code. The details of this implementation are presented in Chapter 3. We present our investigation on potential internal state excitation arising from sympathetic cooling of diatomic molecular ions in Chapter 4. Thereafter we consider an application of cooled molecular ions, namely a Ramsey-like interferometer, based on the molecular rotational dynamics controlled by two time-delayed off resonance femtosecond laser pulses in Chapter 5. The thesis is concluded in Chapter 6 where we present our conclusions along with an outlook on future work.

2 Theoretical methods

In this chapter we shortly review the theoretical background of this thesis. The study of objects at the molecular level are governed by quantum mechanics. Since the present work is concerned with molecular rotation, and the coupling of the angular degree of freedom with external fields, we present the Hamiltonians that generate the rovibrational motion of diatomic molecular ions as well as their interactions with external electric fields. Moreover, we review the classical scattering dynamics of two charged particles which is relevant to our studies on sympathetic cooling. Throughout this thesis, the dynamics of diatomic molecular ions is studied. In the following, we consider the molecule as a rigid rotor and review the dynamics of rigid rotors starting from a classical picture which we then translate into its corresponding quantum description.

2.1 Rigid rotor

Classically, the kinetic energy of a rotating rigid body can be written in terms of the so called *moment of inertia tensor*, I, and the angular momentum, ω [110],

$$T_{rot} = \frac{1}{2}\vec{\omega}^T I \vec{\omega}, \tag{2.1}$$

see Appendix C. The moment of inertia and the angular velocity relate to the angular momentum, $\vec{\mathbf{L}}$, as

$$\vec{\mathbf{L}} = I\vec{\omega}, \tag{2.2}$$

see Appendix C. The moment of inertia tensor is represented by a real symmetrical matrix, and therefore it can always be diagonalized. The eigenvalues are known as the *principal moments of inertia* and the eigenvectors are called the *principal axes* [110]. Labeling the principal axes a, b, c, the expression for the kinetic energy, Eq. (2.1), becomes particularly

simple in terms of the principal moments of inertia,

$$\begin{aligned} T_{rot} &= \frac{1}{2}\left(I_a\omega_a^2 + I_b\omega_b^2 + I_c\omega_c^2\right) \\ &= \frac{L_a^2}{2I_a} + \frac{L_b^2}{2I_b} + \frac{L_c^2}{2I_c}, \end{aligned} \tag{2.3}$$

where the relation between the moment of inertia and the angular momentum, Eq. (2.2), has been used. In particular, for two point particles of mass m_1 and m_2 at distance R apart, rotating about an axis through the common mass center perpendicular to the axis joining the two,

$$I_a = \mu R^2, \quad I_b = I_c = 0. \tag{2.4}$$

Here, I_a corresponds to the moment of inertia parallel to the molecular axis and I_b, I_c correspond to the moment of inertia perpendicular to the axis, $\mu = \frac{m_1 m_2}{m_1+m_2}$ is the reduced mass of the particles. The motion of the relative distance is effectively equivalent to the motion of a single body with the reduced mass.

The kinetic energy operator of a diatomic molecule within the rigid rotor approximation can be obtained by quantizing the kinetic energy in Eq. (2.3) with the moments of inertia given by Eq. (2.4). Since molecules are quantum mechanic objects, they need to be treated within the framework of quantum mechanics. For diatomic molecules, the square of the classical angular momentum, L^2, goes into the square of the total angular momentum operator, $\hat{\mathbf{J}}^2$, and consequently the description of the rotating molecule is given by a rotational Hamiltonian of the form [111]

$$T_{rot} = \frac{L^2}{2\mu R^2} \rightarrow \hat{\mathbf{H}}_{rot} = B\hat{\mathbf{J}}^2, \tag{2.5}$$

where the rotational constant is $B = \frac{1}{2\mu R_e^2}$ and R_e is the equilibrium distance between the two nuclei. We use the quantum mechanical standard notation of $\hat{\mathbf{J}}$ for the total angular momentum, since $\hat{\mathbf{L}}$ is used for the orbital angular momentum of electrons. Here, the eigenfunctions of $\hat{\mathbf{J}}^2$ are the well known spherical harmonics, $Y_j^m(\theta,\phi) = \langle\theta,\phi|j,m\rangle$ [112], where

$$\begin{aligned} \hat{\mathbf{J}}^2\,|j,m\rangle &= \hbar^2 j(j+1)\,|j,m\rangle\,, \quad j = 0,1,2,3\ldots \\ \hat{\mathbf{J}}_z\,|j,m\rangle &= \hbar m\,|j,m\rangle\,, \quad m = -j,-j+1\ldots,0\ldots,j-1,j, \end{aligned} \tag{2.6}$$

and $\hat{\mathbf{J}}_z$ is the z-component of the angular momentum (with the z-axis parallel to the internuclear axis). Therefore, the rotational eigenvalues of a rigid rotor molecule follow from the time-independent Schrödinger equation, $\hat{\mathbf{H}}_{rot}\,|j,m\rangle = E_j\,|j,m\rangle$ with $E_j = Bj(j+1)$. Since the rigid rotor approximation ignores the vibrational degree of freedom, and thereby also rovibrational coupling, it reduces the dimensionality of the problem, and therefore it significantly simplifies the calculations of the molecular dynamics.

2.2 Internal Dynamics of Diatomic Molecules

Rotations in real molecules are never completely rigid and it is sometimes necessary to go beyond this approximation, e.g. when the molecule is particularly floppy, or in particular for highly excited vibrational states where an-harmonic effects of the real potential are more important [113]. Changes in the nuclear configuration do not only have consequences for the moment of inertia of the molecule, but since the electronic configuration also depends on the nuclear configuration, the electrical properties of the molecule, such as their dipole moments and polarizabilities, change with alterations in the nuclear configuration [113]. The theoretical foundation for calculating molecular properties rests on the *Born-Oppenheimer approximation* [114], which we will now discuss.

2.2.1 The Born-Oppenheimer Approximation

In the following description we follow Brandsen and Joachain closely [2, 111]. Molecules (and molecular ions) are bound states of two or more nuclei and electrons. Therefore, the description of a molecule requires, in principle, to solve the Schrödinger equation involving the kinetic energy of all nuclei and electrons as well as the potential energy exchange between the nuclei, between the electrons, and between nuclei and electrons. The Hamiltonian is

$$\hat{\mathbf{H}} = \hat{\mathbf{T}}_N + \hat{\mathbf{T}}_e + \hat{\mathbf{V}}_{NN} + \hat{\mathbf{V}}_{ee} + \hat{\mathbf{V}}_{Ne}. \tag{2.7}$$

Needless to say this is a daunting task. Fortunately, the large mass differences between electrons and nuclei allow us, to a good approximation, to consider the motion of the electrons separately from that of the nuclei (the mass of the lightest nucleus, the proton is approximately 1860 times larger than the mass of the electron). On account of the significantly smaller electron mass, they respond very quickly (practically instantaneously) to changes in the nuclear configuration. We can therefore solve the electronic problem approximately for fixed nuclear configurations, where the total molecular wave function can be written as a product of an electronic, ϕ_k, and nuclear, χ_k, wave function on each electronic surface, k,

$$\Psi(\mathbf{r}, \mathbf{R}) = \sum_k \phi_k(\mathbf{r}; \mathbf{R})\chi_k(\mathbf{R}), \tag{2.8}$$

where the sum runs over all electronic surfaces. Here $\mathbf{r}$ and $\mathbf{R}$ denote the electronic and nuclear coordinates, respectively. Notice that the electronic wave function depends parametrically on the nuclear coordinates. This allows for the so called clamped nuclear approximation, where the nuclear coordinates are frozen and the electronic wave function and eigenenergies are calculated at each nuclear configuration. In this frozen nuclear configuration, the nuclear kinetic energy operator vanishes and the nuclear-nuclear potential energy is just a constant which has no influence on the eigenfunctions, and is therefore left out of

the calculations that are used to obtain the electronic wave function. Once the set of electronic eigenfunctions, $\phi_k(\mathbf{r};\mathbf{R})$, and eigenenergies, $\varepsilon_k(\mathbf{R})$, have been obtained for each fixed nuclear configuration by diagonalization of the electronic Schrödinger equation using quantum chemical methods, see e.g. [114], the nuclear problem can be solved for each potential surface,

$$\left[\hat{\mathbf{T}}_N + \hat{\mathbf{V}}_{NN}(\mathbf{R}) + \varepsilon_k(\mathbf{R})\right] \chi_k(\mathbf{R}) = E\chi_k(\mathbf{R}). \tag{2.9}$$

So the nuclei problem is given by a potential which is a sum of the electronic energy arising from the electrons and the nuclear-nuclear repulsive energy.

The method of separating the electronic and nuclear degrees of freedom, known as the Born-Oppenheimer approximation, is the underpinning approach of most quantum chemical methods and is described in more detail in Appendix A. As shown in the Appendix, the nuclear kinetic operator can couple different electronic surfaces if, for any nuclear configuration, we have $\varepsilon_k(\mathbf{R}) \approx \varepsilon_{k'}(\mathbf{R})$ for a pair of electronic states k, k'. Thus the approximation is only valid for well separated electronic states.

The motion of the two nuclei can be separated into the motion of the center of mass and that of the relative distance between them. The dynamics of the center of mass is irrelevant to the internal electron dynamics and can be integrated out, as long as the two degrees of freedom are separable. In an isolated molecule, with no external forces acting, this is always the case. In a sympathetic cooling scenario of ions, the coupling between the translational and internal degrees of freedom is, in general, negligible [115]. The kinetic energy operator of the nuclei is given by $\hat{\mathbf{T}}_N = -\frac{\nabla^2_{\vec{R}}}{2\mu}$, where the Laplacian, $\nabla^2_{\vec{R}}$, is represented in spherical coordinates as

$$\begin{aligned}\nabla^2_{\vec{R}} &= \frac{1}{R^2}\frac{\partial}{\partial R}\left(R^2\frac{\partial}{\partial R}\right) + \frac{1}{R^2\sin\theta}\frac{\partial}{\partial\theta}\left(\sin\theta\frac{\partial}{\partial\theta}\right) + \frac{1}{R^2\sin^2\theta}\frac{\partial^2}{\partial\phi^2} \\ &\equiv \frac{1}{R^2}\frac{\partial}{\partial R}\left(R^2\frac{\partial}{\partial R}\right) - \frac{1}{R^2}\hat{\mathbf{J}}^2.\end{aligned} \tag{2.10}$$

The Hamiltonian of the internal motion of the molecule is

$$\begin{aligned}\hat{\mathbf{H}}_{rovib} &= -\frac{1}{2\mu R^2}\frac{\partial}{\partial R}\left(R^2\frac{\partial}{\partial R}\right) + V(R) + \frac{1}{2\mu R^2}\hat{\mathbf{J}}^2 \\ &\equiv \hat{\mathbf{T}}_R + V(R) + \frac{1}{2\mu R^2}\hat{\mathbf{J}}^2.\end{aligned} \tag{2.11}$$

Here, $V(R)$ is a Born-Oppenheimer potential curve. The first two terms describe the vibrational dynamics, whereas the third term is the rotational Hamiltonian. Applying the Hamiltonian, Eq. (2.11), to a rovibrational function, $\Psi(R,\theta,\phi) = \sum_{j,m} c_{jm}\frac{u_{jm}(R)}{R}Y_j^m(\theta,\phi)$, leads to the equations that each $u_{jm}(R)$ must satisfy

$$i\frac{\partial}{\partial t}u_{jm}(R) = \left(-\frac{1}{2\mu}\frac{\partial^2}{\partial R^2} + V(R) + \frac{j(j+1)}{2\mu R^2}\right)u_{jm}(R), \tag{2.12}$$

where the angular part has been integrated out using the orthonormality of the spherical harmonics.

2.2.2 Interaction with an electric field

A charge distribution can be expressed by its multi-pole expansion, see e.g. [116], where the first terms are the monopole, dipole and quadrupole moments. The monopole term is simply proportional to the total charge. The electronic density in molecules is, in general, unequally distributed on the constituent atoms and the chemical bonds, which leads to a molecular electric dipole moment if the molecule lacks a center of symmetry [113]. Unless the dipole moment is vanishing by symmetry, it is the leading contribution to the interaction, after the monopole [116]. The molecular dipole moment is $\vec{D}(\vec{R}) = -\sum_i \langle\psi \,|\, \hat{\mathbf{r}}_i \,|\, \psi\rangle + \sum_j Z_j \vec{R}_j$, where the first term is the dipole moment due to the electron distribution in the quantum state $|\psi\rangle$, and is calculated quantum mechanically, and the second term is the dipole contribution from the nuclei of charges Z_j and is calculated classically [114]. The dipole moment is obtained from quantum chemical methods, see [114] for an introduction to modern quantum chemistry and [117] for calculations of electric properties of the MgH^+-ion.

The dipole interaction with an external field is, see e.g. [113],

$$\hat{\mathbf{H}}_{int} = -\vec{D}(\hat{\mathbf{R}}) \cdot \vec{\varepsilon}(t), \tag{2.13}$$

where $\vec{D}(\hat{\mathbf{R}})$ is the dipole moment of the molecule, resulting from its inhomogeneous spatial electron density, and $\vec{\varepsilon}(t)$ is the strength of the external electric field. In the particular case of a diatomic molecule, or molecular ion, the dipole moment is directed along the molecular axis. Let $\hat{R}$ be the unit vector along the internuclear axis and $\hat{\varepsilon}$ the polarization vector of the electric field, which, without loss of generality, is chosen to point along the laboratory $\hat{z}$-axis. Furthermore let θ be the angle between the molecular axis and the electric polarization vector and ϕ the azimutal angle, then

$$\vec{D}(\hat{\mathbf{R}}) = D(\hat{\mathbf{R}})\hat{R} = D(R)(\sin\theta\cos\phi\hat{x} + \sin\theta\sin\phi\hat{y} + \cos\theta\hat{z}), \tag{2.14}$$

$$\vec{\varepsilon}(t) = \varepsilon(t)\hat{z}, \tag{2.15}$$

and the interaction Hamiltonian, Eq. (2.13) becomes

$$\hat{\mathbf{H}}_{int} = -D(\hat{\mathbf{R}})\varepsilon(t)\cos\hat{\theta}. \tag{2.16}$$

Thus, using Eqs. (2.5), (2.9) and (2.16), the final rotational Hamiltonian taking first order multipole interaction with the electric field into account is

$$\hat{\mathbf{H}} = \hat{\mathbf{T}}_R + V(R) + \frac{\hat{\mathbf{J}}^2}{2\mu R^2} - D(\hat{\mathbf{R}})\varepsilon(t)\cos\hat{\theta}. \tag{2.17}$$

Note that $D(\hat{\mathbf{R}}) \equiv 0$ for homonuclear molecules due to symmetry. Therefore, in this case we need to consider the interaction with the dipole moment induced by the field, i.e., the electric dipole polarizability.

A thorough discussion of the polarizability interaction can be found in Ref. [118] and we will be following them closely in the following discussion. Consider an electric field given by a modulated harmonic pulse with frequency ω and modulation envelope $\vec{\varepsilon}_0(t)$,

$$\vec{\varepsilon}(t) = \frac{1}{2}\left(\vec{\varepsilon}_0(t)e^{-i\omega t} + \vec{\varepsilon}_0(t)e^{i\omega t}\right). \tag{2.18}$$

Let the eigenstates of the field-free rotational Hamiltonian be $\{|i\rangle\}$ and denote the energy difference between states $|i\rangle$ and $|j\rangle$ divided by $\hbar$ as $\Delta\omega_{ij}$. The detunings $\Delta\Omega_{ij}^{\pm}$ are defined as

$$\Delta\Omega_{ij}^{+} = \omega - \Delta\omega_{ij}, \tag{2.19}$$

$$\Delta\Omega_{ij}^{-} = \omega + \Delta\omega_{ij}. \tag{2.20}$$

The condition for being on resonance with the transition $|i\rangle \leftrightarrow |j\rangle$ is that either $\Delta\Omega_{ij}^{+} = 0$ or $\Delta\Omega_{ij}^{-} = 0$. When neither condition is met for any pair, i, j, the pulse is off-resonance. For off-resonant interactions, the transition moments are proportional to $e^{i\Delta\Omega_{ij}^{+}t}$ or $e^{i\Delta\Omega_{ij}^{-}t}$ [112] which are rapidly oscillating functions of time. The rapid oscillations lead to cancellations in the transition amplitude and consequently the dipole interaction, when integrated over time, averages to zero [112]. However, notice that the dipole moment is a consequence of the electronic arrangement inside the molecule, an arrangement which can be affected by the presence of the external field [113]. Therefore, the dipole moment is a function of the external field, and the interaction of the field with this induced dipole moment must be considered for off-resonant pulses.

By expanding the dipole moment in a Taylor series as a function of the electric field strength, ε,

$$D_i(\hat{\mathbf{R}};\varepsilon) = D_i(\hat{\mathbf{R}};\varepsilon)\Big|_{\varepsilon=0} + \sum_j \frac{\partial D_i(\hat{\mathbf{R}};\varepsilon)}{\partial\varepsilon_j}\Big|_{\varepsilon=0}\varepsilon_j + \ldots \tag{2.21}$$

we can identify the polarizability tensor, $\overline{\overline{\alpha}}$, with components [43, 113]

$$\alpha_{ij}(\hat{\mathbf{R}};\varepsilon) = \frac{\partial D_i(\hat{\mathbf{R}};\varepsilon)}{\partial\varepsilon_j}\Big|_{\varepsilon=0}. \tag{2.22}$$

The next term in the expansion, the hyper-polarizability $\beta_{ijk}(\hat{\mathbf{R}};\varepsilon) \propto \frac{\partial^2 D_i}{\partial\varepsilon_j\varepsilon_k}\Big|_{\varepsilon=0}$ [43, 113], can become relevant when the polarizability vanishes by symmetry or for very strong fields (the interaction scales as ε^3). According to the Hellmann - Feynman theorem [119], the dependence of the energy on a parameter, P, is given by,

$$\frac{dE}{dP} = \left\langle \Psi \left| \frac{\partial\hat{\mathbf{H}}}{\partial P} \right| \Psi \right\rangle = \left\langle \frac{\partial\hat{\mathbf{H}}}{\partial P} \right\rangle. \tag{2.23}$$

Here, the parameter P is the electrical field strength ε and $|\Psi\rangle$ is the electronic state of the molecule, whence,

$$\frac{dE}{d\varepsilon} = \left\langle \frac{\partial\hat{\mathbf{H}}}{\partial\varepsilon} \right\rangle = -\langle D\rangle, \tag{2.24}$$

which we can integrate

$$E(\varepsilon) - E(0) = \int_0^{\varepsilon} \left\langle \frac{\partial \hat{\mathbf{H}}}{\partial \varepsilon'} \right\rangle d\varepsilon' = -\int_0^{\varepsilon} \langle D \rangle \, d\varepsilon'. \tag{2.25}$$

The electronic energy can then be expressed as

$$E(\varepsilon) = E(0) - \sum_i \left\langle D_i(\hat{\mathbf{R}}; \varepsilon = 0) \right\rangle \varepsilon_i - \frac{1}{2} \sum_{i,j} \left\langle \alpha_{ij}(\hat{\mathbf{R}}; \varepsilon = 0) \right\rangle \varepsilon_i \varepsilon_j - \ldots. \tag{2.26}$$

We identify the polarization interaction term of the Hamiltonian as $\hat{\mathbf{H}}_{pol} = -\frac{1}{2} \sum_{i,j} \alpha_{ij} \varepsilon_{0i}(t) \varepsilon_{0j}(t) \frac{2 + e^{2i\omega t} + e^{-2i\omega t}}{4}$ [118]. Upon neglecting the fast rotating terms, the interaction Hamiltonian takes the form

$$\hat{\mathbf{H}}_{pol}(t) = -\frac{1}{4} \boldsymbol{\varepsilon}_0(t) \overline{\overline{\alpha}} \boldsymbol{\varepsilon}_0(t). \tag{2.27}$$

Explicit formulas for the polarizability interaction within the two-photon rotating wave approximation can be found in [118]. In particular, the polarizability for a particular molecular electronic state g is

$$\boldsymbol{\alpha}_g^{q',q} = \sum_n \left(\frac{\mu_{gn}(q') \mu_{ng}(q)}{\omega_{ng} - \omega} + \frac{\mu_{gn}(q) \mu_{ng}(q')}{\omega_{ng} + \omega} \right), \tag{2.28}$$

where the sum is over all other electronic states n, q and q$'$ denote Cartesian coordinates of the radius vector and $\hbar\omega_{ng}$ is the energy difference between states n and g.

Specializing to a diatomic molecular ion, symmetry requires that the perpendicular principal moments, $\alpha_\perp(\hat{\mathbf{R}})$, of the polarizability tensor, be equal. The polarizability along the symmetry axis of the molecule, the parallel principal moment is $\alpha_{||}(\hat{\mathbf{R}})$. With θ the angle between the symmetry axis of the molecule and the polarization vector of the electric field, the polarization interaction in spherical coordinates is

$$\begin{aligned} -\frac{1}{4} \vec{\varepsilon}_0^{\dagger}(t) \alpha(\hat{\mathbf{R}}) \vec{\varepsilon}_0(t) &= -\frac{|\varepsilon_0(t)|^2}{4} \left(\alpha_\perp(\hat{\mathbf{R}}) \sin^2\theta + \alpha_{||}(\hat{\mathbf{R}}) \cos^2\theta \right) \\ &= -\frac{I(t)}{2\epsilon_0 c} \left(\Delta\alpha(\hat{\mathbf{R}}) \cos^2\theta + \alpha_\perp(\hat{\mathbf{R}}) \right), \end{aligned} \tag{2.29}$$

where use has been made of $\sin^2\theta = 1 - \cos^2\theta$ and defining the polarizability anisotropy $\Delta\alpha(\hat{\mathbf{R}}) = \alpha_{||}(\hat{\mathbf{R}}) - \alpha_\perp(\hat{\mathbf{R}})$ as well as the intensity of the field $I(t) = \frac{1}{2}\epsilon_0 c \varepsilon_0^2(t)$, in terms of the speed of light in vacuum, c, and the vacuum permittivity, ϵ_0. Thus, the total Hamiltonian in the Born-Oppenheimer approximation describing the rovibrational dynamics of a diatomic molecule interacting with an off-resonant electric field is

$$\hat{\mathbf{H}} = \hat{\mathbf{T}}_R + V(\hat{\mathbf{R}}) + \frac{\hat{\mathbf{J}}^2}{2\mu\hat{\mathbf{R}}^2} - \frac{I(t)}{2\epsilon_0 c} \left(\Delta\alpha(\hat{\mathbf{R}}) \cos^2\hat{\theta} + \alpha_\perp(\hat{\mathbf{r}}) \right). \tag{2.30}$$

The quadrupole interaction with the field is insignificant when either the dominant permanent dipole moment is finite or for interactions with off-resonant pulses where the polarizability of the molecule is the important coupling term [118], otherwise it should be considered. The interaction potential of the quadrupole moment of an axially symmetric charge distribution in an external electric field due to a Coulomb potential is given by, see Appendix B,

$$U_Q^a = \frac{Q^a \varepsilon^{3/2}}{4R^3}\left(3\cos^2\theta - 1\right) \rightarrow \hat{\mathbf{H}}_Q = \frac{Q_a \varepsilon^{3/2}}{4\hat{\mathbf{R}}^3}\left(3\cos^2\hat{\theta} - 1\right). \tag{2.31}$$

The rotational Hamiltonian for a diatomic molecule interacting with a Coulomb field via the quadrupole interaction is then

$$H_{quad} = \hat{\mathbf{T}}_R + V(\hat{\mathbf{R}}) + \frac{\hat{\mathbf{J}}^2}{2\mu\hat{\mathbf{R}}^2} + \frac{Q_a \varepsilon^{3/2}(t)}{4\hat{\mathbf{R}}^3}\left(3\cos^2\hat{\theta} - 1\right). \tag{2.32}$$

2.3 Approximations to the rovibrational Hamiltonians

The Hamiltonian, Eq. (2.30) that we have just derived, is the general rovibrational Hamiltonian for a diatomic molecule up to second order for off-resonant light molecule interaction. It operates on both radial and angular coordinates, thus describes both vibrational and rotational degrees of freedom of the molecule. Oftentimes, these degrees of freedoms are adiabatically decoupled during the dynamics and a reduced Hamiltonian is sufficient to describe the dynamics. In particular, when the rotational dynamics is of interest, a reduced Hamiltonian that only operates on the rotational degree of freedom is convenient, in which case the numerical effort involved in the dynamics is diminished by lowering the size of the Hilbert space in which the physical system is represented. In this work, we have made use of two different approximations, namely the *Rigid Rotor Approximation* (RRA) and the *Effective Rotor Approximation* (ERA), which are described in the following two subsections.

2.3.1 Rigid Rotor Approximation

The rigid rotor approximation (RRA) ignores the vibrational motion of the molecule, assuming that the molecule is rigid and does not change its bond length. Hence all radial operators in the Hamiltonian are set to their respective value at the equilibrium distance, R_e, and the Hamiltonian of Eq. (2.30) reduces to

$$\hat{\mathbf{H}}_{pol}(t) = B_e\hat{\mathbf{J}}^2 - \frac{I(t)}{2\epsilon_0 c}\left(\Delta\alpha(R_e)\cos^2\hat{\theta} + \alpha_\perp(R_e)\right), \tag{2.33}$$

where $B_e \equiv \frac{1}{2\mu R_e^2}$ is the rotational constant of the molecule. Analogously, the quadrupole interaction reduces to

$$\hat{\mathbf{H}}_{Qp}(t) = B_e \hat{\mathbf{J}}^2 + \frac{\varepsilon^{3/2}(t) Q_a(R_e)}{4} \left(3\cos^2\hat{\theta} + 1\right). \tag{2.34}$$

Finally, the Hamiltonian including the dipole interaction is

$$\hat{\mathbf{H}}_{dip}(t) = B_e \hat{\mathbf{J}}^2 - D(R_e)\varepsilon(t)\cos\hat{\theta}. \tag{2.35}$$

A real molecule is never completely rigid, and the rotational motion is modified by centrifugal distortion. As a consequence, the rotational energy becomes $E_J \approx Bj(j+1) - Dj^2(j+1)^2$ where $B \approx B_e - a\left(\nu + \frac{1}{2}\right)$ and ν is the vibrational quantum number and corresponds to a shift in the rotational energy due to rovibrational coupling. The first rotation distortion constant, D, arises from the bond stretch due to the rotational motion [111]. The effect of the rovibrational coupling increases with vibrational quantum number and the rotational distortion with rotational quantum number, and therefore the effect is lowest for low vibrational and rotational states. The coefficients a and D are molecule dependent and are smaller for stiffer molecules [113].

2.3.2 Effective Rotor Approximation

A more elaborate approximate model than the RRA is the Effective Rotor Approach [120] (ERA) in which the vibrational motion is taken into account in an average sense, based on an adiabatic separation of the vibrational and rotational degrees of freedom. This is the ansatz of ERA and is motivated by the fact that, in the absence of external fields, the energy and time-scale differences between the rotational and the vibrational motion are typically such that

$$E_{vib} \gg E_{rot},$$
$$\tau_{vib} \ll \tau_{rot}.$$

This ansatz is analogous to the adiabatic Born-Oppenheimer separation of electronic and nuclear degrees of freedom in molecular electronic structure calculations. Here, we present the model in the case of an interaction with an off-resonant fs-laser pulse. The wave function is defined on a Hilbert space of the tensor product of the vibrational and rotational degrees of freedom, and the Hamiltonian of the system can be expressed as

$$\hat{\mathbf{H}} = \hat{\mathbf{H}}_{vib} + \hat{\mathbf{H}}_{rot} + \hat{\mathbf{H}}_{int}, \tag{2.36}$$

where the individual terms of the Hamiltonian are

$$\hat{\mathbf{H}}_{vib} = \sum_{\nu} \varepsilon_{\nu} |\nu\rangle \langle\nu| \otimes \mathbb{I}, \tag{2.37}$$

$$\hat{\mathbf{H}}_{rot} = \frac{1}{2\mu} \sum_{\nu} \left\langle \nu \left| \hat{\mathbf{R}}^{-2} \right| \nu' \right\rangle |\nu\rangle \langle\nu| \otimes \hat{\mathbf{J}}^2, \tag{2.38}$$

$$\hat{\mathbf{H}}^{pol}_{int}(t) = -\frac{I(t)}{2\epsilon_0 c} \left(\Delta\alpha(\hat{\mathbf{R}}) \cos^2 \hat{\theta} + \alpha_{\perp}(\hat{\mathbf{R}}) \right). \tag{2.39}$$

The Schrödinger equation to be solved is

$$\hat{\mathbf{H}}\Psi(R, \theta, \phi) = E\Psi(R, \theta, \phi). \tag{2.40}$$

In analogy with the electron-nuclear Born-Oppenheimer approximation, we write the rovibrational wave function in the electronic ground state as [120]

$$\Psi(R, \theta, \phi) = \sum_{\nu} \psi_{\nu}(R; \theta)\chi_{\nu}(\theta, \phi), \tag{2.41}$$

where $\psi_{\nu}(R; \theta)$ is the vibrational wave function. It depends parametrically on the angle θ, but for diatomic molecules it is independent on ϕ by symmetry. $\chi_{\nu}(\theta, \phi)$ is the rotational wave function. Separating the vibrational and rotational degrees of freedom as discussed above, we focus first on the vibrational, Eq. (2.38), and interaction, Eq. (2.39), parts of the total Hamiltonian, (2.36),

$$\left(\hat{\mathbf{H}}_{vib} + \hat{\mathbf{H}}_{int}(t, R, \theta) \right) \psi_{\nu}(R; \theta) = E_{\nu}(\theta)\psi_{\nu}(R; \theta). \tag{2.42}$$

Since the pulses are off-resonance, the vibrational coupling due to the interaction will effectively average to zero due to the fast oscillation of the laser field. Therefore the effect of the interaction on the vibrational eigenfunctions is expected to be negligible. Then, perturbation theory can be applied and the vibrational wave function can be approximated as $\psi_{\nu}(R; \theta) \approx \psi^{(0)}_{\nu}(R) + \psi^{(1)}_{\nu}(R; \theta)$ [120]. Keeping only the zeroth order contribution, the problem reduces to a purely vibrational one (we drop the superscript)

$$\hat{\mathbf{H}}_{vib}\psi_{\nu}(R) = E_{\nu}\psi_{\nu}(R). \tag{2.43}$$

Using Eq. (2.43), we can find the eigenfunctions $\psi_{\nu}(R)$ for each vibrational state ν. Once the vibrational eigenfunctions are obtained, we can derive an effective Hamiltonian for the angular problem by averaging the radial quantities over the vibrational motion. Neglecting the off-diagonal elements, we integrate over the vibrational motion in a given vibrational state, $|\nu\rangle$,

$$\begin{aligned} \hat{\mathbf{H}}_{\nu}(t) &= \left\langle \nu \left| \hat{\mathbf{R}}^{-2} \right| \nu \right\rangle \frac{\hat{\mathbf{J}}^2}{2\mu} - \frac{I(t)}{2\epsilon_0 c} \left(\left\langle \nu \left| \Delta\alpha(\hat{\mathbf{R}}) \right| \nu \right\rangle \cos^2 \hat{\theta} + \left\langle \nu \left| \alpha_{\perp}(\hat{\mathbf{R}}) \right| \nu \right\rangle \right) + E_{\nu} \\ &= B_{\nu}\hat{\mathbf{J}}^2 - \frac{I(t)}{2\epsilon_0 c} \left(\Delta\alpha_{\nu} \cos^2 \hat{\theta} + \alpha_{\perp,\nu} \right) + E_{\nu}. \end{aligned} \tag{2.44}$$

The expectation values in Eq. (2.44) are calculated from the eigenfunctions obtained from diagonalizing $\hat{\mathbf{H}}_{vib}$ and the subscript ν denotes an average over the vibrational state ν. $B_\nu = \frac{1}{2\mu}\left\langle \nu \left| \hat{\mathbf{R}}^{-2} \right| \nu \right\rangle$ is the rotational constant corresponding to the vibrational state ν. In this way, an effective rotational Hamiltonian can be obtained for each vibrational level by means of radial expectation values [120]. Note that, if the rotational dynamics takes place on a single vibrational level, the vibrational eigenvalue E_ν is simply an additive constant. Since the values of the parameters that enter in the ERA-Hamiltonian are obtained as averages over the full vibrational eigenfunctions rather than just the equilibrium values, it represents an improvement over the RRA-Hamiltonian. However, just like the RRA, it is still susceptible to rotational dispersion effects represented by the rotational distortion which are proportional to $j^2(j+1)^2$ [113].

We have neglected couplings between different vibrational states in the above analysis, which is justified for off-resonance pulses far off any electronic or vibrational resonance. In principle the angular motion can couple to the vibrational degree of freedom. This coupling is negligible for well separated energy scales of the two degrees of freedom [120]. Since the vibrational spacing is the largest for low lying vibrational states, indeed the rotational spacing is very small for vibrational states close to the dissociation energy, the approximation works best for highly bound, i.e., low-lying vibrational states.

2.4 Time evolution

The dynamics of the wave function is generated by the Hamiltonian and given by the time-dependent form of the Schrödinger equation [112]:

$$i\hbar\frac{\partial}{\partial t}\left|\psi(t)\right\rangle = \hat{\mathbf{H}}(t)\left|\psi(t)\right\rangle . \tag{2.45}$$

The evolution of a quantum state from an initial time t_0 to a later time t, $|\psi(t_0)\rangle \to |\psi(t)\rangle$ is determined by the unitary time evolution operator,

$$\left|\psi(t)\right\rangle = \hat{\mathbf{U}}(t,t_0)\left|\psi(t_0)\right\rangle . \tag{2.46}$$

For general time-dependent Hamiltonians that do not commute with themselves at different times the expression for the evolution operator is complicated and involves time ordering. Numerical methods for solving this problem can be found in e.g. [121]. A simplified solution can be found for time-independent Hamiltonians, where the evolution operator reduces to the familiar exponential

$$\hat{\mathbf{U}}(t,t_0) = \exp\left(-i\hat{\mathbf{H}}(t-t_0)\right). \tag{2.47}$$

This is the form of the evolution operator that we will be using in the work presented in this thesis.

3 Numerical methods

Our main goal is to study quantum dynamics, which means we have to numerically integrate the time-dependent Schrödinger equation (2.45). The numerical calculations of quantum dynamics used in the present work are implemented using a computational platform called QDYN [109]. It is a FORTRAN95-based numerical library capable of solving various problems involving quantum systems including statics, time-dependent problems and optimal control, developed inhouse. The library is able to model both open and closed quantum systems. Examples of systems that are treated are atoms, molecules and spin systems [122–127].

In order to perform the numerical integration, we first need to find a representation for the quantum system (wavefunctions and operators). Within the chosen representation, we then obtain a set of coupled differential equations to solve. In quantum mechanics, the wave function is usually, and in particular in the work presented here, defined on an infinite dimensional Hilbert space and the operators, such as the Hamiltonian, also act on this infinite dimensional Hilbert space. Any representation we chose for practical calculations on this Hilbert space is necessarily expressed in a finite dimensional basis. Such a truncation can be achieved by the use of a projection operator, P_N, which projects onto the N-dimensional space spanned by the basis [128]. We can motivate the truncation by noticing that, in a typical simulation, we only sample a finite portion of the energy space, leaving the rest of the energy space unaffected. E.g., interaction with a pulse of finite strength will only be able to couple a finite number of states around the intial state (typically the ground state). Important examples of numerical representations are the spectral- and pseudo-spectral representations. In the former representation a basis set of orthogonal functions is used, whereas in the latter localized functions are used [128].

Which basis is suitable depends on the particular problem under study. One commonly encountered example is when the system is described in terms of Cartesian coordinates, and

then a suitable choice is the Fourier basis [129], which is comprised by the eigenstates of the kinetic energy operator. This representation is already available in QDYN, and application of the Hamiltonian on a wave function in the position representation is

$$\hat{\mathbf{H}}\psi(\mathbf{x}) = -\frac{1}{2m}\nabla^2\psi(\mathbf{x}) + V(\mathbf{x})\psi(\mathbf{x}). \tag{3.1}$$

The action of the potential operator $V(\mathbf{x})$ is performed directly in configuration space, where spatial operators are diagonal, and is therefore given by a simple point-to-point product. The application of the kinetic operator is non-trivial, since $\hat{\mathbf{p}}^2 \to -\nabla^2$ (using atomic units $\hbar = 1$). To avoid the direct application of the ∇^2-operator, the wave function is Fourier-transformed to momentum space $\psi(\mathbf{x}) \to \tilde{\psi}(\mathbf{p})$, where the kinetic operator is diagonal, $\hat{\mathbf{p}}^2\tilde{\psi}(\mathbf{p}) = p^2\tilde{\psi}(\mathbf{p})$, and its action on the wave function is given by a simple point-to point product in momentum space. The resulting function is then transformed back to configuration space by inverse Fourier transformation [129]. Advantages of the Fourier representation is that it is numerically exact and efficient, by the numerically efficient scaling of the FFT [128].

For our purposes, in the study of rotational dynamics of molecular ions, spherical coordinates is the natural representation. Therefore, the methods used by the QDYN-library had to be extended to allow for a spherical coordinates representation. In the first part of this chapter, Section 3.1, we discuss the relevant representations for our implementation of spherical coordinates and we present the numerical methods used for the implementation of the radial- and angular coordinate calculations. For the angular coordinates, we have implemented two additional methods, the Discrete Variable Representation (DVR) discussed in Section 3.1.1 and the Finite Basis Representation (FBR) in Section 3.1.2. A thorough description of these methods can be found in e.g. [128]. In the second part of this chapter we shortly describe the numerical time-propagation method. For the present work, we use one of the several methods available in QDYN, based on the expansion of the time evolution operator in Chebychev polynomials [129].

3.1 Representation of wave functions and operators

For the purpose of solving the rovibrational dynamics of diatomic molecular ions, spherical coordinates are the natural representation, $\Psi = \Psi(r,\theta,\phi) = \sum_{j,m} c_{j,m}\frac{u_{jm}(r)}{r}Y_j^m(\theta,\phi)$, where the angular part of the wave function has been expanded in the eigenfunctions of the angular kinetic energy operator, $Y_j^m(\theta,\phi)$, i.e., the spherical harmonics. Applying the rovibrational Hamiltonian, Eq. (2.11), to this wave function results in

$$\hat{\mathbf{H}}_{eff}(r)u_{j,m}(r) = -\frac{1}{2\mu}\frac{d^2u_{j,m}(r)}{dr^2} + V_{eff}(r)u_{j,m}(r), \tag{3.2}$$

for the radial part. Here $V_{eff}(r) = V(r) + \frac{j(j+1)}{2\mu r^2}$ and μ is the reduced mass of the molecule or molecular ion. Therefore, the radial degree of freedom can be represented by the methods of Ref. [129], already available in QDYN.

Rotations can be regarded as motion on the surface of a sphere, for which the spherical harmonics form a complete basis on $[-1, 1]$ [130]. Thus, any function defined on the sphere can be expressed as a linear combination of the spherical harmonics,

$$\psi(\theta, \phi) = \sum_{j=0}^{\infty} \sum_{m=-j}^{j} c_{j,m} Y_j^m(\theta, \phi). \tag{3.3}$$

The inner product of two functions on the sphere is

$$\langle \chi, \psi \rangle = \int_{\Omega} \chi^*(\theta, \phi), \psi(\theta, \phi) d\Omega, \tag{3.4}$$

where Ω is the solid angle. Since the spherical harmonics are orthonormal w.r.t. this inner product, the expansion coefficients, $c_{j,m}$, are given by

$$c_{j,m} = \int_{\Omega} Y_j^{*m}(\theta, \phi) \psi(\theta, \phi) d\Omega. \tag{3.5}$$

Of particular interest for our study is the special case when $m = 0$. In this case the expansion in Eq. (3.3) reduces to

$$\psi(x) = \sum_{j=0}^{\infty} a_j \tilde{P}_j(x), \tag{3.6}$$

where $x = \cos\theta$, and the normalized Legendre polynomials $\{\tilde{P}_j(x)\}_{j=0}^{\infty}$ are obtained from the Legendre polynomials $\{P_j(x)\}_{j=0}^{\infty}$. The Legendre polynomials form a complete basis in $[-1, 1]$ and satisfy $\int_{-1}^{1} P_l(x) P_n(x) dx = \frac{2}{2l+1} \delta_{l,n}$ [130], from which it follows that the functions $\tilde{P}_l(x) = \sqrt{\frac{2l+1}{2}}$ satisfy the orthonormality relation

$$\left\langle \tilde{P}_l \middle| \tilde{P}_n \right\rangle = \int_{-1}^{1} \tilde{P}_l(x) \tilde{P}_n(x) dx = \delta_{l,n}. \tag{3.7}$$

The wavefunctions in Eqs. (3.3) and (3.6) are expanded in a basis of orthogonal functions. These functions can be used as a spectral representation upon truncation to finite dimension. As we have discussed previously, one can also find a pseudo-spectral representation for the wave function. We will now start our discussion on the representations that have been implemented into QDYN as part of the work of this thesis by one such method.

3.1.1 Discrete Variable Representation (DVR)

For this part we will be following [128] closely. For the particular case in which $m = 0$ and $x = \cos\theta$, we aim to construct the basis functions of a representation in which the operator

$X = \cos(\theta)$, and consequently any operator $\cos^n \theta$, is diagonal [128]. There are several ways to construct a numerical representation of a function. One of the possibilities is to use the so-called grid collocation, where the numerical solution is exact on a finite set of points $\{x_\alpha\}_{\alpha=1}^N$,

$$\psi(x) \to (\psi(x_1), \psi(x_2), ..., \psi(x_N))^T. \tag{3.8}$$

The DVR is a pseudo-spectral method [131], in which the expansion of the wave function coincides with the original wave function on a set of grid points $\{x_\alpha\}_{\alpha=1}^N$,

$$\tilde{\psi}(x_\alpha) = \psi(x_\alpha) = \sum_{j=0}^{N-1} a_j \tilde{P}_j(x_\alpha), \tag{3.9}$$

for a set of global functions $\{\tilde{P}_j(x)\}_{j=0}^{N-1}$, for which the normalized Legendre polynomials are appropriate to our problem [130].

We therefore need a connection between the global basis set in Eq. (3.9) and the local representation in Eq. (3.8). The link is found in the collocation method of Gaussian quadrature [132], or more precisely the Gauss-Legendre quadrature [128], which is a standard way of evaluating definite integrals by approximating them by a weighted sum of the function value at specific points within the domain of integration. If the overlap $\langle \phi, \psi \rangle$ is evaluated using N evaluation points, one obtains an N-point Gaussian quadrature of the form [128]:

$$\langle \chi, \psi \rangle = \int_{-1}^{1} \chi^*(x)\psi(x)dx = \sum_{\alpha=1}^{N} w_\alpha \chi^*(x_\alpha)\psi(x_\alpha), \tag{3.10}$$

where the w_α' s are the weights, the x_α' s are the sampling points, and we have restricted to the domain $[-1, 1]$, where the Legendre polynomials are defined. In general, an N-point quadrature contains $2N$ unknown points (N weights and N quadrature points). Thus, the Gauss-quadrature is numerically exact for polynomials of order $2N - 1$ or lower [132].

Using the orthonormality relation of Legendre polynomials, Eq. (3.7) and Eq. (3.10), we notice that

$$\delta_{l,n} = \sum_{\alpha=1}^{N} w_\alpha \tilde{P}_l(x_\alpha)\tilde{P}_n(x_\alpha). \tag{3.11}$$

Defining a matrix $\mathbf{A}$, with elements $A_{\alpha,l} = \sqrt{w_\alpha}\tilde{P}_l(x_\alpha)$, it follows from Eq. (3.11) that $\mathbf{A}$ is unitary, $\mathbf{A}^\dagger = \mathbf{A}^{-1}$. Therefore, a unitary transformation on the Legendre polynomials can be defined as

$$\Theta_\alpha(x) \equiv \sum_j A_{\alpha,j}\tilde{P}_j(x). \tag{3.12}$$

Since the functions $\Theta_\alpha(x)$ satisfy

$$\begin{aligned}\Theta_\alpha(x_\beta) &= \sum_j A_{\alpha,j}\tilde{P}_j(x_\beta) = \frac{1}{\sqrt{\omega_\beta}}\sum_j A_{\alpha,j}A_{\beta,j} \\ &= \frac{1}{\sqrt{\omega_\beta}}\sum_j A_{\alpha,j}A^*_{j,\beta} = \frac{1}{\sqrt{\omega_\beta}}\mathbf{A}\mathbf{A}^\dagger = \frac{\delta_{\alpha,\beta}}{\sqrt{\omega_\beta}},\end{aligned} \tag{3.13}$$

they can be used as a basis for a pseudo-spectral collocation method such that $\psi(x) = \sum_{\alpha=1}^{N}\gamma_\alpha\Theta_\alpha(x)$. Seeing that the unitary transformation preserves orthonormality, we can obtain the coefficients γ_α as [128]

$$\begin{aligned}\int \Theta^*_\beta(x)\psi(x)dx &= \sum_\alpha \gamma_\alpha \int \Theta^*_\beta(x)\Theta_\alpha(x)dx \\ &= \sum_\alpha\sum_{i,j}\gamma_\alpha A^*_{\beta,i}A_{\alpha,j}\underbrace{\int \tilde{P}^*_i(x)\tilde{P}_j(x)dx}_{\delta_{i,j}} \\ &= \sum_\alpha \gamma_\alpha \underbrace{\sum_j A^*_{\beta,j}A_{\alpha,j}}_{(\mathbf{A}\mathbf{A}^\dagger)_{\alpha,\beta}} = \gamma_\beta.\end{aligned} \tag{3.14}$$

On the other hand,

$$\begin{aligned}\int \Theta^*_\beta(x)\psi(x)dx &= \sum_\delta \omega_\delta \underbrace{\Theta^*_\beta(x_\delta)}_{\delta_{\beta,\delta}/\sqrt{\omega_\delta}}\psi(x_\delta) \\ &= \sqrt{\omega_\beta}\psi(x_\beta),\end{aligned} \tag{3.15}$$

which leads to expansion coefficients of the form

$$\gamma_\beta = \sqrt{\omega_\beta}\psi(x_\beta), \tag{3.16}$$

and the wavefunctions can be expressed as

$$\psi(x) = \sum_\alpha \gamma_\alpha\Theta_\alpha(x) = \sum_\alpha \sqrt{\omega_\beta}\psi(x_\alpha)\Theta_\alpha(x), \tag{3.17}$$

or

$$\psi(x) \to (\sqrt{w_1}\psi(x_1), \sqrt{w_2}\psi(x_2), ..., \sqrt{w_N}\psi(x_N))^T. \tag{3.18}$$

In this representation, the potential energy operator is given by $V_{\alpha,\beta} = V(x_\alpha)\delta_{\alpha,\beta}$, and its action on the wave function is

$$V(x)\psi(x) \to (\sqrt{w_1}V(x_1)\psi(x_1), \sqrt{w_2}V(x_2)\psi(x_2), .., \sqrt{w_N}V(x_N)\psi(x_N))^T. \tag{3.19}$$

The expression for the angular momentum operator $\hat{\mathbf{J}}^2$ can be found recalling that $\hat{\mathbf{J}}^2\tilde{P}_j(x) = j(j+1)\tilde{P}_j(x)$ and expanding the wavefunction in the $\tilde{P}_j(x)$ basis [128]. Let $\phi(x) = \hat{\mathbf{J}}^2\psi(x)$.

Its representation in the DVR-basis is $\phi(x) = \sum_\beta \sqrt{\omega_\beta}\phi(x_\beta)\Theta_\beta(x)$. Then,

$$\begin{aligned}\gamma_\beta = \sqrt{\omega_\beta}\phi(x_\beta) &= \sqrt{\omega_\beta}\sum_j a_j \hat{\mathbf{J}}^2 \tilde{P}_j(x_\beta) \\ &= \sqrt{\omega_\beta}\sum_j \sum_\alpha A^*_{\alpha,j}\gamma_\alpha j(j+1)\frac{A_{\beta,j}}{\sqrt{\omega_\beta}} \\ &= \sum_\alpha \left(\sum_j \underbrace{A^*_{\alpha,j} j(j+1) A_{\beta,j}}_{\mathbf{J}^2_{DVR}} \right) \gamma_\alpha,\end{aligned} \tag{3.20}$$

where we identify the matrix in the parenthesis

$$\sum_j A^*_{\alpha,j} j(j+1) A_{\beta,j} = \sum_j (\mathbf{A})_{\beta,j}\, j(j+1) \left(\mathbf{A}^\dagger\right)_{j,\alpha}$$

as the representation of the angular momentum operator,

$$\mathbf{J}^2_{DVR} = \mathbf{A}\mathbf{J}^2\mathbf{A}^\dagger, \tag{3.21}$$

where $\mathbf{J}^2 = diag(0, 2, ..., j(j+1), ...)$. Here, we notice an analogy between the DVR-representation of the kinetic energy operator and its representation in a Fourier basis for Cartesian coordinates. The form of the kinetic operator is that of a unitary matrix $\mathbf{A}^\dagger$ that transforms the wave function to the conjugate space where the action of the kinetic operator is represented by a diagonal matrix $\mathbf{J}^2$, followed by the inverse transformation $\mathbf{A}$ back to the original space. In the Cartesian case, the transformation between configuration space and momentum space is performed using the efficient fast Fourier transform method and its inverse. Although there exists a fast Legendre transform [133], there does not exist a fast inverse Legendre transform, and therefore, for the DVR-representation, application of the full matrix, Eq. (3.21), is required.

In summary, the DVR-representation is analogous to the Fourier representation in Cartesian coordinates. In the DVR-representation, operators of the form $\cos^n(\theta)$ are represented by a diagonal matrix, just as local operators are in Cartesian coordinates. In both methods, the kinetic energy operator is implemented by first transforming to the corresponding reciprocal space where its representation is diagonal, and then the operator can be applied by vector multiplication in reciprocal space followed by an inverse transformation to configuration space. In DVR, this is realized by representing the kinetic energy operator as a full matrix. This can also be done for the Fourier representation, see e.g. [134], but here the efficient fast and inverse fast Fourier transforms are used to transform between configuration and reciprocal space. The fast Fourier transforms scale as $N \log N$ in comparison to N^2 for direct matrix-vector multiplication for a basis of size N [128], therefore providing a more efficient numerical representation of the kinetic energy operator.

3.1.2 Finite Basis Representation (FBR)

Alternatively to the DVR representation, one can construct a spectral representation, called the *Finite Basis Representation* (FBR). We start by considering the special case where $m = 0$. For this case, one can construct a representation using the (normalized) Legendre polynomials $\tilde{P}_j(x) = \langle x \,|\, j \rangle$ as a basis, where the matrix elements of a general operator are given by $O_{j',j} = \left\langle j' \middle| \hat{\mathbf{O}} \middle| j \right\rangle$. Since the Legendre polynomials satisfy

$$\hat{\mathbf{J}}^2 \tilde{P}_j(x) = j(j+1)\tilde{P}_j(x), \tag{3.22}$$

the matrix elements of the kinetic energy operator are simply given by $\left\langle j' \middle| B\hat{\mathbf{J}}^2 \middle| j \right\rangle = Bj(j+1)\delta_{j'j},\ j = 0, 1, 2, ..., j_{max}$. Therefore the kinetic energy operator is diagonal in this basis. By comparison with Eq. (3.21), we see that the transformation that relates the DVR and the Finite Basis Representation (FBR) $\mathbf{J}^2_{FBR} = \mathbf{A}^\dagger \mathbf{J}^2_{DVR} \mathbf{A}$ is given by the same transformation Matrix, $\hat{\mathbf{A}}$, that was used in the application of the $\hat{\mathbf{J}}^2$-operator in the DVR-method [128]. This transformation is analogous to the Fourier transform in the radial coordinate that renders the kinetic energy matrix diagonal.

The interaction operators relevant here, are proportional to either $x = \cos\theta$ or $\cos^2\theta$. These operators are not diagonal in the FBR, but the matrix elements of the operator $\hat{\mathbf{X}} = \cos\hat{\theta}$ can be found using the recurrence relation of the Legendre polynomials, Eq. (D.9),

$$(j+1)\sqrt{\frac{1}{2j+3}}\tilde{P}_{j+1}(x) = (2j+1)x\sqrt{\frac{1}{2j+1}}\tilde{P}_j(x) - j\sqrt{\frac{1}{2j-1}}\tilde{P}_{j-1}(x), \tag{3.23a}$$

where $j > 1$, and

$$\tilde{P}_0(x) = \frac{1}{\sqrt{2}}, \quad \tilde{P}_1 = \sqrt{\frac{3}{2}}x, \tag{3.23b}$$

and by multiplying with $\tilde{P}_{j'}(x)$ and using Eq. (D.7) we obtain [130]

$$\begin{aligned} \left(X^{FBR}\right)_{j',j} &= \int_{-1}^{1} \tilde{P}_{j'}(x) x \tilde{P}_j(x) dx \\ &= \frac{j+1}{\sqrt{(2j+3)(2j+1)}}\delta_{j',j+1} + \frac{j}{\sqrt{(2j+1)(2j-1)}}\delta_{j',j-1}. \end{aligned} \tag{3.24}$$

From this expression we immediately recognize the selection rule $\Delta j = \pm 1$. Eq. (3.24) is the matrix representation for the operator $\hat{\mathbf{X}}$ in the FBR-representation. The matrix representation for $\hat{\mathbf{X}}^2$ can be found by multiplying the recurrence relation Eq. (3.23a) by x

and repeating the process,

$$\begin{aligned}\left(X^2_{FBR}\right)_{j',j} = \int_{-1}^{1} \tilde{P}^*_{j'}(x)x^2\tilde{P}_j(x)dx =& \frac{(j+1)(j+2)}{(2j+1)(2j+3)}\sqrt{\frac{2j+1}{2j+5}}\delta_{j',j+2} \\ &+ \frac{1}{2j+1}\left(\frac{(j+1)^2}{2j+3} + \frac{j^2}{2j-1}\right)\delta_{j',j} \\ &+ \frac{j(j-1)}{(2j+1)(2j-3)}\sqrt{\frac{2j+1}{2j-3}}\delta_{j',j-2}.\end{aligned} \tag{3.25}$$

In summary, for $m = 0$, both the FBR and DVR allow for certain operators to be represented by diagonal matrices, the kinetic energy operator in the former and the potential operator in the latter representation. For our purposes, the difference between the two representations lies in how they represent the non-diagonal operators, where the FBR, on account of the recurrence relation, Eq. (3.23), provides a representation in banded, i.e. sparse, matrices for the potential operators, whereas the DVR requires a full matrix to represent the kinetic energy operator. Since the FBR-representation makes full use of the selection rules of the relevant potential operators, it serves as a more efficient representation of the rotational dynamics than the DVR-representation.

3.1.3 Uncoupled m-representation

Given that the problems in this thesis, the FBR representation is numerically more efficient than the DVR representation, we now extend the treatment to include non-zero m-states using the FBR representation. We still restrict ourselves to a Hamiltonian which conserves m, i.e., $\Delta m = 0$. This treatment is relevant for problems where the initial ensemble contains mixed rotational states, including non-zero m, e.g. a thermal initial ensemble, but where m is a good quantum number. This is the case, e.g., when the polarization vector of the external electric field driving the transition is constant, and if there are two pulses, both linearly polarized in the same direction. The relevant basis functions are now the associated Legendre functions, $P^m_j(x)$, with fixed m. Note that for a fixed m, j cannot attain values lower than $|m|$, and therefore $j_{min} = |m|$, which implies that the representation of the kinetic energy operator needs to be modified to

$$BJ^2_{j',j} = Bj(j+1)\delta_{j',j}, \quad |m| \leq j \leq j_{max}. \tag{3.26}$$

The matrix elements of the operator $\hat{\mathbf{X}}$ are obtained from the normalized associated Legendre functions, Eq. (D.13), and the recurrence relation Eq. (D.14), see Appendix D [130],

$$\begin{aligned}X^m_{j',j} &= \int_{-1}^{1} \tilde{P}^m_{j'}(x)x\tilde{P}^m_j dx \\ &= \sqrt{\frac{(j+m+1)(j-m+1)}{(2j+3)(2j+1)}}\delta_{j',j+1} + \sqrt{\frac{(j+m)(j-m)}{(2j+1)(2j-1)}}\delta_{j',j-1}.\end{aligned} \tag{3.27}$$

Applying the recursion relation twice, we obtain the matrix representation for $\hat{\mathbf{X}}^2$ [130],

$$\begin{aligned}\left(X^2\right)^m_{j',j} =& \frac{1}{2j+3}\sqrt{\frac{(j+m+2)(j+m+1)(j-m+1)(j-m+2)}{(2j+5)(2j+1)}}\delta_{j',j+2} \\ &+ \left(\frac{(j+m+1)(j-m+1)}{(2j+3)(2j+1)} + \frac{(j+m)(j-m)}{(2j+1)(2j-1)}\right)\delta_{j',j} \\ &+ \frac{1}{2j-1}\sqrt{\frac{(j+m)(j+m-1)(j-m)(j-m-1)}{(2j+1)(2j-3)}}\delta_{j',j-2}.\end{aligned} \tag{3.28}$$

3.1.4 Coupled m-representation

In order to treat operators that couple different m-states, such as e.g. $\sin\hat{\theta}e^{\pm i\hat{\phi}}$, a full representation, i.e., one that includes all $2j+1$ m-states for each j, needs to be implemented. In the FBR-representation, the wave function is written as $|\psi\rangle = \sum_{j=0}^{\infty}\sum_{m=-j}^{j} c_{j,m}\,|j,m\rangle$,

$$\psi \rightarrow \begin{pmatrix} c_{j=0,m=0} \\ c_{j=1,m=-1} \\ c_{j=1,m=0} \\ c_{j=1,m=1} \\ \vdots \\ c_{j=j_{max},m=j_{max}} \end{pmatrix}, \tag{3.29}$$

where $\langle\phi,\theta\,|\,j,m\rangle = Y_j^m(\theta,\phi)$. The index i of the wave function is related to the quantum numbers (j,m) by

$$i = (j+1)^2 - j + m = j(j+1) + m + 1. \tag{3.30}$$

The matrix elements of the kinetic energy operator are simply $B\left\langle j',m'\right|\hat{\mathbf{J}}^2\left|\,j,m\right\rangle = Bj(j+1)\delta_{j',j}\delta_{m',m}$, or

$$\hat{\mathbf{J}}^2 = diag(0,2,2,2,\ldots,\underbrace{j(j+1)}_{2j+1\,\text{times}},\ldots,\ldots,\underbrace{j_{max}(j_{max}+1)}_{2j_{max}+1\,\text{times}}). \tag{3.31}$$

Examples of operators that couple m-states are

$$\begin{aligned}\hat{\mathbf{O}}_1 &= \sin\hat{\theta}\cos\hat{\phi} = \sin\hat{\theta}\frac{\exp\left(i\hat{\phi}\right)+\exp\left(-i\hat{\theta}\right)}{2} \\ &= \sqrt{\frac{2\pi}{3}}\left(Y_1^{-1}(\theta,\phi) - Y_1^1(\theta,\phi)\right)\end{aligned} \tag{3.32}$$

$$\begin{aligned}\hat{\mathbf{O}}_2 &= \sin\hat{\theta}\sin\hat{\phi} = \sin\hat{\theta}\frac{\exp\left(i\hat{\phi}\right)-\exp\left(-i\hat{\theta}\right)}{2i} \\ &= i\sqrt{\frac{2\pi}{3}}\left(Y_1^{1}(\theta,\phi) - Y_1^{-1}(\theta,\phi)\right)\end{aligned} \tag{3.33}$$

The non-zero matrix elements of the operators can be found by the integrals

$$\begin{aligned}(O_1)_{i',i} &= \int_\Omega Y_{j'}^{m'*}(\theta,\phi)\sin\theta\cos\phi Y_j^m(\theta,\phi)\sin\theta d\theta d\phi \\ &= \frac{1}{2}\sqrt{\frac{2\pi}{3}}\left(\int_\Omega Y_{j'}^{m'*}(\theta,\phi)Y_1^{-1}Y_j^m(\theta,\phi)\sin\theta d\theta d\phi\right. \\ &\left. - \int_\Omega Y_{j'}^{m'*}(\theta,\phi)Y_1^{1}Y_j^m(\theta,\phi)\sin\theta d\theta d\phi\right),\end{aligned} \tag{3.34}$$

and similarly

$$\begin{aligned}(O_2)_{i',i} &= \int_\Omega Y_{j'}^{m'*}(\theta,\phi)\sin\theta\sin\phi Y_j^m(\theta,\phi)\sin\theta d\theta d\phi \\ &= \frac{i}{2}\sqrt{\frac{2\pi}{3}}\left(\int_\Omega Y_{j'}^{m'*}(\theta,\phi)Y_1^{1}Y_j^m(\theta,\phi)\sin\theta d\theta d\phi\right. \\ &\left. - \int_\Omega Y_{j'}^{m'*}(\theta,\phi)Y_1^{-1}Y_j^m(\theta,\phi)\sin\theta d\theta d\phi\right),\end{aligned} \tag{3.35}$$

where i' and i are obtained from (j',m') and (j,m) from Eq. (3.30). Recalling that the spherical harmonics are given by $Y_j^m(\theta,\phi) = (-1)^m\frac{1}{\sqrt{2\pi}}\tilde{P}_j^m(\cos\theta)e^{im\phi}$, where $\tilde{P}_j^m(\cos\theta)$ are the normalized associated Legendre functions, the matrix elements of the operator $\hat{\mathbf{O}}_1$ are obtained from integrals of the type

$$\begin{aligned}(O_1)_{i',i} &= \int_\Omega Y_{j'}^{*m'}(\theta,\phi)\sin\theta e^{\pm i\phi}Y_j^m(\theta,\phi)\sin\theta d\theta d\phi \\ &= (-1)^{m'+m}\int_0^{2\pi}\frac{e^{i(m-m'\pm1)}}{2\pi}d\phi\int_0^\pi \tilde{P}_{j'}^{m'}(\cos\theta)\sin\theta\tilde{P}_j^m(\cos\theta)\sin\theta d\theta \\ &= (-1)\delta_{m',m\pm1}\int_{-1}^1 \tilde{P}_{j'}^{m'}(x)\sqrt{1-x^2}\tilde{P}_j^m(x)dx,\end{aligned} \tag{3.36}$$

where $x = \cos\theta$. The factor $\delta_{m',m\pm1}$ in Eq. (3.36) implies the selection rule

$$\Delta m = \pm 1. \tag{3.37}$$

The integral can be solved by making use of the recurrence relations Eq. (D.15), see Appendix D, with the result

$$\begin{aligned}\int_{-1}^1 \tilde{P}_{j'}^{m-1}(x)\sqrt{1-x^2}\tilde{P}_j^m(x)dx =& \sqrt{\frac{(j-m+1)(j-m+2)}{(2j+3)(2j+1)}}\delta_{j',j+1} \\ &- \sqrt{\frac{(j+m-1)(j+m)}{(2j+1)(2j-1)}}\delta_{j',j-1},\end{aligned} \tag{3.38a}$$

$$\begin{aligned}\int_{-1}^1 \tilde{P}_{j'}^{m+1}(x)\sqrt{1-x^2}\tilde{P}_j^m(x)dx =& -\sqrt{\frac{(j+m+2)(j+m+1)}{(2j+3)(2j+1)}}\delta_{j',j+1} \\ &+ \sqrt{\frac{(j-m)(j-m-1)}{(2j+1)(2j-1)}}\delta_{j',j-1},\end{aligned} \tag{3.38b}$$

from which we obtain another selection rule

$$\Delta j = \pm 1. \tag{3.39}$$

The final representation of the operator $\hat{\mathbf{O}}_1$ takes the form

$$\mathbf{O}_1 = \frac{1}{2}\begin{pmatrix} 0 & \sqrt{\frac{2}{3}} & 0 & -\sqrt{\frac{2}{3}} & 0 & \dots \\ \sqrt{\frac{2}{3}} & 0 & 0 & 0 & \frac{2}{\sqrt{5}} & \dots \\ 0 & 0 & 0 & 0 & 0 & \dots \\ -\sqrt{\frac{2}{3}} & 0 & 0 & 0 & 0 & \dots \\ 0 & \frac{2}{\sqrt{5}} & 0 & 0 & 0 & \dots \\ \vdots & \vdots & \vdots & \vdots & \vdots & \ddots \end{pmatrix} \tag{3.40}$$

and we see that it is indeed given by a sparse matrix. Repeated usage of the recurrence relations enable us to obtain the representations for other relevant operators, such as $\cos\hat{\theta}\sin\theta e^{\pm i\hat{\phi}}$, $\sin^2\hat{\theta}$ and $\sin^2\hat{\theta}e^{\pm i2\hat{\phi}}$.

3.1.5 Effective application of angular potential operators in the FBR-representation

Since, for problems of interest here, potential operators in the FBR-representation are given by sparse matrices, they can in principle be applied to wavefunctions via efficient matrix vector multiplication routines available to sparse matrices. Such methods use a re-indexing method to retain the matrix elements around the band of non-zero elements, thus reducing the amount of matrix elements that are equal to zero [128]. Since we have obtained analytical expressions for the non-zero matrix elements along with the selection rules, we can directly apply the non-zero elements of the matrix to the wave function in such a way as to respect the selection rules. In doing so, we do away with direct matrix-vector multiplication altogether. This is particularly important in a coupled m-representation where for each j there are $2j+1$ m-states. Consequently, the dimension of the matrices would be $(j_{max}+1)^2 \times (j_{max}+1)^2$ since $\sum_{j=0}^{j_{max}}(2j+1) = (j_{max}+1)^2$, compared to $(j_{max}+1)\times(j_{max}+1)$ for an uncoupled representation. Here j_{max} is the maximum j-state included in the representation. This would lead to a tremendous scaling of the numerical effort with increasing j_{max}. In contrast, for sparse matrices the number of non-zero elements scales as $j_{max}+1$ [132], i.e., the latter scales as j_{max}, whereas the application of the full matrix scales as j_{max}^4.

3.2 Time propagation

In order to compute the time evolution of the wavefunction, Eq. (2.46), we need to represent the time evolution operator on a time grid. For problems where time ordering is important

when numerically solving the Schrödinger equation, e.g. for optimal control theory, coherent control, pump-probe spectroscopy and in reactive scattering, a method which utilizes iterative time ordering as proposed by Ndong et. al. [121] is available in QDYN. For our purposes, the time interval is chosen such that within each sub interval the Hamiltonian can be regarded, to a good approximation, as constant, i.e. $\hat{\mathbf{H}}(t) \approx \hat{\mathbf{H}}\left(\frac{t_{i+1}+t_i}{2}\right)$ for $t_i \leq t \leq t_{i+1}$. Let $\tilde{t}_i \equiv \frac{t_{i+1}+t_i}{2}$. Then the time evolution operator is approximated by Eq. (2.47),

$$\hat{\mathbf{U}}(t_{i+1}, t_i) \approx \exp\left(\frac{-i}{\hbar}\hat{\mathbf{H}}(\tilde{t}_i)\Delta t\right) \tag{3.41}$$

with $\Delta t = t_{i+1} - t_i$. Here, one can make use of the property $\hat{\mathbf{U}}(t_2, t_0) = \hat{\mathbf{U}}(t_2, t_1)\hat{\mathbf{U}}(t_1, t_0)$ and repeatedly apply the time evolution operator for the full time interval $[t_0, t_{final}]$. The idea of many methods of numerical applications of the evolution operator is to use an expansion in polynomials [135]

$$\hat{\mathbf{U}}(\Delta t) = e^{-i\hat{\mathbf{H}}\Delta t} \approx \sum_n a_n P_n\left(-i\hat{\mathbf{H}}\Delta t\right). \tag{3.42}$$

Numerical calculations obtained from Taylor expansion lead to error accumulation and large deviations for longer time intervals and is therefore not suitable for practical applications [135]. The authors propose a method in which the exponential is expanded in the Chebychev polynomials instead [135]. It is attractive since the expansion series is quickly convergent, and the error of the method is evenly spaced in energy space. This is the method that we have used in our work and we will follow their work closely in our discussions. The implementation of the method into QDYN was performed by Goerz [136]. These polynomials distribute the error uniformly on the integration domain. The expansion coefficients are given by [135]

$$a_n\left(\frac{\alpha}{2}\right) = -i\int_{-i}^{i} \frac{\phi_n(z)e^{i\alpha z}}{\sqrt{1-|z|^2}}dz = (2-\delta_{n,0})J_n(\alpha). \tag{3.43}$$

where $\alpha = \Delta E \Delta t$ and $\Delta E = E_{max} - E_{min}$ is the spectral radius. The functions $J_n(\alpha)$ are the Bessel functions of the first kind. They decay exponentially whenever $n > \alpha$, so the number of expansion coefficients, N, will be on the order of the time-energy phase space [135]. It is therefore easy to find an N such that the error of time propagation will be on the order of machine precision, or in other words numerically exact.

For propagation in the time interval $t \in [t_i, t_{i+1}]$, $|\psi(t_i)\rangle \rightarrow |\psi(t_{i+1})\rangle$, the wave function $|\psi(t_{i+1})\rangle$ is then obtained from the wave function $|\psi(t_i)\rangle$ as [137]

$$|\psi(t_{i+1})\rangle = \exp\left(-i\frac{\tilde{E}\Delta t}{2}\right)\sum_n a_n(\alpha)\phi_n\left(-i\hat{\mathbf{H}}_{norm}\right)|\psi(t_i)\rangle, \tag{3.44}$$

with $\tilde{E} = E_{max} - E_{min}$. The application of the Hamiltonian on the wave function is greatly simplified by the recurrence relation satisfied by the Chebyschev polynomials,

$$\phi_{n+1}(z) = -2iz\phi_n(z) + \phi_{n-1}(z), \quad \phi_0(z) = 1, \quad \phi_1(z) = z, \tag{3.45}$$

and consequently

$$\begin{aligned} |\psi_{n+1}(t_i)\rangle &= -2i\hat{\mathbf{H}}_{norm}(t_i)\,|\psi_n(t_i)\rangle + |\psi_{n-1}(t_i)\rangle\,, \\ |\psi_1(t_i)\rangle &= |\psi_0(t_i)\rangle\,, \quad |\psi_2(t_i)\rangle = \hat{\mathbf{H}}_{norm}(t_i)\,|\psi_1(t_i)\rangle\,. \end{aligned} \tag{3.46}$$

As a result, time propagation of the wave function is obtained by iterative application of the Hamiltonian to the wave function followed by multiplication of a global the phase factor $\exp\left(-i\frac{\tilde{E}\Delta t}{2}\right)$ [137].

In concludion, when time ordering can be ignored, and the time-evolution operator can be approximated as an exponential, we can expand it in the Chebychev polynomials. This expansion has the advantage of distributing the error evenly on the integration domain, in contrast to e.g. a Taylor expansion. Additionally, the expansion coefficients decay exponentially for higher order terms than the argment, i.e., volume of the phase space, facilitating in the choise of the number of terms to keep in the expansion. The rapid decay for the high order terms allows us to systematically chose the number of expansion coefficients to drive the numerical error below machine precision, and thereby obtain a numerically exact method for expanding the time-evolution operator.

4

Sympathetic Cooling and Rotational Excitation

In this chapter we study sympathetic cooling, i.e, the cooling of one particle via some other particle, of diatomic molecular ions using laser-cooled atomic trapped ions as coolant. In this particular case the cooling mechanism is provided by the mutual Coulomb repulsion between the molecular ion and the coolant. The translational motion is cooled down by successive collisions with the atomic ions, which are kept cool by continuous laser cooling, during the sympathetic cooling process. Such arrangement can be implemented experimentally by producing the ions in an external trap and later introducing them into a trap containing pre cooled atomic ions used as coolants [107]. The electric field, originating on the coolants, which mediate the cooling can also couple to the internal states or the molecular ions, potentially leading to internal excitation of the molecular ion. As quantum technological applications, e.g., precision measurements, rely on well prepared initial states to take advantage of the quantum effects, such excitations can lead to severe loss of performance. It is therefore of utmost importance to minimize such internal excitations. In particular, we analyze the potentially detrimental rotational excitation of the molecular ions and the timescales associated with the cooling process. We consider a setup in which diatomic molecular ions have been prepared in their internal ground state but are in a translationally high energy state. Once the molecular ions are introduced into the trap they are susceptible to the trapping potential. Therefore, when reaching the center of the trap the potential energy has been completely converted into kinetic energy, and the molecular ions are expected to have kinetic energies on the order of the trap potential. So, in an actual experiment, the potential depth sets the minimum scale of the scattering energy in a cooling process.

An overview over sympathetic cooling of molecular ions is presented in section 4.1, and our model to treat the scattering process is presented section 4.2. We discuss single collisions in section 4.3, where polar and apolar molecular ions couple differently to the field produced by the atomic ions and are therefore studied independently, before discussing the full cooling

cycle in section 4.4. The main results of our study are presented in section 4.5. We conclude this chapter with our conclusions in section 4.6. The work presented here shall be published in Refs. [138, 139].

4.1 The basic concept of sympathetic cooling of molecular ions

As discussed in Chapter 1, laser cooling is frequently employed as a means to cool atoms and atomic ions, a method that is not, in general, applicable to molecules and molecular ions. Therefore, laser cooled atomic ions are frequently used as precursors for molecular ion cooling. Sympathetic cooling of molecular ions is achieved by the energy transfer resulting from a series of scattering events mediated by their Coulomb interaction with the ultra-cold atomic ions, which lead to a reduction of their translational kinetic energy [44, 45, 140–144]. However, in addition to the desired cooling of the translational motion of the molecular ion, its internal degrees of freedom also couple to the atomic ion's Coulomb field, leading to rotational and, in principle, vibrational excitations. As experiments rely on well defined initial states and significant internal excitations would eventually lead to an incoherent, uncontrollable initial state unsuitable to high precision experiments, it is of importance to perform cooling in such a way as to avoid such excitations. The success of sympathetic cooling is determined by a fast cooling rate and sufficiently small internal excitation. In the present chapter both these topics are addressed. We estimate both the cooling rates in different cooling scenarios as well as the accumulated internal excitations associated with a full cooling cycle. We derive an approximate closed expression for an upper bound of the accumulated rotational excitation in terms of molecular parameters (i.e., rotational and coupling constants) and the initial scattering energy, to ensure the relevance of the results beyond the specific molecules studied here.

We consider a system of pre-cooled ultra-cold atomic ions forming a Coulomb crystal inside a Paul trap, where molecular ions in a translationally high energy state, but in their internal ground state, are brought into the trap for sympathetic cooling. Paul traps accomplish trapping of ions by a combination of static and radio frequency (RF) electric fields [78,145]. In particular, linear Paul traps consist of four cylindrical electrodes, arranged collinearly with the four end caps forming the edges of a square [145]. Confinement of the ions in the radial direction is provided by an RF-voltage $\Phi_0 = V_0 - V_{RF} \cos \Omega t$, with V_{RF} and Ω the amplitude and the frequency of the RF-field, and the ions are confined in the axial (z) direction by applying an electrostatic voltage V_{EC} to the eight end caps [145]. The RF-field is vanishing in the axial direction which offers storage of many particles with little so-called micro-motion [46]. The micro-motion is an oscillatory small motion at frequency Ω. The

amplitude of this motion is slow for appropriate trap parameters, indeed the amplitude is proportional to the so-called Matheiu parameter, $q = \frac{2QV_{RF}}{M\Omega r_0^2}$ if $q \ll 1$ [146, 147], where M and Q are the mass and charge of the ion . In this regime, one can obtain a static effective pseudo-potential that ignores the micro-motion all together and one can approximate the interaction of the ions with the trap by neglecting micro-motion. Close to the center of the trap, the resulting potential is approximately harmonic and the cylindrical symmetry allows for trapping a large number of ions along the symmetry line (z-axis) of the trap. Therefore, close to the center the potential is harmonic and respects the cylindrical symmetry of the trap geometry [46],

$$U_{trap}(r,z) = \frac{M}{2}\left(\omega_r^2 r^2 + \omega_z^2 z^2\right), \tag{4.1}$$

with $r = \sqrt{x^2+y^2}$. The axial frequency is given by $\omega_z = \sqrt{\frac{2\kappa_t Q V_{EC}}{M}}$, and the radial frequency is $\omega_r = \sqrt{\omega_0^2 - \frac{\omega_z^2}{2}}$, with κ_t being a trap-geometry constant, $\omega_0 = \frac{QV_{RF}}{2M\Omega r_0^2}$, and r_0 is the distance to the center of the trap. Since the masses of the atomic and molecular ions are generally different and the trap frequencies depend on the masses, the crystallization leads to a so called bi-component crystal, where the lighter species is found inside, at lower radial distances, than the heavier species [45, 145, 148]. The radial separation has its origin in the mass-dependent radial trap frequency [145].

4.2 Model of the atom-molecule interaction

The energies associated with the translational and rotational dynamics of the molecular ion are well separated in a scattering event. While typical initial scattering energies range from 0.1 eV to 10 eV, the rotational energy scale is of the order of 10^{-4} eV. This significant energy separation is the basis of our model. It allows us to disregard the rotational dynamics when considering the translational motion and the rotational motion can be treated separately. Indeed, the relative motion between the ions is treated classically [149, 150] while disregarding all internal degrees of freedom, i.e., assuming elastic scattering. Consequently, the energy transfer during the collision may be treated as a textbook example of scattering between two charged point particles interacting via the mutual Coulomb repulsion. This is true as long as the molecular and atomic ions are not in contact with each other at any time during the scattering process, i.e., as long as their wave functions do not overlap. This means that our model is valid for scattering energies where the distance between the ions remains considerably larger than the extension of the molecular ion, which can be estimated from the equilibrium inter-nuclear radius.

The energy scale set by typical molecular rotational constants are on the same scale as the interaction energy resulting from the coupling to the Coulomb field of the atomic coolant ion, which is sufficiently strong to induce rotational transitions on the molecular ion even

for moderate scattering energies. The rotational motion is therefore treated fully quantum mechanically and separately from the translational motion.

Finally, due to the significantly larger energy difference between the vibrational energy levels as compared to the rotational levels, vibrational excitations are not expected to play any role in the internal dynamics and will therefore be neglected in our model. As an example, the rotational constant of MgH^+ is on the order of 10^{-5} Hartree, see Table 4.I, whereas the harmonic vibrational constant is on the order of 1700 cm^{-1} [117] or $\sim 8 \cdot 10^{-3}$ Hartree.

In a real cooling experiment the molecular ion is not only interacting with a single atomic coolant in the trap, but will, at least in principle, experience the effect of all atomic coolants in the trap. We therefore need to consider the collective effects of the coolants in the Coulomb crystal. The full interaction between the ions in a real Coulomb crystal is complicated, involving a large number of degrees of freedom. A tool to simulate the dynamics of a crystal usually employed is molecular dynamics (MD) simulations which take the effect of the trap, mutual Coulomb interaction, interaction with the RF-field and stochastic forces into account [27]. The term crystal is not entirely truthful, indeed, since at typical experimental temperatures $\sim$ mK the ions are not frozen, but do diffuse between different lattice 'sites' [46]. One collective effect of particular significance is the heating of the crystal due to interactions with the RF-field. MD-simulations indicate that the effect is very small under normal experimental conditions [151], and we will therefore neglect this effect in our model.

To summarize, our model is built on the following considerations:

1. The energy transfer is described by classical scattering between two charged point particles.
2. The rotational motion is treated separately from the translational motion and fully quantum mechanically.
3. The vibrational motion is neglected.
4. Micro-motion and collective effects of the crystal are neglected.

4.2.1 Classical collisions

By assumption of our model, the translational dynamics is treated as a purely classical collision of two point particles, with collective effects in the crystal neglected. Additionally, cooling is assumed to take place through scattering with co-trapped atomic ions forming a Coulomb crystal at the center of a linear Paul trap. The radial confinement is significantly

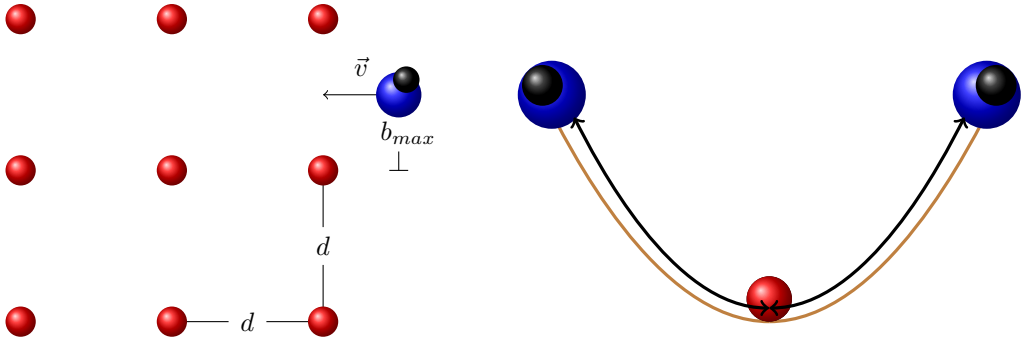

Figure 4.1: Schematics of a molecular ion colliding with atomic ions inside a harmonic trap. The low kinetic energy of the atomic ions and their mutual repulsion together with the confinement provided by the trap lead to the ions condensing to a crystal shape. If the interatomic distance, d, is small, the molecular ion interacts with many atoms close to the crystal center and comes to a stop in its first passing of the crystal (left panel). In this scenario the trap is negligible in the interaction zone and is not shown in the left panel. Notice that the maximum impact parameter is $b_{max} = \frac{d}{2}$. If d is very large and comparable to the characteristic length scale of the trap, the molecular ion interacts only with one of the atoms in the crystal during its passing. The molecular ion then moves under the influence of the trap in the cooling process (right panel).

stronger and, close to the center, the effect of the trap on the axial degree of freedom is not taken into account. The Hamiltonian describing the trap potential in the radial direction close to the trap center is given by

$$H_{trap}(\vec{x},\vec{p}) = \frac{p^2}{2M_{mol}} + \frac{M_{mol}\omega^2 x^2}{2}, \tag{4.2}$$

where $\vec{x}$ and $\vec{p}$ are the molecular position and momentum vectors respectively, M_{mol} is the mass of the molecular ion and ω is the radial trap frequency. We consider molecular and atomic ions with unit charge, so the Coulomb potential (in atomic units) is given by $V(r) = \frac{1}{r}$ [114]. Depending on the distance d between the atomic ions, we have two limiting scenarios, see Figure 4.1. When d is comparable to the trap dimension, the molecular ion collides on average only once on each passing of the trap center. This scenario will be referred to as *single ion cooling*. The molecule returns to the crystal under the influence of the trap potential so the time between collisions is set by the trap frequency. Consequently, we must take the effect of the trap into account, where typical trap frequencies are usually in the 100 kHz to 1 MHz range. Therefore, these are the values to be considered here. At the opposite limit, where d is much smaller than the characteristic length scale of the trap, the molecular ion undergoes several scattering events and loses all its kinetic energy during a single passing at the center of the trap. In this limit, referred to as *crystal cooling*, the effect of the trap can be neglected. These two scenarios are depicted in the panels of Figure 4.1.

Now consider a molecular ion just produced in its internal ground state and introduced into a trap containing a Coulomb crystal of cold atomic ions. As the molecular ion is

introduced into the trap, its kinetic energy is

$$E_L = \frac{1}{2} M_{mol} v_L^2, \tag{4.3}$$

where v_L is the speed of the molecular ion as measured in the lab-frame, indicated by the subscript L. The collision process is, however, best described in the Center of Momentum (CM) frame. The CM energy is not only dependent on the molecule and its initial kinetic energy, but also depends on the mass of the atomic coolant used. The relation between E_L and the relative energy, E, in the CM frame is

$$E = \frac{\mu}{M_{mol}} E_L, \tag{4.4}$$

where $\mu = \frac{M_{atom} M_{mol}}{M_{atom}+M_{mol}}$ is the reduced mass. Neglecting external fields, the relative motion of the atom-molecule pair is described by Kepler's law of motion [110]. Thus, the scattering process is characterized by the scattering energy in the center of momentum frame, E, the orbital angular momentum, l, the charges of the atomic and molecular ions (via the potential) and the reduced mass, μ, as given by the Hamiltonian

$$H(r, p_r) = \frac{p_r^2}{2\mu} + \frac{l^2}{2\mu r^2} + V(r) = E, \tag{4.5}$$

where $V(r) = \frac{1}{r}$ is the Coulomb potential in atomic units, where both ions are of unit charge (in atomic units) and p_r is the radial momentum. Notice that the Hamiltonian, Eq. (4.5), is cyclic in the generalized coordinate θ and hence l is a constant of motion. Furthermore, at large separations ($r \to \infty$) only the first term contributes to the scattering energy, $\frac{p_0^2}{2\mu} = E$, in which case $p_r \to p_0$. Here, $p_0 = \sqrt{2\mu E}$, is the radial momentum at infinite (in practice very large) distance, at which the potential and angular momentum terms in Eq. (4.5) are negligible. In this limit, the constant orbital momentum is given by the product of the impact parameter, b, see Figure 4.2, and the momentum p_0,

$$l = b p_0 = b\sqrt{2\mu E}. \tag{4.6}$$

The minimal distance, r_0, between molecular and atomic ions during scattering occurs at the turning point where $p_r = 0$ in Eq. (4.5),

$$r_0 = \frac{1}{2E} + \sqrt{\left(\frac{1}{2E}\right)^2 + b^2}, \tag{4.7}$$

where Eq. (4.6) has been used to replace l with b. Note that as $b \to 0$, $r_0 \to \frac{1}{E} \equiv r_{00}$, thus defining r_{00} as the minimal distance for zero impact parameter.

By assumption of our model, the collisions are elastic (the inelastic energy corresponding to the rotational excitation is negligible in comparison to the translational energy transfer), and therefore, no energy transfer takes place in the center of mass frame. We are interested

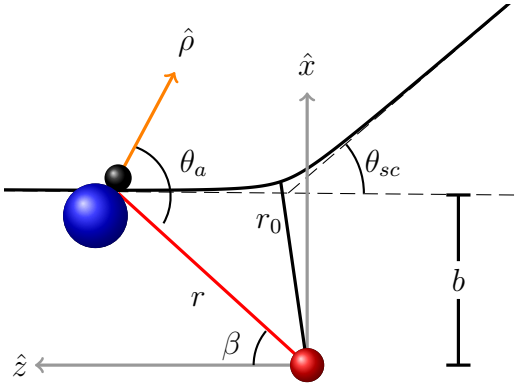

Figure 4.2: Schematics of the scattering event between a molecular ion (blue and black spheres) and a coolant (red sphere) as seen in the center of mass frame. The black parabola indicates the trajectory going from left to right.

in the molecular kinetic energy in the lab reference frame (4.3). The energy transfer in the lab frame, δE_L for a collision at CM-energy E and impact parameter b is given by

$$\delta E_L = E_L - E'_L = \frac{2\xi\left[1-\cos\left(\theta_{sc}(E,b)\right)\right]}{(1+\xi)^2}E_L, \tag{4.8}$$

where, for a Coulomb interaction between two charges, q_{at} and q_{mol}, respectively, the scattering angle θ_{sc} in Figure 4.2 is given by [110]

$$\theta_{sc} = 2\sin^{-1}\left(\frac{1}{\sqrt{1+\left(\frac{2Eb}{q_{at}q_{.mol}}\right)^2}}\right). \tag{4.9}$$

We will typically work with unit charges, so that $q_{at} = q_{mol} = 1$. Since $\frac{\delta E_L}{E_L} = \frac{\delta E}{E}$, we can write Eq. (4.8) in terms of the CM energy

$$\delta E = E - E' = \frac{2\xi\left[1-\cos\left(\theta_{sc}(E,b)\right)\right]}{(1+\xi)^2}E. \tag{4.10}$$

For elastic scattering, which is considered here, we have $\xi = \frac{M_{mol}}{M_{at}}$ [110]. Note that the function $\frac{\xi}{(1+\xi)^2}$ has its maximum at $\xi = 1$ which implies that the maximum energy transfer occurs when $M_{mol} = M_{at}$, which in practice means that cooling is most effective when the atomic ion used as coolant has a similar mass as the molecular ion being cooled.

4.2.2 Quantum rotations

In our studies, it is the mutual Coulomb interaction between the coolant ion and the molecular ion that provides the mechanism for cooling of the translational degree of freedom via repeated collisions. The Coulomb field due to the coolant can also result in unwanted internal excitation of the molecular ion by coupling to its rotational degree of freedom. We

will now present a quantum mechanical description of the interaction between the molecular ions and the Coulomb field originating from the atomic ion coolants.´

Since the scattering occurs on a plane, we may choose a unit vector $\hat{z}$ along the direction of the initial velocity, and a vector $\hat{x}$ perpendicular to it, as the basis vectors to span the scattering plane. In the special case of head-on collisions, the plane reduces to a line along the $\hat{z}$-direction. The electric field, $\vec{\varepsilon}$ (pointing along the red line in Figure 4.2), is spanned by the $\hat{x}$ and $\hat{z}$ vectors, while the molecular axis $\hat{\rho}$ requires, in general, three space directions $\hat{x}, \hat{y}, \hat{z}$. A schematic representation of this layout is shown in Figure. 4.2, where θ_a denotes the angle between the electric field due to the atomic ion coolant and the molecular axis. In terms of the angle β, defined in Eq. (4.27), we have $\hat{\varepsilon} = \cos\beta\hat{z} + \sin\beta\hat{x}$ and $\hat{\rho} = \sin\theta\cos\phi\hat{x} + \sin\theta\sin\phi\hat{y} + \cos\theta\hat{z}$, which relates the angle θ_a to the angles θ, β and ϕ,

$$\cos\theta_a = \hat{\varepsilon}_0 \cdot \hat{\rho} = \cos\beta\cos\theta + \sin\beta\sin\theta\cos\phi. \tag{4.11}$$

Notice that ε_0 is a function of E and b, Eqs. (4.7) and (4.25). Here, θ is θ_a at infinite molecular and atomic ion separation, i.e., for $\beta = 0$. The angle ϕ is the angle between the projection of $\hat{\varepsilon}_0$ on the $\hat{x}$-$\hat{y}$-plane and the $\hat{x}$-axis (the $\hat{y}$-axis points into the paper in Figure 4.2). We are interested in the rotational dynamics of the molecular ion during the scattering process, and the possible excitation of its internal states as a result of its interaction with the electric field of the atomic ion. In terms of a standard electric multipole expansion of the field-ion interaction, the dominant interaction terms correspond to the monopole, responsible for the cooling of the translational degree of freedom, followed by the dipole and quadrupole terms responsible for the rotational dynamics. The dipole interaction term is given by

$$V_D = -D\varepsilon\cos\theta_a, \tag{4.12}$$

where D is the molecular dipole moment (calculated at the equilibrium distance r_e), ε is the field strength and θ_a is the angle between the electric field and the molecular axis, see Figure 4.2. Here, polar and apolar molecular ions couple differently to the field due to the atomic coolant, since polar ions possess a permanent dipole moment D, whereas in apolar ions D vanishes due to symmetry. Nevertheless, in the case of apolar molecular ions, with no permanent dipole moment, a dipolar moment is induced by the field. The interaction of the field with the induced dipole of a diatomic apolar molecular gives rise to a polarizability contribution of the form

$$V_\alpha = -\frac{\varepsilon^2}{4}\left(\Delta\alpha\cos^2\theta_a + \alpha_\perp\right), \tag{4.13}$$

where $\Delta\alpha$ is the polarizability anisotropy of the molecular ion and $\alpha_\perp$ is the polarizability perpendicular to the molecular axis. Finally, the quadrupole interaction with the field is, for both polar and apolar molecular ions,

$$V_Q = \frac{Q_a\varepsilon^{3/2}}{4}\left(3\cos^2\theta_a - 1\right), \tag{4.14}$$

where Q_a is the permanent quadrupole moment of the molecule along the molecular axis. See Chapter 2 and Appendix B for details.

As we treat the molecule as a rigid rotor (see Section 2.1), the rotational kinetic energy is given by

$$\hat{\mathbf{H}}_{rot} = B\hat{\mathbf{J}}^2, \tag{4.15}$$

where the rotational constant $B = \frac{1}{2\mu r_e^2}$, with r_e the internuclear equilibrium distance, and the rotational energy of state j is $j(j+1)B$. The rotational constant sets a rotational time scale

$$T_{rot} = B^{-1}. \tag{4.16}$$

The relative strength of the dipole and quadrupole interactions with respect to the rotational kinetic energy can be then estimated considering their maximal strengths,

$$\chi_D = \frac{D\varepsilon_0}{B}, \quad \chi_\alpha = \frac{\Delta\alpha\varepsilon_0^2}{4B}, \quad \chi_Q = \frac{3Q_a\varepsilon_0^{3/2}}{4B}. \tag{4.17}$$

For $\chi_{D/\alpha/Q} \ll 1$ we expect negligible rotational excitation resulting from the corresponding interaction, whereas a large value indicates that a large degree of excitation is expected. Since ε_0 depends on both E and b, χ_D, χ_α and χ_Q depend on molecular quantities as well as on the scattering energy (measured in the CM-frame) and the impact parameter,

$$\chi_D(b,E) = \frac{D}{B}\frac{1}{\left(\frac{1}{2E} + \sqrt{\left(\frac{1}{2E}\right)^2 + b^2}\right)^2} \xrightarrow{b\to 0} \frac{D}{B}E^2, \tag{4.18a}$$

$$\chi_{\Delta\alpha}(b,E) = \frac{\Delta\alpha}{4B}\frac{1}{\left(\frac{1}{2E} + \sqrt{\left(\frac{1}{2E}\right)^2 + b^2}\right)^4} \xrightarrow{b\to 0} \frac{\Delta\alpha}{4B}E^4, \tag{4.18b}$$

$$\chi_Q(b,E) = \frac{3Q_a}{4B}\frac{1}{\left(\frac{1}{2E} + \sqrt{\left(\frac{1}{2E}\right)^2 + b^2}\right)^3} \xrightarrow{b\to 0} \frac{3Q_a}{4B}E^3. \tag{4.18c}$$

For a given scattering energy, and for head-on collisions, the ratio $\frac{\chi_Q}{\chi_D} = \frac{3Q_a}{4D}E$ is $0.025E$ and $0.12E$ (E in eV) for the molecular ions MgH^+ and HD^+, respectively, indicating that we can therefore neglect the quadrupole term in our model for these molecular ions. Notice that HD^+ has a particularly small dipole moment, see Table 4.I. Its small dipole moment is a consequence of it being an isotopomeric to H_2^+, a molecular ion which has no permanent dipole moment, due to symmetry. The non-zero dipole moment of HD^+ comes from the difference in reduced mass of the two isotopomers, which in turn leads to a shift in the center of mass of the molecular ion, and consequently a shift in the dipole moment [114]. Care must therefore be taken in general when neglecting the quadrupole interaction of molecular ions isotopomeric to apolar species, e.g., $^{16}O^{18}O^+$ or $^{14}N^{15}N^+$.

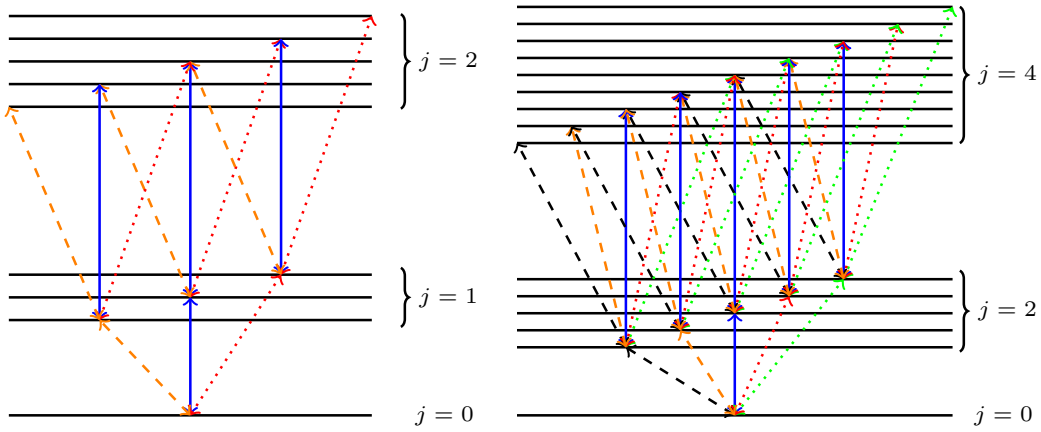

Figure 4.3: Allowed rotational transitions. Polar molecular ions (left) and non-polar molecular ions (right). Each j state has $2j+1$ sub states $m_j = -j, -j+1, ..., 0, ..., j-1, j$. Blue arrows indicate transitions which conserve m_j ($\Delta m_j = 0$). These transitions are the only valid ones for head-on collisions.

With $\hat{\rho}$ the unit vector along the internuclear axis of the molecular ion, see Figure 4.2, the Hamiltonian describing the rotational dynamics of polar molecular ions is

$$\begin{aligned}\hat{\mathbf{H}}_p &= B\hat{\mathbf{J}}^2 - D\varepsilon(t)\cos\hat{\theta}_a \\ &= B\hat{\mathbf{J}}^2 - D\varepsilon(t)(\cos\beta\cos\hat{\theta} + \sin\beta\sin\hat{\theta}\cos\hat{\phi}),\end{aligned} \tag{4.19}$$

where $\vec{D} = D\hat{\rho}$ is the permanent dipole moment of the molecular ion directed along the axis connecting the two nuclei, see Figure 4.2, and $\vec{\varepsilon}(t) = \varepsilon(t)\hat{\varepsilon}$ is the electric field due to the atomic ion. Since we are modeling the molecular ion as a rigid rotor, the value of the dipole moment is taken to be the dipole moment at the equilibrium distance. Moreover, as the eigenstates of Eq. (4.19) are the spherical harmonics, we obtain the following selection rules for the transition matrix elements of the interaction terms of Hamiltonian Eq. (4.19) in this basis,

$$\langle j, m|\cos\hat{\theta}|j', m'\rangle, \quad \Delta j = \pm 1, \quad , \Delta m = 0, \tag{4.20a}$$

$$\langle j, m|\sin\hat{\theta}\cos\hat{\phi}|j', m'\rangle, \quad \Delta j = \pm 1, \quad \Delta m = \pm 1, \tag{4.20b}$$

as depicted in the left panel of Figure 4.3. The most prominent difference between these two interaction terms is that $\sin\hat{\theta}\cos\hat{\phi}$ mixes different m-states whereas $\cos\hat{\theta}$ does not. In the particular case of head-on collisions, $\beta = 0$ throughout the scattering event and Eq. (4.19) reduces to

$$\hat{\mathbf{H}}_p = B\hat{\mathbf{J}}^2 - D\varepsilon(t)\cos\hat{\theta}, \quad \text{(head-on collision)}, \tag{4.21}$$

from which we see that head-on collisions do not mix different m-states.

As opposed to polar molecular ions, for apolar molecular ions we cannot discard the quadrupole interaction. Indeed, for the apolar ions considered here, the quadrupole interaction dominates over the induced-dipole interaction. For example, for N_2^+ at 2 eV $\frac{\chi_Q}{\chi_{\Delta\alpha}} \approx 8$.

The quadrupole interaction decreases more gradually than does the polarizability interaction and will therefore remain the dominating interaction also throughout the scattering event. Thus, for apolar molecular ions with no permanent dipole moment, the Hamiltonian describing the rotational dynamics is

$$\begin{aligned}\hat{\mathbf{H}}_{np} &= B\hat{\mathbf{J}}^2 - \frac{\varepsilon^2(t)}{4}\left(\Delta\alpha\cos^2\hat{\theta}_a + \alpha_\perp\right) + \frac{Q_a\varepsilon^{3/2}(t)}{4}\left(3Q_a\cos^2\hat{\theta}_a + 1\right) \\ &= B\hat{\mathbf{J}}^2 - \frac{\varepsilon^2(t)}{4}\Big[\Delta\alpha(\cos^2\beta\cos^2\hat{\theta} \\ &+ 2\cos\beta\sin\beta\cos\hat{\theta}\sin\hat{\theta}\cos\hat{\phi} + \sin^2\beta\sin^2\hat{\theta}\cos^2\hat{\phi}) + \alpha_\perp\Big].\end{aligned} \tag{4.22}$$

Here $\Delta\alpha$ is the polarizability anisotropy and $\alpha_\perp$ is the polarizability perpendicular to the molecular axis. For head-on collisions, the Hamiltonian reduces to

$$\hat{\mathbf{H}}_{np} = B\hat{\mathbf{J}}^2 - \frac{\varepsilon^2(t)}{4}\left(\Delta\alpha\cos^2\hat{\theta} + \alpha_\perp\right) + \frac{\varepsilon^{3/2}(t)}{4}\left(3Q_a\cos^2\hat{\theta} + 1\right), \quad \text{(head-on collision)}. \tag{4.23}$$

For apolar molecular ions, we obtain the following selection rules

$$\langle j, m|\cos^2\hat{\theta}|j', m'\rangle, \quad \Delta j = \pm 2, 0, \quad \Delta m = 0, \tag{4.24a}$$

$$\left\langle j, m\left|\cos\hat{\theta}\sin\hat{\theta}\cos\hat{\phi}\right|j', m'\right\rangle, \quad \Delta j = \pm 2, 0 \quad \Delta m = \pm 1, \tag{4.24b}$$

$$\left\langle j, m\left|\sin^2\hat{\theta}\cos^2\hat{\phi}\right|j', m'\right\rangle, \quad \Delta j = \pm 2, 0 \quad \Delta m = \pm 2, 0, \tag{4.24c}$$

as depicted in the right panel of Figure 4.3.

4.2.3 Modeling the electric field originating from the atomic ion

The Coulomb field originating from the atomic ion and felt by the molecular ion, both of unit charge, is a function of the relative distance, r, between the two ions,

$$\tilde{\varepsilon}(r) = \frac{1}{r^2}, \tag{4.25}$$

whereas in the Hamiltonians that generate the rotational dynamics for polar and apolar molecular ions, Eqs. (4.19), (4.22), respectively, the electric field enters as a function of time. The link between the radial and temporal coordinates is found from the classical Hamiltonian (4.5). We obtain $t = t(r)$ by solving Eq. (4.5) for p_r and recalling that $p_r = \mu\frac{dr}{dt}$. The result is a separable differential equation with solution

$$t = \int_0^t dt' = \sqrt{\frac{\mu}{2E}}\int_{r_0}^{r}\frac{dr'}{\sqrt{1 - \frac{r_{00}}{r'} - \left(\frac{b}{r'}\right)^2}}, \tag{4.26}$$

where Eq. (4.6) is used to express b in terms of l. Notice that the time $t > 0$ obtained from Eq. (4.26) refers to the time passed after the molecular ion has reached the turning point

r_0. Times prior to reaching the turning point, $t < 0$, are found by symmetry. For non-zero impact parameter, the orientation of the electric field direction w.r.t. the molecular ion will change over the orbit. The angle β between the actual direction of the electric field due to the atomic ion along the orbit and its initial direction (see Figure 4.2) is given by [110]

$$\begin{aligned}
\beta &= \int_{\infty}^{r} \frac{bds}{s^2\sqrt{\left(1-\frac{V(s)}{E}\right)-\frac{b^2}{s^2}}}, \quad r \in [r_0,\infty), \quad t<0, \\
\beta &= \int_{\infty}^{r_0} \frac{bds}{s^2\sqrt{\left(1-\frac{V(s)}{E}\right)-\frac{b^2}{s^2}}} \\
&+ \int_{r_0}^{r} \frac{bds}{s^2\sqrt{\left(1-\frac{V(s)}{E}\right)-\frac{b^2}{s^2}}}, \quad r \in [r_0,\infty), \quad t>0.
\end{aligned} \tag{4.27}$$

In terms of the angle β, the electric field experienced by the molecular ion, due to the atom's charge, is expressed as

$$\vec{\varepsilon}(t;E,b) = \varepsilon(t;E,b)\left(\cos\beta(t;E,b)\hat{z} + \sin\beta(t;E,b)\hat{x}\right). \tag{4.28}$$

From Eq. (4.26), we see that the time traversed in the orbit depends on the scattering energy, the reduced mass of the scattering system, and the impact parameter. Thus, the electric field becomes a function $\varepsilon = \varepsilon(t;E,\mu,b)$.

The particular case of head-on collisions ($b = 0$) is of special interest since the field reaches maximum strength and consequently we expect it to show the largest effect on the molecular rotational levels. In this case, the angular momentum of the scattering molecule is $l = 0$, since the momentum is either parallel or anti-parallel to the inter-particle radius vector (see Figure 4.2). The minimal inter nuclear distance is reached when $p_r = 0$ and thus, $E = V(r)$, and

$$r_0 = 1/E. \tag{4.29}$$

Using relation (4.29) and substituting $V(r) = 1/r$, the integral to be solved reduces to

$$t = \int_0^t dt' = \sqrt{\frac{\mu r_0}{2}} \int_{r_0}^{r} \frac{dr'}{\sqrt{1-r_0/r'}}. \tag{4.30}$$

The solution of integral (4.30) has the form

$$t(r) = \sqrt{\frac{\mu r_0^3}{2}}\left[\frac{r}{r_0}\sqrt{1-r_0/r} + \frac{1}{2}\ln\left(\frac{\sqrt{1-r_0/r}+1}{|\sqrt{1-r_0/r}-1|}\right)\right], \tag{4.31}$$

where the prefactor $\frac{\tau}{2} \equiv \sqrt{\frac{\mu r_0^3}{2}}$ has time dimensions, and the first term is always the largest. For short distances, $r \sim r_0$, the second term can be approximated by a Taylor expansion around $r = r_0$,

$$t(r) \approx \frac{\tau}{2}\left(\frac{r}{r_0}\sqrt{1-\frac{r_0}{r}} + \sqrt{1-\frac{r_0}{r}}\right). \tag{4.32}$$

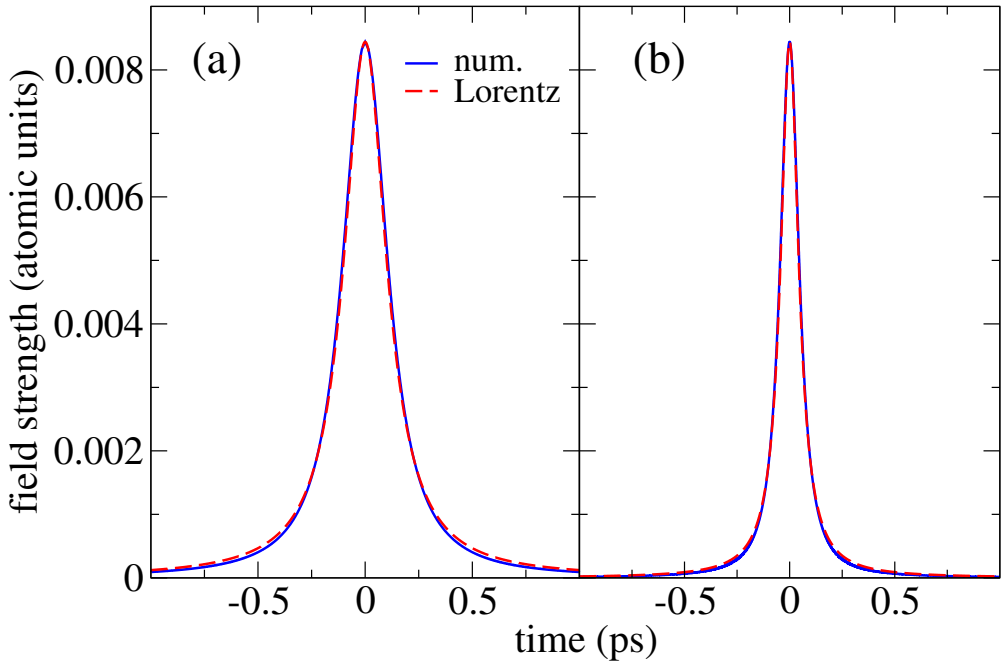

Figure 4.4: The electric field due to the atomic ion field felt by a polar molecular ion during a head-on scattering event at 2.5 eV along with a fit to a Lorentzian profile. (a) $^{24}MgH^+$ / $^{24}Mg^+$-scattering, (b) HD^+ / Be^+.

The latter can be rewritten to take the form

$$\left(\frac{t(r)}{\frac{\tau}{2}}\right)^2 = \left(\frac{r}{r_0}\right)^2 \left[\underbrace{\frac{5}{4} - \left(\frac{r_0}{r} - \frac{1}{2}\right)^2}_{a^2}\right] - 1, \tag{4.33}$$

where the factor a^2 takes values within the interval $[1, 1.25]$, and will hereafter be approximated by $a^2 = 1$. Eq. (4.33) can then be rearranged to obtain a Lorentzian form for Eq. (4.25)

$$\varepsilon(t) = \varepsilon_0 \frac{\left(\frac{\tau}{2}\right)^2}{t^2 + \left(\frac{\tau}{2}\right)^2}, \tag{4.34}$$

where the maximum electric field is $\varepsilon_0 = \frac{1}{r_0^2}$, and the full width at half maximum ($FWHM$) is given by $\tau = \sqrt{2}\sqrt{\mu r_0^3} = \sqrt{2}\sqrt{\frac{\mu}{E^3}}$. The full time dependence of the electric field during a head-on collision of $^{24}MgH^+$ / $^{24}Mg^+$ and HD^+ / $^9Be^+$ at a scattering energy of 2.5 eV is plotted in Figure 4.4. A Lorentzian numerical fitting of the curves leads to a FWHM value of

$$\tau = 1.86\sqrt{\frac{\mu}{E^3}}. \tag{4.35}$$

with a least square error of $R \sim 10^{-7}$. The long range character of the Coulomb field is reflected in the Lorentzian profile. The wings represent a gradual onset and retreat of the

	$^{24}MgH^+$	HD^+	$^{14}N_2^+$	H_2^+	$^{127}I_2^+$
B (10^{-5}H)	2.88	9.96	0.90	12.69	0.015
D (at.units)	1.18	0.34	-	-	-
$\Delta\alpha$ (at.units)	-	-	9.12	3.72	55.64
$\alpha_\perp$ (at.units)	-	-	9.62	1.71	∼37
Q_a (at.units)	1.072	1.52*	1.74	1.52	12.154
μ (at.units)	22473.21	4155.36	32463.57	3024.57	74056.55

Table 4.I: Rotational constant B, dipole moment D, polarizability anisotropy $\Delta\alpha$, perpendicular anisotropy $\alpha_\perp$ and quadrupole moment Q_Z of a few molecular ions as well as reduced mass μ of molecular ion and coolant ($^{24}MgH^+$ for MgH^+, $^9Be^+$ for HD^+, H_2^+, $^{48}Ca^+$ for N_2^+ and I_2^+), all in atomic units. * No values cited at NIST, we use the value given for H_2^+ [152]. For the quadrupole moments we have used the values from MP2-Def2TZVPP (Møller-Plesset perturbation theory) cited at [152]. For MgH^+ the results obtained from DFT-calculations vary significantly from the results from Møller-Plesset perturbation theory ($Q_a = 0.460$ for DFT PBEPBE-Def2TZVPP). We find that the results between the two methods differ moderately for the other molecular ions concidered here.

electric field as experienced by the molecular ion in a scattering event. In practice, this implies that in order to represent a scattering event, a time grid that extends significantly longer than the FWHM of the field is required.

From the FWHM and the rotational constant, Eq. (4.16), we can define a dimensionless time parameter,

$$\kappa = B\tau = 1.86 \cdot B\sqrt{\frac{\mu}{E^3}} \tag{4.36}$$

such that $\kappa \ll 1$ corresponds to a fast scattering regime and $\kappa \gg 1$ to a slow scattering regime.

4.3 Single collisions

In this section we present the population excitations that arise in a single collision between the molecular ions and the coolants, so we solve the Schrödinger equation numerically for the Hamiltonians, Eqs. (4.19) and (4.22). Based on the results of the numerical calculations we identify two different regimes, from which we aim to derive analytical expressions that provide an estimate to the excitations.

Molecular ion	r_e (Bohr)	E (eV)	E_L (eV)
MgH^+	≈ 3	9	18
HD^+, N_2^+, H_2^+	≈ 2	13.6	$\gg 10$
I_2^+	≈ 5.3	5.4	10.0

Table 4.II: Table of the equilibrium molecular radii, r_e, of molecular ions used in this work along with the scattering energy E which corresponds to $r_0 = r_e$ for a head-on collision.

4.3.1 Model validity

Before discussing the results of the model, we test the validity of the assumptions that it is based upon. Firstly, we estimate the effect of the RF-field on the population excitation and under what conditions the classical point particle nature of the scattering particles can be assumed.

Neglecting the RF-field of the trap

Our model accounts for scattering as the only source for rotational excitation. However, as described in Chapter 1, in a real experimental situation, RF-fields are responsible for the radial confinement of the ions and are therefore always present in the trap. Their presence might also have an impact on the rotational distribution of the molecular ions. As a result, we need to verify that the RF-fields present in the experiment do not contribute to rotational population excitation within the cooling process. Since the time period of the RF-field is on the order of 100 ns, much longer than the dynamics of a scattering event between the molecular ions and the coolants (on the order of 100 ps), the two events are decoupled from each other, and we can consider the electric field generated by the coolant as the only source of rotational excitation of the molecular ion.

Modeling the scattering pair as classical point particles

The classical description of the ion-ion collision relies on the assumption that the wave functions of the molecular and atomic ions do not overlap, i.e. the ion-ion distance is far greater than the molecular radius. The molecular ion reaches its closest distance with the atomic ion for head-on collisions, for which the minimum distance, Eq. (4.7), reduces to $r_0 = \frac{1}{E}$. The equilibrium distances for the molecular ions considered here are presented in Table 4.II along with the scattering energy for which $r_0 = r_e$ at head-on collisions. As we see from the table, the scattering energies, as measured in the lab frame, for which overlap occurs are at 10 eV or higher. Keeping in mind that typical trap potential depths are up

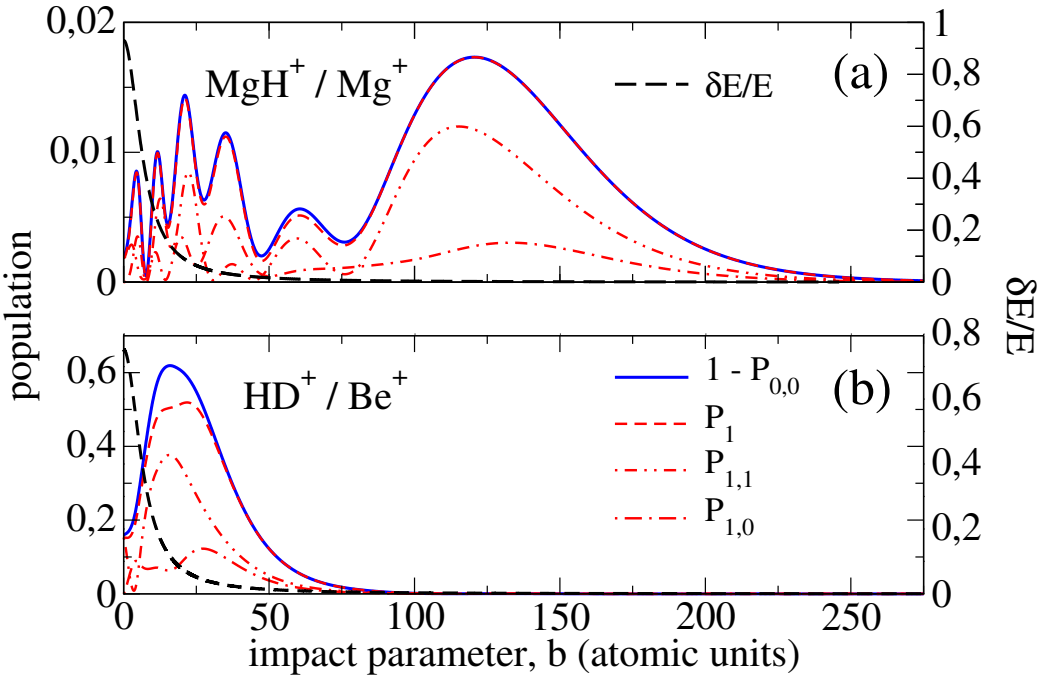

Figure 4.5: Final rotational population after one scattering event with energy $E = 2$ eV as a function of the impact parameter b, given in atomic units, for (a) MgH^+ / Mg^+ and (b) HD^+ / Be^+. The fractional energy transfer is shown as well (black dashed lines).

to 10 eV, and this is the maximum depth considered here we conclude that our model is justified for the experimental conditions considered in this work.

Neglecting vibrational excitations

Vibrational excitations may occur when the dipole moment changes with bond length. Upon Taylor expanding the dipole moment around the equilibrium distance, the first term is $\frac{dD}{dx}|_0 x$, with x the deviation from equilibrium. In the harmonic approximation, the transition moment of x between the vibrational states $\nu = 0 \rightarrow \nu = 1$ is $\sqrt{\frac{1}{2\mu_{vib}\omega_0}}$ [113]. The difference in energy between the two states is given by $\Delta E = \omega_0$, where ω_0 is the vibrational frequency. Apolar molecular ions lack a permanent dipole moment due to symmetry, a fact that does not change with internuclear distance. Here, vibrational excitations may occur if the polarizability changes with distance, and the selection rules lead to a possible transition $\nu = 0 \rightarrow \nu = 2$ [113], and therefore $\Delta E = 2\omega_0$. Notice that the vibrational energy scale set by $\omega_0 \sim 10^{-3}H$ is typically significantly larger than the energy scale set by the rotational constant, $B \sim 10^{-5}H$. Therefore, the vibrational period is typically ~ 100 times shorter than the rotational period. As we will see in the discussion on polar molecular ions, the rotational dynamics is near-adiabatic, and therefore the vibrational dynamics will certainly be

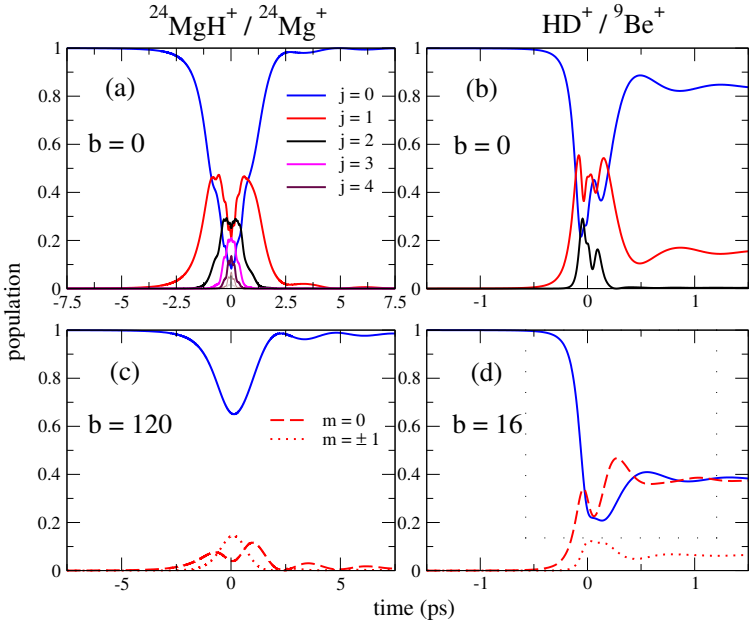

Figure 4.6: Population dynamics during one scattering event with energy $E = 2$ eV and impact parameter b, given in atomic units, for MgH^+ / Mg^+ (a,c) and HD^+ / Be^+ (b,d). (a,b) show the dynamics at $b = 0$, whereas (c,d) for the impact parameter that leads to the most population excitation. The collision involves adiabatic dynamics for head-on collisions (a,b) and tends to more non-adiabatic (c,d). The dynamics is qualitatively the same for other polar molecular species.

adiabatic. We will therefore neglect vibrational excitations and only consider the rotational degree of freedom in our model.

4.3.2 Polar molecular ions

When we study the population excitation at fixed scattering energy as a function of the impact parameter, for polar molecular ions we immediately encounter a counter-intuitive result. Contrary to what would be expected for the largest χ_D-value, numerical integration of the Schrödinger equation generated by the Hamiltonian, Eq. (4.21), show that the largest population transfer does not occur for head-on collisions, $b = 0$, c.f. Figure 4.5. Indeed, the rotational population transfer (blue) can potentially attain its maximum for large impact parameters, as is demonstrated in panels (a) and (b) for MgH^+ / Mg^+ and HD^+ / Be^+ scattering respectively. Note that the fractional translational energy transfer, Eq. (4.58), (black dashed lines) has its maximum for head-on collisions, whereas the maximum rotational transfer occurs at high values of the impact parameter where cooling is inefficient. As a consequence we can have significant population excitation at impact parameters with little cooling, see Figure 4.5. Notice in particular the low final population excitation for MgH^+ at small impact parameters, in particular for head-on collisions. The ratio of the

interaction energy to the rotational kinetic energy, see Eq. (4.17), $\chi_D \approx 220$ for 2 eV and head-on collisions, a number that would suggest vast population transfer, on account of the significantly larger interaction energy over the kinetic energy. We do not, however, observe such large population transfer in the simulations. For HD^+ / Be^+-scattering, maximum excitation occurs at smaller impact parameters, but we observe a significantly higher population transfer, even though the corresponding χ_D-value for HD^+ is about 18. Notice that in both cases most excited population ends up in the $j = 1$-sub states (red) and not in higher excited states, which is also a surprise given the high interaction strength.

The apparent absence of correlation between the χ_D-value and the final excitation becomes clear when studying the population dynamics. Although the final rotational excitation is very small, the effect of the field on the rotational dynamics is significant during the collision, c.f. Figure 4.6. In particular, for MgH^+ and head-on collision, the intermediate excitation leads to population of several rotational levels and the ground state is temporarily almost completely depleted, while most of the population returns to the ground state after the collision event, see Figure 4.6(a). Notice the lower intermediate population transfer for HD^+ (b) as compared to MgH^+, but its larger final population transfer. This trend also holds for nonzero values of b, as shown for $b = 120$ and 16 where the maximum final excitation occurs for MgH^+/HD^+, respectively (c,d). Therefore, no correlation between the value of χ_D and the final population excitation can be established. A high χ_D-value is, however, associated with a strong intermediate excitation dynamics, on account of the large maximum interaction energy. This is closely related to the energy shift of the rotational states as a function of scattering energy observed in Figure 4.7. These results suggest a near adiabatic dynamics within the high field limit for polar species. We therefore compute an estimation for the final excitation in the frame of an adiabatic approximation. The fact that most of the excited population is transferred to the $j = 1$ sub-states suggest that a two-level model in the adiabatic, or field-dressed, picture can be pursued.

Adiabatic dynamics means that the rate of change of the Hamiltonian is slow in comparison to the natural time scale set by the inverse of the instantaneous differences in the eigenenergies of the Hamiltonian. Therefore, consider the instantaneous eigenstates $|\psi_\iota(t)\rangle$ of a time-dependent Hamiltonian $\hat{\mathbf{H}}(t)$,

$$\hat{\mathbf{H}}(t)\,|\psi_\iota(t)\rangle = E_\iota(t)\,|\psi_\iota(t)\rangle\,, \tag{4.37}$$

with eigenenergies $E_\iota(t)$, where we use the labels ι, ι' to denote the states of the adiabatic (field-dressed) basis to distinguish them from the field-free basis j, j'. Any state $|\Psi(t)\rangle$ can be expanded into the time-dependent eigenstates,

$$|\Psi(t)\rangle = \sum_\iota c_\iota(t) e^{i\Theta_\iota(t)}\,|\psi_\iota(t)\rangle\,, \tag{4.38}$$

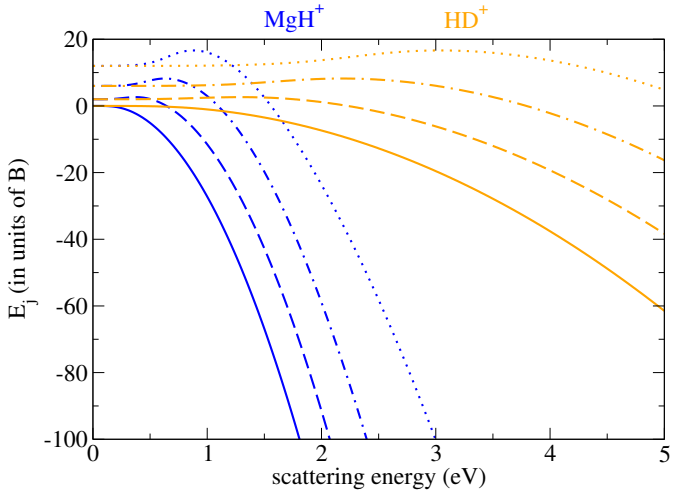

Figure 4.7: Eigenvalues (in units of the rotational constant B) of the Hamiltonian, Eq. (4.19), as a function of the scattering energy for zero impact parameter. Solid, dashed, dashed dotted and dotted lines represent the states $j = 0$, $j = 1$, $j = 2$, $j = 3$ respectively. The field strength is calculated at $t = \frac{\tau}{2\sqrt{3}}$ so that $\varepsilon\left(t = \frac{\tau}{2\sqrt{3}}\right) = \frac{3\varepsilon_0}{4} = \frac{3E^2}{4}$. The reason is that transitions in the adiabatic picture are proportional to the time rate of change of the Hamiltonian (Eq. (4.39)), which attains its maxima at $t = \pm\frac{\tau}{2\sqrt{3}}$.

where $\Theta_\iota(t) = -\int_{-\infty}^{t} E_\iota(t')dt'$. Inserting the expansion (4.38) into the time-dependent Schrödinger equation leads to the expression for the expansion coefficient,

$$\dot{c}_{\iota'}(t) = -c_{\iota'}\left\langle \psi_{\iota'}(t) \middle| \dot{\psi}_{\iota'}(t) \right\rangle - \sum_{\iota' \neq \iota} c_\iota(t) e^{i\Delta\Theta_{\iota\iota'}(t)} \frac{\left\langle \psi_{\iota'}(t) \middle| \partial_t \hat{\mathbf{H}}(t) \middle| \psi_\iota(t) \right\rangle}{E_\iota(t) - E_{\iota'}(t)}. \tag{4.39}$$

Details on how to arrive at Eq.(4.39) are presented in Appendix E.2. Eq. (4.39) is formally equivalent to the Schrödinger equation. For completely adiabatic dynamics, the second term vanishes (the time variation of the Hamiltonian is infinitely slow) and no transitions from the initial state take place in the field-dressed basis. In a near adiabatic approximation, the second term, containing the time rate of change of the Hamiltonian, is treated as small and approximations can be used to obtain an analytical expression for the population excitation.

In the adiabatic limit, the full solution (with initial state $\iota = 0$) is given by $c_0(t) = e^{i\gamma_0(t)}$, where $\gamma_0(t) = \int_{t_0}^{t} \left\langle \psi_{\iota'=0}(t') \middle| \dot{\psi}_{\iota'=0}(t') \right\rangle dt'$ is the Berry phase [112]. Assuming a near adiabatic dynamics, $c_0(t) \sim e^{i\gamma_0(t)}$ and $|c_{\iota'}(t)| \ll 1, \iota' \neq 0$. Then, integrating Eq. (4.39) term by term,

$$\begin{aligned} c_{\iota'}(t) &\approx \int_{-\infty}^{t} e^{i\gamma_0(t')} e^{i\Delta\Theta_{0\iota'}(t')} \frac{\left\langle \psi_{\iota'}(t') \middle| \partial_t \hat{\mathbf{H}}(t') \middle| \psi_0(t') \right\rangle}{E_{\iota'}(t') - E_0(t')} dt' \\ &= D\varepsilon_0 \left(\frac{\tau}{2}\right)^2 \int_{-\infty}^{t} \frac{2t'}{\left(t'^2 + \left(\frac{\tau}{2}\right)^2\right)^2} \frac{\langle \psi_{\iota'}(t') \,|\, \cos\theta_a \,|\, \psi_0(t') \rangle}{E_{\iota'}(t') - E_0(t')} e^{i(\gamma_0(t') + \Delta\Theta_{0\iota'}(t'))} dt'. \end{aligned} \tag{4.40}$$

In order to estimate Eq. (4.40) we require further approximations. In the low field limit, the eigenstates and eigenenergies are not significantly altered by the presence of the field, see HD^+ in Figure 4.7, and we expect to be able to use a reduced basis of free-field states to describe the field-dressed states. Evaluating the coefficient, Eq. (E.15), in the low-field limit we make the approximation that $\Delta\Theta_{0\iota'}(t) \approx \Delta E_{\iota'0}t$, where $\Delta E_{\iota'0}$ is constant. This approximation is expected to work better for low interaction scattering, i.e., low χ_D, since the effect on the eigenenergies increases with χ_D. In this limit we also approximate $\gamma_0(t) \approx 0$. This is motivated by noting that now, the wave field dressed ground state is close to the field-free ground state, and the time derivative of the wave function that enters in the integrand of $\gamma_0(t)$ approximately brings down a factor of $E_0 = 0B$, making $\gamma_0(t) \approx 0$. In doing so, we expect that the reduced phase rotation leads to an overestimation of the population excitation. In the extreme low-field limit, Eq. (E.15) becomes

$$c(\chi_D, \kappa) = i\frac{\pi}{2\sqrt{3}}\chi_D\kappa e^{-\kappa}. \tag{4.41}$$

We can improve the accuracy of this approximation by considering a two level approximation of the field-dressed basis in the field free basis, see Appendix E.2.1, where we obtain the expansion coefficient as

$$c(\chi_D, \kappa) = i\frac{\pi}{2\sqrt{3}}\frac{\chi_D\kappa}{\sqrt{1+\frac{\chi_D^2}{3}}}\exp\left(-\kappa\sqrt{1+\frac{\chi_D^2}{3}}\right). \tag{4.42}$$

Arriving at this expression we have made the approximations $\gamma_0(t) = 0$ and we have evaluated the eigenenergies at maximum field strength. In a real scattering event the eigenenergies are not constant, but vary over time. The first approximation leads to an overestimation of the excitation, since finite oscillations lead to more cancellation than zero oscillations. The effect of the second approximation is not so straightforwardly found due to the non-monotonic dependence of Eq. (4.42) on χ_D. We can use this expression to predict at which value of b maximum excitation takes place. Since the maximum occurs at the same values of χ_D for $|c|^2$ as for c itself, we will consider the derivative of the absolute square with respect to χ_D,

$$\frac{\partial|c(\chi_D,\kappa)|^2}{\partial\chi_D} = 2\left(\frac{\pi}{2\sqrt{3}}\right)^2\chi_D\kappa^2\exp\left(-2\kappa\sqrt{1+\frac{\chi_D^2}{3}}\right)\left[1-\frac{\chi_D^2}{3}\kappa\sqrt{1+\frac{\chi_D^2}{3}}\right]. \tag{4.43}$$

Setting the partial derivative to zero we get

$$\chi_D^2\kappa\sqrt{1+\frac{\chi_D^2}{3}} = 3. \tag{4.44}$$

As an estimate we can set the expression in the square root equal to one, from which we get the approximate relation

$$\chi_{D*} \approx \sqrt{\frac{3}{\kappa}} \tag{4.45}$$

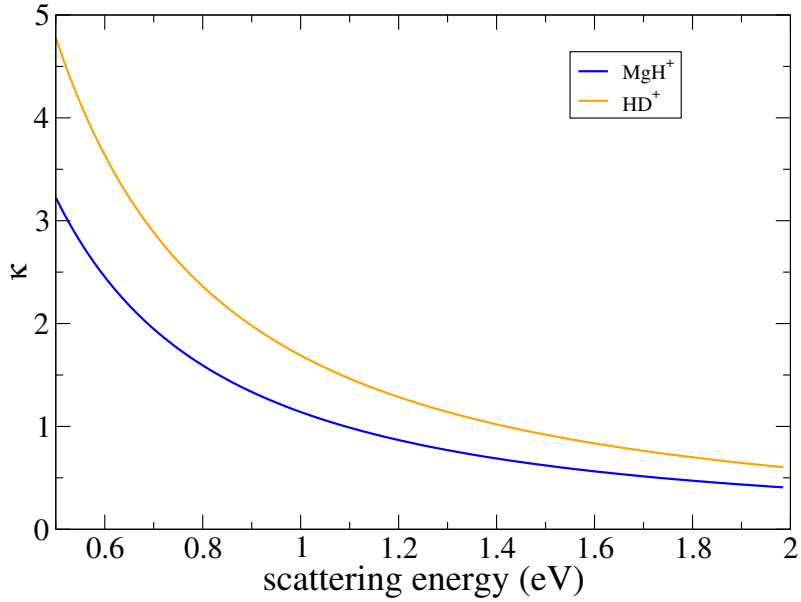

Figure 4.8: κ at b_*, i.e. Eq. (4.45) as a function of the scattering energy for HD^+.

at maximum population transfer. This expression allows us to estimate the value of χ_D at maximum population transfer for a given scattering energy. Furthermore, we can use Eqs. (4.18a) and (4.45) to estimate the value of b at which maximum population transfer occurs as a function of scattering energy for a given scattering pair, i.e., solve for b at $\chi_D = \chi_{D*}$ The result is

$$b \approx \sqrt{\left(\sqrt{\frac{D}{B}}\sqrt{\frac{\kappa}{3}} - \frac{1}{2E}\right)^2 - \left(\frac{1}{2E}\right)^2}. \tag{4.46}$$

After finding an analytical estimate for the excited state expansion coefficient, Eq. (4.42), it is of relevance to estimate when the adiabatic picture is applicable. Typically that is when the rotational time is short compared to the duration of the field, i.e., when $\kappa > 1$ (or even $\gg 1$). This estimate can only be reliable when the internal rotational structure is not significantly altered by the field so as to leave $T_{rot} \propto B^{-1}$. This is typically the case for HD^+, as can be seen from Figure 4.7. For HD^+ we can therefore estimate that the adiabatic picture is only relevant for scattering energies below 1.5 eV, as can be seen from Figure 4.8.

We now compare the population excitation obtained from the absolute square of Eq. (4.42), i.e., the analytical estimate, to the population obtained from numerical integration with the Hamiltonian Eq. (4.19). The results are presented in Figure 4.9 for HD^+. We see that the analytical formula comes near at reproducing the numerical results, without being particularly accurate. In particular, for low scattering energies, upper panel, the analytical results

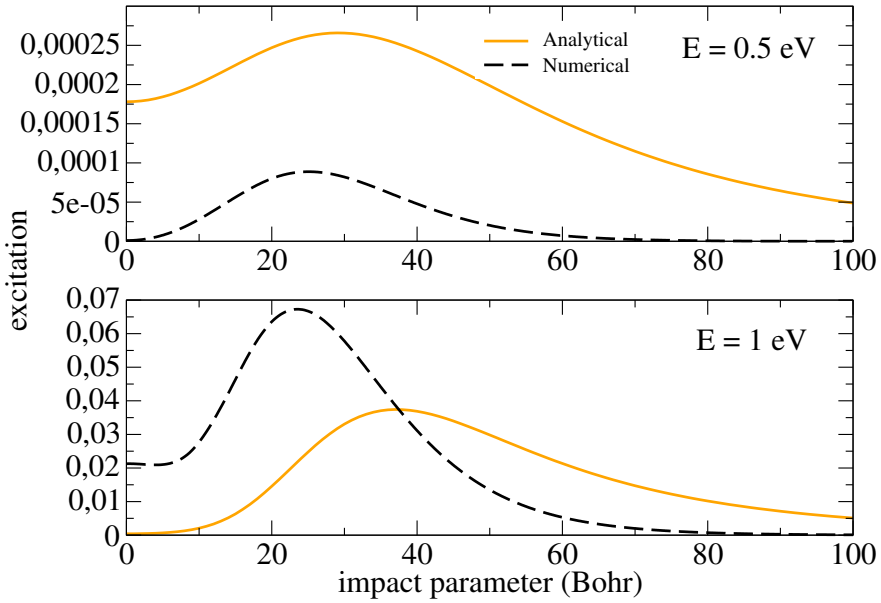

Figure 4.9: Population excitation of HD^+ as a function of impact parameter for two scattering energies, where $\kappa > 1$. The analytical results refer to the absolute square of Eq. (4.42), and numerical to full numerical integration of Eq. (4.19).

are overestimating the numerical results. At this low scattering energy we expect both the adiabatic picture and two-level approximation to be valid, so the disagreement needs a more detailed explanation. We notice that we have completely ignored the phase $\gamma(t)$ in our expression, Eq. (4.42), and as a result we expect our expression to overestimate the population excitation due to less cancellations due to neglect of oscillations. Furthermore, we have simply made the replacement $2B \to 2B\sqrt{1+\frac{\chi_D^2}{3}}$ for the energy difference when evaluating the excitation. In a real scattering event the energy difference changes continually between these two extreme values. It is not straightforward to estimate whether the effect of neglecting this gradual change leads to an over- or underestimation of the resulting excitation due to the nonlinear dependence on χ_D in Eq. (4.42). These two effects are relevant to low values of b, where the admixture of the excited state is more pronounced. For large enough values of b, Eq. (4.42) converges to Eq. (4.41), which ignores the effects that we just have discussed. Here the overestimation is likely due to our approximation in treating κ as independent of b (and evaluated at $b = 0$). This was motivated by the observed gradual dependence on b. In fact, κ is an increasing function of b and due to the exponential dependence on κ, we conclude that our model will overestimate the excitation at large b. As the energy increases, the agreement starts to become less convincing. Since at 1 eV we estimate $\kappa \approx 2$, it is not likely that the disagreement is due to loss of adiabaticity, but more likely a consequence of the lack of accuracy of the two-level model, see Appendix E.2.4 for a discussion of the two-level approximation. Guided by these results we suggest a strategy on how to estimate the population excitation in the low field limit:

Molecule	B (10^{-5} H)	D (atomic units)	μ (m_e)	$\frac{D}{B}$ (10^5)	$\sqrt{BD\mu}$
MgH^+	2.28	1.18	≈ 22500	≈ 0.5	≈ 0.78
MgD^+	1.5	1.18	≈ 22500	≈ 0.8	≈ 0.63
MgT^+	1.04	1.18	≈ 22500	≈ 1.1	≈ 0.53
CaH^+	2.15	2.35	≈ 30000	≈ 1.1	≈ 1.07

Table 4.III: Molecular parameters of molecular ions whose rotational states are significantly affected by the electric field. Note that μ depends on the mass of the coolant as well as the mass of the molecular ion.

1. Diagonalize the Hamiltonian, Eq. (4.19), over the relevant scattering energies to obtain the rotational eigenvalues as a function of scattering energies. If the eigenenergies do not alter significantly over the relevant interval, we are in the low-field limit. (Alternatively one can say that if χ_D is not much larger than one, then we are in this limit).

2. If we are in the low field limit, we must also verify that the adiabatic picture is relevant. To this end we use Eq. (4.45) to estimate when $\kappa > 1$. If so, the model can give physically relevant results.

3. If both approximations are justified, we use the absolute square of Eq. (4.42) to estimate the excitation.

In summary, for polar molecular ions whose internal states are not significantly affected by the field from the coolant, i.e., with a low χ_D-value, exemplified here by HD^+, we were able to derive a simplified model which could estimate the rotational excitation with some confidence. In our model we have use a basis of two free-field states to represent the field-dressed state in the presence of the field arising from the coolant. The limited basis size is questionable for the highest energies we have considered here. Based on the convergence of the eigenenergies, Figure E.1, a basis of three levels should provide a more accurate estimate. This would be particularly important, given that the molecule HD^+ is on the low $\frac{D}{B}$-ratio, suggesting that the internal states of most molecules would be more affected by the atomic field. We also find an estimate for at which scattering energy $\kappa = 1$, i.e. we can estimate at what scattering energies the adiabatic picture remains relevant.

We now continue by analysing the population excitation in the opposite limit, i.e., the high-field limit, see Appendix E.2 for details. In this limit the Hamiltonian approaches a two-dimensional harmonic oscillator. First, note that Eq. (E.29) from the discussion of the high-field limit in Appendix E.2.1 tells us that the cosine transition moment in the harmonic limit goes into $\frac{\theta_0^2}{2} = \sqrt{\frac{1}{2\chi_D}}$, which means that scattering with a high χ_D-value tends to lead to a higher degree of alignment. This is illustrated in Figure 4.10, where

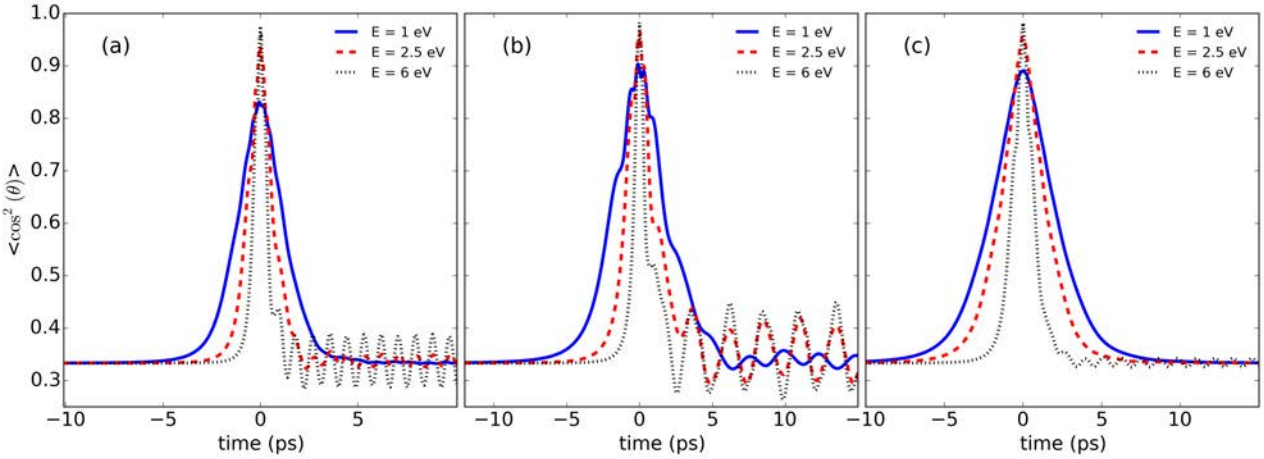

Figure 4.10: The alignment factor $\langle \cos^2 \theta \rangle$ as function of time at head-on collisions for different scattering energies, E. The different panels show different scattering pairs (a): MgH^+ - Mg^+, (b): MgT^+ - Mg^+, (c): CaH^+ - Ca^+.

the alignment factor $\langle \cos^2 \theta_a \rangle$ is shown as a function of scattering time. We see from the figure that the alignment is an increasing function of scattering energy, as expected from the stronger interaction arising from the closer approach of the molecular ion from the coolant. In Figure 4.10, panels (a) and (b) represent scattering pairs of almost identical scattering masses and therefore the same FWHM at a given scattering energy. The molecular ions in these panels also have the same dipole moment, but significantly different rotational constants, see Table 4.III, and therefore different interaction to kinetic energy ratio (χ_D-value) at a given scattering energy, with the larger ratio found in panel (b). The larger excitation seen from the larger oscillations in the alignment factor after collision in panel (b) is consistent with its larger χ_D-value. However, when we compare panels (b) and (c), both showing examples of systems with nearly identical χ_D-value at a given scattering energy, we see a considerably difference in final excitation. Indeed, the final excitation in panel (c) is the smallest of all three scattering pairs, whereas the excitation in panel (b) is the largest, at any given scattering energy. The alignment factors observed in the three figures, suggest that the maximum alignment is correlated with the χ_D-value in the scattering process, but that neither value is correlated with the population transfer.

We therefore need some other indicator of population transfer. We find that in the harmonic (high field) limit the expansion coefficient is

$$c_2^0(t) = -\frac{1}{2}\int_{t_0}^{t} \frac{t'}{t'^2 + \left(\frac{\tau}{2}\right)^2} \exp\left(i3\omega_H \frac{\tau}{2} \ln\left(\frac{t' + \sqrt{t'^2 + \left(\frac{\tau}{2}\right)^2}}{t_0 + \sqrt{t_0^2 + \left(\frac{\tau}{2}\right)^2}}\right)\right) dt', \tag{4.47}$$

see Appendix E.2.1. Here t_0 is an arbitrary starting time. We remind that $\omega_H = \sqrt{2D\varepsilon_0 B}$ and $\tau = 1.86\sqrt{\frac{\mu}{E^3}}$. Therefore, the phase factor in Eq. (4.47) is $\propto \sqrt{DB\mu}$ for a given

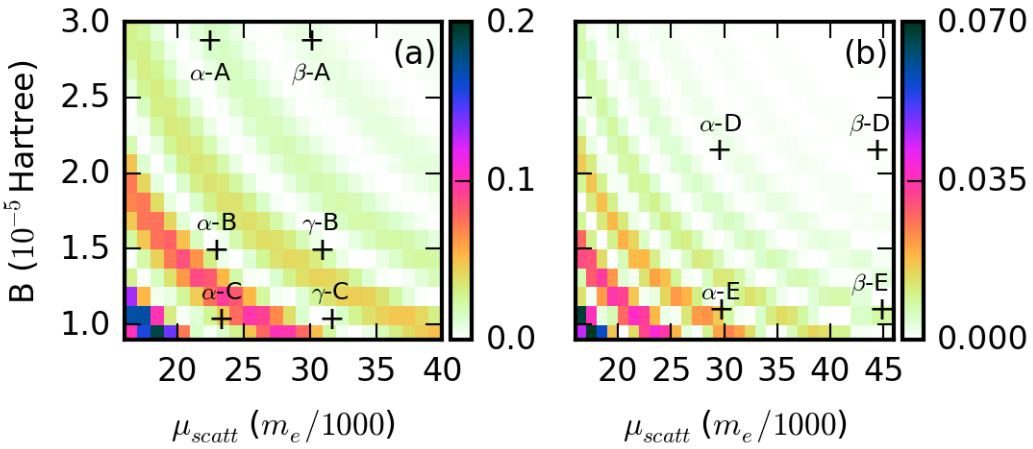

Figure 4.11: Population excitation as function of the rotational constant, B, and the reduced mass, μ, for two dipole couplings, $D = 1.18$ (i.e. the dipole moment of MgH^+) in left panel and $D = 2.34$ (i.e. the dipole moment of CaH^+) in the right panel. The scattering energy is $E = 2.5$ eV. The coolants are denoted with Greek letters, $\alpha = Mg^+$, $\beta = Ca^+$, $\gamma = Ba^+$. The molecular ions are designated by Latin letters, A =MgH^+, B =MgD^+, C =MgT^+, D =CaH^+, E =CaD^+.

scattering energy, and for head-on collisions the phase factor is $\propto \frac{1}{\sqrt{E}}$. A larger phase factor, $\omega_H \tau$, leads to faster oscillations, and thereby more cancellation of population transfer. When comparing Eq. (4.47) to the plots in Figure 4.11, where the population excitation is shown as a function of the rotational constant and reduced scattering mass for a scattering energy $E = 2.5$ eV. In the left panel, a lower dipole moment is used ($D = 1.18$) and a larger dipole moment in the right panel ($D = 2.34$). The faster oscillations in the right panel are also consistent with the larger phase factor associated with larger values of D. Since $\omega_H \tau \propto \frac{1}{\sqrt{E}}$ at head-on collisions, we expect to find more excitations for higher energies, which is consistent with the larger oscillations in $\langle \cos^2 \theta \rangle$, corresponding to more excitations, as seen in Figure 4.10. Based on the harmonic behavior in the high-field limit and numerical simulations we were able to conclude that low excitation is to be expected if the quantity $DB\mu$, with μ the reduced scattering mass of the molecular and atomic ions, is high. This is clearly mirrored in Figure 4.11, where the population excitations decrease as we go to the upper right corner (high $B\mu$-values) and we clearly observe less population transfer throughput in pane (b), corresponding to higher D-value. Notice that these results translates into the importance of the coolant (via the reduced mass μ) on the population excitation. Here care should be taken, however, since the mass of the coolant also determines the effectiveness of cooling (the closer in mass to the molecular ion the more efficient the cooling) and therefore this factor must also be considered in the choice of coolant.

The agreement of Eq. (4.47) with the numerical results presented in Figure 4.11 is only qualitative. A difficulty in analysing the dynamics in the high-field limit arises from the

fact that during scattering the field changes continually from zero through the low- and middle-field ranges before reaching the high-field limit. We made an attempt at matching the low- and high-field limits in our model, but could not find satisfactory results, see Appendix E.2 for further details. Therefore, for molecular ions whose rotational states are significantly affected by the presence of the field due to the atomic ion, we cannot find a reliable analytical estimate for the population transfer. Our results indicate, however, that we can use the product of the characteristic energy in the harmonic limit with the $FWHM$ of the Lorentzian field, $\omega_H \tau$, to order the population excitation, i.e., a higher value of this product gives less population excitation than a lower value of the product.

In conclusion, estimating the population transfer for polar molecular ions turned out to be a challenging task. Nevertheless, for polar molecular ions with a low $\frac{D}{B}$-ratio, such as HD^+, with D the dipole moment and B the rotational constant, we were able to derive a simplified model which could estimate the rotational excitation with some confidence. In the other limit, i.e., molecular ions with a high $\frac{D}{B}$-ratio, estimating the population transfer turned out to be even more difficult. Our results in this limit suggests that we can expect more rotational excitation with increasing scattering energy and less rotational excitation with increasing values of the product μDB.

4.3.3 Apolar molecular ions

In contrast to polar molecular ions, the maximum population transfer for apolar molecules does occur at $b = 0$, see Figure 4.12 where numerical integration of the Schrödinger equation under the Hamiltonian (4.22) is presented (blue and red lines) along with the fractional translational energy transfer (black lines) as a function of the impact parameter. Therefore, a significant energy transfer is observed whenever population excitations occur. Here the left y-axes denote population excitation and the right y-axes denote relative translational energy transfer. Notice the vastly different excitations observed for the two different molecular ions, i.e., the two different scales of the left y-axes in the two panels. Also notice that most of the excited population occurs for the m-conserving part of the interaction resulting in most of the excited population reaching the $m = 0$ sub-level. Although the final excitation is vastly different in panels (a) and (b) it is moderate even in the scattering shown in panel (a) which displays the most excitation.

The intermediate population excitation also remains small throughout the entire scattering, c.f. Figure 4.13. Although the dynamics is not generally adiabatic, we see that it approaches the adiabatic limit for low scattering energies as $\tau \to T_{rot} = B^{-1}$, i.e., as $\kappa \to 1$, see Eq. (4.36), in Figure 4.13 (a) (red striped lines) where the dynamics is shown for a scattering energy of 1 eV. Note the two different y-axes, corresponding to the scattering pairs N_2^+/Ca^+ (left and blue) and H_2^+/Be^+ (right and red), indicating a larger affect on

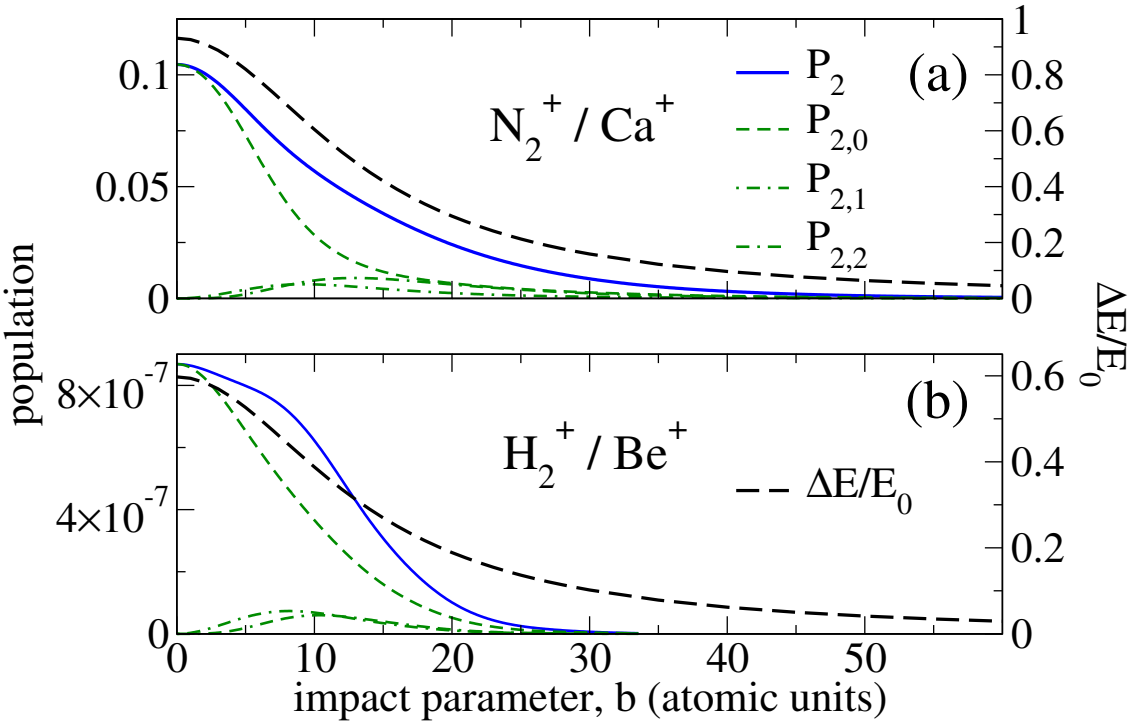

Figure 4.12: Population transfer from numerical integration of the Schrödinger equation under the Hamiltonian Eq. (4.22) and fractional translational kinetic energy transfer, $\frac{\Delta E}{E_0}$, in one collision as function of the impact parameter, b at $E = 1$ eV for apolar molecular ions. (a) $^{14}N_2$-$^{48}Ca^+$ and (b) H_2^+-$^9Be^+$.

the former scattering pair, as expected from the different values of the rotational constant and polarizability polarizability between the two pairs, see Table 4.I. Also notice the non-negligible, but small, population excitation for the former scattering pair. The relatively small final excitation is a result of the near-adiabatic dynamics, as indicated by the width of the trace of the blue curve being comparable to the rotational time. For higher scattering energies, Figure 4.13 (b), τ takes on smaller values, and so does κ, leading to a non-adiabatic dynamics. The population dynamics is illustrated for N_2^+/Ca^+ and H_2^+/Be^+-scattering at higher scattering energies. In panel (b) the scattering dynamics is shown for $\chi_Q\kappa \approx 3$ for both scattering systems. The nearly identical excitation dynamics suggests that the value of this product is the decisive factor for the population excitation in this limit. Note that in both high and low energy scattering regimes the numerical simulations suggest that we can expect low to moderate intermediate rotational population excitation.

The moderate effect on the rotational population distribution observed in the numerical simulations suggest that first order perturbation theory (PT) can be applied to estimate the population excitation for apolar molecular ions. In this case, the final-time amplitude of the lowest excited rotational state $|2,0\rangle$ after a single collision at energy E and impact

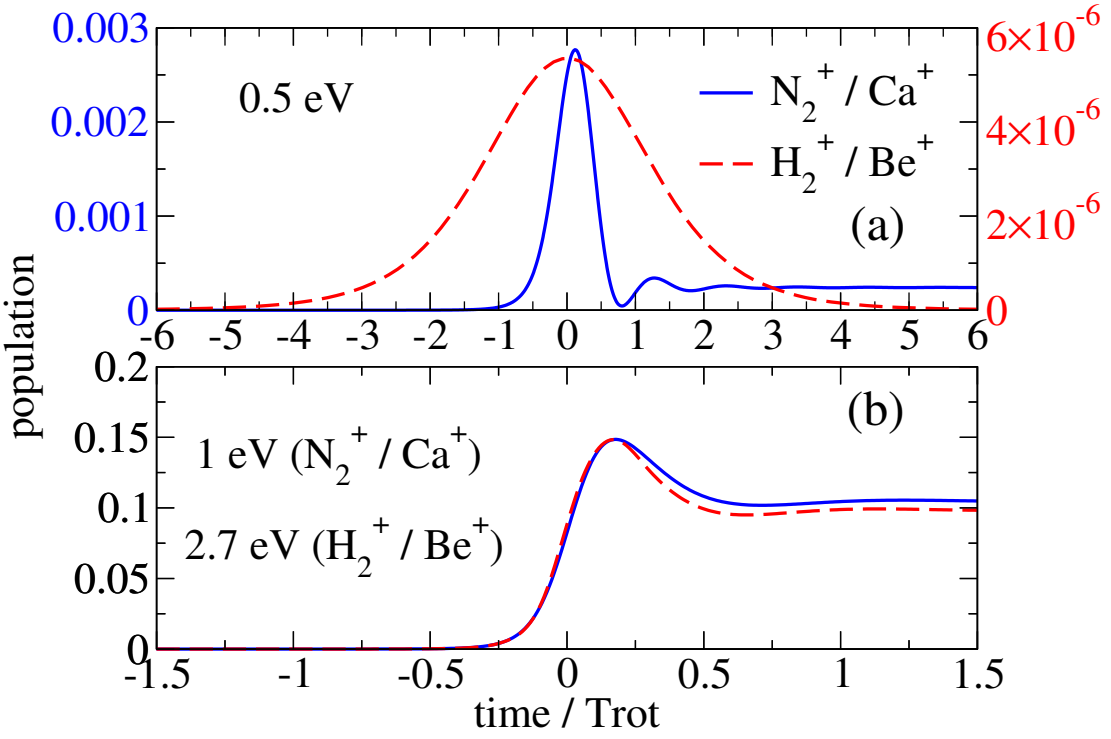

Figure 4.13: Population excitation from the dynamics generated by the Hamiltonian Eq. (4.22) as a function of time of a head-on scattering event with energy E indicated in the panels. (a) For low scattering energies the motion approaches the adiabatic limit as the FWHM of the electric field approaches the rotational time $T_{rot} = B^{-1}$. Here the left scale is for N_2^+ / Ca^+ and the right scale is for H_2^+ / Be^+. (b) Higher scattering energies lead to a narrower FWHM and adiabaticity is lost. The dynamics is shown for two different scattering energies, both corresponding to $\chi_Q \kappa \approx 3$, indicating that the excitation is to a large degree determined by the product $\chi_Q \kappa$. The dynamics is qualitatively the same for other apolar molecular species.

parameter b, is given by

$$c^{(1)}_{2,0}(E,b) = -i \int_{-\infty}^{\infty} \left\langle 2,0 \left| \hat{\mathbf{H}}_{int} \right| 0,0 \right\rangle e^{i6Bt} dt. \tag{4.48}$$

The contribution to the population excitation due to the polarizability interaction in Hamiltonian (4.22) of Eq. (4.48) yields

$$\begin{aligned} c_{\Delta\alpha}(E,b) &= -i\frac{\Delta\alpha\varepsilon_0^4}{4}\left(\frac{\tau}{2}\right)^4 \int_{-\infty}^{\infty} \frac{e^{i6Bt}}{\left(t^2 + \left(\frac{\tau(E)}{2}\right)^2\right)^2} dt \left\langle 2,0 \left| \cos^2\theta \right| 0,0 \right\rangle \\ &= -i\chi_\alpha(E,b) B \left(\frac{\tau}{2}\right)^4 \int_{-\infty}^{\infty} \frac{e^{i6Bt}}{\left(t^2 + \left(\frac{\tau(E)}{2}\right)^2\right)^2} dt \left\langle 2,0 \left| \cos^2\theta \right| 0,0 \right\rangle . \end{aligned} \tag{4.49}$$

The parameter $\chi_\alpha(E,b)$, defined in Eq. (4.18b), is a function of both the scattering energy and impact parameter through the maximum electric field strength $\varepsilon_0(E,b)$. Note that

within our model this is the only quantity determining the population excitation that depends on the impact parameter b. The integral Eq. (4.49) is easily evaluated using Cauchy's integral formula for derivatives, $f'(z_0) = \frac{1}{2\pi i}\oint_\gamma \frac{f(z)dz}{(z-z_0)^{n+1}}$, after noticing that the denominator can be rewritten as $\frac{1}{\left(t^2+\left(\frac{\tau}{2}\right)^2\right)^2} = \frac{1}{\left(t+i\frac{\tau}{2}\right)^2\left(t-i\frac{\tau}{2}\right)^2}$. In our case $n=1$ and γ is the union of the interval $[-R,R,]$ on the real axis and the semicircle in the upper half of the complex plane of radius R centered at the origin. As $R\to\infty$, the contribution to the integral from the semicircle goes to zero, and we obtain

$$c_{\Delta\alpha}(\chi_\alpha,\kappa) = -i\frac{\pi}{4}\chi_\alpha\kappa(1+3\kappa)e^{-3\kappa}\left\langle 2,0\left|\cos^2\theta\right|0,0\right\rangle. \tag{4.50}$$

Notice that the expansion coefficient depends on χ_α and κ, Eq. (4.36), and not on τ and B separately.

Excitation due to the quadrupole interaction term of Hamiltonian (4.22) in Eq. (4.48) is obtained as

$$\begin{aligned} c_Q(E,b) &= +i\frac{3Q_Z\varepsilon_0^{3/2}(E,b)}{4}\left(\frac{\tau}{2}\right)^3\int_{-\infty}^{\infty}\frac{e^{i6Bt}}{\left(t^2+\left(\frac{\tau(E)}{2}\right)^2\right)^{3/2}}dt\left\langle 2,0\left|\cos^2\theta\right|0,0\right\rangle \\ &= i\chi_Q(E,b)B\left(\frac{\tau}{2}\right)^3\int_{-\infty}^{\infty}\frac{e^{i6Bt}}{\left(t^2+\left(\frac{\tau(E)}{2}\right)^2\right)^{3/2}}dt\left\langle 2,0\left|\cos^2\theta\right|0,0\right\rangle. \end{aligned} \tag{4.51}$$

Here, the integral is not of the form of a Cauchy integral formula for derivatives. However, by the variable transformation $t=\frac{\tau}{2}\tan u$, the integral over time in Eq. (4.51) can be written as

$$\left(\frac{\tau}{2}\right)^2\int_{-\infty}^{\infty}\frac{e^{i6Bt}dt}{\left(t^2+\left(\frac{\tau}{2}\right)^2\right)^{3/2}} = \int_{-\frac{\pi}{2}}^{\frac{\pi}{2}}\cos u e^{i3\kappa\tan u}du \equiv f(\kappa). \tag{4.52}$$

In this form we see explicitly that the value of the integral only depends on $\kappa(E)$ just as the polarizability term. An analytical approximation to the integral, Eq. (4.52), can be found by differentiating under the integral sign, using Leibniz' rule and solving the resulting differential equation, with the result

$$f(\kappa)\approx 2\sqrt{1+6\kappa}e^{-3\kappa}, \tag{4.53}$$

see Appendix F for details. The analytical expression approximates the numerical result of the integral, Eq. (4.52), well for all κ, as observed in Figure 4.14. With the integral Eq. (4.52) solved, the excited state expansion coefficient due to the quadrupole interaction is

$$c_Q(\chi_D,\kappa)\approx i\chi_Q\kappa\sqrt{1+6\kappa}e^{-3\kappa}\left\langle 2,0\left|\cos^2\theta\right|0,0\right\rangle. \tag{4.54}$$

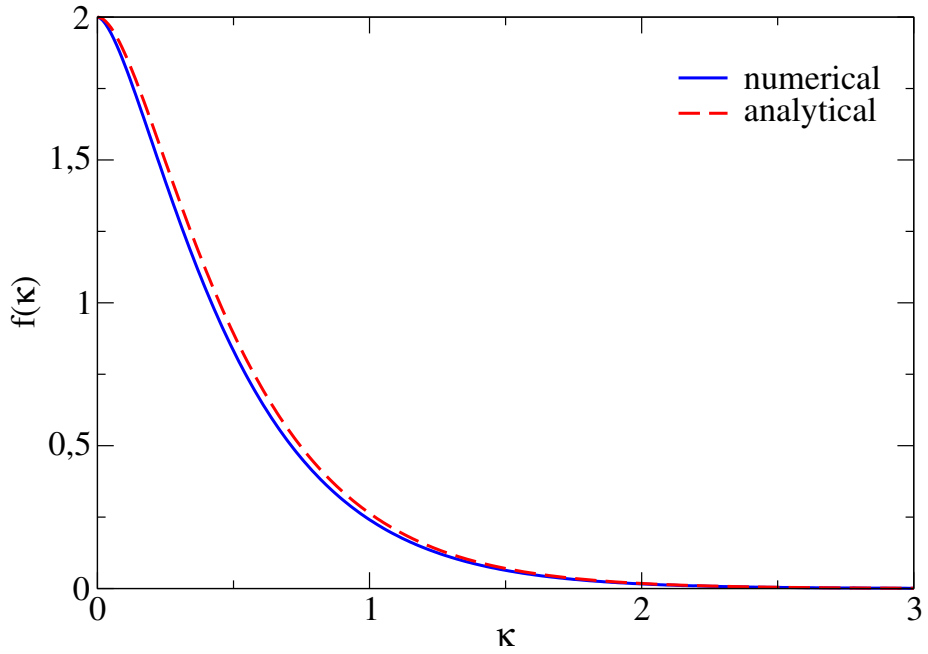

Figure 4.14: The function $f(\kappa) = \int_{-\pi/2}^{\pi/2} \cos u e^{3i\kappa \tan u} du$, Eq. (4.52) and its analytical approximation $f(\kappa) = 2\sqrt{1+6\kappa}e^{-3\kappa}$, Eq. (4.53).

The form of $f(\kappa)$ arises by assuming the ground state as initial state, and due to the selection rule $\Delta j = 2$ we have $\Delta E = 6B$. In general, with $\Delta j = 2$ we have $\Delta E_j = (4j+6)B$ for an initial state with rotational quantum number j. Consequently, in general $f(\kappa) \approx 2\sqrt{1+(4j+6)\kappa}e^{(2j+3)\kappa}$. This treatment is of relevance e.g. when the even rotational states are forbidden by symmetry, in which case the ground states correspond to $j = 1, \quad m = 0, \pm 1$ and consequently $\Delta E = 10B$. In this case we also have to consider the transition matrix elements $\langle 3, m \,|\, \cos^2\theta \,|\, 1, m \rangle$, where $m = 0, \pm 1$.

Notice that for both the polarizability- and the quadrupole interactions the excitation depends on two parameters, $\chi_{\alpha/Q}$ and κ, which relate to molecular properties, the scattering energy and the impact parameter. The relative contribution of the two interactions is given by the ratio

$$\frac{|c_{\Delta\alpha}|^2}{|c_Q|^2} = \left(\frac{\pi}{4}\right)^2 \left(\frac{\chi_{\Delta\alpha}}{\chi_Q}\right)^2 \frac{(1+3\kappa)^2}{1+6\kappa}. \tag{4.55}$$

At the scattering energies relevant to us the quadrupole interaction is the dominant contribution. Scattering at even higher energies would eventually lead to a dominating polarizability interaction, since $\frac{\chi_\alpha}{\chi_Q} \propto E^2$. At high energies (corresponding to low κ) we also have $\frac{(1+3\kappa)^2}{1+6\kappa} \to 1$ and the relative importance only depends on the ratio (squared) of the two χ-factors, and for scattering systems and energies typical in this work favours the importance of the quadrupole interaction. We see that Eq. (4.54) quantifies the qualitative picture in Figure 4.13 (a) and (b) in that as κ increases, i.e. the low energy limit, the exponential

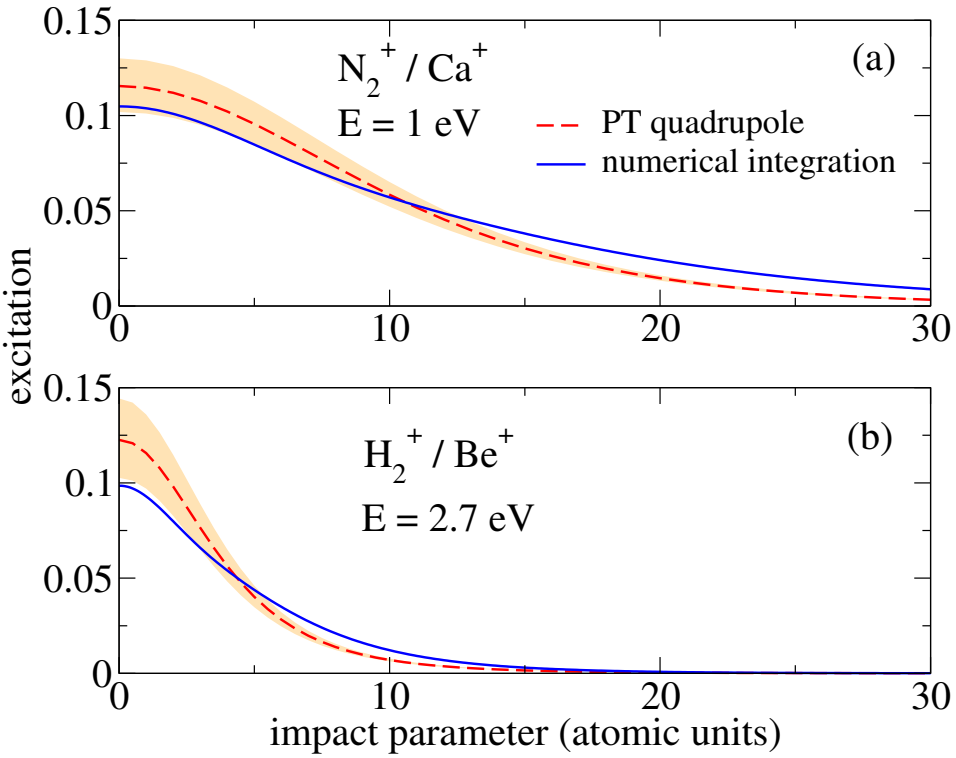

Figure 4.15: Comparison between excitation as obtained from numerical integration of the Schrödinger equation generated by the Hamiltonian Eq. (4.22) and as obtained from the quadrupole interaction (absolute square of Eq. (4.54). The shaded region shows the maximum deviation due to the polarizability interaction, where the excitation takes values in $|c_Q|^2 + |c_{\Delta\alpha}|^2 \pm 2|c_Q||c_{\Delta\alpha}|$, with $|c_{\Delta\alpha}|$ the absolute square of Eq. (4.49).

factor suppresses population transfer, corresponding to the adiabatic limit, and in the limit of small κ, i.e. high energy scattering, the excitation coefficient becomes proportional to $\chi_Q\kappa$.

The actual population excitations can be confidently obtained from perturbation theory including only the quadrupole interaction, c.f. Figure 4.15. The population excitation is shown as function of the impact parameter for the analytical expression of the quadrupole interaction (absolute square of Eq. (4.54)) and compared to the numerical simulation of the Schrödinger Equation, Eq. (4.22), including both the polarizability- and quadrupole interactions. The analytical results are given with margins (shaded region) obtained from including the polarizability interaction, $|c_Q|^2 + |c_{\Delta\alpha}|^2 \pm 2|c_Q||c_{\Delta\alpha}|$. The agreement between analytical and numerical results is good, in particular for low b. Notice that the margins increase for small b, as is expected since a larger field strength favors the polarizability interaction, as expected from the ratio $\frac{|c_{\Delta\alpha}|^2}{|c_Q|^2}$, which increases with increasing energy. The more rapid decrease in excitation with increasing b for the analytical- as compared to the

full numerical calculations is likely due to the neglect of the transitions to non-zero m-states as suggested by Figure 4.12.

In conclusion, our investigation has shown that first order perturbation theory, taking the quadrupole interaction into account, provides an analytical estimate for rotational excitations of molecular ions in scattering processes by atomic ions. The analytical estimate allows us to easily apply our treatment to any apolar molecule, and not just the species considered here.

4.4 Modeling a complete cooling cycle

We now turn our attention to the cooling cycle, which comprises a series of scattering events between the molecular ion and the atomic coolant ions. Each collision transfers a fraction of the translational energy from the molecular ion to the coolant, as given by Eq. (4.8), leading to an accumulative reduction of the molecular ion's kinetic energy. We are interested in the time scales and the expected internal rotational excitation associated with the cooling process in the crystal and single ion scenarios. For this purpose it is convenient to partition the energy interval between the maximal (initial) and minimal (final) translational energies (E_{max} and E_{min}) of the molecular ion into sub-intervals. If the partition is dense enough, we can treat all energy-dependent quantities, such as the energy transfer, as constants within each interval. The number of collisions required to lower the molecular ion's translational energy for each given sub-interval will be a central quantity in the study of the cooling cycle. Another central quantity in the scattering theory is the impact parameter, and we will start our study of a complete cooling cycle with it.

4.4.1 Averaging over the impact parameter

In an experimental situation, the impact parameter is not controllable and therefore we need to average over all its possible values. In doing so we obtain a typical energy transfer at a given energy, E. We will consider two cooling scenarios: cooling by a single atom (SA) and a large Coulomb crystal (CC). In the single ion scenario the distance between the atomic ions is assumed to be so large that the molecular ion will only interact with one single atomic ion each time the molecular ion passes the crystal. The molecular ion moves under the influence of the trap, Eq. (4.2). We assume the atom to be in the trap ground state such that the characteristic length at scattering energy E is

$$\sigma = \sqrt{\frac{E_L}{M_{mol}\omega^2}} = \sqrt{\frac{E}{\mu\omega^2}}. \tag{4.56}$$

Since the scattering process is torque-free, it will take place in a plane. The distribution of the impact parameter is symmetric around the z axis in Figure 4.2 such that

$$\langle f(b)\rangle_{si} = \frac{1}{\sigma^2}\int_0^\infty f(b)\exp\left(-\frac{b^2}{2\sigma^2}\right)bdb, \tag{4.57a}$$

where $\langle\rangle_{si}$ denotes the average with respect to the impact parameter in the single ion scenario. In the crystal cooling limit, the radial scale is set by b_{max}, see Figure 4.1, where $b_{max} \ll \sigma$. In this case $e^{-\frac{b_{max}^2}{2\sigma^2}} \sim 1$ always holds, and

$$\langle f(b)\rangle_c = \frac{2}{b_{max}^2}\int_0^{b_{max}} f(b)bdb \tag{4.57b}$$

is the average in the crystal scenario. Note that the maximum impact parameter is given by $b_{max} = \frac{d}{2}$, see left panel of Figure 4.1.

4.4.2 Energy and and population transfer

Now that we know how to average functions over b, we can convert functions that depend on both the scattering energy and impact parameter into typical (i.e. averaged over b) functions of the scattering energy alone. We begin by considering the energy transfer associated with a collision. Let the initial translational energy of the molecular ion be E_{max} and the final energy be E_{min}. For a given scattering energy, the typical transfer of kinetic energy from the molecular ion to the coolant, $\langle\delta E_L\rangle$, is given by the average with respect to the impact parameter of Eq. (4.8). The average for the single ion- and crystal cooling scenarios are obtained from Eqs. (4.57a) and (4.57b), respectively. The total energy transferred in a cycle of N collisions is then

$$\Delta E_L = \sum_{i=0}^{N-1}\langle\delta E_L\rangle(E_i). \tag{4.58}$$

If the energy transfer in each collision is very small compared to the collision energy, then the energy transfer is approximately constant over several collisions, $n(E_i)$ and, assuming that the energy interval ΔE_L is not too large,

$$\Delta E_L \approx n(E)\langle\delta E_L\rangle(E) \Rightarrow n(E) \approx \frac{\Delta E_L}{\langle\delta E_L\rangle(E)} = \frac{\Delta E}{\langle\delta E\rangle(E)}, \tag{4.59}$$

thus defining $n(E)$. A partition of the full energy interval $[E_{max}, E_{min}]$ into m subintervals such that

$$E_0 = E_{max} > E_1 > ... > E_i > E_{i+1} > ... > E_N = E_{min} \tag{4.60}$$

allows us to rewrite Eq. (4.58) as

$$\Delta E_L = \sum_{i=0}^{m-1} n(E_i)\langle\delta E_L\rangle(E_i). \tag{4.61}$$

In particular, in the crystal cooling scenario, the single collision energy transfer is obtained from Eq. (4.8),

$$\langle \delta E_L \rangle_c (E) = \frac{2}{b_{max}^2} \int_0^{b_{max}} \delta E_L(b, E) b db = \frac{\xi \log\left((2b_{max}E)^2 + 1\right)}{(1+\xi)^2 b_{max}^2 E}, \tag{4.62}$$

see Appendix F.5 for the details of the calculations. From the average energy transfer we can get an analytical result for $n(E)$,

$$n(E; \Delta E, b_{max}) = \frac{(1+\xi)^2 b_{max}^2 E}{\xi \log\left((2b_{max}E)^2 + 1\right)} \Delta E, \tag{4.63}$$

using Eqs. (4.4), (4.9), (4.57b) and (4.59). The quantity $n(E)$ is central in our model, since it is directly related to the total cooling time and excitation as we will discuss in the next two sections. Obviously the total number of collisions in a full cycle can be obtained by simply summing up the number of collisions on each subinterval, $N = \sum_{i=1}^{m} n(E_i) \Delta E_L$, which becomes an integral in the limit $\Delta E_L \to dE$ as

$$N = \frac{(1+\xi)^2 b_{max}^2}{\xi} \int_{E_f}^{E_i} \frac{E}{\log\left((2b_{max}E)^2 + 1\right)} dE. \tag{4.64}$$

The number of collisions needed to lower the energy from E_i to E_{i+1}, $n(E_i)$, also allows us to estimate the total excitation in a full cycle from the single collision excitations. Let the initial internal state of the molecular ion be the rovibrational ground state and let the population excitation after a single collision at energy E and impact parameter b be $\epsilon(E, b)$. Then the remaining ground state population after the collision is $P_0(E, b) = 1 - \epsilon(E, b)$. The average single collision excitation with respect to b at energy E is $\tilde{\epsilon}(E) = \langle \epsilon(E, b) \rangle$. On a given sub-interval, i, the remaining rotational ground state population is

$$\begin{aligned} P_i = (1 - \tilde{\epsilon}(E_i))^{n(E_i)} &= \sum_{k=0}^{n(E_i)} \frac{n(E_i)!}{k!(n(E_i)-k)!} \tilde{\epsilon}(E_i)^k \\ &= 1 - n(E_i)\tilde{\epsilon}(E_i) + \frac{n(E_i)(n(E_i)-1)}{2} \tilde{\epsilon}(E_i)^2 \mp \dots \\ &\approx 1 - n(E_i)\tilde{\epsilon}(E_i). \end{aligned} \tag{4.65}$$

The remaining rotational ground state population after the full cooling cycle is obtained by multiplying the partial remaining populations, $P = \Pi_{i=1}^{N} P_i$, which results to first order in $n(E_i)\tilde{\epsilon}(E_i)$, in a full cycle excitation $\Phi_\Sigma = 1 - P$ given by

$$\Phi_\Sigma \approx \sum_{i=1}^{N} n(E_i)\tilde{\epsilon}(E_i). \tag{4.66}$$

Keeping in mind that we are looking for an upper bound and not an exact formula for the excitation, we can justify retaining only the first order term by arguing that if the excitation in a single collision is large enough to motivate retaining higher order terms then certainly the accumulated excitation from many collisions will already be detrimental to any realistic experiment.

4.5 Results for a complete cooling cycle

We will now turn our attention to the complete cooling cycle. In this section we will investigate the timescales of a complete cycle in the two limiting scenarios as well as the estimated accumulated excitation of the cycle. In order to do so, we need to estimate the collision frequency between the molecular ions and the coolant ions, as well as the number of collisions that are required to complete the cooling cycle. Additionally, we will need the single collision excitations and, in particular, their averages over the impact parameter in order to obtain an estimate for the accumulated excitation in the cooling process, Eq. (4.66). In both aspects, the sub partition of the energy interval as well as the quantity $n(E_i)$ will be of importance for us.

4.5.1 Cooling time scales

We begin our discussion of the cooling time scales with the crystal cooling scenario, Figure 4.1(a), in which the frequency between collisions, ν_c, is given by the ratio of the initial speed of the molecule v_L and the distance between the atomic ions d,

$$\nu_c(E) = \frac{v_L}{d} = \frac{1}{2b_{max}}\sqrt{\frac{2E_L}{M_{mol}}} = \frac{1}{2b_{max}}\sqrt{\frac{2E}{\mu}}. \tag{4.67}$$

Consequently, the time between collisions is $t(E) = \nu_c^{-1}(E)$, and remembering the partitioning of the energy interval, Eq. (4.60), we can estimate the cooling time for each subinterval, i, as $t_c(E_i) = \frac{n_c(E_i)}{\nu_c(E_i)}$. With $n_c(E_i)$ given by Eq. (4.63), we arrive at the explicit formula

$$t_c(E_i) = \frac{\sqrt{2\mu}(1+\xi)^2 b_{max}^3 \sqrt{E_i}}{\xi \log\left((2b_{max}E_i)^2 + 1\right)}\Delta E_i. \tag{4.68}$$

The cooling time of the complete cycle, T_c, is the sum of Eq. (4.68) from each subinterval (4.60), which in the limit of infinitesimal subintervals becomes an integral,

$$\begin{aligned} T_c &= \frac{\sqrt{2\mu}(1+\xi)^2 b_{max}^3}{\xi} \sum_{i=0}^{m-1} \frac{\sqrt{E_i}}{\log\left((2b_{max}E_i)^2 + 1\right)}\Delta E_i \\ &\underset{\Delta E \to dE}{\to} \frac{\sqrt{2\mu}(1+\xi)^2 b_{max}^3}{\xi} \int_{E_i}^{E_f} \frac{\sqrt{E}}{\log\left((2b_{max}E)^2 + 1\right)} dE. \end{aligned} \tag{4.69}$$

In the single ion scenario, the collision frequency is determined by the trap frequency, ω,

$$\nu_{si} = 2\frac{\omega}{2\pi}, \tag{4.70}$$

where the prefactor of two arises since the molecular ion passes the crystal twice in one period, see right panel of Figure 4.1. The time between collisions t_{si} is

$$t_{si} = \nu_{si}^{-1} = \frac{\pi}{\omega} = \pi\sigma\sqrt{\frac{\mu}{E}}. \tag{4.71}$$

The expression for the energy transfer in the single ion scenario, Eq. (4.57a), is more complicated, so a direct calculation of the total cooling time is not possible. Nevertheless, we can estimate the energy transfer as

$$\langle \delta E \rangle_{si} = \frac{1}{\sigma^2} \int_0^\infty \delta E(b, E) \exp\left(-\frac{b^2}{2\sigma^2}\right) b db < \frac{1}{\sigma^2} \int_0^\infty \delta E(b, E) b db, \tag{4.72}$$

Combining this estimate with Eqs. (4.59) and (4.71), a lower limit to the cooling time of the subinterval i is obtained,

$$T_{si,i} > \frac{\pi \sigma^3 \sqrt{\frac{\mu}{E}}}{\int_0^\infty \delta E(b, E) b db} \Delta E, \tag{4.73}$$

Using Eqs. (4.68) and (4.73), we obtain a comparison of the cooling time on each subinterval between the two scenarios as,

$$\frac{T_{si,i}}{T_{c,i}} > \frac{\frac{\omega}{\pi}\sigma^2}{\sqrt{\frac{\mu}{2E}} b_{max}^3} = \sqrt{2}\pi \left(\frac{\sigma}{b_{max}}\right)^3, \tag{4.74}$$

where we have used Eq. (4.56) to relate ω to σ. Since, typically $\sigma \gg b_{max}$, it is to be expected that the cooling timescales are significantly larger in the single ion cooling scenario than in the crystal cooling scenario. Note that, in our estimate of T_{si} we have treated σ as a constant with respect to the scattering energy, when actually $\sigma \propto \sqrt{E}$, and will consequently decrease in the cooling process. Therefore, as it stands our inequality is not quite justified. One can, however, find an average $\tilde{\sigma}$ with respect to energy, see Appendix F.6. We find that $\tilde{\sigma} \approx \frac{6}{7}\sigma(E_{max})$, in the limit that $E_{min} \to 0$, cf. Eq. (F.24). Therefore, we need to include a correction factor $\left(\frac{6}{7}\right)^3 \approx 0.63$ to the right-hand side of Eq. (4.74) whence estimating the single ion timescale.

In order to estimate the cooling times in a realistic experimental setup, we consider the timescale in a representative cooling process of $^{24}MgH^+$-ions using $^{24}Mg^+$ as coolant. The energy E shall be reduced from 2 eV down to 0.01 eV. We consider the crystal cooling setup with the crystal parameter $d = 10^5$. In the calculations we make use of $\Delta E = 0.01$ in Eq. (4.69) and the timescale of the cooling process is estimated to be approximately $2 \cdot 10^{-3}$ s. The timescale in a single ion cooling scenario can be obtained from the crystal cooling time in combination with Eq. (4.73). Considering a trap frequency of 1 MHz, we estimate the timescale to be 10^5 s (roughly 24h) for the single ion scenario, and 15h when taking the correction factor into account. The timescale for cooling of other molecular ions considered in this work is on the same order of magnitude or longer. Hence, due to timescale constraints, we conclude that the crystal scenario is the only experimentally feasible alternative and therefore only the crystal cooling scenario will be considered in the following.

n	$\langle \delta E_L \rangle$ (eV)	ncoll	our time (ms)	ref. time* (ms)
10	$1.15 \cdot 10^{-5}$	$3.47 \cdot 10^{4}$	$3.53 \cdot 10^{-1}$	$\approx 4.6 \cdot 10^{-1}$
20	$4.80 \cdot 10^{-5}$	$8.34 \cdot 10^{3}$	$8.48 \cdot 10^{-2}$	$\approx 1.3 \cdot 10^{-1}$
30	$1.14 \cdot 10^{-4}$	$3.50 \cdot 10^{3}$	$3.56 \cdot 10^{-2}$	$\approx 6.0 \cdot 10^{-2}$
40	$2.11 \cdot 10^{-4}$	$1.89 \cdot 10^{3}$	$1.93 \cdot 10^{-2}$	$\approx 3.6 \cdot 10^{-2}$

Table 4.IV: Effect of the charge of the ion coolant on the cooling time. Starting energy is $E_L = 0.4$ eV and the final energy is 0.0 eV. A crystal cooling scenario where $d = 3.3 \cdot 10^5$ Bohr is considered and the scattering pair is $^{100}HCI^{n+}$-$^{24}Mg^{+}$. The collision frequency was estimated from the initial speed and mean free path and found to be $\approx$ 280 MHz. *ref. time corresponds to the time obtained in figure 6 of ref. [153].

Since we have made some simplifying assumptions in our model of the cooling cycle, in particular we have ignored collective effects in the crystal, such as micromotion and coupling between coolants, we need to make sure that the assumptions are justified. We test the performance of our model in the crystal cooling scenario against the more elaborate method of molecular dynamics (MD), which take such effects into account. We have found such simulations treating the cooling process of highly charged ions ($^{100}HCI^{n+}$) in a strongly coupled laser-cooled plasma of MgH^{+} in Ref. [153]. The authors study the effect of the charge (n+), number of collisions, on the stopping time. They consider cooling from an initial scattering energy $E_L = 0.4$ eV and a final scattering energy of 0.0 eV and a scenario in which the density of coolants $n_{Mg} = 4.23 \cdot 10^{13}\ m^{-3}$. This corresponds to a mean free path, $l_{mfp} = \left(\frac{4\pi n_{Mg}}{3}\right)^{-1/3} \approx 3.3 \cdot 10^5$ Bohr which we take as the crystal parameter d. We calculate the average energy transfer, number of collisions and total scattering time as a function of n, using our model. Instead of $q_{at}q_{mol} = 1$ in Eq. (4.9), we now use $q_{at}q_{mol} = n$. The results are summarized in Table 4.IV. We notice that our stopping times are consistently smaller than that of the reference, but within half the values listed there, and with better agreement for lower values of n. For example, at $n = 10$ our results are at $\approx 77\%$ of the times in the reference. Given that, in our work, $n = 1$, we expect the agreement to be even better. We therefore conclude that our model is in reasonable agreement with the MD-simulations, i.e., we see that collective effects do not significantly affect the collision dynamics, in particular not for systems with low or moderate values of n.

4.5.2 Accumulated excitation for polar molecular ions

As we have found in our studies of single collisions involving polar molecular ions colliding with the atomic ion coolants, we cannot in general find an analytical expression for the rotational population excitation. We will therefore focus on finding the accumulated excitation in a cooling process only in the low field case, for which we were able to obtain an

analytical expression for the single collision excitation, see Section 4.3.2. The accumulated rotational excitation of polar molecular ions after a full cooling cycle was estimated using Eq. (4.66). The single collision excitation is obtained from both numerical integration of the Schrödinger equation, Eq. (4.19) and, when the two-level approximation is valid, as the sum of the modulus squared of Eqs. (4.42). In either case, the excitations are obtained as a function of b at each energy E and finally as the average over b, Eq. (4.57b). In the two-level approximation we obtain

$$\tilde{\epsilon}(E) = \frac{(\pi\kappa)^2}{6b_{max}^2}\int_0^{b_{max}} \frac{\chi_D^2(b,E)}{\left(1+\frac{\chi_D^2(b,E)}{3}\right)} \exp\left(-2\kappa\sqrt{1+\frac{\chi_D^2(b,E)}{3}}\right) b\, db. \tag{4.75}$$

The accumulated excitation is presented in Figure 4.16(a). The numerical simulations (dashed and shadowed lines) show that the accumulated excitation is lower for MgH^+ than for HD^+, in line with the lower single collision excitation. The accumulated excitations obtained from numerical simulations predict a total excitation of 0.05 at $E \approx 1.8$ and 1.25 eV for MgH^+ and HD^+, respectively. This excitation represents an upper limit to the excitation for typical quantum technological experiments to be viable [107]. By Eq. (4.4) these energies correspond to $E_L \approx 3.5, 1.6$ eV in the lab frame for MgH^+ and HD^+ respectively. The analytical estimation where the typical single collision excitation obtained from Eq. (4.75) is fairly accurate for HD^+ (solid line), although not nearly as accurate as the estimate for apolar molecular ions. This is to be expected since perturbation theory was significantly more accurate in estimating the single collision excitation for apolar ions than the estimate based on the adiabatic picture relevant to polar ions. However, for sufficiently large values the approximation will start to underestimate the actual population obtained from numerical integration. However, this occurs for scattering energies where the total excitation has well exceeded the tolerance limit of 0.05. We start seeing such behaviors for scattering energies around $E = 1.5$ eV. Notice that the parameter $\kappa \to 1$ as $E \to 1.5$ eV for HD^+/Be^+ and we can therefore attribute the underestimating of the population excitation to the breakdown of the adiabatic approximation. The two-level approximation is not applicable for MgH^+ and analytical results are therefore not included for this species.

4.5.3 Accumulated excitation for apolar molecular ions

For apolar molecular ions, an estimate for the rotational excitation in a single collision was obtained using first-order time-dependent perturbation theory (PT). In order to calculate the accumulated excitation in the full cycle, we need to average the absolute square of Eq. (4.51), $|c_{2,0}^{(1)}(E,b)|^2$, w.r.t. the impact parameter b. All the quantities in Eq. (4.51) are independent of b except for $\chi_Q^2(E,b) = \left(\frac{3Q_Z\varepsilon_0^{3/2}(E,b)}{4B}\right)^2$ with $\varepsilon_0^3(E,b) = \frac{1}{\left(\frac{1}{2E}+\sqrt{\left(\frac{1}{2E}\right)^2+b^2}\right)^6}$.

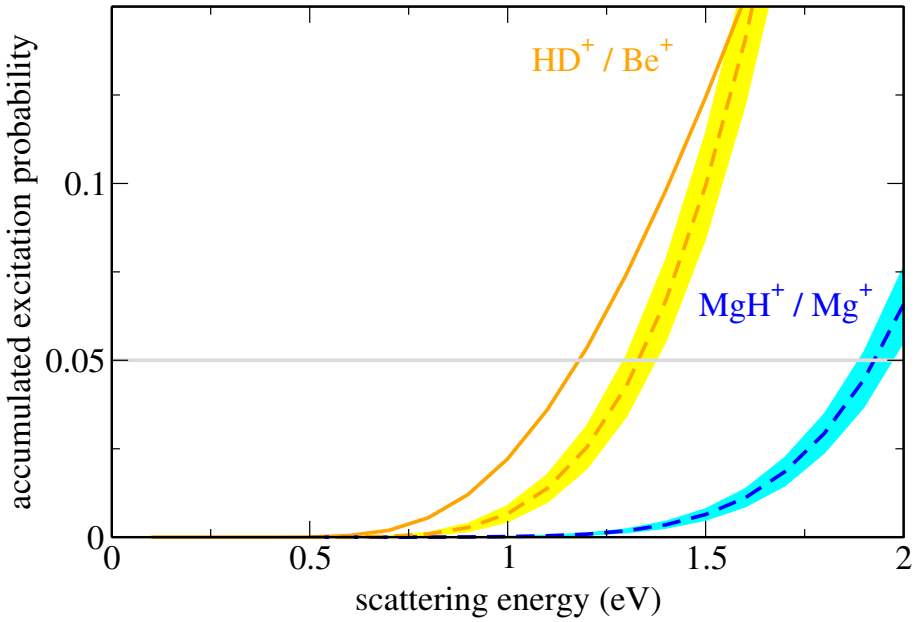

Figure 4.16: (a) Accumulated excitation probability, Eq. (4.66), for polar molecular ions after a full cooling cycle, $d = 1 \times 10^5$ Bohr, as a function of the initial scattering energy with $E_{final} = 0.1\,\text{eV}$. For HD^+ we compare the estimate (solid line) based on the 2-level approximation, Eq. (4.75) (with $dE = 0.1\,\text{eV}$) to full numerical simulations (dashed lines, $dE = 0.1$ eV, also included for MgH^+). Within each interval dE, the excitation occurring in a single collision, $\tilde{\epsilon}$, can be evaluated at the highest and lowest energy, E_i and $E_i - dE$, defining the shaded region, or taken to be the arithmetic mean, indicated by the dashed lines. The horizontal gray line marks an excitation level of 5%.

The average in the crystal cooling scenario is obtained by using Eq. (4.57b),

$$\left\langle \chi_Q^2 \right\rangle (E) = \left(\frac{3Q_Z}{4B}\right)^2 \frac{2}{b_{max}^2} \int_0^{b_{max}} \frac{b\, db}{\left(\frac{1}{2E} + \sqrt{\left(\frac{1}{2E}\right)^2 + b^2}\right)^6}\,. \tag{4.76}$$

Since $b_{max} \gg \frac{1}{2E}$, the contribution of the upper limit to the integral is negligible such that

$$\frac{2}{b_{max}^2} \int_0^{b_{max}} \varepsilon_0^3 b\, db \approx \frac{3}{10 b_{max}^2} E^4, \tag{4.77}$$

see Appendix F.3. Once this average is obtained, Eq. (4.76) is approximately

$$\left\langle \chi_Q^2 \right\rangle (E) \approx \frac{27}{160 b_{max}^2} \left(\frac{Q_a}{B}\right)^2 E^4. \tag{4.78}$$

Following the same procedure for the polarizability interaction results in

$$\left\langle \chi_{\Delta\alpha}^2 \right\rangle (E) \approx \frac{1}{84 b_{max}^2} \left(\frac{\Delta\alpha}{B}\right)^2 E^6, \tag{4.79}$$

where we have used Eqs. (4.57b) and (4.18b), see Appendix F.4 for details. The relative strengths of the two interactions is

$$\frac{\left\langle \chi^2_{\Delta\alpha} \right\rangle (E)}{\left\langle \chi^2_Q \right\rangle (E)} = \frac{40}{567} \left(\frac{\Delta\alpha}{Q_a} \right)^2 E^2. \tag{4.80}$$

Using Eq. (4.78) to replace χ^2_Q with its average over b in the absolute square of Eq. (4.54), the average population excitation in first order PT is approximated by

$$\begin{aligned} \tilde{\epsilon}(E) &= \left\langle \left| c^{(1)}_{2,0}(E) \right|^2 \right\rangle \approx \frac{4}{45 b^2_{max}} \left\langle \chi^2_Q \right\rangle (E) \kappa^2 (1+6\kappa) e^{-6\kappa} \\ &= 1.86^2 \frac{1}{150 d^2} \left(\frac{3Q_Z}{4} \right)^2 \mu E \left(1 + 1.86 \cdot 6 \sqrt{\frac{\mu}{E^3}} B \right) e^{-1.86 \cdot 6 \sqrt{\frac{\mu}{E^3}} B}, \end{aligned} \tag{4.81}$$

where we have used $d = 2b_{max}$. Using Eq. (4.81) in Eq. (4.66), we arrive at an analytical estimate for the accumulated excitation probability at the end of the cooling process,

$$\begin{aligned} \Phi_\Sigma &\approx \sum_{i=1}^{N} n(E_i) |c^{(1)}_Q(E_i)|^2 \\ &= 1.86^2 \frac{2(1+\xi)^2 \mu}{75\xi} \left(\frac{3Q_Z}{4} \right)^2 \sum_{i=1}^{N} \frac{E_i^2 \left(1 + 1.86 \cdot 6 \sqrt{\frac{\mu}{E_i^2}} B \right) e^{-1.86 \cdot 6 \sqrt{\frac{\mu}{E_i^3}} B}}{\log\left((d \cdot E_i)^2 + 1 \right)} \Delta E \,, \end{aligned} \tag{4.82}$$

where μ is the reduced mass, Q_Z is the zz-component of the quadrupole moment tensor, B the rotational constant of the molecular ion, and d the lattice spacing. Taking the limit $\Delta E_i \to dE$ in Eq. (4.82), the accumulated excitation is expressed as an integral,

$$\begin{aligned} \Phi_\Sigma &\approx 1.86^2 \frac{3(1+\xi)^2 \mu Q_Z^2}{200\xi} \times \\ &\int_{E_i}^{E_f} \frac{E^2 \left(1 + 1.86 \cdot 6 \sqrt{\frac{\mu}{E^3}} B \right) e^{-1.86 \cdot 6 \sqrt{\frac{\mu}{E^3}} B}}{\log\left((d \cdot E)^2 + 1 \right)} dE \,. \end{aligned} \tag{4.83}$$

Note that the final estimate for the accumulated excitation probability at the end of the cooling process only depends on the molecular parameters and initial scattering energy.

For simplicity, we have only accounted for the dominant quadrupole interaction in the PT. Figures 4.17(a) and (b) compare the results obtained with PT and the full dynamics, using Eq. (4.22), confirming both validity of PT and insignificance of the polarizability interaction for N_2^+/Ca^+ and H_2^+/Be^+. This suggests to use Eq. (4.83) to make predictions for other molecular species, such as iodine, shown in Figure 4.17(c). For the popular example of N_2^+ [154–157], we expect excitation of more than a few percent only for initial scattering energies well above 1.5 eV. However, for very heavy molecules with small rotational constants, such as I_2^+, significant rotational excitation is expected already for initial energies of a few hundred meV.

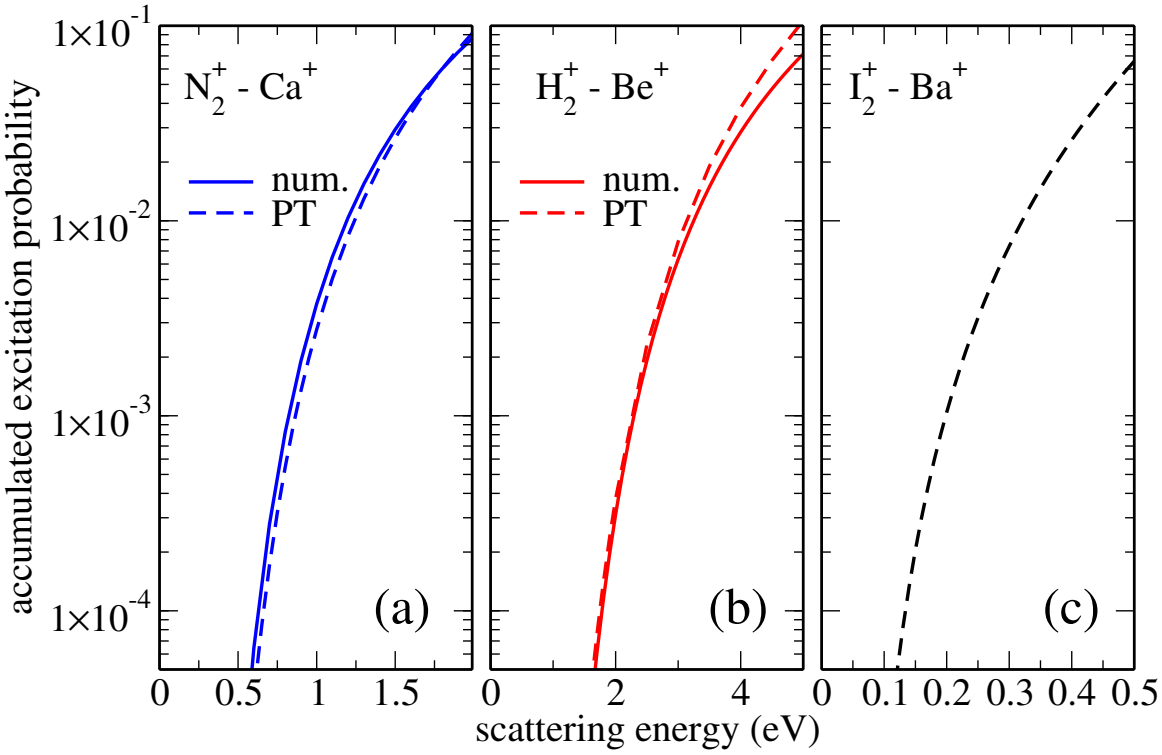

Figure 4.17: Accumulated excitation for apolar molecular ions after a full cooling cycle as function of the initial scattering energy, comparing full numerical calculations (dashed lines) to PT (solid lines, $d = 1 \times 10^5$ Bohr), accounting only for the quadrupole interaction.

In Figure 4.17, we have assumed $d = 1 \times 10^5$ Bohr but numerical simulations suggest the final excitation probability to only very weakly depend on the value of d or even on the cooling scenario (data not shown). Note that the values of the ratio, Eq. (4.80) amount to approximately $6.1 \cdot 10^{-3}$ for N_2^+/Ca^+ at $E = 1.5$ eV, $1.14 \cdot 10^{-2}$ for H_2^+/Be^+ at $E = 4$ eV and $5.9 \cdot 10^{-4}$ for $I_2^+/^{137}Ba^+$ at $E = 0.5$ eV, respectively. These relative strengths justify our neglecting the polarizability interaction in calculating the rotational excitation. We can use Eq. (4.4) to relate these energies to the corresponding lab frame energies and they amount to roughly 9.8 eV (H_2^+/Be^+), 3.25 eV (N_2^+/Ca^+) and 1.14 eV (I_2^+/Ba^+). In typical situations involving quantum technologies, excitation higher than 0.05 would be detrimental to the accuracy of the experiment [107]. Notice that only for H_2^+/Be^+-scattering is the total accumulated excitation lower than or similar to the cutoff at 0.05 for trap depths up to 10 eV. For the example of I_2^+/Ba^+-scattering, the critical excitation, 0.05, can be reached already at trap depths of ~ 1 eV.

4.6 Conclusions and Outlook

We have theoretically studied rotational excitation of molecular ions during sympathetic cooling using pre-cooled atomic ions assumed to be situated inside a linear Paul trap. We identify two limiting scenarios defined by the interatomic spacing between the pre-cooled atomic ion at the center of the trap. In the single ion scenario, the spacing is so large that the molecular ion only interacts with one atomic ion during each passage past the center of the trap. In the opposite limit, the crystal cooling scenario, the atomic ions are so close to each other that the molecular ion comes to a full stop in the first passage through the crystal due to multiple collisions. We find that the two limiting scenarios do not significantly change the final degree of collision-induced rotational excitation. However, translational cooling with a single atomic ion is dramatically slower than cooling in the crystal scenario and will generally be impractical.

Also, in the scattering process, the molecular ions experiences an approximately Lorentzian temporal electric field due to the atomic coolant, where the wings provide a very gradual on- and offset of the field strength. Since the interaction with the external field goes with the first power in the field for polar molecular ions and $\frac{3}{2}$-power for apolar molecular ions, the resulting interaction with the external field affects the two types of molecular ions in a completely different way.

By comparison with a full numerical integration of the Schrödinger equation taking both the quadrupole and polarizability interactions into account, the population excited in a single collision for apolar molecular ions is found be quite accurately estimated using first order perturbation theory taking only the dominant quadrupole interaction (for the scattering energies and molecular ions in our work) into account. Additionally the analytical form of the population excitation obtained from PT allows us to derive a closed-form estimate of the accumulated population excitation which solely depends on the molecular parameters and initial scattering energy. Finally, we find that it is sufficient to account only for the quadrupole interaction and disregard the polarizability interaction for the molecular ions studied in our work. Since higher scattering energies favour the polarizability interaction, this situation might change for molecular ions that collide at higher energies. Finally, for a wide range of apolar molecular ions, we find the internal state to be preserved for initial energies of 1 eV and above, eventually limited by close-encounter interactions disregarded in the present treatment.

In contrast, for polar molecular ions the coupling is generally in the high field limit. Since the dipole coupling is linear in the field strength and since the field profile is nearly Lorentzian, there is, however, a near adiabatic rotational dynamics, which greatly suppresses the final rotational excitation in spite of a high intermediate excitation. A large ratio of interaction to kinetic energy favours adiabaticity, and adiabaticity can be easily lost, e.g.

for molecular ions with low dipole moments, such as the important example HD^+. The treatment in the adiabatic limit is significantly more complicated than in the perturbative regime. Indeed, we have found that a general treatment is not applicable. In the high-field limit all we can do is order the rotational excitation in decreasing order of the product of parameters $\omega_H \tau \propto \sqrt{BD\mu}$, where ω_H is the characteristic energy in the high-field (harmonic) limit. In the low-field limit we have found an analytic formula for the rotational excitation based on a representation of the adiabatic states, using a minimal basis of two free-field states. Within this approximation, we can estimate the excitation for sympathetic cooling where the field of the atomic coolant does not significantly affect the rotational states of the molecular ion. Nevertheless, our estimate here is significantly less accurate. Consequently, an accurate estimate requires a full quantum-dynamical treatment based on numerical integration of the Schrödinger equation. These simulations suggest that a large ratio of interaction too kinetic energy leads to the counter-intuitive result of a low accumulated excitation. Indeed, we see that we expect MgH^+ to withstand significant accumulated excitation up to scattering energies of 2 eV in the center of mass frame, whereas HD^+ suffers significant accumulated excitation at just above 1 eV.

When extending sympathetic cooling to polyatomics, we expect rotational excitation to be more critical, both because of more degrees of freedom with low-energy spacings and the physical size of the molecular ions making close-encounter interactions more likely. The latter deserve a more thorough investigation in future work as they might provide a new avenue for controlling collisions due to the extremely large fields present in a close encounter. The control knob would be the initial collision energy which can be varied via the choice of the molecular ion's position in the trap during photo-ionization, or by injecting low-energetic molecular ions from an external source into the trap. The same techniques could also be used to experimentally test our present predictions for diatomics.

5

Rotational State Interferometry using Diatomic Molecular Ions

5.1 Introduction

In this chapter we present a Ramsey-type interferometer based on molecular rotational states [158]. The interferometer can be implemented on a trapped and sympathetically cooled MgH^+-molecular ion [108] within a Coulomb crystal in a Paul trap. The molecular ion is translationally cold (sub-Kelvin temperatures) and in its vibronic ground state. In an ideal interferometric setup, the molecule would initially be in a pure rotational state. Reaching this reference state is a major experimental challenge and in a realistic experimental situation one has to conform to working with an initial ensemble of rotational states. Current experimental techniques are capable of constructing narrow initial rotational distributions. Specifically, a non-thermal ensemble of rotational states with a $j = 2$-population corresponding to a thermal ensemble at $T = 20$ K has been achieved [47, 48]. In this work we will consider three different initial states, the ideal ground state, the above-mentioned non-thermal ensemble which we will call the experimental (exp.) ensemble and a thermal ensemble at 20 K, and compare the performance of the interferometer resulting from the different initial states.

We investigate the dependence of the accuracy of the resulting interferogram on the uncertainty of the initial population distribution as well as population measurement errors. As an application, we show that this system can be employed as a working interferometer, which can be applied for the accurate measurement of the polarizability anisotropy. The potentially very long interrogation times with trapped ions can make such an interferometer extremely sensitive. The work on the interferometer is published in Ref. [158].

5.2 Presenting the Interferometer

When it comes to interference of quantum objects with internal energy structure, like atoms or molecules, the method of Ramsey interferometry, involving two-level objects, has been particularly successful [3]. Ramsey interferometry is based on Rabi cycling. Rabi cycling is a standard textbook example of dynamics in a two level system (consisting e.g. of two isolated electronic states of an atom). The system interacts with an external electric or magnetic field. The energy difference of the two states is $\Delta E = \hbar\omega_{21}$. Consider the interaction with a harmonic field with frequency ω_0. Assuming the system initially in its ground state, and invoking the rotating wave approximation [5], the excitation probability is $P_{1\to2}(t) = \frac{H_{12}^2}{\Delta^2+H_{12}^2}\sin^2\frac{\Omega}{2}t$ where $\Delta = \omega_0 - \omega_{21}$ and H_{12} is the matrix element of the interaction Hamiltonian connecting the two states and $\Omega = \sqrt{\Delta^2 + H_{12}^2}$ is the Rabi frequency. Pulses which satisfy $\Omega t = \pi$ are called π-pulses and they induce the largest possible excitation, which attains its maximum $P_{1\to2} = 1$ when $\Delta = 0$, i.e. when the system is in resonance with the oscillating field. In the Ramsey method, the single pulse is replaced with two $\frac{\pi}{2}$-pulses ($\Omega t = \frac{\pi}{2}$) [6]. The effect of one such a pulse is to transform the ground state into a coherent superposition of equal weights of the two-level system. In the original Ramsey setup, a beam of collinear atoms was passed through two short interaction zones with an intermediate, much longer interaction free zone [6]. In modern day applications of a Ramsey setup, the atoms frequently remain stationary and two time delayed $\frac{\pi}{2}$-pulses are applied to the atoms, .i.e., the interferometer relies on temporal rather than spatial separation. Due to the different phase evolution of the two states in field-free conditions and the equal population created by the first pulse, an excitation between 0 and 1 can be obtained by varying the intra-pulse delay. Here each pulse is analogous to the interaction region and the time between the pulses takes the role of the interaction free region. Indeed, the pulses take the role of beam splitters and the time delay that of interference arms in interferometer experiments of light.

Here, we propose a Ramsey-type interferometer based on the rotational populations of a cold-trapped MgH^+-ion. The basic idea of the interferometer is to use a two-pulse arrangement to manipulate the rotational state populations of the molecular ion, as is shown schematically in Figure 5.1. In contrast to the Ramsey setup, we will employ off-resonance pulses which couple to the polarizability anisotropy of the molecule ion. An initial pulse creates a wave packet in analogy with the superposition state in atom interferometry. In the subsequent free evolution, each field-free eigenstate in the wave packet acquires a specific phase, equivalent to specific optical path lengths acquired in light interferometry. Next, a second off-resonance pulse is applied at a controllable time delay τ. The final rotational state population distribution is sensitive to the individual phases of the eigenstates acquired during the free evolution between the two pulses. As a consequence, the final field-free

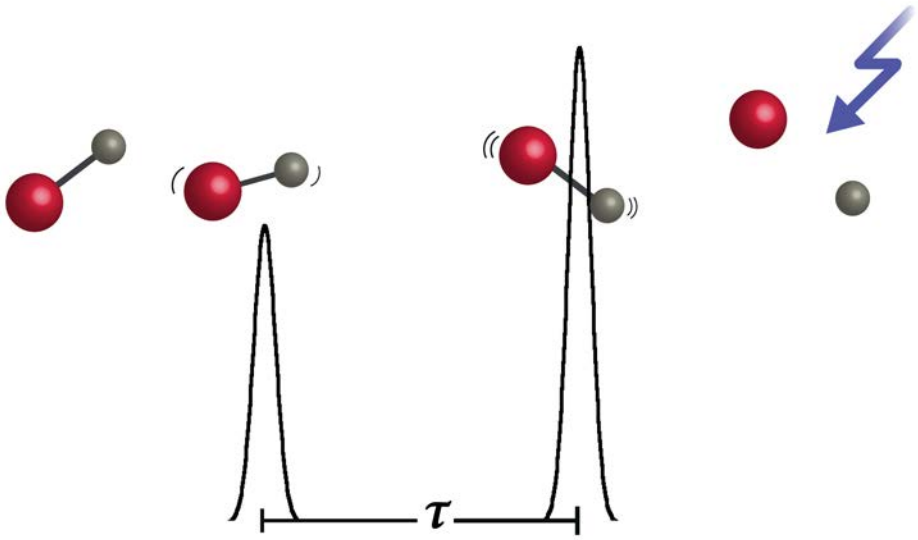

Figure 5.1: Schematic illustration of a rotational Ramsey-type interferometer with time evolving from left to right. A sympathetically cooled MgH^+ molecular ion, initially prepared in its ground state, interacts with a first off-resonant laser pulse (the Mg^+ coolant ion is not shown). Then the resulting wave packet evolves freely for a controllable time delay τ, until a second pulse is applied, generating a new wave packet. This step is sensitive to the relative individual phases of the free-field states that make up the wave packet prior to the second pulse and thus on the time delay. The final rotational populations are measured by a state-sensitive dissociation pulse (blue arrow).

populations define an interferogram as a function of the time delay between the two pulses. The final rotational populations can be measured by a rotational state selective resonance-enhanced multi-photon dissociation (REMPD) [26, 48].

The quality of an interferometric setup can be assessed by the visibility, which in our setup is

$$V_j = \frac{|c_{j,max}|^2 - |c_{j,min}|^2}{|c_{j,max}|^2 + |c_{j,min}|^2}\,, \tag{5.1}$$

where $|c_{j,max}|^2$ ($|c_{j,min}|^2$) is the maximum (minimum) population of the jth state. In our case, the maximum (minimum) populations are analogous to the maximum (minimum) intensities in light interferometry. The visibility of the resulting interferogram depends on the laser pulse parameters and the initial state. In particular, the visibility can be altered by varying the intensity of the second pulse.

As an application of the interferometer, the measurement of the molecular polarizability anisotropy is discussed, taking into account experimental uncertainties of the initial popu-

lations as well as population measurement errors. The interferometric method to determine the static dipole polarizabilities discussed here represents, for molecular ions, an interesting alternative to microwave spectroscopy typically used [159, 160]. Conversely, if the polarizability is known to high accuracy, the interferometric technique may be used to probe local electric fields, like the radio-frequency fields at the position of the molecular ion in a linear Paul trap.

5.3 Theoretical framework

We utilize a two-pulse scheme of linearly polarized Gaussian pulses with parallel polarization vectors. The laser pulses are far off-resonance from any transition in the ion and are linearly polarized along the laboratory fixed z-axis. In terms of the molecular polarizability anisotropy, $\Delta\alpha(\hat{\mathbf{r}})$ and the molecular polarizability perpendicular to the inter-atomic axis $\alpha_\perp(\hat{\mathbf{r}})$, and taking $\hbar = 1$, the Hamiltonian describing the rovibrational motion of the molecular ion and its interaction with the off-resonant field is given by

$$\hat{\mathbf{H}}_{2D} = \hat{\mathbf{T}}_r + V(\hat{\mathbf{r}}) + \frac{\hat{\mathbf{J}}^2}{2m\hat{\mathbf{r}}^2} - \frac{I(t)}{2\epsilon_0 c}\left(\Delta\alpha(\hat{\mathbf{r}})\cos^2\hat{\theta} + \alpha_\perp(\hat{\mathbf{r}})\right) \tag{5.2}$$

where the first two terms describe the radial kinetic and potential energy respectively, $\hat{\mathbf{J}}^2$ is the orbital angular momentum operator, $I(t)$ the intensity profile of the laser pulse and θ is the angle between the polarization vector of the laser pulse and the inter-atomic axis. With linear and parallel pulse polarizations, the Hamiltonian (5.2) is independent of the azimutal angle ϕ, which leads to the first selection rule $\Delta m = 0$. A second selection rule arises from the $\cos^2\theta$-term which leads to $\Delta j = 0, \pm 2$. As the pulses are non-resonant with any transitions between internal states of the ion the dipole term is absent in Eq. (5.2). Therefore, the leading term of the light-matter interaction is the two-photon coupling via the ion's polarizability.

Furthermore, since for low-lying rovibrational levels, the vibrational energy is much larger than the rotational energy, the two degrees of freedom can be adiabatically separated [161] leading to the effective rotor approximation (ERA), described in Section 2.3.2. Within the ERA, all $\hat{\mathbf{r}}$-dependent quantities in Eq. (5.2) are replaced by their expectation values w.r.t. the vibrational eigenstate ν,

$$\hat{\mathbf{H}}_\nu = B_\nu \hat{\mathbf{J}}^2 - \frac{I(t)}{2\epsilon_0 c}\left(\langle\Delta\alpha\rangle_\nu \cos^2\hat{\theta} + \langle\alpha_\perp\rangle_\nu\right), \tag{5.3}$$

with $B_\nu = \frac{1}{2m}\langle r^{-2}\rangle_\nu$. Since the molecular ion can be considered to be in its vibrational ground state [69], and vibrational transitions are suppressed by the off-resonance pulse, we will consider only one vibrational state, $\nu = 0$ throughout. The ERA neglects rovibrational couplings and rotational dephasing but goes beyond the rigid rotor approximation, since its

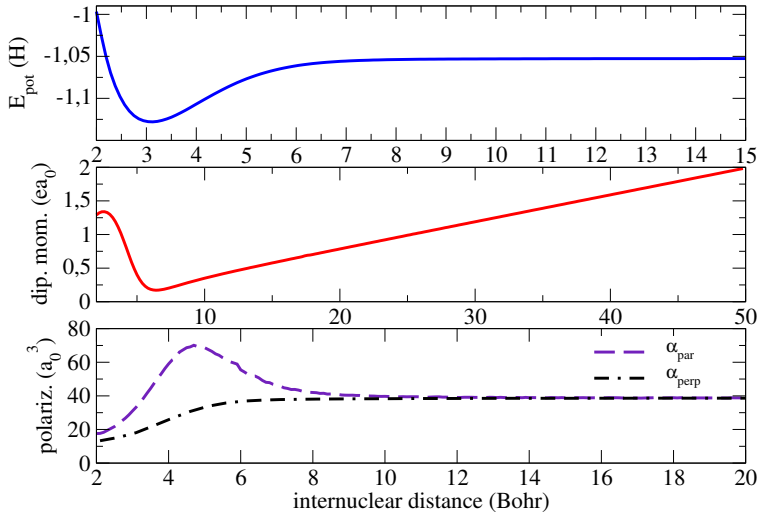

Figure 5.2: Potential energy (upper panel), electric dipole moment (middle panel) and polarizabilities (lower panel) of the electric ground state of the MgH^+-ion as functions of the inter nuclear distance. The data is obtained from Ref. [117].

$B_{\nu=0}$	$\langle\Delta\alpha\rangle_{\nu=0}$	$\langle\alpha_\perp\rangle_{\nu=0}$
$6.3685\,\mathrm{cm}^{-1}$	$3.6634\cdot10^{-25}\,\mathrm{cm}^3$	$7.3268\cdot10^{-25}\,\mathrm{cm}^3$

Table 5.I: Parameters of the ERA-Hamiltonian, Eq. (5.3) for MgH^+.

parameters are obtained by integrating over the vibrational motion instead of just replacing $\hat{\mathbf{r}}$ by the equilibrium distance, c.f. Section 2.3.1. In calculating these averages, we have made use of the potential curve and polarizabilities obtained from Ref. [117], see Figure 5.2, and the corresponding values of the molecule parameters involved in the Hamiltonian Eq. (5.3) are listed in Table 5.I. They are found to be in good agreement with the experimental values of Ref. [162].

The free rotational eigenstates $|j,m\rangle$ have energy eigenvalues $E_j = j(j+1)B$ (in units where $\hbar = 1$), i.e. they are degenerate with respect to m. Here, the eigenstates $|j,m\rangle$ relate to the associated Legendre functions $P_j^m(\theta)$ by

$$\chi_{j,m}(\theta) = \langle\theta\,|\,j,m\rangle = P_j^m(\theta). \tag{5.4}$$

The dynamics is characterized by the rotational period, $\tau_{rot} = \hbar/(2B_{\nu=0})$, and for MgH^+ $\tau_{rot} \approx 420\,\mathrm{fs}$. This short rotational period is a consequence of the large difference in the atomic masses and the small hydrogen mass. At time t, a general wave packet is given by

$$|\chi(t)\rangle = \sum_{j,m} c_{j,m}\,|j,m\rangle\,e^{-iE_jt}, \tag{5.5}$$

and the correlation function, $C(t)$, of the wave packet is given by

$$C(t) = \langle\chi(0)\,|\,\chi(t)\rangle = \sum_{j,m} |c_{j,m}|^2 e^{-iE_jt}. \tag{5.6}$$

Wave packet revivals are defined as times T, for which the wave packet returns to its initial state. For such times the correlation function must satisfy

$$C(T) = C(0). \tag{5.7}$$

That is, the conditions $2\pi k_j = E_j T$ with k_j integer need to be fulfilled simultaneously for all j which make up the wave packet $|\chi(t)\rangle$. Once the wave packet has reached the first revival, it will keep returning to its initial state at integer (n) times of the revival time $C(nT) = C(0)$ as long as the dynamics remains coherent. This revival time should show up in an interferogram as periodic repetition of the final state populations as function of the time delay between the pulses, i.e., the interferogram can probe the correlation function. In addition, the correlation function $C(t)$ relates to its Fourier transformation $\tilde{C}(E)$ by

$$C(t) = \frac{1}{2\pi}\int_{-\infty}^{\infty} \tilde{C}(E) e^{-iEt} dE \tag{5.8}$$

$$\tilde{C}(E) = \int_{-\infty}^{\infty} C(t) e^{iEt} dt \tag{5.9}$$

In the particular case when $C(t)$ is given by Eq. (5.6), its Fourier transform takes the simple form

$$\tilde{C}(E) = \sum_j |c_j|^2 \delta(E - E_j), \tag{5.10}$$

which simply returns the population on each eigenstate at its corresponding energy.

Laser pulses are represented using a Gaussian envelope,

$$\varepsilon_0(t) = \varepsilon_0 e^{-(t-t_1)^2/2\tau_\varepsilon^2}, \tag{5.11}$$

with ε_0 the electric field amplitude, t_1 the center of the pulse and τ_ε the pulse duration. The intensity of the field is given by $I(t) = \frac{1}{2}\epsilon_0 c \varepsilon_0^2 e^{-(t-t_1)^2/\tau_\varepsilon^2} = I_0 e^{-(t-t_1)^2/2\tau_I^2}$, which define I_0 and τ_I in terms of ε_0 and τ_ε. The pulse has a full width at half maximum (FWHM) $\Gamma = \sqrt{8\ln 2}\tau_I$. The pulse fluence, P, is given by

$$P(I_0, \Gamma) = \int_{-\infty}^{\infty} \varepsilon^2(t) dt = \frac{2}{\epsilon_0 c}\int_{-\infty}^{\infty} I(t) dt, \tag{5.12}$$

which for our Gaussian pulse envelope becomes

$$P(I_0, \tau_I) = \frac{2}{\epsilon_0 c}\sqrt{\frac{\pi}{4\ln 2}} I_0 \tau_I \,. \tag{5.13}$$

For Gaussian pulses and for constant fluence $P = P_0$, the intensity and pulse duration are inversely proportional. Similarly, for two time-delayed pulses, the intensity of the field, $I(t)$, is given by

$$I(t) = I_0 \left(e^{-(t-t_1)^2/2\tau_I^2} + \beta e^{-(t-t_2)^2/2\tau_I^2} \right)^2, \tag{5.14}$$

where $t_{1,2}$ denotes the temporal centers of the pulses, β a scaling factor, and τ_I the pulse duration. Now, define $\tau = t_2 - t_1$ to be the delay between the two pulses. Notice that for $\tau \simeq \tau_I$ the interference term in Eq. (5.14) is important whereas for $\tau \gg \tau_I$ the pulses become independent.

In order to optimize the precision of the interferometer, the initial state should be as pure as possible and, ideally, the molecule should initially be in its ground rotational state ($j = 0$). In a real experiment, however, a completely pure initial state cannot be fully realized. However, recent experiments with MgH^+ ions trapped in a cryogenic environment have achieved a nearly 80% rotational ground state population using helium buffer gas cooling [47]. In the actual experiment we intend to emulate in this work, the initial incoherent ensemble is prepared in current room-temperature experiments by rotational cooling [48]. In this case, the ground state population of the ensemble $P_0 \sim 0.38$ is roughly the same as a thermal ensemble at $T \approx 20$ K. The most general initial rotational state is an incoherent ensemble of rotational states $|j, m\rangle$ described by the density operator, $\hat{\rho}$:

$$\hat{\rho}(t = 0) = \sum_{j=0}^{\infty} \sum_{m=-j}^{j} a_j \, |j, m\rangle \, \langle j, m| \, . \tag{5.15}$$

The expansion coefficients are independent on m since the states $|j, m\rangle$ are degenerate w.r.t. m and in a realistic experimental situation they will thermalize to even populations, dependent only upon j. When the initial ensemble is given by the pure ground state, $a_j = \delta_{j,0}$, and for a thermal ensemble $a_j = g_j \exp(-\beta E_j)/Z$ with $g_j = 2j + 1$, $\beta = 1/k_B T$ and $Z = \sum_j g_j \exp(-\beta E_j)$ the partition function. For our experimental initial state the values of a_j are taken from Ref. [48].

Assuming that the timescale of the interferometer is much shorter than any decoherence time, the time evolution is coherent and the density operator at time t is obtained from $\hat{\rho}(t = 0)$ by

$$\hat{\rho}(t) = \hat{\mathbf{U}}(t) \hat{\rho}(0) \hat{\mathbf{U}}^{\dagger}(t) \, .$$

Inserting Eq. (5.15), the time-dependent population of the state j', with all corresponding m-states taken into account, is then obtained as

$$\rho_{j',j'}(t) = \sum_{j=0}^{\infty} a_j \sum_{m=-j}^{j} \left| \langle j', m| \, \hat{\mathbf{U}}(t) \, |j, m\rangle \right|^2 . \tag{5.16}$$

Since the Hamiltonian is cyclic in the azimutal angle, ϕ, it conserves m and each m state may be considered separately, reducing the numerical effort in the calculations. Thus, it is not necessary to propagate the full density operator to obtain the final populations, but each pure state $|j, m\rangle$ contained in the initial ensemble can be propagated separately, and the partial population resulting from the particular pure state $\left| \left\langle j', m \right| \hat{\mathbf{U}}(t) \left| j, m \right\rangle \right|^2$ is added up incoherently with its proper weight, a_j, to yield the total transferred population

corresponding to j'. The population contribution to the initial density matrix is found negligible for $j > 6$ and therefore the summation over the initially populated values of j in Eq. (5.16) can be truncated at $j_{max}^{ini} = 6$. The basis set expansion in the Legendre polynomials is found to be converged for $j_{max} = 20$, provided $I_0 \leq 4 \times 10^{13}$ W/cm^2.

5.4 Results

In this section the workings of the rotational interferometer is presented. We begin by discussing and testing the validity of the ERA model. We first verify that no vibrational excitations take place during the interaction. To this aim, we calculate the final field-free vibrational populations as the molecule interacts with a single femtosecond pulse using the ERA and compare it with the corresponding populations obtained using the full 2D model of Eq. (5.3). Additionally, since the ERA is formally identical to the RRA, it too neglects centrifugal distortions. The centrifugal distortions scale as j^4, and therefore the associated timescale as $\frac{1}{j^4}$ [113]. Consequently, to test the validity of neglecting the centrifugal distortions, we must estimate the centrifugal distortion time scales [113]. After validating our model, we analyze the rotational dynamics during the interaction with a single pulse. The influence of pulse parameters such as intensity (I_0) and duration (τ_I) on the final rotational state populations is discussed. We then present the results of the full rotational dynamics which constitute the interferometer. The impact of a non-pure initial state on the visibility of the resulting interferogram is presented and analyzed. The possibility and limitations of implementing such interferometer to measure the polarizability of molecules is discussed.

5.4.1 Performance of the Effective Rotor Approximation

Vibrational excitations

Dipole interactions can induce vibrational level transitions when the dipole transition energies and the central wave length of the laser are in resonance. The central wavelength, λ_c, for which the dipole transition becomes resonant with the $\nu_0 \rightarrow \nu_1$ transition, is about $\lambda_c = \frac{hc}{\Delta E_{0\rightarrow 1}}$. By diagonalizing Eq. (5.3) we obtain the value $\Delta E \approx 1534.00$ cm^{-1}, which corresponds to a central wavelength of $\lambda_c \approx 6.5$ μm. The laser pulses, in the experimental setup we are simulating, have $\lambda_c \approx 800$ nm, i.e. they are off resonance with the vibrational transition. Simulations of the vibrational dynamics under a pulse with this wavelength for a population starting at the ground vibrational level, yield a total population of vibrationally excited states of about 10^{-5} to 10^{-6}, depending on the laser intensity, see Figure 5.3. Thus, vibrational excitations are negligible at the relevant intensities in this study. This is not surprising given the energy difference between the ground and first excited vibrational level.

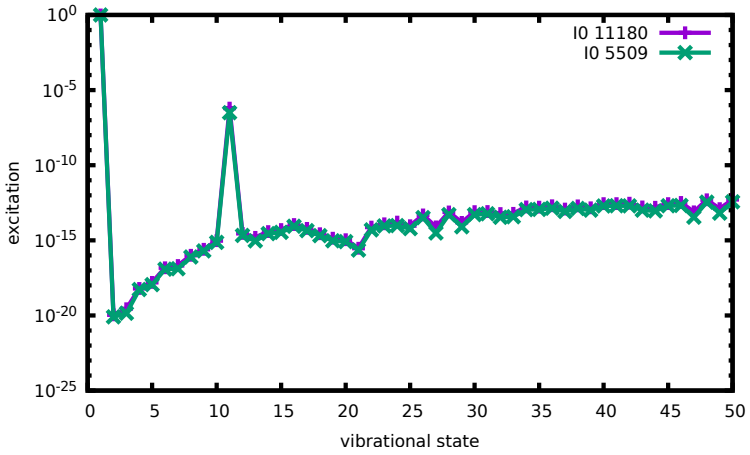

Figure 5.3: Vibrational excitation induced by the dipole interaction.

It is only for $v \approx 10$ that vibrational transitions may become resonant. However, the matrix elements for these transitions is so small that they play essentially no role. Consequently, the interaction part of the Hamiltonian is solely given by the off resonant part.

ERA vs the full 2D Hamiltonian

The centrifugal distortion can be accounted for by dropping the ERA, that is, by calculating the full rovibrational dynamics. Therefore, as a test of the ERA against the full 2D-model, we consider a situation where a molecular ion, initially in its ground state $|\nu, j, m\rangle = |1, 0, 0\rangle$, interacts with a single 100 fs Gaussian laser pulse. We compare the final state populations of the $j = 0, 2, 4, 6$ states as a function of of the maximum intensity, I_0, in Figure 5.4. As we can see from the figure, the model works fine for the states up to $j = 6$ for the intensities considered. However, our numerical simulations show that the ERA and 2D-model differ significantly for $j = 8$ already at moderate laser intensities I_0. Quantitatively, the absolute difference in the final-time population is found to be within 0.01 for $j = 0, ..., 6$ and intensities $I_0 \leq 1 \times 10^{13}$ W cm^2. The relative error amounts to less than one percent for up to $j = 4$ and intensities up to 1×10^{13} W cm^2. For intensities 1×10^{13} W cm^2 $\leq I_0 \leq 4 \times 10^{13}$ W cm^2 , the absolute error due to the ERA is within 0.015 for $j = 0, ..., 6$, whereas the relative error reaches 10–15%. While both absolute and relative errors become larger for higher j states, the ERA is applicable for our purposes since low-lying j states ($j \leq 6$) are most relevant for interferometry and only moderate pulse intensities will be considered to ease experimental feasibility.

The ERA-Hamiltonian is in its form equivalent to the rigid rotor approximation, only with improved parameters since its parameters take their values from the average over the relevant vibrational eigen function. As such, it does not take rovibrational couplings into

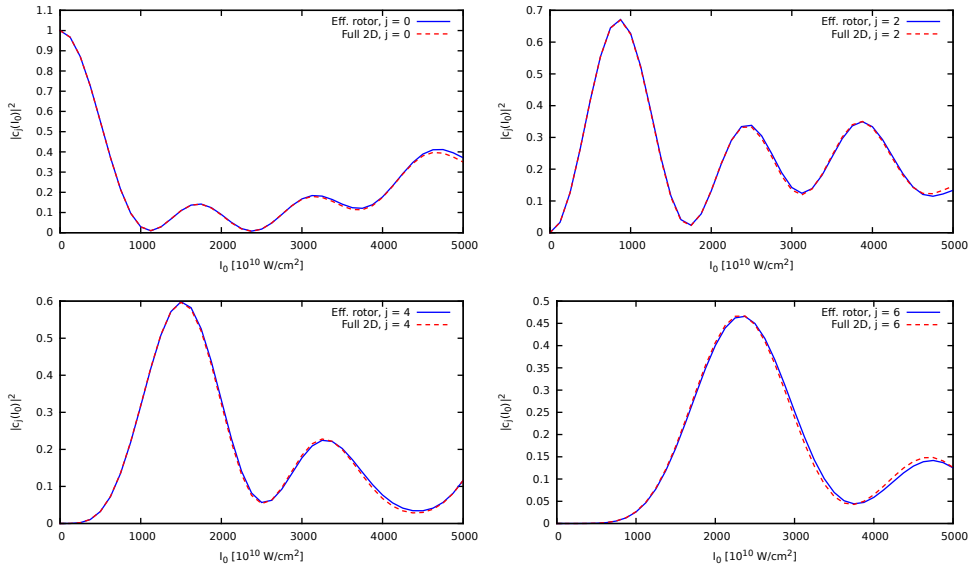

Figure 5.4: Rotational state excitations as function of pulse intensity as obtained within the Effective Rotor Approximation (blue) vs. Full Hamiltonian (red). The initial state is $j = 0$.

account, in particular decoherence due to rovibrational coupling. Here we estimate the decoherence times and compare them to the time-scale in a realistic experiment. Using a Morse approximation for the potential energy, the vibration-rotation energy is

$$\begin{aligned} E_{\nu,j} &= \omega_e\left(\nu+1/2\right) - \omega_e x_e\left(\nu+1/2\right)^2 + B_e j(j+1) - D_e j^2(j+1)^2 - \alpha_e\left(\nu+1/2\right) j(j+1) \\ &= \underbrace{B_e\left[1-\frac{\alpha_e}{B_e}\left(\nu+1/2\right)\right]}_{\approx B_\nu} j(j+1) - D_e j^2(j+1)^2 + \underbrace{\omega_e(\nu+1/2)+\omega_e x_e(\nu+1/2)^2}_{E_\nu} \\ &\approx B_\nu j(j+1) - D_e j^2(j+1)^2 + E_\nu \end{aligned} \tag{5.17}$$

where the constants are given by [111]

$$\alpha = \frac{3\hbar^3\omega_0}{4\mu\alpha r_e^3 D_e}\left(1-\frac{1}{\alpha r_e}\right), \quad D_e = \frac{\hbar^4}{4\mu^2\alpha^2 r_e^6 D_e}. \tag{5.18}$$

The constant D_e is the first rotational distortional constant and for MgH^+ $D_e = 3.6 \cdot 10^{-4}$ cm^{-1} [152]. We can now estimate the dephasing time, T_2, from the uncertainty relation $\Delta t = \hbar/\Delta E$, by letting $\Delta t \to T_2$ and $\Delta E \to D_e j^2(j+1)^2$. The decoherence times for the relevant rotational states are listed in Table 5.II. We see that for a wave packet made up of rotational states up to $j = 6$ the decoherence time is 7.6 ps. Of course if the experiment can be carried out with states up to $j = 4$ only, a significant increase in coherence time can be achieved, up to 34 ps.

We conclude that vibrational excitations are negligible for the off-resonance pulses at the considered pulse intensities and and that the ERA is justified even for high laser intensities,

j	0	2	4	6
T_2 (ps)	∞	410	36	7.6

Table 5.II: Estimation of the rotation decoherence times T_2 due to centrifugal distortion for different rotational states j.

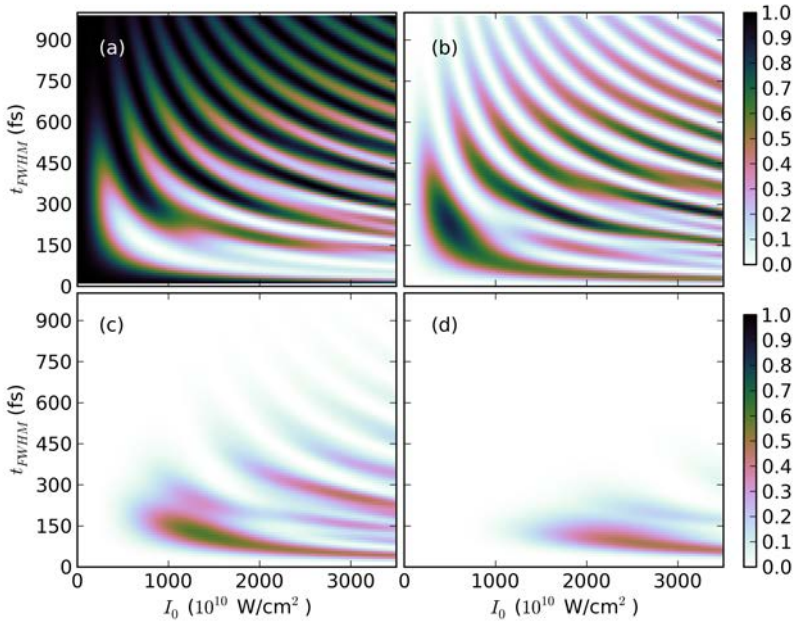

Figure 5.5: Final population of field-free rotational states (a: $j = 0$, b: $j = 2$, c: $j = 4$, d: $j = 6$) after interaction with a single laser pulse as function of pulse intensity and duration. The initial state is $j = 0$.

as long as the dynamics only involves rotational states up to $j = 6$ and that rotational decoherence limits the experimental timescale to 7.6 ps for these rotational states.

5.4.2 Creating a rotational wave packet by a single femtosecond laser pulse

We first consider the ground state ($j = 0$, $m = 0$) as the initial state. A femtosecond laser pulse creates a rotational wave packet which, due to the selection rules, is composed by states with $j = 0, 2, 4, \ldots$ and $m = 0$. A Gaussian pulse envelope is assumed, and the laser interaction with the molecule is off-resonance. As a consequence, the wave packet is only determined by the intensity and duration of the pulse. The dependence of the final rotational state populations on pulse intensity and duration is shown in Figure 5.5 for $j = 0, 2, 4, 6$. Horizontal cuts correspond to curves of constant pulse duration, while vertical

cuts correspond to constant intensity. Several hyperbolas are clearly visible in the figure. These correspond to curves of constant pulse fluence, cf. Eq. (5.13), suggesting that it is the pulse fluence that determines the population transfer. The figures tell us how close we can mimic a Ramsey interferometer as used with atoms [163]. They indicate that the nearest analogy can be made for pulse parameters corresponding to the upper left part of each panel in Figure 5.5, where the molecule can be described as a two-level system to a very good approximation, consisting of the states $j = 0$ and $j = 2$. Although being a two-level system, in this parameter region the population of the latter state is always lower than that of the former. For slightly larger values I_0, the final populations show a more complicated behavior for short pulses $\tau_I \lesssim 300$ fs, with more states being significantly populated. A wide range of pulse parameters gives rise to significant population of $j = 2$, see the lower left corner of Figure 5.5 (b). This parameter space is interesting since if this can be coupled with a high population in the ground state as well we can expect to achieve a high visibility for our interferometer. Notice however, that when the population grows to become comparable to that of the ground state, it is associated with a non-negligible population of the $j = 4$-state which inhibits a perfect 50%-50% superposition of the states $j = 0$ and $j = 2$, and thereby impedes a full analogy to a Ramsey interferometer. For intensities larger than $0.8 \times 10^{13}\,\mathrm{W/cm^2}$ and pulses shorter than 150 fs, a significant population of the $j = 4$ state is observed.

In a typical experimental setup, the limited pulse duration is fixed on the order of 100 fs, whereas the intensity can be varied. Therefore, it is of interest to study how the final rotational state populations depend on the maximum intensity for typical pulse durations. We find that the dependence is qualitatively the same for the typical pulse durations $\tau_I = 50, 75, 100$ fs, see Figure 5.6. We observe an approximate two-level system behavior at lower intensity only, and deviations from this simple picture are found before we can reach equal population of the first two states. The relative importance of the higher rotational states increases for shorter pulses, suggesting that a closer analogy to a Ramsey interferometer can be obtained for longer pulse durations. Notice though, that although we cannot truly realize the equal population, the results suggest that we can come close. Notice for example that for a 100 fs pulse and $I_0 \approx 0.5 \cdot 10^{13}$ W/cm^2, we achieve $|c_0|^2 = |c_2|^2 \approx 0.47$ and $|c_4|^2 \approx 0.06$ while all other are negligible, as indicated by I_0^* in Figure 5.7.

According to Eq. (5.16), when the initial state is given by an incoherent ensemble, we need to propagate several pure states to obtain the final state population. In particular, states for which $m \neq 0$ are initially populated. Although the interaction conserves the m-quantum number, the measurement technique to measure the final rotational states is only sensitive to the j-quantum number and cannot discern different m-sub states (for $j = 0$ there is only one sub state $m = 0$ whereas for $j = 2$ there are five sub states $m = 0, \pm 1, \pm 2$). Since the ground state is only connected to other states for which $m = 0$,

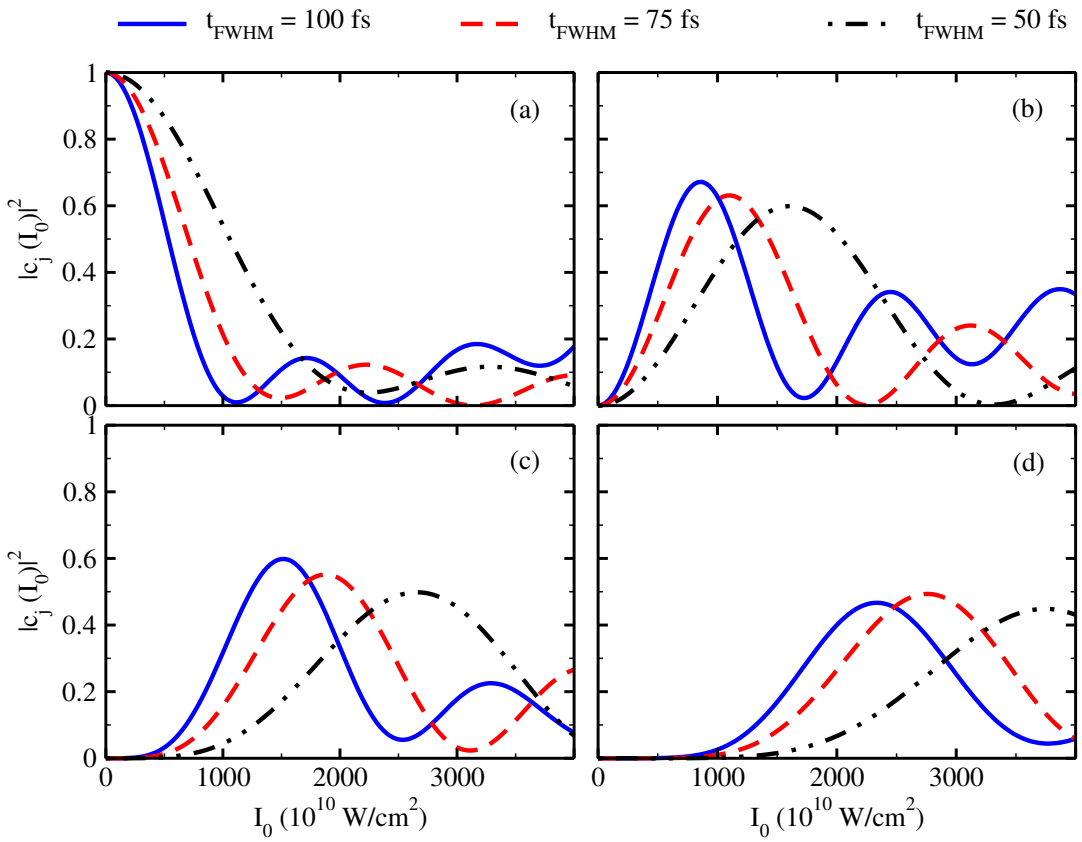

Figure 5.6: Resulting field-free population as function of pulse intensity for three typical experimental widths: 50,75,100 fs. (a): $j = 0$, (b): $j = 2$, (c): $j = 4$, (d): $j = 6$.

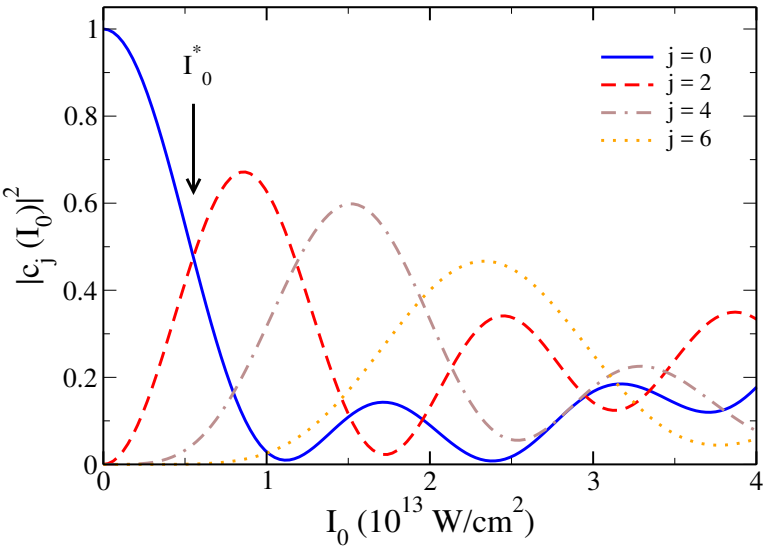

Figure 5.7: Final population of field-free rotational states after interaction with a single 100 fs pulse as a function of pulse intensity. The arrow at I_0^* indicates the laser intensity for which equal population of the states $j = 0$ and $j = 2$ is obtained.

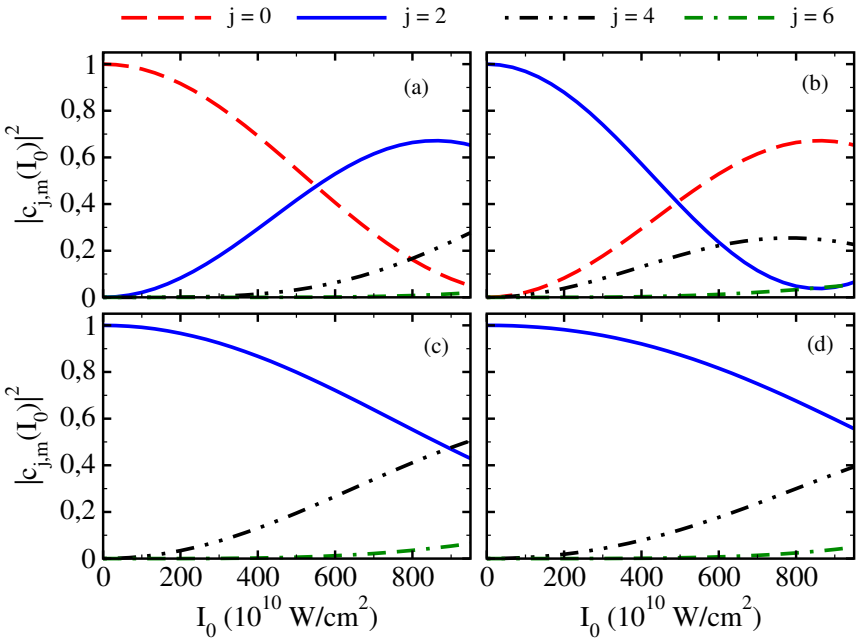

Figure 5.8: Final field-free populations of field free rotational states after interaction with a 100 fs pulse for various initial states, $|j,m\rangle$. (a): $|j,m\rangle = |0,0\rangle$, (b): $|j,m\rangle = |2,0\rangle$, (c): $|j,m\rangle = |2,1\rangle$, (d): $|j,m\rangle = |2,2\rangle$.

measurements on the final ground state population are expected to be less affected by the non-purity of the initial ensemble. Due to the selection rule, $\Delta j = 0, \pm 2$, all states with $m = 0$ have direct interaction with both their nearest neighbors, except the ground state (where the transition $\Delta j = -2$ cannot occur), which only has direct transition to the $j = 2, m = 0$ state. Therefore, the only way to achieve an approximate $50 - 50\%$ admixture is by choosing the ground state as the initial state, as illustrated in Figure 5.8 (a), (b). Since the associated Legendre functions become less aligned along the laser polarization vector with increasing m, the matrix element that causes transitions between different states $j \to j'$, $m \to m$ is $\propto \langle j', m \,|\, \cos^2\theta \,|\, j, m \rangle$, decreases with increasing m for fixed j, j', thereby making higher m-states more inert, i.e. less active to undergo transition at a given pulse strength. Therefore, high m-states that are necessarily present in initial ensemble containing high j-states will be transitionally inactive, and therefore less detrimental to the performance of the interferometer. The decreasing transition tendency with increasing m is illustrated in Figure 5.8 (b)-(d) for $j = 2, m = 0, 1, 2$.

The final state populations obtained from the initial ensembles given in Ref. [48] (experimental distribution) and the thermal ensemble at 20 K (thermal distribution), are shown in Figure 5.9 as functions of I_0 for $\tau_I = 100$ fs. Note that the final $j = 0$ population has the same dependence on I_0 for both ensembles, differing only by a small offset in initial population. The dependence is also qualitatively the same as for the pure initial state in

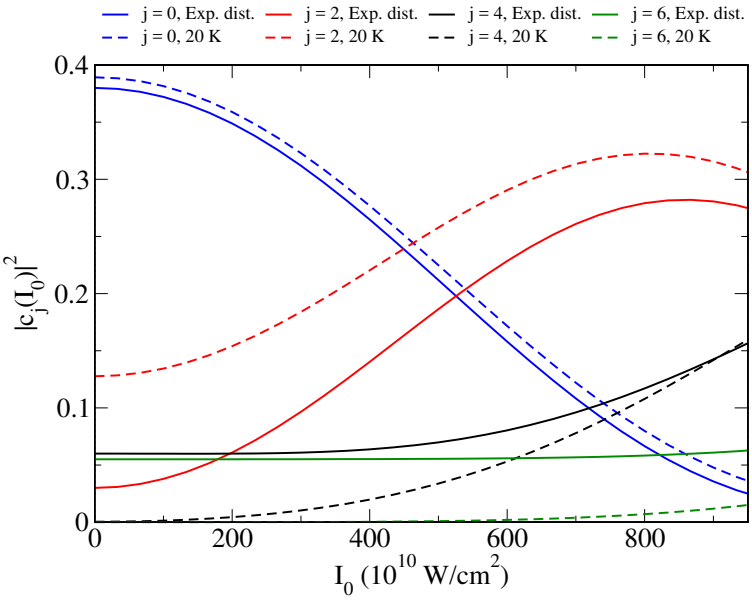

Figure 5.9: Resulting population of the field-free eigenstates after a single 100 fs pulse as a function of pulse intensity. The initial states are the experimental incoherent ensemble and a thermal ensemble at 20 K.

Figure 5.7, indicating that the ensemble dynamics is dominated by $j = 0$, at least for the intensities examined in Figure 5.9. For states $j \neq 0$ the two different initial ensembles lead to clear distinct population excitation dependence on I_0. Most notably is the significantly larger initial population of $j = 2$ for the thermal ensemble, leading to a pronounced reduction in contrast between the $j = 0$ and $j = 2$ populations. The initial populations of the $j = 4, 6$-states are negligible for the thermal ensemble, but non-zero for the experimental ensemble. They are however not significantly affected by the interaction, at least for intensities up to 0.5×10^{13} W/cm^2. This is a promising result in view of obtaining high-visibility interferograms even with incoherent initial states.

5.4.3 Creating and Probing Rotational Wavepackets Using a Sequence of Two Femtosecond Laser Pulses

Our interferograms are defined by the final populations resulting from interacting with two laser pulses separated by a time-delay τ. Let us consider an interferometric setup where the initial state is taken to be the ground state $|j, m\rangle = |0, 0\rangle$. Additionally, the intensities and duration of the two pulses are chosen equal, $I_0 = I_0^* \approx 0.5{\cdot}10^{13}$ W/cm^2 and $\tau_I = 100$ fs unless otherwise stated. Using these pulse parameters, the initial wave packet is composed mainly by the two lowest rotational eigenstates with populations $|c_0|^2 = |c_2|^2 \approx 0.47$ with a small contribution from the second excited state $|c_4|^2 \approx 0.06$, all other states negligible. With this setup we can achieve high visibility interferograms, at least when obtained form the

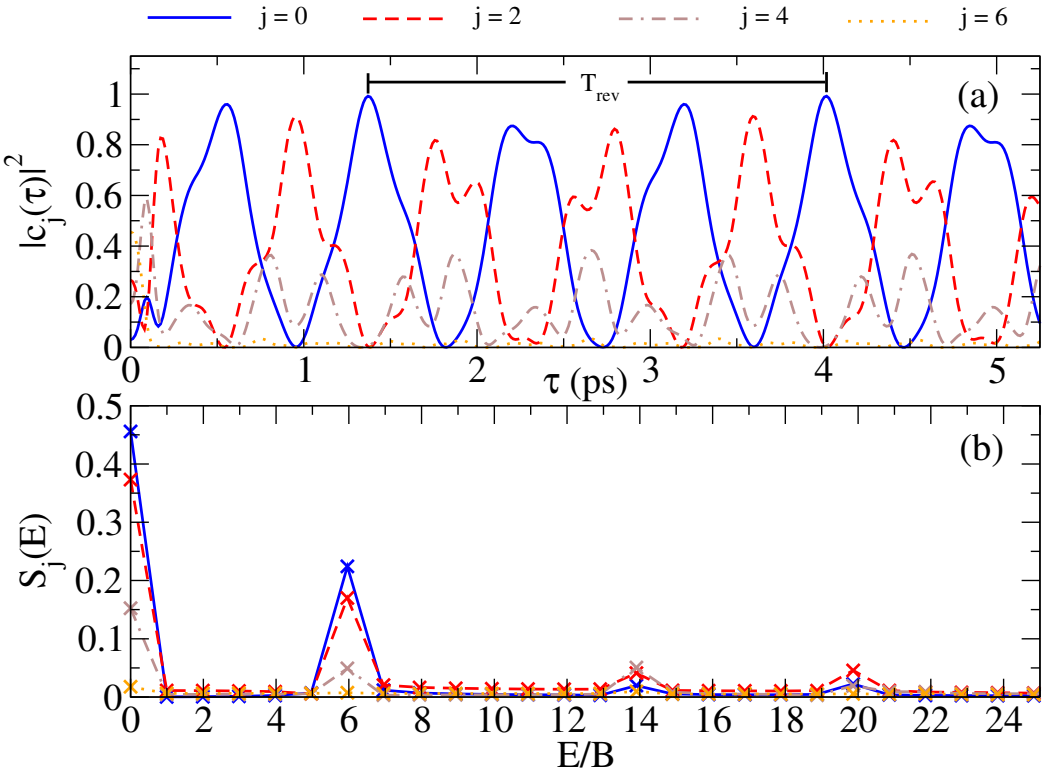

Figure 5.10: a: Interferogram, i.e., the final populations of the field-free rotational states, obtained after interaction of the molecule with two laser pulses, as a function of time delay. Both pulses have $I_0 \approx 0.5 \times 10^{13}$ W/cm^2 (as indicated by the arrow in Figure 5.7) and $\tau_I = 100$ fs. b: Spectrum S_j of the populations shown in panel (a).

final populations of either $|0,0\rangle$ ($V_0 \approx 1$) or $|2,0\rangle$ ($V_2 \approx 0.9$), mirroring the near $50-50\%$ superposition of these states, see Figure 5.10 (a). The interferogram repeats itself with a periodicity $T_{rev} \approx 2.6$ ps, consistent with the revival time obtained from the correlation function of a wave packet consisting of the states $j = 0, 2, 4, 6$ ($m = 0$), $T_{rev} = \pi/B \approx 2.6$ ps, see Eq. (5.6). Notice that the interferogram contains states up to $j = 6$. The decoherence time for that state is 7.6 ps, about three times the revival time of the interferogram.

Let us now examine the potentially detrimental effect of incoherence in the initial states on such interferograms. The interference patterns for the pure initial state of Figure 5.10 and the experimental distribution of Ref. [48] (experimental distribution) and a 20 K thermal ensemble are presented in Figure 5.11. When measuring the final population of $j = 0$, the two incoherent ensembles give practically identical results, cf. Figure 5.11(a). Their delay-dependence is qualitatively the same as that of the pure initial state, but the maximum amplitudes are reduced from close to one down to about 0.4. Nonetheless, since the minimum of the interferogram is close to zero, the visibility, V_0, is only slightly reduced, to 0.96 for the experimental distribution and 0.91 for the thermal ensemble.

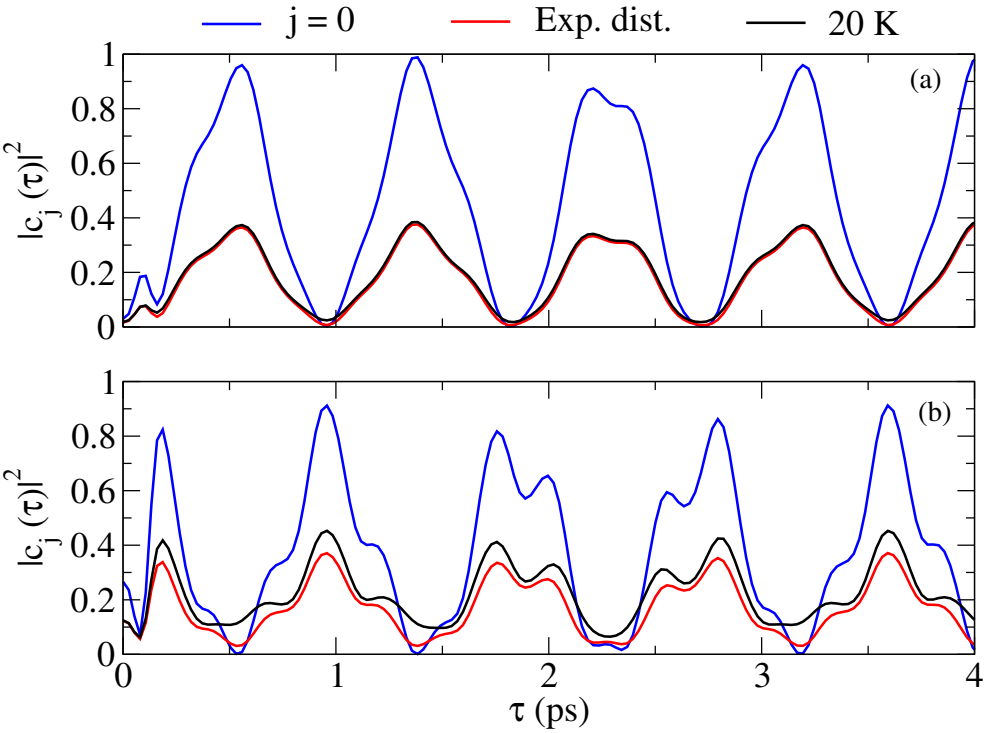

Figure 5.11: Interferograms for incoherent initial states, corresponding to the experimental distribution obtained in Ref. [48] (red) and a thermal ensemble at 20 K (black), compared to that of a pure initial state with $j = 0$ (blue): Final populations of the field-free rotational states (a: $j = 0$, b: $j = 2$) as a function of pulse delay. Pulse parameters as in Figure 5.10.

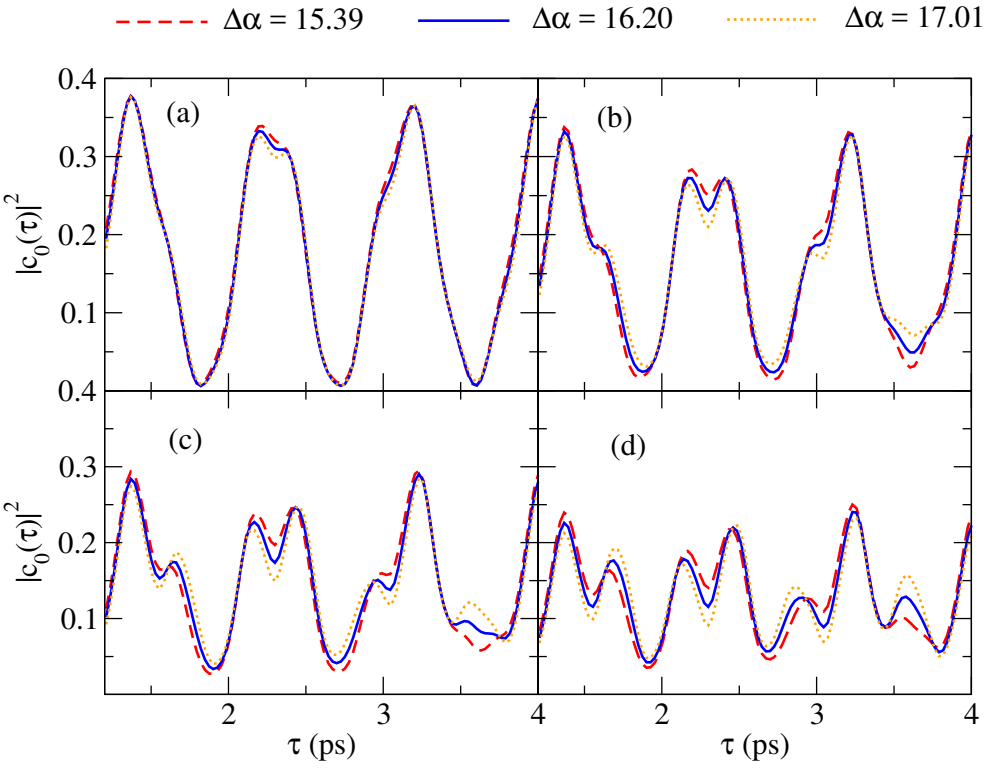

Figure 5.12: Interferograms, i.e., final $j = 0$ populations as function of delay, for different values of the polarizability anisotropy $\Delta\alpha$ and increasing intensity of the second pulse (a: identical pulse intensities, b: $I_0^2 = 1.4I_0^1$, c: $I_0^2 = 1.6I_0^1$, d: $I_0^2 = 1.8I_0^1$). The pulse duration is $\tau_I = 100$ fs for both pulses, and the intensity of the first pulse is $I_0^1 = 0.55 \times 10^{13}$ W/cm^2. The initial state corresponds to the experimental distribution of Ref. [48].

The results from Sec. 5.4.3 show that a high visibility can be achieved in the interferograms obtained through the final state population of the ground rotational state, $j = 0$, even for an incoherent ensemble that can be obtained in actual experimental setups [48]. For $j = 2$ (Figure 5.11(b)), the maximum population amounts to about 0.4, at least for the experimental distribution. The interferograms of the incoherent ensembles differ visibly from each other, and they also differ qualitatively from the interferogram of the pure initial state. This simply reflects the fact that the dynamics of the $j = 2$ state is affected by more states in the initial ensemble (both $m = 0$ and $m \neq 0$). If one wants to test the composition of the initial state interferometrically, measurement of $j = 2$ is therefore preferred to $j = 0$. The visibility of the interferograms for $j = 2$ is reduced, compared to the pure state, to 0.85 for the experimental distribution of Ref. [48] and to 0.76 for the thermal state. These results are encouraging in view of the feasibility of a rotational interferometer. Thus, we can conclude that incoherence in the initial state does not preclude interferometry, in particular if one measures the $j = 0$ population.

5.4.4 Prospect of measuring the polarizability anisotropy

Our analysis of the visibility suggests that molecular rotational state interferometers can be employed to determine molecular parameters, e.g. the polarizability anisotropy. To further investigate this possibility, interferograms obtained by measuring the final $j = 0$ population for values of $\Delta\alpha$ around the *ab initio* calculated value of $16.20\,\mathrm{a}_0^3$, namely, $17.01\,\mathrm{a}_0^3$ (5% larger) and $15.39\,\mathrm{a}_0^3$ (5% smaller) have been computed and are displayed in Figure 5.12. Notwithstanding the fine visibility ($V_0 = 0.97$), the resulting interferograms obtained from these three values of the polarizability anisotropy are nearly identical whenever the maximum intensity of the second pulse is kept equal to that of the first one, see Figure 5.12 (a). The interferograms become more distinguishable when the intensity of the second pulse is increased with respect to the first one (Figure 5.12 (b)-(d)). In particular, we notice a large difference in the interferograms for $I_0^2 = 1.6 I_0^1$, see panel (c). The enhanced distinguishability is most pronounced at $\tau \sim 1.2$, 2.3 and 3.5 ps. The better distinguishability comes at the price of a slightly deteriorated visibility $V_0 \sim 0.79$. Such clear differences should still be observable, even when inevitable error bars are taken into account.

For the parameters used in Figure 5.12 (c), measurement errors of the $j = 0$ state amounting to 2% and 5% are assumed in the interferograms in Figure 5.13(a) and (b). We previously found that increasing the strength of the second pulse leads to a larger distinguishability between the interferograms. Here we test the ability to distinguish the interferograms taking experimental errors into account. In the case of 2% measurement error (a) the interferograms are easily distinguishable from each other in various intervals, ($\tau \in [1.5, 2.0], [2.7, 2.9], [3.45, 3.75]$ ps). For 5% measurement error (b), however, only the

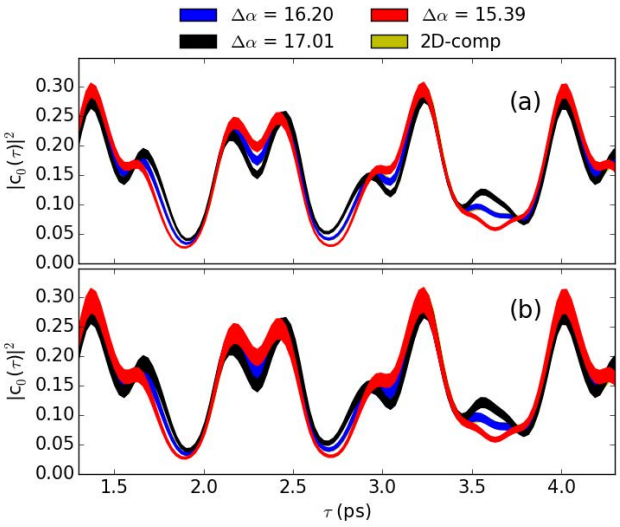

Figure 5.13: Interferograms corresponding to different values of $\Delta\alpha$. Initial state is the experimental distribution with 2% uncertainty in initial population taking into account. Panel (a): 2% population measurement uncertainty, (b): 5% population measurement uncertainty.

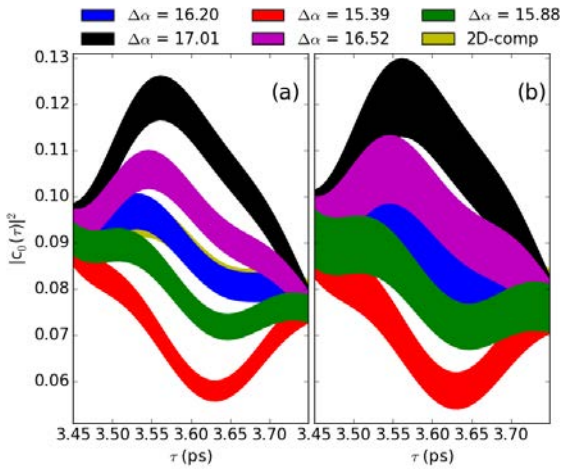

Figure 5.14: Interferograms corresponding to different values of $\Delta\alpha$. Zoom in on the pulse delay interval $\tau \in [3.45, 3.75]$ ps. Initial state is the experimental distribution with 2% uncertainty in initial population taking into account. Panel (a): 2% population measurement uncertainty, (b): 5% population measurement uncertainty.

latter interval allows for confident distinguishability. Within this region, the interferometer is particularly sensitive to small variations in the molecular polarizability anisotropy. A close up image of this region is shown in Figure 5.14, where two more values of $\Delta\alpha$, 16.52 and 15.88 have been included, corresponding to a 2% larger (lower) value of the polarizability anisotropy w.r.t the *ab-initio* value. We see that for 2% measurement error, the interferometer is readily sensitive to $\pm 2\%$ shifts in $\Delta\alpha$, whereas for 5% measurement error, they are not so readily distinguishable.

Our results for the sensitivity of the interferometer account, to some extent, for experimental errors by averaging over many wave packet calculations. Still, the errors may behave differently for the ERA and the full rovibrational dynamics. It is therefore instructive to verify that our conclusions are not invalidated by the limitations of the ERA. Interferograms obtained using the ERA for the *ab initio* value of $\Delta\alpha$ and from full two-dimensional calculations, using Hamiltonian (5.2) are displayed in Figures. 5.13 and 5.14. Small deviations in the error bars between ERA and 2D model can be observed. In particular, in Figure 5.13(b) and 5.14(b), these differences are small and our stated conclusions still hold. That is, the sensitivity of the interferometer to changes in the polarizability anisotropy of $\pm 2\%$ ($\pm 5\%$) requires the measurement errors not to exceed the same level.

5.5 Conclusions and Outlook

From this study, we can conclude that a Ramsey-type interferometer, based on the rotational wave packet dynamics of a trapped, cooled MgH^+ molecular ion, using off-resonant femtosecond laser pulses, can be implemented using current experimental capabilities. In contrast to the typical atom interferometry, where two isolated levels for Rabi cycling can be found, the application of the second pulse leads to rotational ladder climbing in the molecular case. The visibility of the resulting interferogram is only perfect for $j = 0$, while around 90% for $j = 2$, for a pure initial state with $j = 0$, $m = 0$.

Preparing a molecule perfectly in its rovibrational ground state can be experimentally challenging. However, we found that a ground state population of 98% decreases the visibility to 96% for $j = 0$ and to 85% for $j = 2$. For a thermal distribution with a rotational temperature of 20 K, high-visibility interferograms can still achieved.

For the MgH^+ ion considered here, the required intensities are of the order of 10^{12} W/cm^2 for 100 fs laser pulses. Thus, the implementation of a rotational Ramsey interferometer, combining standard trapping and cooling techniques for molecular ions with 800 nm femtosecond laser pulses is experimentally feasible. Such an interferometer could find applications for the measurement of the molecular polarizability anisotropy, with a sensitivity of $\pm 2\%$ and

$\pm 5\%$ for experimental uncertainties in the initial populations and population measurement errors respectively, and assuming the same degree of experimental inaccuracy.

Another interesting application of the interferometer would be to study the dependence of the molecular polarizability anisotropy on the inter nuclear separation. This could be achieved for instance by recording rotational interferograms for several vibrational states or using the full rovibrational dynamics. Since the potential energy curve is only known approximately, it might be difficult, in both approaches, to separate out the effects that arise from the potential and the the r-dependence of the polarizability anisotropy. The potential can, however, be measured by means of resonant spectroscopy, e.g., IR-spectroscopy or vibrational or electronic spectroscopy. If the polarizability is known to high accuracy, e.g. by interferometric means, we remind that the interferometer can be used to probe local electric fields, like, e.g., the radio-frequency fields at different positions within a (linear) Paul trap. More importantly, our interferometric setup is general, and the method presented here can be applied using other molecular ions species, provided the laser light does not drive resonant transitions.

6 Conclusions and outlook

Quantum technology (QT), where the quantum properties of matter and light are utilized to enhance the performance of technology, i.e., quantum information processing and computing or quantum-enhanced spectroscopy, is a fast growing research field. Atoms and atomic ions have played a decisive role in implementing quantum technologies. Presently much focus is put on molecular ions, which because of more degrees of freedom allow for greater versatility than atomic systems. Diatomic molecular ions, both polar and apolar, are natural systems to expanding on atomic ions, since they represent the next simplest systems. The additional degree of freedom coming from molecular rotations has been of particular interest to implement e.g. quantum information processing [34, 43, 55]. A prerequisite to be able to utilize molecular ions in quantum technological applications is that they have been cooled to sufficiently low temperatures for their quantum nature to manifest itself. An other important prerequisite for QT applications is the ability to accurately manipulate the quantum system under consideration. In order to achieve control over the system one needs to accurately know the molecular parameters of the system that enter into the Hamiltonian, such as e.g. the polarizability anisotropy and permanent dipole moment.

In this dissertation we have studied diatomic molecular ions in the context of QT. In particular, we have presented two theoretical investigations concerning the dynamics of cold diatomic molecular ions in a linear Paul trap. As a part of this study we have addressed the problem of cooling the molecular ions, and in particular sympathetic cooling of diatomic molecular ions with a special focus on the possibly detrimental rotational state excitation during the cooling process. Additionally, we have presented an application for cold molecular ions as as a sensitive interferometric measurement device based on the rotational state population.

Here, we have studied the method of **sympathetic cooling**, which utilizes already cold atoms (atomic ions) to prepare cold molecules (molecular ions) via repeated energy trans-

ferring collisions. One of its main advantages is that it is a general method, independent on the internal structure of the system being cooled. In particular, for ionic species, the strong Coulomb coupling provides an effective cooling of the translational degree of freedom, but at the same time, the Coulomb field arising from the coolant atomic ion couples to the molecular rotational states may cause a rotational redistribution which can render quantum technological applications non-viable. Therefore, in order to quantify the viability of sympathetic cooling, we intend to estimate the rotational excitations resulting from repeated collisions between the molecular ion and coolant during the cooling cycle.

We have proposed a simple, semiclassical model, based on the energy separation of the translational and rotational degrees of freedom, to estimate the extent of the rotational redistribution for diatomic molecular ions based on the initial translational scattering energy and molecular parameters, such as rotational constants and dipole moments, in the case of polar species, and quadrupole moment, applicable for apolar molecular species. Our studies have shown that an accurate estimation of the population excitation, as a closed formula, can be found for apolar molecular ions from first order perturbation theory where the quadrupole interaction is taken into account. Polar molecular ions which possess a permanent dipole moment interact linearly with the field. This, in general, leads to a stronger coupling to the rotational degree of freedom, but not necessarily to larger redistribution, since the gradual variation of the field implies a near adiabatic dynamics. The gradual variation of the field greatly suppresses the rotational redistribution, but also makes the analysis of the rotational dynamics more difficult. Indeed, only for moderate coupling between the external field and the rotational states, as exemplified with the HD^+ ion in our work, has an analytical expression for the population excitation been found. This expression gives a fairly good estimate to the numerically obtained excitation, but is less accurate than for apolar species and tends to overestimate the excitation and can therefore serve as a close upper bound to the numerical excitation. In our investigation, we have exclusively studied molecular ions initially prepared in their absolute internal ground state. Methods for preparing molecular ions are not limited to the ground state, however. As an example, the rotational spectrum for apolar molecular ions, is made up of either entirely even or odd rotational states, as determined by the particular symmetries of the molecular ion. For odd rotational states, the ground state is then excluded by symmetry, and is therefore missing. Irrespective of the reason, our closed formula is straightforwardly extendable to treat such a scenario.

The crystal constant, i.e., the inter-atomic distance between the ions forming the Coulomb crystal in the trap, has a strong impact on how efficient the cooling is, and does greatly influence the cooling time, effectively making only the crystal scenario feasible. In contrast, we have found that it has very little impact on the final rotational excitation. Depending on the inter-atomic distance within the crystal we identify and investigate two different cooling scenarios, the crystal and single ion scenarios. These correspond to the two limiting cases

of a real cooling experiment. Within the crystal scenario, an analytical expression for the average energy transfer as a function of energy has been derived, and the number of collisions required to lower the kinetic energy by a given amount was approximated. No exact expression can be found in the single ion cooling scenario, but a lower bound is possible to obtain. The number of collisions allow us to estimate the timescales of the cooling process in both scenarios, from which we conclude that the crystal cooling is the only practically feasible scenario.

Once cold temperatures have been achieved for the molecular ions, one can take advantage of the quantum nature that is manifest at these low temperatures for quantum control applications. In the second part of this work, we have proposed a **Ramsey like interferometer** implemented on the rotational states of an ultra-cold MgH^+ ion using off-resonant time-delayed fs laser pulses. Our setup will work for other molecular species as well as long as the laser does not drive resonant transitions. In our setup the pulses take the role of beam splitters in typical light interferometry. The molecular ions form a Coulomb crystal with a lattice constant large enough to allow for single ion addressability by the fs laser pulses used in the experiment. The ions are situated within an ultra-high vacuum environment, with storage capabilities that can even exceed hours, allowing for experiments of long interaction and observation times. We have found that, given the experimental conditions provided by sympathetically cooled molecular ions in a Paul trap, our interferometric setup is capable of sensitive measurements. In particular, we have demonstrated that accurate measurements of molecular polarizabilities at equilibrium distance are feasible using existing experimental setups. In particular, achieving a pure initial rotational state is an experimentally challenging task, and in practice a perfect pure state can not be realized. However, our interferometric setup is still capable of high precision measurements of the polarizabilities, from initial ensembles that are achievable from available experimental techniques. Conversely, when recording the interferogram on excited states, which are more susceptible to the composition of the initial ensemble, the interferometer could be utilized as an instrument to determine the individual populations of the initial rotational ensemble.

In this work, we have addressed two important aspects of quantum technology, cooling of quantum systems in order that their quantum properties manifest themselves and an interferometric scheme that is capable of measuring molecular parameters, such as the polarizability anisotropy, as well as the initial rotational ensemble of molecular ions. Important examples of current research where cooling and manipulation of molecular rotational states are within quantum information processing and quantum non-destructive measurements, see e.g. [104]. Our studies presented in this thesis could therefore be well suited for the preparation and characterization of molecular ions used for these purposes. An-other interesting venue of study is cold chemical collisions and the dependence of the cross section on the orientation or alignment of molecular species.

Diatomics also represent a natural bridge between the studies of atomic systems and technology based on polyatomic molecular systems. Polyatomics, with a promise to be more versatile systems, e.g. as robust systems for quantum error-correcting codes for information processing and storage [34], are more difficult to manipulate and to cool down due to their more complex internal structure. Therefore, they present a tougher challenge to cool down. In principle, our model can be extended to treat polyatomics by replacing the Hamiltonian of a linear rotor by that of a symmetric or asymmetric top. However, due to the larger physical size of polyatomic molecules close-encounters are becoming more likely, and extra care has to be taken in the justification of our semi-classical model. It would nevertheless be interesting to identify the validity range of our approach. Also, the more complex energy structure and different selection rules of polyatomics makes them a tougher challenge. A wide range of applications of the rotational and torsional degrees of freedom of cooled molecules in quantum technology are being proposed, see [43] for a thorough overview. Among the applications are using optimal control techniques to obtain full 3D-control of the rotational motion using elliptical laser light and control of torsional bending in molecular electronics.

As we have discussed in this thesis, QT is a vividly studied research field with potential applications within e.g. high precision spectroscopy and information processing and storage that can outperform the classical counterparts. Cold molecular ions are promising systems on which to implement QT, and particularly the rotational degree of freedom is of major importance. Diatomic molecular ions play an important role in extending the applications of atomic systems as they provide more degrees of freedom, and thereby more versatility in comparison to atomic systems, but are simpler systems than polyatomic ions, and are thus easier to manipulate and to cool. Based on the progress of diatomic systems, the natural step is the study of polyatomic species, which provide even more degrees of freedom, and therefore even greater versatility. With the latest technological advances, we can now exert control over the quantum world and create a bright quantum future.

Appendices

A

Born-Oppenheimer Approximation

A molecule is a bound state of electrons, whose coordinates are collectively labelled with $\mathbf{r}$ and one or more nuclei, whose coordinates are labelled $\mathbf{R}$. The problem of finding the molecular structure is solved by the time-independent Schrödinger equation

$$\hat{\mathbf{H}}\Psi(\mathbf{r},\mathbf{R}) = E\Psi(\mathbf{r},\mathbf{R}), \tag{A.1}$$

where the total Hamiltonian is the sum of the kinetic energies of the electrons and nuclei and the electron-electron, nucleus,nucleus and electron nuclei interactions respectively

$$\hat{\mathbf{H}} = \hat{\mathbf{T}}_N + \hat{\mathbf{T}}_e + \hat{\mathbf{V}}_N + \hat{\mathbf{V}}_e + \hat{\mathbf{V}}_{N,e}, \tag{A.2}$$

with

$$\begin{aligned} \hat{\mathbf{T}}_N &= -\sum_n \frac{\nabla^2_{\vec{R}}}{2M_n}, \quad \hat{\mathbf{T}}_e = -\sum_n \frac{\nabla^2_{\vec{r}}}{2m_e} \\ \hat{\mathbf{V}}_N &= \sum_n \sum_{m<n} \frac{Z_n Z_m}{|\mathbf{R}_n - \mathbf{R}_m|}, \quad \hat{\mathbf{V}}_e = \sum_i \sum_{j<i} \frac{1}{|\mathbf{r}_i - \mathbf{r}_j|} \\ \hat{\mathbf{V}}_{N,e} &= -\sum_n \sum_i \frac{Z_n}{|\mathbf{R}_n - \mathbf{r}_i|}, \end{aligned} \tag{A.3}$$

and $\Psi(\mathbf{r},\mathbf{R})$ is the molecular wave function. Since the nuclei are much heavier than the electrons, $M_N \gg m_e$ (the lightest nucleus, the proton is approximately 1830 times heavier than the electron), the electrons immediately respond to any change in the nuclear positions and they are therefore always relaxed in an equilibrium state for any given configuration of the nuclei. This suggests that the total molecular wave function can approximately be written in terms of a set of electronic wave functions, $\phi_k(\mathbf{r};\mathbf{R})$ which depend parametrically on the nuclear coordinates, i.e. for each $\mathbf{R}$ we have a different electronic wave function, and a set of nuclear wave functions $\chi_k(\mathbf{R})$, where k labels the various molecular electronic states.

$$\Psi(\mathbf{r},\mathbf{R}) = \sum_k \phi_k(\mathbf{r};\mathbf{R})\chi_k(\mathbf{R}), \tag{A.4}$$

The $\phi_k(\mathbf{r};\mathbf{R})$ are an orthonormal set of functions

$$\int \phi_l^*(\mathbf{r};\mathbf{R})\phi_k(\mathbf{r};\mathbf{R})d\mathbf{r} = \delta_{lk}. \tag{A.5}$$

Furthermore, since the electrons, due to their much smaller masses, move much faster than the nuclei, the latter can be considered frozen with respect to the motion of the electrons. For a frozen nuclear configuration the nuclear kinetic energy vanishes and additionally the nuclear potential represents a scalar quantity which only shifts the eigenvalue, but does not affect the eigenfunctions. Within these approximations we define the electronic Hamiltonian as

$$\hat{\mathbf{H}}_e = \hat{\mathbf{T}}_e + \hat{\mathbf{V}}_e + \hat{\mathbf{V}}_{ne} \tag{A.6}$$

and the electronic problem reduces to the eigenvalue equation

$$\hat{\mathbf{H}}_e\phi_k(\mathbf{r};\mathbf{R}) = \varepsilon_k(\mathbf{R})\phi_k(\mathbf{r};\mathbf{R}), \tag{A.7}$$

where $\varepsilon_k(\mathbf{R})$ is the electronic potential energy due to the electrons at each nuclear configuration, $\mathbf{R}$. Since the nuclear dynamics takes place in the average potential arising from the electronic motion it is obtained by multiplying Eq. (A.1) with $\phi_l^*(\mathbf{r};\mathbf{R})$ from the left and integrate. Using Eqs. (A.5) and (A.7) we arrive at

$$\sum_k \left[\int \phi_l^*(\mathbf{r};\mathbf{R})\hat{\mathbf{T}}_N\phi_k(\mathbf{r};\mathbf{R})d\mathbf{r} + (V_N(\mathbf{R}) + \varepsilon_k(\mathbf{R}))\delta_{lk}\right]\chi_k(\mathbf{R}) = E\chi_l(\mathbf{R}) \tag{A.8}$$

So it is the nuclear kinetic energy operator that mixes electronic states. Let's have a closer look at it,

$$\begin{aligned}\frac{1}{2M_n}\int \phi_l^*(\mathbf{r};\mathbf{R})\nabla^2_{\mathbf{R}}(\phi_k(\mathbf{r};\mathbf{R})\chi_k(\mathbf{R}))d\mathbf{r} &= \frac{1}{2M_n}\int \phi_l^*(\mathbf{r};\mathbf{R})\left(\nabla^2_{\mathbf{R}}\phi_k(\mathbf{r};\mathbf{R})\right)d\mathbf{r}\chi_k(\mathbf{R}) \\ + \frac{1}{2M_n}\int \phi_l^*(\mathbf{r};\mathbf{R})2\nabla_{\mathbf{R}}\phi_k(\mathbf{r};\mathbf{R})d\mathbf{r}\cdot\nabla_{\mathbf{R}}\chi_k(\mathbf{R}) &+ \frac{1}{2M_n}\nabla^2_{\mathbf{R}}\chi_k(\mathbf{R})\delta_{lk},\end{aligned} \tag{A.9}$$

where we have used the orthogonality of the $\phi_k(\mathbf{r};\mathbf{R})$ in the third term on the right hand side. Consequently, only the first two terms couple the electronic states by the action of $\nabla_{\mathbf{R}}$ on the electronic function, and if these were zero we would have no mixing of electronic wave functions. Once again the much smaller electronic mass relative to the mass of any nucleus allows the electron to respond to any change in the nuclear configuration, i.e. the dependence of the electronic wave functions on the nuclear coordinate is much more gradual than the dependence on the electronic coordinates. These terms are therefore neglected, leading to a much simpler, decoupled nuclear problem. However, neglecting the term containing the mixed derivatives is non-trivial. First notice that the diagonal term of the mixed derivative is indeed zero. From Eq. (A.5)

$$0 = \nabla_{\mathbf{R}}\langle\phi_k\,|\,\phi_k\rangle = \langle\nabla_{\mathbf{R}}\phi_k\,|\,\phi_k\rangle + \langle\phi_k\,|\,\nabla_{\mathbf{R}}\phi_k\rangle\,. \tag{A.10}$$

Since the $|\phi_k\rangle$ can always be chosen real due to time-invariance we have $\langle\phi_k\,|\,\nabla_{\mathbf{R}}\phi_k\rangle = 0$. However, consider the commutator

$$\begin{aligned}\phi_l^*(\mathbf{r};\mathbf{R})[\nabla_{\vec{R}},\hat{\mathbf{H}}_e]\phi_k(\mathbf{r};\mathbf{R}) &= \phi_l^*(\mathbf{r};\mathbf{R})\nabla_{\vec{R}}\hat{\mathbf{H}}_e\phi_k(\mathbf{r};\mathbf{R}) - \phi_l^*(\mathbf{r};\mathbf{R})\hat{\mathbf{H}}_e\nabla_{\vec{R}}\phi_k(\mathbf{r};\mathbf{R}) \\ &= (\varepsilon_k(\mathbf{R}) - \varepsilon_l(\mathbf{R}))\,\phi_l^*(\mathbf{r};\mathbf{R})\nabla_{\vec{R}}\phi_k(\mathbf{r};\mathbf{R}) \\ &\Rightarrow \qquad . \qquad \text{(A.11)} \\ \phi_l^*(\mathbf{r};\mathbf{R})\nabla_{\vec{R}}\phi_k(\mathbf{r};\mathbf{R}) &= \frac{\phi_l^*(\mathbf{r};\mathbf{R})[\nabla_{\vec{R}},\hat{\mathbf{H}}_e]\phi_k(\mathbf{r};\mathbf{R})}{\varepsilon_k(\mathbf{R}) - \varepsilon_l(\mathbf{R})}\end{aligned}$$

The denominator on the right hand side of the last line means that the mixed derivative term will blow up whenever $\varepsilon_k(\mathbf{R}) \approx \varepsilon_l(\mathbf{R})$ and the approximation is only justified for well separated potential surfaces. This includes degenerate electronic states of course, but also energy states that become close at certain nuclear configurations. Whenever the approximation is valid we can integrate out the electronic wave function and we obtain the Hamiltonian for the nuclear motion

$$\hat{\mathbf{H}}_N\chi_k(\mathbf{R}) = \left(-\sum_n \frac{\nabla_{\mathbf{R}}^2}{2M_n} + \sum_n\sum_{m<n}\frac{Z_nZ_m}{|\mathbf{R}_n - \mathbf{R}_m|} + \varepsilon_k(\mathbf{R})\right)\chi_k(\mathbf{R}) = E\chi_k(\mathbf{R}) \qquad \text{(A.12)}$$

B

Multipole Expansion

Consider an isolated system (I) with a charge density $\rho(\mathbf{r}')$. It can be e.g. a molecule or a molecular ion. Consider also another, external, system (E) which produces a potential $\phi_e(\mathbf{r})$. The total potential can be expressed as a sum of two separate contributions, one from the external source volume end on from charges within the volume $\phi(\mathbf{r}) = \phi_e(\mathbf{r}) + \phi_i(\mathbf{r})$. We are interested in the contribution from the $\phi_e(\mathbf{r})$-term. Let the origin be at the center of mass of system (I), and Taylor expand around $\mathbf{r}' = \mathbf{0}$ to obtain (using Cartesian coordinates)

$$\begin{aligned}\phi_e(\mathbf{r}') = &\phi_e(\mathbf{0}) \\ &+ \frac{\partial \phi_e}{\partial x'}x' + \frac{\partial \phi_e}{\partial y'}y' + \frac{\partial \phi_e}{\partial z'}z' \\ &+ \frac{1}{2}\left[\frac{\partial^2 \phi_e}{\partial x'^2}x'^2 + \frac{\partial^2 \phi_e}{\partial y'^2}y'^2 + \frac{\partial^2 \phi_e}{\partial z'^2}z'^2\right. \\ &\left. + 2\frac{\partial^2 \phi_e}{\partial x' \partial y'}x'y' + 2\frac{\partial^2 \phi_e}{\partial x' \partial z'}x'z' + 2\frac{\partial^2 \phi_e}{\partial y' \partial z'}y'z'\right] + ...\end{aligned} \tag{B.1}$$

From the first term we simply get the monopole energy

$$U_M = \int_{V'} \rho(\mathbf{r}')dV'\phi_e(\mathbf{0}) = Q\phi_e(\mathbf{0}) \tag{B.2a}$$

whereas, from $\mathbf{E} = -\nabla\phi_e$, the second line gives us

$$U_D = -\int_{V'} \mathbf{r}'\rho(\mathbf{r}')dV' \cdot \mathbf{E} = -\mathbf{p} \cdot \mathbf{E} = -pE\cos\theta_a, \tag{B.2b}$$

which we recognise as the dipole interaction. Here $p = |\mathbf{p}|$, $E = |\mathbf{E}|$ and θ_a is the angle between the molecular axis and the polarization vector of the electric field.

In order to make progress with the remaining terms, note that the potential ϕ_e is source free at the system-volume and must therefore satisfy the Laplace equation $\nabla^2\phi_e = 0$. We

will add the suitable term $-\frac{1}{6}\nabla^2\phi_e$ to the expansion. We obtain the quadrupole term as

$$\begin{aligned} U_Q = \frac{1}{6}\int_{V'}\rho(\mathbf{r}')\Big[&(3x'^2-r^2)\frac{\partial^2\phi_e}{\partial x'^2}+3x'y'\frac{\partial^2\phi_e}{\partial x'\partial y'}+3x'z'\frac{\partial^2\phi_e}{\partial x'\partial z'}\\ &+3y'x'\frac{\partial^2\phi_e}{\partial y'\partial x'}+(3y'^2-r^2)\frac{\partial^2\phi_e}{\partial y'^2}+3y'z'\frac{\partial^2\phi_e}{\partial y'\partial z'}\\ &+3z'x'\frac{\partial^2\phi_e}{\partial z'\partial x'}+3z'y'\frac{\partial^2\phi_e}{\partial z'\partial y'}+(3z'^2-r^2)\frac{\partial^2\phi_e}{\partial z'^2}\Big]dV' \end{aligned} \tag{B.2c}$$

Once again, since $\mathbf{E} = -\nabla\phi_e(\mathbf{r}')|_{\mathbf{r}'=\mathbf{0}}$

$$\begin{aligned} U_Q = -\frac{1}{6}\Big[&\int_{V'}\rho(\mathbf{r}')(3x'^2-r^2)dV'\frac{\partial E_{x'}}{\partial x'}+\int_{V'}\rho(\mathbf{r}')3x'y'dV'\frac{\partial E_{x'}}{\partial y'}+\int_{V'}\rho(\mathbf{r}')3x'z'dV'\frac{\partial E_{x'}}{\partial z'}\\ &+\int_{V'}\rho(\mathbf{r}')3y'x'dV'\frac{\partial E_{y'}}{\partial x'}+\int_{V'}\rho(\mathbf{r}')(3y'^2-r^2)dV'\frac{\partial E_{y'}}{\partial y'}+\int_{V'}\rho(\mathbf{r}')3y'z'dV'\frac{\partial E_{y'}}{\partial z'}\\ &+\int_{V'}\rho(\mathbf{r}')3z'x'dV'\frac{\partial E_{z'}}{\partial x'}+\int_{V'}\rho(\mathbf{r}')3z'y'dV'\frac{\partial E_{z'}}{\partial y'}+\int_{V'}\rho(\mathbf{r}')(3z'^2-r^2)dV'\frac{\partial E_{z'}}{\partial z'}\Big], \end{aligned} \tag{B.3a}$$

where $r^2 = x'^2 + y'^2 + z'^2$. So, the quadrupole energy is the dyadic product

$$U_Q = -\frac{1}{6}Q : \nabla E = -\frac{1}{6}Tr(Q\nabla\mathbf{E}) \tag{B.4}$$

between the quadrupole moment tensor, Q with matrix elements

$$Q_{ab} = \int_{V'}\rho(\mathbf{r}')(3x'_a x'_b - r^2\delta_{ab})dV' \tag{B.5}$$

and the gradient of the electric field

$$(\nabla\mathbf{E})_{ab} = \frac{\partial E_{x'_a}}{\partial x'_b}. \tag{B.6}$$

Notice that since $x'^2 + y'^2 + z'^2 = r^2$ the quadrupole tensor is trace-less,
$Tr(Q) = \int_{V'}\rho(\mathbf{r}')\left(3x'^2+3y'^2+3z'^2-3r^2\right)dV' = 0$.

We seek the quantum Hamiltonian of a molecular ion interacting with a Coulomb field via its polarizability and its quadrupole moment. The molecular ion is modeled as a rigid rotor. Let' s define a Cartesian coordinate system fixed on the molecular ion, $\hat{X}$, $\hat{Y}$, $\hat{Z}$ and a fixed Cartesian system $\hat{x}$, $\hat{y}$, $\hat{z}$.

$$\hat{Z} = \sin\theta\cos\phi\hat{x} + \sin\theta\sin\phi\hat{y} + \cos\theta\hat{z} \tag{B.7a}$$

$$\hat{r} = \cos\beta\hat{x} + \sin\beta\hat{y} \tag{B.7b}$$

$$\hat{r}\cdot\hat{Z} = \cos\theta_a = \cos\beta\cos\theta + \sin\beta\sin\theta\cos\phi \tag{B.7c}$$

For a cylindrically symmetric object $Q_{ab} = 0$ when $a \neq b$ and $Q_{xx} = Q_{yy}$. Therefore the quadrupole moment for an object of cylindrical symmetry is

$$Q_{cyl} = Q_{zz}\begin{pmatrix}-\frac{1}{2}&0&0\\0&-\frac{1}{2}&0\\0&0&1\end{pmatrix} = -\frac{Q_{zz}}{2}\begin{pmatrix}1&0&0\\0&1&0\\0&0&1\end{pmatrix} + \frac{3Q_{zz}}{2}\begin{pmatrix}0&0&0\\0&0&0\\0&0&1\end{pmatrix} \tag{B.8}$$

Likewise the gradient tensor can be written as

$$\nabla \mathbf{E} = \begin{pmatrix} \partial_X E_X & \partial_Y E_X & \partial_Z E_X \\ \partial_X E_Y & \partial_Y E_Y & \partial_Z E_Y \\ \partial_X E_Z & \partial_Y E_Z & \partial_Z E_Z \end{pmatrix} \tag{B.9}$$

Therefore the product is

$$Q\nabla \mathbf{E} = -\frac{Q}{2} \begin{pmatrix} \partial_X E_X & \partial_Y E_X & \partial_Z E_X \\ \partial_X E_Y & \partial_Y E_Y & \partial_Z E_Y \\ \partial_X E_Z & \partial_Y E_Z & \partial_Z E_Z \end{pmatrix} + \frac{3Q}{2} \begin{pmatrix} 0 & 0 & 0 \\ 0 & 0 & 0 \\ \partial_X E_Z & \partial_Y E_Z & \partial_Z E_Z \end{pmatrix} \tag{B.10}$$

and consequently he interaction energy is

$$U = -\frac{1}{6} \left(-\frac{Q}{2} \nabla \cdot \mathbf{E} + \frac{3Q}{2} \partial_Z E_Z \right) = -\frac{Q}{4} \partial_Z E_Z, \tag{B.11}$$

where $\nabla \cdot \mathbf{E} = 0$ by Gauss' s law.

In particular, for a Coulomb field we have

$$E_Z = \frac{1}{r^2} \cos\theta_a = \frac{Z}{\left(X^2 + Y^2 + Z^2\right)^{3/2}} \tag{B.12}$$

and so

$$\frac{\partial E_Z}{\partial Z} = -3 \frac{Z^2}{\left(X^2 + Y^2 + Z^2\right)^{5/2}} + \frac{1}{\left(X^2 + Y^2 + Z^2\right)^{3/2}}, = -\frac{1}{r^3} \left(3\cos^2\theta_a - 1 \right) \tag{B.13}$$

leading up to the quadrupole energy

$$U_Q = \frac{Q_{ZZ}}{4r^3} \left(3\cos^2\theta_a - 1 \right). \tag{B.14}$$

C

Inertia Tensor

For any rotating rigid body the velocity $\vec{v}_i$ associated with a mass point i within the body is related to the angular velocity of the rigid body and the mass point' s distance from the center of rotation, $\vec{r}_i$, by

$$\vec{v}_i = \vec{\omega} \times \vec{r}_i \tag{C.1}$$

Therefore, the energy of the rotational motion is of all mass points of the rigid body is given by

$$T_{rot} = \frac{1}{2} \sum_i^N m_i \vec{v}_i^2 = \frac{1}{2} \sum_i^N m_i \left(\vec{\omega} \times \vec{r}_i\right)^2 . \tag{C.2}$$

The cross product can be expressed in terms of the Levi-Civita tensor as $(\vec{\omega} \times \vec{r})_i = \epsilon_{ijk} \omega_j r_k$, with

$$\epsilon_{ijk} = \begin{cases} 1, & i,j,k \text{ an even permutation of 1,2,3} \\ -1, & i,jk, = 1,2,3 \text{ an odd permutation of 1,2,3} \\ 0, & \text{otherwise.} \end{cases} \tag{C.3}$$

Now the we can express the square as

$$\begin{aligned} (\vec{\omega} \times \vec{r}) \cdot (\vec{\omega} \times \vec{r}) &= \sum_i \epsilon_{ijk} \omega_j r_k \epsilon_{ilm} \omega_l r_m \\ &= \left(\delta_{jl}\delta_{km} - \delta_{jm}\delta_{kl}\right) \omega_j \omega_l r_k r_m \\ &= \omega_j^2 r_k^2 - \omega_j \omega_k r_j r_k. \end{aligned} \tag{C.4}$$

So the rotational energy is expressed as

$$T_{rot} = \frac{1}{2} \vec{\omega}^T I \vec{\omega}, \tag{C.5}$$

where I is the moment of inertia tensor, which in an arbitrary reference frame is represented by the matrix

$$I = \begin{pmatrix} I_{xx} & I_{xy} & I_{xz} \\ I_{yx} & I_{yy} & I_{yz} \\ I_{zx} & I_{zy} & I_{zz} \end{pmatrix} . \tag{C.6}$$

The matrix elements are given from Eqs. (C.2,C.4, C.5) and for example $I_{xx} = \sum_i m_i \left(y_i^2 + z_i^2\right)$ and $I_{zy} = -\sum_i m_i z_i y_i$. The angular momentum of the rotating system is given by

$$\begin{aligned} \vec{L} &= \sum_i \vec{r}_i \times \vec{p}_i \\ &= \sum_i m_i \vec{r}_i \times (\vec{\omega} \times \vec{r}_i) \\ &= \sum_i m_i \left(\vec{\omega} r_i^2 - \vec{r}_i \left(\vec{r}_i \cdot \vec{\omega}\right)\right). \end{aligned} \tag{C.7}$$

Here the identity $\vec{a} \times \left(\vec{b} \times \vec{c}\right) = \vec{b}\left(\vec{a} \cdot \vec{c}\right) - \vec{c}\left(\vec{a} \cdot \vec{b}\right)$ has been used.

Considering the product $I\vec{\omega}$ we obtain

$$I\vec{\omega} = \sum_i m_i \begin{pmatrix} \omega_x \left(y_i^2 + z_i^2\right) - x_i \left(\omega_y y_i + \omega_z z_i\right) \\ \omega_y \left(x_i^2 + z_i^2\right) - y_i \left(\omega_x x_i + \omega_z z_i\right) \\ \omega_z \left(x_i^2 + y_i^2\right) - z_i \left(\omega_x x_i + \omega_y y_i\right) \end{pmatrix}. \tag{C.8}$$

By adding $0 = \omega_x x_i^2 - \omega_x x_i^2$ to the x-component we get

$$\begin{aligned} \left(I\vec{\omega}\right)_x &= \sum_i m_i \left(\omega_x \left(x_i^2 + y_i^2 + z_i^2\right) - x_i \left(\omega_x x_i + \omega_y y_i + \omega_z z_i\right)\right) \\ &= \sum_i m_i \left(r_i^2 \vec{\omega} - \vec{r}_i \left(\vec{r}_i \cdot \vec{\omega}\right)\right)_x. \end{aligned} \tag{C.9}$$

Continuing this process for the y, z-axes we conclude that

$$\vec{L} = I\vec{\omega}. \tag{C.10}$$

By inspection the matrix of the inertia tensor is clearly real and symmetric, i.e. Hermitian. Hence, its eigenvalues are real and the corresponding eigenvectors are orthogonal. I.e. we seek the solutions to the equation

$$\begin{vmatrix} I_{xx} - \lambda & I_{xy} & I_{xz} \\ I_{yx} & I_{yy} - \lambda & I_{yz} \\ I_{zx} & I_{zy} & I_{zz} - \lambda \end{vmatrix} = 0 \tag{C.11}$$

The eigenvectors are called principal axes and are particularly important. The kinetic energy now becomes particularly simple, since the cross terms vanish,

$$\begin{aligned} T_{rot} &= \frac{1}{2}\left(I_a \omega_a^2 + I_b \omega_b^2 + I_c \omega_c^2\right) \\ &= \frac{L_a^2}{2I_a} + \frac{L_b^2}{2I_b} + \frac{L_c^2}{2I_c} \end{aligned} \tag{C.12}$$

For linear point masses

$$I_a = \mu r^2, \quad I_b = I_c = 0 \tag{C.13}$$

and therefore the rotational energy is

$$T_{rot} = \frac{L_a^2}{2\mu r^2} \tag{C.14}$$

D Polynomials

Orthogonal polynomials play an important role in physics. They are solutions to many differential equations central to physics. The most used polynomials in physics are functions that arises in Sturm-Liouville (SL) theory. These polynomials, $y(x)$, defined on an interval $[a, b]$, satisfy second order differential equations that can be written in Sturm-Liouville form [130]

$$-\frac{d}{dx}\left[p(x)\frac{d}{dx}\right]y(x) + q(x)y(x) = \lambda\omega(x)y(x), \tag{D.1}$$

for given functions $p(x)$ and $q(x)$. The function $\omega(x)$ is called a weight function and λ a constant. One may define the SL-operator

$$L = \frac{1}{\omega(x)}\left[-\frac{d}{dx}\left(p(x)\frac{d}{dx}\right) + q(x)\right], \tag{D.2}$$

an then Eq. (D.1) becomes an eigenvalue equation

$$Ly(x) = \lambda y(x). \tag{D.3}$$

The operator L is is self adjoint on the interval $[a, b]$ and therefore its eigenvalues are real and its eigenfunctions are orthogonal [130]

$$\int_a^b y_n(x)y_m(x)\omega(x)dx = c_{n,m}\delta_{n,m} \tag{D.4}$$

D.1 Legendre polynomials

One of the most frequently encountered examples of Sturm-Liouville functions in physics are the Legendre polynomials, $P_l(x)$. Their defining differential equation is, in SL-form is

$$-\frac{d}{dx}\left[\left(1-x^2\right)\frac{d}{dx}\right]P_l(x) = l(l+1)P_l(x), \quad l = 0, 1, 2, 3\ldots \tag{D.5}$$

These polynomials are defined on the interval $[-1, 1]$ and the normalization condition is

$$\int_{-1}^{1} P_l(x)P_n(x)dx = \sqrt{\frac{2}{2l+1}}\delta_{l,n}. \tag{D.6}$$

Defining $\tilde{P}_l(x) = \sqrt{\frac{2l+1}{2}}P_l(x)$ leads to the orthonormality relation,

$$\int_{-1}^{1} \tilde{P}_l(x)\tilde{P}_n(x)dx = \delta_{l,n}. \tag{D.7}$$

The Legendre polynomials satisfy the following recurrence relation

$$\begin{aligned} P_0(x) = 1, \quad P_1 = x \\ (l+1)P_{l+1}(x) = (2l+1)xP_l(x) - lP_{l-1}(x), \end{aligned} \tag{D.8}$$

which, combined with the normalization, Eq. (D.7), gives the recurrence relation for the normalized polynomials, $\tilde{P}_l(x)$

$$\begin{aligned} \tilde{P}_0(x) = \frac{1}{\sqrt{2}}, \quad \tilde{P}_1 = \sqrt{\frac{3}{2}}x \\ (l+1)\sqrt{\frac{1}{2l+3}}\tilde{P}_{l+1}(x) = (2l+1)x\sqrt{\frac{1}{2l+1}}\tilde{P}_l(x) - l\sqrt{\frac{1}{2l-1}}\tilde{P}_{l-1}(x). \end{aligned} \tag{D.9}$$

Rearranging and taking integrals, using the orthonormality relation, Eq. (D.7) the matrix elements of the operator $\hat{\mathbf{x}} = \cos\hat{\theta}$ in the $\tilde{P}_l$ basis are obtained,

$$\begin{aligned} X_{l'l} &= \int_{-1}^{1} \tilde{P}_{l'}(x)x\tilde{P}_l(x)dx \\ &= (l+1)\sqrt{\frac{1}{(2l+3)(2l+1)}}\delta_{l'l+1} + l\sqrt{\frac{1}{(2l+1)(2l-1)}}\delta_{l'l-1}, \end{aligned} \tag{D.10}$$

where the term containing $\delta_{l'l-1}$ is only defined for $l > 0$.

The associated Legendre functions are obtained from the Legendre polynomials by

$$P_l^m(x) = (-1)^m(1-x^2)^{m/2}\frac{d^m}{dx^m}P_l(x) \tag{D.11}$$

and they satisfy the normalization condition for fixed m

$$\int_{-1}^{1} P_k^m(x)P_l^m(x)dx = \frac{2(l+m)!}{(2l+1)(l-m)!}\delta_{k,l}. \tag{D.12}$$

From the normalization condition, Eq. (D.12), we can define the normalized associated Legendre functions

$$\tilde{P}_l^m(x) = \sqrt{\frac{(2l+1)(l-m)!}{2(l+m)!}}P_l^m(x). \tag{D.13}$$

The associated Legendre functions satisfy a number of recurrence relations. Here we list the ones that are of relevance to us. For fixed m ($\Delta m = 0$)

$$(l-m+1)P_{l+1}^m(x) = (2l+1)xP_l^m - (l+m)P_{l-1}^m(x). \tag{D.14}$$

For $\Delta m = \pm 1$

$$\sqrt{1-x^2}P_l^m(x) = \frac{1}{2l+1}\left(-P_{l+1}^{m+1}(x) + P_{l-1}^{m+1}(x)\right) \tag{D.15a}$$

$$\sqrt{1-x^2}P_l^m(x) = \frac{1}{2l+1}\left((l-m+1)(l-m+2)P_{l+1}^{m-1}(x) - (l+m-1)(l+m)P_{l-1}^{m-1}(x)\right) \tag{D.15b}$$

D.2 Chebyschev polynomials

The Chebyschev differential equation is

$$\left(1-x^2\right)\frac{d^2y}{dx^2} - x\frac{dy}{dx} + n^2y = 0, \quad n = 0, 1, 2, 3\ldots \tag{D.16}$$

They satisfy the following recursion relation

$$T_{n+1}(x) = 2xT_n(x) - T_{n-1}(x), \quad T_0(x) = 1, \quad T_1(x) = x \tag{D.17}$$

and the orthonormality condition

$$\langle T_m, T_n\rangle \int_{-1}^{1} \frac{T_m(x)T_n(x)}{\sqrt{1-x^2}}dx = \begin{cases} \frac{\pi}{2}\delta_{m,n} & \text{for } m \neq 0, \quad n \neq 0 \\ \pi & \text{for } m = n = 0 \end{cases} \tag{D.18}$$

The expansion coefficients are

$$a_n = \int_{-1}^{1} \frac{T_n(x)f(x)}{\sqrt{1-x^2}}dx, \tag{D.19}$$

for a function $f(x) = \sum_{n=0}^{\infty} a_n T_n(x)$. In particular for an exponential function they are

$$a_n(\alpha) = \int_{-1}^{1} \frac{T_n(x)e^{-i\alpha x}}{\sqrt{1-x^2}}dx = (2-\delta_{n,0})(-i)^n J_n(\alpha). \tag{D.20}$$

Because the $J_n(x)$ decay exponentially for $n > x$ so do the expansion coefficients, $a_n(\alpha)$, decay exponentially for $n > \alpha$.

The complex Chebyschev polynomials $\phi_n(\omega) = T_n(-i\omega)$, $\omega \in [-i, i]$. The orthogonality relation for them is

$$\langle \phi_m, \phi_n\rangle = -i\int_{-i}^{i} \frac{\phi_m(\omega)\phi_n^*(\omega)}{\sqrt{1-|\omega|^2}}dx = \begin{cases} \frac{\pi}{2}\delta_{m,n} & \text{for } m \neq 0, \quad n \neq 0 \\ \pi & \text{for } m = n = 0 \end{cases} \tag{D.21}$$

They satisfy the following recursion relation

$$\phi_{n+1}(\omega) = 2\omega\phi_n(\omega) - \phi_{n-1}(\omega), \quad \phi_0(\omega) = 1, \quad \phi_1(\omega) = \omega. \tag{D.22}$$

We can expand functions in terms of the complex Chebychev polynomials $f(\omega) = \sum_{n=0}^{\infty} a_n\phi_n(\omega)$ and we obtain the expansion coefficients as

$$a_n = -i\int_{-i}^{i} \frac{\phi_n(\omega)f(\omega)}{\sqrt{1-|\omega|^2}}d\omega, \tag{D.23}$$

and in particular for an exponential function they are

$$a_n(\alpha) = -i\int_{-i}^{i} \frac{\phi_n^*(\omega)e^{\alpha\omega}}{\sqrt{1-|\omega|^2}}d\omega = (2-\delta_{n,0})J_n(\alpha). \tag{D.24}$$

E

Approximation Methods

E.1 Perturbation Theory

In time dependent perturbation theory the total Hamiltonian $\hat{\mathbf{H}}(t)$ is usually written in terms of an time independent unperturbed term, $\hat{\mathbf{H}}_0$, and an interaction term, $\hat{\mathbf{H}}_{int}(t)$, which is small compared to the unperturbed part. By this is meant that the eigenstates and eigenvalues of the unperturbed part are not significantly altered by the interaction,

$$\hat{\mathbf{H}}(t) = \hat{\mathbf{H}}_0 + \hat{\mathbf{H}}_{int}(t). \tag{E.1}$$

The eigenvalues and eigenvectors of $\hat{\mathbf{H}}_0$ are supposed to be known

$$\hat{\mathbf{H}}_0 \left|j\right\rangle = E_j \left|j\right\rangle, \quad \forall j. \tag{E.2}$$

It is convenient to transform our system to the interaction picture, or Dirac picture, which is achieved by the unitary transformation

$$\left|\psi\right\rangle_I = \hat{\mathbf{U}}_0^\dagger(t) \left|\psi\right\rangle = e^{i\hat{\mathbf{H}}_0 t} \left|\psi\right\rangle. \tag{E.3}$$

By applying the Schrödinger equation in the ket $\left|\psi\right\rangle_I$ in the interaction picture we arrive, using Eqs. (E.3) and (E.1), at the corresponding Hamiltonian in the interaction picture,

$$\begin{aligned} i\partial_t \left|\psi\right\rangle_I &= -\hat{\mathbf{H}}_0 \left|\psi\right\rangle_I + \hat{\mathbf{U}}_0^\dagger(t) i\partial_t \left|\psi\right\rangle \\ &= -\hat{\mathbf{H}}_0 \left|\psi\right\rangle_I + \hat{\mathbf{U}}_0^\dagger(t) \left(\hat{\mathbf{H}}_0 + \hat{\mathbf{H}}_{int}(t)\right) \hat{\mathbf{U}}_0(t)\hat{\mathbf{U}}_0^\dagger(t) \left|\psi\right\rangle \\ &= \hat{\mathbf{U}}_0^\dagger(t)\hat{\mathbf{H}}_{int}(t)\hat{\mathbf{U}}_0(t) \left|\psi\right\rangle_I \\ &\equiv \hat{\mathbf{H}}_I(t) \left|\psi\right\rangle_I, \end{aligned} \tag{E.4}$$

where use has been made of Eq. (E.1), $\hat{\mathbf{U}}_0^\dagger(t)\hat{\mathbf{U}}_0(t) = 1$ and the fact that any operator commutes with any function of itself, thus leading to cancellation of the first two terms. In

fact, any operator transforms in the same manner $\hat{\mathbf{O}}_I(t) = \hat{\mathbf{U}}_0^\dagger(t)\hat{\mathbf{O}}(t)\hat{\mathbf{U}}_0(t)$. Indeed they must in order for observables, $\left\langle \hat{\mathbf{O}}(t) \right\rangle_\psi$, to remain invariant under the transformation,

$$\left\langle \hat{\mathbf{O}} \right\rangle_\psi = \left\langle \psi \,\middle|\, \hat{\mathbf{O}} \,\middle|\, \psi \right\rangle = \left\langle \psi \,\middle|\, \hat{\mathbf{U}}_0(t)\hat{\mathbf{U}}^\dagger(t)\hat{\mathbf{O}}\hat{\mathbf{U}}_0(t)\hat{\mathbf{U}}_0^\dagger(t) \,\middle|\, \psi \right\rangle =_I \left\langle \psi \,\middle|\, \hat{\mathbf{O}}_I \,\middle|\, \psi \right\rangle_I \tag{E.5}$$

Formally we can write

$$|\psi(t)\rangle_I = \hat{\mathbf{U}}_I(t)\,|\psi(0)\rangle_I \tag{E.6}$$

By using Eqs. (E.4) and (E.6) we see that the evolution operator $\hat{\mathbf{U}}_I(t)$ satisfies a Schrödinger-like equation

$$i\partial_t \hat{\mathbf{U}}_I(t) = \hat{\mathbf{H}}_I(t)\hat{\mathbf{U}}_I(t), \tag{E.7}$$

which upon integration yields

$$\hat{\mathbf{U}}_I(t) = \hat{\mathbf{U}}_I(0) - i\int_0^t dt' \hat{\mathbf{H}}_I(t')\hat{\mathbf{U}}_I(t'). \tag{E.8}$$

This integral equation can be iteratively solved by inserting the expression for $\hat{\mathbf{U}}_I(t)$ in the right hand side of Eq. (E.8) and the identity $\hat{\mathbf{U}}_I(0) = 1$, resulting in the so called Dyson series

$$\begin{aligned} \hat{\mathbf{U}}_I(t) = 1 - i\int_0^t dt' \hat{\mathbf{H}}_I(t') + (-i)^2 \int_0^t \int_0^{t'} dt' dt'' \hat{\mathbf{H}}_I(t')\hat{\mathbf{H}}_I(t'') \\ + ... + (-i)^n \int_0^t ... \int_0^{t^{(n-1)}} dt' ... dt^{(n)} \hat{\mathbf{H}}_I(t') ... \hat{\mathbf{H}}_I(t^{(n)}). \end{aligned} \tag{E.9}$$

Assuming that initially our state is one of the eigenstates, k of $\hat{\mathbf{H}}_0$, $|\psi(0)\rangle_I = |k\rangle$ we obtain the expansion coefficient for the final state $|\psi(t)\rangle_I = \sum_j c_j(t)\,|j\rangle$ after interaction to zeroth and first order as

$$c_j^{(0)}(t) = \left\langle j \,\middle|\, \hat{\mathbf{U}}_0^{(0)}(t) \,\middle|\, k \right\rangle = \delta_{jk}, \tag{E.10a}$$

$$c_j^{(1)}(t) = \left\langle j \,\middle|\, \hat{\mathbf{U}}_I^{(1)}(t) \,\middle|\, k \right\rangle = \delta_{jk} - i\int_0^t dt' \left(H_I(t')\right)_{jk} e^{i\omega_{jk}t'}. \tag{E.10b}$$

E.2 Adiabatic picture

E.2.1 Obtaining the expansion coefficients

Consider the instantaneous eigenstates $|\psi_n(t)\rangle$ of a time-dependent Hamiltonian $\hat{\mathbf{H}}(t)$

$$\hat{\mathbf{H}}(t)\,|\psi_\iota(t)\rangle = E_\iota(t)\,|\psi_\iota(t)\rangle\,, \tag{E.11}$$

with instantaneous eigenenergies $E_\iota(t)$. Any state $|\Psi(t)\rangle$ can be expanded into the time-dependent eigenstates, $|\Psi(t)\rangle = \sum_\iota c_\iota e^{i\Theta_\iota(t)}\,|\psi_\iota(t)\rangle$, where $\Theta_\iota = -\int_{-\infty}^t E_\iota(t')dt'$. Inserting the expansion of $|\Psi(t)\rangle$ into the time-dependent Schrödinger equation,

$$i\partial_t\,|\psi(t)\rangle = \hat{\mathbf{H}}\,|\psi(t)\rangle\,, \tag{E.12}$$

and multiplying both sides by $\langle\psi_{\iota'}(t)|$, we obtain

$$\dot{c}_{\iota'}(t) = -c_{\iota'}(t)\left\langle\psi_{\iota'}(t)\,\middle|\,\dot{\psi}_{\iota'}(t)\right\rangle - \sum_{\iota\neq\iota'} c_{\iota}(t)e^{i\Delta\Theta_{\iota\iota'}(t)}\left\langle\psi_{\iota'}(t)\,\middle|\,\dot{\psi}_{\iota}(t)\right\rangle. \tag{E.13}$$

Differentiating Eq. (E.11) w.r.t. time, then multiplying with $\langle\psi_{\iota'}(t)|$ from the left and rearranging, we find

$$\left\langle\psi_{\iota'}(t)\,\middle|\,\dot{\psi}_{\iota}(t)\right\rangle = \frac{\left\langle\psi_{\iota'}(t)\,\middle|\,\partial_t\hat{\mathbf{H}}(t)\,\middle|\,\psi_{\iota}(t)\right\rangle}{E_{\iota}(t) - E_{\iota'}(t)}, \qquad \iota\neq\iota', \tag{E.14}$$

where we have used $\langle\psi_{\iota'}(t)\,|\,\psi_{\iota}(t)\rangle = \delta_{\iota'\iota}$. Assuming a nearly adiabatic dynamics, $|c_{\iota=0}(t)| \sim 1$ and $|c_{\iota}(t)| \ll 1, \iota \neq 0$. We can then write $c_0(t) \sim e^{i\gamma_0(t)}$, where $\gamma_0(t)$ is the Berry phase [112]. We can integrate Eq. (E.13),

$$c_{\iota'}(t) \approx \int_{-\infty}^{t} e^{i\gamma_0(t)}e^{i\Delta\Theta_{0\iota'}(t')}\frac{\left\langle\psi_{\iota'}(t')\,\middle|\,\partial_t\hat{\mathbf{H}}(t')\,\middle|\,\psi_0(t')\right\rangle}{E_{\iota'}(t') - E_0(t')}dt'. \tag{E.15}$$

In order to evaluate the expansion coefficient, Eq. (E.15) we need to make further approximations. In the following we will evaluate it in the low- and high field limits.

Evaluation of the expansion coefficient in the low-field limit

In order to evaluate the coefficient, Eq. (E.15) in the low-field limit, we make the approximation that $\Delta\Theta_{0\iota'}(t) \approx \Delta E_{\iota'0}t$, where $\Delta E_{\iota'0}$ is constant. In this approximation the state $|\psi_0(t)\rangle$ is going to be approximately the field-free ground state, and consequently the Berry phase is approximately zero [112]. This approximation is expected to work better for low interaction scattering, i.e. low χ_D, since the effect on the eigenenergies increases with χ_D. Within this approximation we may then write

$$c_{\iota'}(t) \approx \frac{D\varepsilon_0}{\Delta E_{\iota'0}}\left(\frac{\tau}{2}\right)^2\int_{-\infty}^{\infty} e^{i\Delta E_{\iota'0}t}\frac{2tdt}{\left(t^2 + \left(\frac{\tau}{2}\right)^2\right)^2}\left\langle\psi_{\iota'}\,|\cos\theta_a|\,\psi_0\right\rangle. \tag{E.16}$$

Making use of the Fourier relation between the transform of a function and its derivative

$$c_{\iota'}(t) \approx iD\varepsilon_0\left(\frac{\tau}{2}\right)^2\int_{-\infty}^{\infty}\frac{e^{i\Delta E_{\iota'0}t}dt}{\left(t + i\frac{\tau}{2}\right)\left(t - i\frac{\tau}{2}\right)}\left\langle\psi_{\iota'}\,|\cos\theta_a|\,\psi_{\iota=0}\right\rangle, \tag{E.17}$$

we obtain an expression that can be solved by Cauchy's integral formula

$$c_{\iota'}(t) \approx i\frac{\pi}{2}D\varepsilon_0\tau e^{-\frac{\Delta E\tau}{2}}\left\langle\psi_{\iota'}\,|\cos\theta_a|\,\psi_{\iota=0}\right\rangle. \tag{E.18}$$

In the low field limit we can use the field free states, i.e. $\iota = 0 \leftrightarrow j = 0$. In this limit we have $\Delta E_{\iota 0} = 2B$ and $\langle\cos\theta_a\rangle = \frac{1}{\sqrt{3}}$. The expansion coefficient is then

$$c_{\iota'}(t) \approx i\frac{\pi}{2\sqrt{3}}\chi_D\kappa e^{-\kappa}. \tag{E.19}$$

As an improvement to the field-free limit we consider the perturbative limit, in which we let the field-dressed states be described by a superposition of a minimal free-field basis. In this limit the lowest eigenvalues are $E_\pm = B\left(1 \pm \sqrt{1+\frac{\chi_D^2}{3}}\right)$, and consequently $\Delta E = 2B\sqrt{1+\frac{\chi_D^2}{3}}$. Therefore, letting $2B \to 2B\sqrt{1+\frac{\chi_D^2}{3}}$ in Eq. (E.18) we have

$$c_{\iota=2}(t) \approx i\frac{\pi}{2}\chi_D \kappa e^{-\kappa\sqrt{1+\frac{1}{3}\chi_D^2}} \langle \psi_{\iota=2} \,|\, \cos\theta_a \,|\, \psi_{\iota=0}\rangle \tag{E.20}$$

We will now proceed to calculate the transition moment. Consider the Hamiltonian Eq. (4.15). A minimal basis representation is given by the states $|0,0\rangle$ and $|1,0\rangle$, in which we can represent the Hamiltonian as

$$\hat{\mathbf{H}} \to \begin{pmatrix} 0 & V \\ V & 2B \end{pmatrix}. \tag{E.21}$$

Here $V = -\frac{D\varepsilon}{\sqrt{3}}$. The eigenvectors of the Hamiltonian Eq. (E.21) are

$$\psi_0 = \frac{1}{\sqrt{E_1^2+V^2}} \begin{pmatrix} E_2 \\ -V \end{pmatrix} \tag{E.22a}$$

and

$$\psi_1 = \frac{1}{\sqrt{E_0^2+V^2}} \begin{pmatrix} E_1 \\ -V \end{pmatrix} \tag{E.22b}$$

with the corresponding eigenvalues

$$E_0 = B - \sqrt{B^2+V^2} \tag{E.23a}$$

$$E_1 = B + \sqrt{B^2+V^2}, \tag{E.23b}$$

and consequently $\Delta E = 2\sqrt{B^2+V^2} = 2B\sqrt{1+\frac{\chi_D^2}{3}}$. Let's now evaluate some combinations of E_0 and E_1 that follow from Eq. (E.23). The sum of the eigenenergies is easily evaluated to be $E_0 + E_1 = 2B$, $E_0E_1 = -V^2$ and $E_0^2 + E_1^2 = 2\left(2B^2+V^2\right)$. The representation of the transition operator in the minimal field free basis is

$$\cos\theta_a = \frac{1}{\sqrt{3}} \begin{pmatrix} 0 & 1 \\ 1 & 0 \end{pmatrix}. \tag{E.24}$$

Now let's consider the transition moment,

$$\begin{aligned} \langle \psi_{\iota'=2} \,|\, \cos\theta_a \,|\, \psi_{\iota=0}\rangle &= \frac{1}{\sqrt{\left(E_0^2+V^2\right)\left(E_1^2+V^2\right)}} \begin{pmatrix} E_0, & V \end{pmatrix} \frac{1}{\sqrt{3}} \begin{pmatrix} 0 & 1 \\ 1 & 0 \end{pmatrix} \begin{pmatrix} E_1 \\ V \end{pmatrix} \\ &= \frac{V\left(E_0+E_1\right)}{\sqrt{3}\sqrt{\left(E_0^2+V^2\right)\left(E_1^2+V^2\right)}} \\ &= \frac{2BV}{\sqrt{3}\sqrt{4V^2}\sqrt{B^2+V^2}} \\ &= \frac{1}{\sqrt{3}\sqrt{1+\frac{\chi_D^2}{3}}}. \end{aligned} \tag{E.25}$$

Using this result for the transition moment in Eq. (E.20), we obtain the expansion coefficient

$$c_{\iota=2}(t) \approx= i\frac{\pi}{2}\frac{\chi_D\kappa}{\sqrt{1+\frac{\chi_D^2}{3}}}e^{-\kappa\sqrt{1+\frac{1}{3}\chi_D^2}}, \tag{E.26}$$

which is our final result in the low-field limit.

High field limit of the polar Hamiltonian

In the high field limit the molecule is forced to align with the external field. The remaining kinetic energy fights the field and the molecule describes so called librating motion, i.e. restrained rotation. The trigonometric functions in the Laplacian and in the interaction term can be approximated by $\cos\theta \approx 1-\frac{\theta^2}{2}$ and $\sin\theta \approx \theta$. The Hamiltonian is now approximately

$$\hat{\mathbf{H}} = -B\left(\frac{1}{\theta}\frac{\partial}{\partial\theta}\left(\theta\frac{\partial}{\partial\theta}\right)+\frac{1}{\theta^2}\frac{\partial^2}{\partial\phi^2}\right)+\frac{1}{2}D\varepsilon\theta^2 - D\varepsilon, \tag{E.27}$$

i.e. the polar angle θ takes the role of the radial coordinate in 2D-polar coordinates and the azimutal angle ϕ that of the standard polar angle. Assuming a separation of variables $\psi(\theta,\phi) = g(\theta)e^{im\phi}$, the function $g(\theta)$ satisfies

$$g''(\theta)+\frac{1}{\theta}g'(\theta)+\left(\tilde{E}-\frac{1}{\theta^2}m^2-\frac{1}{2}\chi\theta^2\right)g = 0, \tag{E.28}$$

where $\tilde{E} = \frac{E}{B}+\chi$. Considering Eq. (E.28) for large θ where terms 2 and 4 are negligible we obtain $g(\theta) \sim \exp\left(-\frac{\theta^2}{2\theta_0^2}\right)$, where $\frac{1}{\theta_0^2} = \sqrt{\frac{\chi_D}{2}}$. Therefore, a suitable ansatz is $g(\theta) = h(\theta)\exp\left(-\frac{\theta^2}{2\theta_0^2}\right)$. We are interested in the two lowest, even solutions to this equation, i.e., $m = 0$. It can be seen, by insertion into Eq. (E.28), that the two functions $h_0(\theta) = 1$ and $h_2(\theta) = \left(\frac{\theta}{\theta_0}\right)^2 - 1$ are solutions, provided

$$\frac{1}{\theta_0^2} = \sqrt{\frac{1}{2}\chi_D}, \tag{E.29}$$

and the corresponding eigenvalues are $\tilde{E}_0 = \sqrt{2\chi_D}$ and $\tilde{E}_2 = 3\sqrt{2\chi_D}$. According to Sturm-Liouville theory the equation (E.28) is not in self-adjoint form, but the integrating factor is simply θ. The standard integration interval would be $[0,\infty]$, but we have $\theta \in [0,\pi]$. If, however, $\theta_0 \ll \pi$ we may approximately let $\pi \to \infty$. Then, the eigenfunctions are orthonormal with respect to the inner product

$$\langle\psi_1,\psi_2\rangle = \int_0^{2\pi}\int_0^{\infty}\psi_1^*(\theta,\phi)\psi_2(\theta,\phi)\theta d\theta d\phi \tag{E.30}$$

and are given by

$$\psi_0^0(\theta,\phi) = \frac{1}{\sqrt{\pi\theta_0^2}}\exp\left(-\frac{\theta^2}{2\theta_0^2}\right), \tag{E.31a}$$

$$\psi_2^0(\theta,\phi) = \frac{\left(\frac{\theta}{\theta_0}\right)^2 - 1}{\sqrt{\pi\theta_0^2}} \exp\left(-\frac{\theta^2}{2\theta_0^2}\right), \tag{E.31b}$$

with the corresponding eigenvalues

$$E_{0,0} + D\varepsilon = \sqrt{2BD\varepsilon}, \tag{E.32a}$$

$$E_{0,2} + D\varepsilon = 3\sqrt{2BD\varepsilon}. \tag{E.32b}$$

We therefore see that the zero-point energy in the harmonic limit is

$$\omega_H = \sqrt{2DB\varepsilon}. \tag{E.33}$$

In order to evaluate the matrix element of $\cos\theta \approx 1 - \frac{\theta^2}{2}$ in the harmonic limit,notice that for $n = 2k \quad k = 0, 1, 2, 3...$

$$\frac{2}{\theta_0^2}\int_0^\infty \theta^n \theta e^{-\frac{\theta^2}{\theta_0^2}} d\theta = n!! \left(\frac{\theta_0^2}{2}\right)^{\frac{n}{2}}. \tag{E.34}$$

Therefore,

$$\begin{aligned}\left\langle 2,0 \left| -\frac{\theta^2}{2} \right| 0,0 \right\rangle &= -\frac{1}{2}\frac{2}{\theta_0^2}\int_0^\infty \left(\left(\frac{\theta}{\theta_0}\right)^2 - 1\right)\theta^3 \exp\left(-\frac{\theta^2}{\theta_0^2}\right) d\theta \\ &= -\frac{1}{2}\left(\frac{4!!}{\theta_0^2}\left(\frac{\theta_0^2}{2}\right)^2 - 2!!\frac{\theta_0^2}{2}\right) = -\frac{1}{2}\theta_0^2\end{aligned} \tag{E.35}$$

E.2.2 The Berry and dynamical phases

In the adiabatic limit the second term of Eq. (E.13) tends to zero and we are left with a separable differential equation for $c_{\iota=0}(t)$, which has the solution ($c_{\iota=0}(t=0) = 1$)

$$c_{\iota=0}(t) = e^{i\int_{-t_0}^{t_0} \langle \psi_{\iota=0}(t) \,|\, \dot{\psi}_{\iota=0}(t)\rangle \, dt} \equiv e^{i\gamma_0}. \tag{E.36}$$

From Eq. (E.31a), $\psi_0^0(\theta,\phi) = \frac{1}{\sqrt{\pi\theta_0^2}} \exp\left(-\frac{\theta^2}{2\theta_0^2}\right)$, with eigenvalue $E_0 = \sqrt{2BD\varepsilon}$, and therefore

$$\begin{aligned}\gamma_0(t) &= \sqrt{2D\varepsilon_0 B}\frac{\tau}{2}\int_{t_0}^{t} \frac{dt'}{\sqrt{t'^2 + \left(\frac{\tau}{2}\right)^2}} \\ &= \sqrt{2D\varepsilon_0 B}\frac{\tau}{2}\ln\left(\frac{t + \sqrt{t^2 + \left(\frac{\tau}{2}\right)^2}}{t_0 + \sqrt{t_0^2 + \left(\frac{\tau}{2}\right)^2}}\right).\end{aligned} \tag{E.37}$$

The dynamical phase, $\Theta_{0,\iota'}$ is

$$\begin{aligned}\Theta_{0,\iota'}(t) &= 2\sqrt{2D\varepsilon_0 B}\frac{\tau}{2}\int_{t_0}^{t} \frac{dt'}{\sqrt{t'^2 + \left(\frac{\tau}{2}\right)^2}} \\ &= 2\sqrt{2D\varepsilon_0 B}\frac{\tau}{2}\ln\left(\frac{t + \sqrt{t^2 + \left(\frac{\tau}{2}\right)^2}}{t_0 + \sqrt{t_0^2 + \left(\frac{\tau}{2}\right)^2}}\right)\end{aligned} \tag{E.38}$$

Combining Eqs. (E.37) and (E.38), we obtain the total phase

$$\gamma_0(t) + \Theta_{0,\iota'}(t) = 3\omega_H \frac{\tau}{2} \ln\left(\frac{t + \sqrt{t^2 + \left(\frac{\tau}{2}\right)^2}}{t_0 + \sqrt{t_0^2 + \left(\frac{\tau}{2}\right)^2}}\right), \tag{E.39}$$

where we have used Eq. (E.33) for the harmonic zero point energy.

E.2.3 The matrix element

The non-phase part of the derivative is

$$\begin{aligned}\frac{\left\langle \iota' \left| \frac{\partial \hat{\mathbf{H}}(t)}{\partial t} \right| 0 \right\rangle}{\Delta E_{\iota',0}(t)} &= -D\frac{d\varepsilon(t)}{dt}\frac{\langle \iota' \,|\, \cos\theta_a(t) \,|\, 0\rangle}{\Delta E_{\iota',0}(t)} = -2D\varepsilon_0 \left(\frac{\tau}{2}\right)^2 \frac{t}{\left(t^2 + \left(\frac{\tau}{2}\right)^2\right)^2} \frac{\theta_0^2}{2} \frac{\sqrt{t^2 + \left(\frac{\tau}{2}\right)^2}}{2\sqrt{2D\varepsilon_0 B}\frac{\tau}{2}} \\ &= -\sqrt{\frac{\chi_D}{2}}\frac{\tau}{2}\frac{t}{\left(t^2 + \left(\frac{\tau}{2}\right)^2\right)^{3/2}}\frac{\theta_0^2}{2} = -\frac{1}{2}\frac{t}{\left(t^2 + \left(\frac{\tau}{2}\right)^2\right)},\end{aligned} \tag{E.40}$$

where in the last line we have used $\theta_0^2 = \sqrt{\frac{2}{\chi_D}}\frac{\sqrt{t^2+\left(\frac{\tau}{2}\right)^2}}{\tau/2}$. It is remarkable that this expression becomes independent on the dipole moment, rotational constant and field strength. Notice also, that our expression, the angle increases without bound as the field diminishes. Combining Eqs. (E.35), (E.39) and (E.40) we obtain for the expansion coefficient in the high field limit

$$c_2^0(t) = -\frac{1}{2}\int_{t_0}^{t} \frac{t}{t'^2 + \left(\frac{\tau}{2}\right)^2} \exp\left(i3\omega_H \frac{\tau}{2} \ln\left(\frac{t' + \sqrt{t'^2 + \left(\frac{\tau}{2}\right)^2}}{t_0 + \sqrt{t_0^2 + \left(\frac{\tau}{2}\right)^2}}\right)\right) dt'. \tag{E.41}$$

E.2.4 Basis set comparison

In the low-field limit we have made the approximation that the field-dressed states can be represented by a minimal basis consisting of two field-free states. We now address the issue of convergence of the minimal basis. Keeping in mind our previous finding that $\kappa = 1$ at around a scattering energy of $E \approx 1.5$ eV, i.e. we expect to have adiabatic dynamics for scattering energies below 1.5 eV. Looking at the energy differences as a function of scattering energy for different sizes of the field-free states used to form the field-dressed states we see that two field-free states ($N = 2$) are not sufficient to reproduce the converged energy difference, $N = 5$, see Figure E.1. We see that the energy difference is overestimated by $N = 2$. We notice that already at $N = 3$ can the energy difference be approximately achieved.

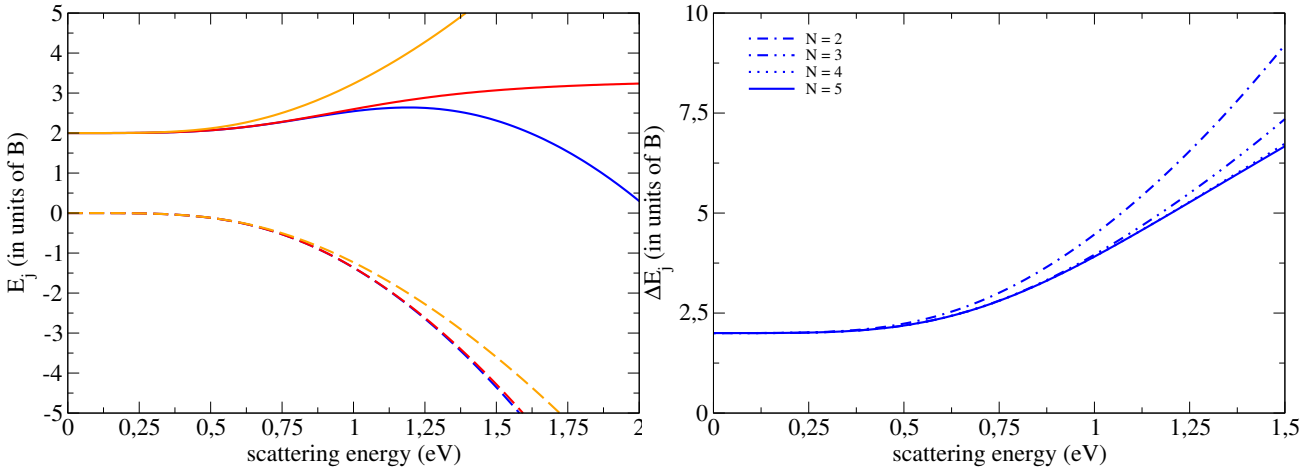

Figure E.1: Comparison of the eigenenergies for different numbers of field-free states, N, used as basis set to represent the field-dressed states as function of scattering energy for the HD^+ ion. Left panel: Rotational eigen-energies as a function of the scattering energy. Striped lines indicate the ground state $J = 0$ and the solid lines indicate the state $J = 1$. Blue lines use a basis of $N = 5$ free-field states, red $N = 3$ and orange $N = 2$. Right panel: Energy difference between the first two field dressed states using different numbers of field-free states, (N), to represent them.

F

Evaluation of integrals

F.1 Evaluation of $f(\kappa) = \int_{-\pi/2}^{\pi/2} \cos u e^{i3\kappa \tan u} du$

We wish to evaluate the integral

$$f(\kappa) = \int_{-\pi/2}^{\pi/2} \cos u e^{i3\kappa \tan u} du. \tag{F.1}$$

First notice that

$$f(0) = \int_{-\pi/2}^{\pi/2} \cos u du = 2. \tag{F.2}$$

We continue by considering the derivative of $f(\kappa)$ with respect to κ and make use of Leibniz' rule of differentiating under the integral

$$f'(\kappa) = 3i \int_{-\pi/2}^{\pi/2} \cos u \tan u e^{i3\kappa \tan u} du = 3i \int_{-\pi/2}^{\pi/2} \sin u e^{i3\kappa \tan u} du. \tag{F.3}$$

Next we integrate by parts and using $\cos u e^{3i\kappa \tan u}\big|_{-\pi/2}^{\pi/2} = 0$ we get

$$\begin{aligned} f'(\kappa) &= -9\kappa \int_{-\pi/2}^{\pi/2} \cos u (1 + \tan^2 u) e^{i3\kappa \tan u} du \\ &= -9\kappa f(\kappa) - 9\kappa \frac{1}{(3i)^2} \frac{d^2 f(\kappa)}{d\kappa^2} \\ &= \kappa \frac{d^2 f(\kappa)}{d\kappa^2} - 9\kappa f(\kappa), \end{aligned} \tag{F.4}$$

where in the second line we have made use of $\frac{1}{3i} \frac{\partial}{\partial \kappa} e^{i3\kappa \tan u} = \tan u e^{i3\kappa \tan u}$. So, $f(\kappa)$ satisfies the differential equation

$$f''(\kappa) - \frac{1}{\kappa} f'(\kappa) - 9f(\kappa) = 0. \tag{F.5}$$

Notice, that for large κ, the middle term is suppressed by the $\frac{1}{\kappa}$ dependence, and hence in this limit

$$f''(\kappa) - 9f(\kappa) = 0 \tag{F.6}$$

with the solutions $f(\kappa) = Ae^{3\kappa} + Be^{-3\kappa}$. Since we are looking for square integrable functions that are finite for $\kappa \to \infty$, we must require $A = 0$. Our ansatz is therefore to look for $f(\kappa) = Bg(\kappa)e^{-3\kappa}$, where $g(\kappa)$ is to be found. From Eq. (F.5) we arrive at the differential equation for $g(\kappa)$,

$$\kappa g''(\kappa) - (1 + 6\kappa)\, g'(\kappa) + 3g(\kappa) = 0. \tag{F.7}$$

We make the ansatz

$$\begin{cases} g(\kappa) = \sqrt{1+6\kappa} \\ g'(\kappa) = \frac{3}{\sqrt{1+6\kappa}} \\ g''(\kappa) = -\frac{9}{\sqrt{1+6\kappa}^3} \end{cases} \tag{F.8}$$

from which

$$3g(\kappa) - (1 + 6\kappa)\, g'(\kappa) = 0 \tag{F.9}$$

follows. We have therefore approximately solved the integral as long as the second derivative term $-\frac{9\kappa}{\sqrt{1+6\kappa}^3} \approx 0$. With this functional form and Eq. (F.2) we obtain $B = 2$, with the final result

$$f(\kappa) \approx 2\sqrt{1+6\kappa}e^{-3\kappa}. \tag{F.10}$$

The approximation becomes exact when $\kappa \to 0$ and $\kappa \to \infty$ and the error $-\frac{9\kappa}{\sqrt{1+6\kappa}^3}$ has an extremum at $\kappa = \frac{1}{3}$, where the absolute value of the error is $\frac{1}{\sqrt{3}} \approx 0.58$.

F.2 Evaluation of $\left\langle \varepsilon_0^2 \right\rangle_{CC}$

Let $r = \frac{1}{2E}$. With wxmaxima we evaluate

$$\begin{aligned} \left\langle \varepsilon_0^2 \right\rangle_{CC} &= \frac{2}{b_{max}^2} \int_0^{b_{max}} \frac{bdb}{\left(r + \sqrt{r^2+b^2}\right)^4} \\ &= \frac{2}{b_{max}^2} \left(\frac{-3b_{max}^4 + \sqrt{b_{max}^2 + r^2}\left(8b_{max}^2 r + 8r^3\right) - 12b_{max}^2 r^2 - 3r^4}{6b_{max}^6} + \frac{1}{12r^2} \right) \end{aligned} \tag{F.11}$$

With $b_{max} \gg r$, the main contribution from the first term in the parenthesis is $-\frac{1}{2b_{max}^2} \ll \frac{1}{12r^2}$. Therefore,

$$\left\langle \varepsilon_0^3 \right\rangle_{CC} \approx \frac{2}{b_{max}^2} \frac{1}{12r^2} = \frac{2}{3b_{max}^2} E^2. \tag{F.12}$$

F.3 Evaluation of $\langle \varepsilon_0^3 \rangle_{CC}$

Let $r = \frac{1}{2E}$. With wxmaxima we evaluate

$$\begin{aligned}\langle \varepsilon_0^3 \rangle_{CC} &= \frac{2}{b_{max}^2} \int_0^{b_{max}} \frac{bdb}{\left(r + \sqrt{r^2 + b^2}\right)^6} \\ &= \frac{2}{b_{max}^2} \left(\frac{-5b_{max}^6 + \sqrt{b_{max}^2 + r^2}\left(24b_{max}^4 r + 88b_{max}^2 r^3 + 64r^5\right) - 60b_{max}^4 r^2 - 120b_{max}^2 r^4 - 64r^6}{20b_{max}^{10}} + \frac{3}{320r^4} \right)\end{aligned} \tag{F.13}$$

With $b_{max} \gg r$, the main contribution from the first term in the parenthesis is $-\frac{1}{4b_{max}^4} \ll \frac{3}{320r^4}$. Therefore,

$$\langle \varepsilon_0^3 \rangle_{CC} \approx \frac{2}{b_{max}^2} \frac{3}{320r^4} = \frac{3}{10b_{max}^2} E^4. \tag{F.14}$$

F.4 Evaluation of $\langle \varepsilon_0^4 \rangle_{CC}$

Let $r = \frac{1}{2E}$. With wxmaxima we evaluate

$$\begin{aligned}\langle \varepsilon_0^4 \rangle_{CC} &= \frac{2}{b_{max}^2} \int_0^{b_{max}} \frac{bdb}{\left(r + \sqrt{r^2 + b^2}\right)^8} \\ &= \frac{2}{b_{max}^2} \times \\ &\left(\frac{-7b_{max}^8 + \sqrt{b_{max}^2 + r^2}\left(48b_{max}^6 r + 368b_{max}^4 r^3 + 704b_{max}^2 r^5 + 384r^7\right) - 168b_{max}^6 r^2 - 672b_{max}^4 r^4 - 896b_{max}^2 r^6 - 64r^8}{42b_{max}^{14}} + \right. \\ &\left. \frac{1}{672r^6} \right)\end{aligned} \tag{F.15}$$

With $b_{max} \gg r$, the main contribution from the first term in the parenthesis is $-\frac{1}{6b_{max}^6} \ll \frac{1}{672r^6}$. Therefore,

$$\langle \varepsilon_0^4 \rangle_{CC} \approx \frac{2}{b_{max}^2} \frac{1}{672r^6} = \frac{4}{21b_{max}^2} E^6. \tag{F.16}$$

F.5 Evaluation of $\langle \delta E_L \rangle_{CC}$

Notice that $\langle \delta E_L \rangle_{CC} = \frac{2\xi}{(1+\xi)^2}(1 - \langle \cos\theta_{sc} \rangle_{CC}) E_L$, so in order to evaluate $\langle \delta E_L \rangle_{CC}$ we need to find $\langle \cos\theta_{sc} \rangle_{CC}$, and the result is

$$\begin{aligned}\langle \cos\theta_{sc} \rangle_{CC} &= \frac{2}{b_{max}^2} \int_0^{b_{max}} b \cos\left(2\sin^{-1}\left(\frac{1}{\sqrt{1 + (2Eb)^2}}\right)\right) db \\ &= -\frac{1}{2(Eb_{max})^2} \ln\left(1 + (2Eb_{max})^2\right) - 1\end{aligned} \tag{F.17}$$

$$\langle \delta E_L \rangle_{CC} = \frac{2\xi}{(1+\xi)^2} \left(1 - \langle \cos\theta_{sc} \rangle_{CC}\right) E_L = \frac{\xi}{(1+\xi)^2} \frac{\ln\left(1 + (2Eb_{max})^2\right)}{(Eb_{max})^2} E_L \tag{F.18}$$

We can cast this into an expression of the CM-energy by Eq. (4.4)

$$\langle \delta E \rangle_{CC} = \frac{\xi}{(1+\xi)^2} \frac{\ln\left(1+(2Eb_{max})^2\right)}{Eb_{max}^2} \tag{F.19}$$

F.6 An estimate of an average of $\sigma(E)$ in the single ion cooling scenario

The average of $\sigma(E) = \sqrt{\frac{E}{\mu\omega^2}}$ in the single ion cooling scenario, from an initial scattering energy E_{max} to a final scattering energy E_{min}, can be estimated by

$$\tilde{\sigma} = \frac{1}{N} \int_{E_{min}}^{E_{max}} \sigma(E) n(E)\, dE, \tag{F.20}$$

where the total number of collisions is

$$N = \int_{E_{min}}^{E_{max}} n(E)\, dE \tag{F.21}$$

and $n(E)$ is given by Eq. (4.63), i.e. we will approximate $n(E)\, dE \approx \frac{(1+\xi)^2\sigma^2 E}{\xi \log((2\sigma E)^2+1)}\, dE$. Since the logarithm changes slowly compared to other factors in the integrand we will treat it as a constant, $\frac{1}{\log(\tilde{x}^2+1)}$, for some $2\sigma(E_{min})E_{min} < \tilde{x} < 2\sigma(E_{max})E_{max}$. With this approximation we arrive at

$$N \approx \frac{\alpha}{3}\left(E_{max}^3 - E_{min}^3\right), \tag{F.22}$$

where $\alpha = \frac{(1+\xi)^2}{\xi} \frac{1}{\mu\omega^2} \frac{1}{\log(\tilde{x}^2+1)}$. Now, Eq. (F.20) becomes

$$\tilde{\sigma} \approx \frac{\frac{2\alpha}{7}\sqrt{\frac{1}{\mu\omega^2}}\left(E_{max}^{7/2} - E_{min}^{7/2}\right)}{\frac{\alpha}{3}\left(E_{max}^3 - E_{min}^3\right)}. \tag{F.23}$$

Assuming that the lower energy is much smaller than the maximum, or $E_{min} \to 0$, we obtain

$$\tilde{\sigma} \approx \frac{6}{7}\sqrt{\frac{1}{\mu\omega^2}} E_{max}^{1/2} = \frac{6}{7}\sigma(E_{max}). \tag{F.24}$$

List of Figures

List of Tables

Bibliography

[1] A. A. Michelson and E. W. Morley, "LVIII. On the relative motion of the earth and the luminiferous æther," *The London, Edinburgh, and Dublin Philosophical Magazine and Journal of Science*, vol. 24, no. 151, pp. 449–463, 1887.

[2] B. H. Brandsen and C. J. Joachain, *Quantum Mechanics, Second edition.* Prentice Hall, 2000.

[3] N. F. Ramsey, *Molecular Beams.* Oxford University Press, 1956.

[4] I. I. Rabi, "Space quantization in a gyrating magnetic field," *Physical Review*, vol. 51, no. 8, p. 652, 1937.

[5] C. J. Foot, *Atomic physics*, vol. 7. Oxford University Press, 2005.

[6] N. F. Ramsey, "A molecular beam resonance method with separated oscillating fields," *Physical Review*, vol. 78, no. 6, p. 695, 1950.

[7] D. J. Tannor and S. A. Rice, "Control of selectivity of chemical reaction via control of wave packet evolution," *The Journal of Chemical Physics*, vol. 83, no. 10, pp. 5013–5018, 1985.

[8] D. J. Tannor, R. Kosloff, and S. A. Rice, "Coherent pulse sequence induced control of selectivity of reactions: Exact quantum mechanical calculations," *The Journal of Chemical Physics*, vol. 85, no. 10, pp. 5805–5820, 1986.

[9] M. Shapiro and P. Brumer, "Laser control of product quantum state populations in unimolecular reactions," *The Journal of Chemical Physics*, vol. 84, no. 7, pp. 4103–4104, 1986.

[10] M. Shapiro, J. W. Hepburn, and P. Brumer, "Simplified laser control of unimolecular reactions: Simultaneous (ω_1, ω_3) excitation," *Chemical Physics Letters*, vol. 149, no. 5-6, pp. 451–454, 1988.

[11] A. P. Peirce, M. A. Dahleh, and H. Rabitz, "Optimal control of quantum-mechanical systems: Existence, numerical approximation, and applications," *Physical Review A*, vol. 37, pp. 4950–4964, Jun 1988.

[12] Y. Silberberg, "Quantum coherent control for nonlinear spectroscopy and microscopy," *Annual review of physical chemistry*, vol. 60, pp. 277–292, 2009.

[13] D. Goswami, "Optical pulse shaping approaches to coherent control," *Physics Reports*, vol. 374, no. 6, pp. 385–481, 2003.

[14] M. Guesmi, P. Veselá, and K. Žídek, "Targeted generation of complex temporal pulse profiles," *Scientific reports*, vol. 12, no. 1, pp. 1–12, 2022.

[15] S. J. Glaser, U. Boscain, T. Calarco, C. P. Koch, W. Köckenberger, R. Kosloff, I. Kuprov, B. Luy, S. Schirmer, T. Schulte-Herbrüggen, *et al.*, "Training Schrödinger's cat: quantum optimal control," *The European Physical Journal D*, vol. 69, no. 12, pp. 1–24, 2015.

[16] A. Acín, I. Bloch, H. Buhrman, T. Calarco, C. Eichler, J. Eisert, D. Esteve, N. Gisin, S. J. Glaser, F. Jelezko, S. Kuhr, M. Lewenstein, M. F. Riedel, P. O. Schmidt, R. Thew, A. Wallraff, I. Walmsley, and F. K. Wilhelm, "The quantum technologies roadmap: a European community view," *New Journal of Physics*, vol. 20, p. 080201, aug 2018.

[17] W. P. Schleich, K. S. Ranade, C. Anton, M. Arndt, M. Aspelmeyer, M. Bayer, G. Berg, T. Calarco, H. Fuchs, E. Giacobino, *et al.*, "Quantum technology: from research to application," *Applied Physics B*, vol. 122, no. 5, p. 130, 2016.

[18] M. A. Lombardi, T. P. Heavner, and S. R. Jefferts, "NIST primary frequency standards and the realization of the SI second," *NCSLI Measure*, vol. 2, no. 4, pp. 74–89, 2007.

[19] P. R. Berman, ed., *Atom Interferometry*. Academic Press, 1997.

[20] https://www.npl.co.uk/insights/atomic-clocks-in-emerging-quantum-industries, 2022 (accessed November 11, 2022).

[21] A. D. Ludlow, "An optical clock to go," *Nature Physics*, vol. 14, no. 5, pp. 431–432, 2018.

[22] J. Grotti, S. Koller, S. Vogt, S. Häfner, U. Sterr, C. Lisdat, H. Denker, C. Voigt, L. Timmen, A. Rolland, *et al.*, "Geodesy and metrology with a transportable optical clock," *Nature Physics*, vol. 14, no. 5, pp. 437–441, 2018.

[23] C. L. Degen, F. Reinhard, and P. Cappellaro, "Quantum sensing," *Review of Modern Physics*, vol. 89, p. 035002, Jul 2017.

[24] I. Kortunov, S. Alighanbari, M. Hansen, G. Giri, V. Korobov, and S. Schiller, "Proton–electron mass ratio by high-resolution optical spectroscopy of ion ensembles in the resolved-carrier regime," *Nature physics*, vol. 17, no. 5, pp. 569–573, 2021.

[25] M. S. Safronova, D. Budker, D. DeMille, D. F. J. Kimball, A. Derevianko, and C. W. Clark, "Search for new physics with atoms and molecules," *Reviews of Modern Physics*, vol. 90, p. 025008, Jun 2018.

[26] K. Højbjerre, A. K. Hansen, P. S. Skyt, P. F. Staanum, and M. Drewsen, "Rotational state resolved photodissociation spectroscopy of translationally and vibrationally cold MgH^+ ions: toward rotational cooling of molecular ions," *New Journal of Physics*, vol. 11, no. 5, p. 055026, 2009.

[27] R. Krems, B. Friedrich, and W. Stwalley, *Cold Molecules: Theory, Experiment, Applications*. CRC Press, 2009.

[28] L. Santos, G. Shlyapnikov, P. Zoller, and M. Lewenstein, "Bose-Einstein condensation in trapped dipolar gases," *Physical Review Letters*, vol. 85, no. 9, p. 1791, 2000.

[29] K. Ohmori, "Wave-Packet and Coherent Control Dynamics," *Annual Review of Physical Chemistry*, vol. 60, pp. 487–511, 2009.

[30] K. Ohmori, H. Katsuki, H. Chiba, M. Honda, Y. Hagihara, K. Fujiwara, Y. Sato, and K. Ueda, "Real-time observation of phase-controlled molecular wave-packet interference," *Physical Review Letters*, vol. 96, p. 093002, Mar 2006.

[31] H. Katsuki, K. Hosaka, H. Chiba, and K. Ohmori, "Read and write amplitude and phase information by using high-precision molecular wave-packet interferometry," *Physical Review A*, vol. 76, p. 013403, Jul 2007.

[32] N. F. Scherer, R. J. Carlson, A. Matro, M. Du, A. J. Ruggiero, V. Romero-Rochin, J. A. Cina, G. R. Fleming, and S. A. Rice, "Fluorescencedetected wave packet interferometry: Time resolved molecular spectroscopy with sequences of femtosecond phaselocked pulses," *The Journal of Chemical Physics*, vol. 95, no. 3, pp. 1487–1511, 1991.

[33] N. F. Scherer, A. Matro, L. D. Ziegler, M. Du, R. J. Carlson, J. A. Cina, and G. R. Fleming, "Fluorescence-detected wave packet interferometry. II. Role of rotations and determination of the susceptibility," *The Journal of Chemical Physics*, vol. 96, no. 6, pp. 4180–4194, 1992.

[34] V. V. Albert, J. P. Covey, and J. Preskill, "Robust encoding of a qubit in a molecule," *Physical Review X*, vol. 10, p. 031050, Sep 2020.

[35] D. DeMille, "Quantum computation with trapped polar molecules," *Physical Review Letters*, vol. 88, no. 6, p. 067901, 2002.

[36] O. Dulieu and A. Osterwalder, *Cold chemistry: molecular scattering and reactivity near absolute zero*. Royal Society of Chemistry, 2017.

[37] A. D. Dörfler, E. Yurtsever, P. Villarreal, T. González-Lezana, F. A. Gianturco, and S. Willitsch, "Rotational-state-changing collisions between N_2^+ and Rb at low energies," *Phys. Rev. A*, vol. 101, p. 012706, Jan 2020.

[38] A. D. Dörfler, P. Eberle, D. Koner, M. Tomza, M. Meuwly, and S. Willitsch, "Long-range versus short-range effects in cold molecular ion-neutral collisions," *Nature communications*, vol. 10, no. 1, pp. 1–10, 2019.

[39] P. Rabl, D. DeMille, J. M. Doyle, M. D. Lukin, R. Schoelkopf, and P. Zoller, "Hybrid quantum processors: molecular ensembles as quantum memory for solid state circuits," *Physical Review Letters*, vol. 97, no. 3, p. 033003, 2006.

[40] P. Peter Atkins and J. De Paula, *Atkins' Physical Chemistry*. Oxford University Press, 2014.

[41] T. Seideman, "Rotational excitation and molecular alignment in intense laser fields," *The Journal of Chemical Physics*, vol. 103, no. 18, pp. 7887–7896, 1995.

[42] H. Stapelfeldt and T. Seideman, "Colloquium: Aligning molecules with strong laser pulses," *Review of Modern Physics*, vol. 75, no. 2, p. 543, 2003.

[43] C. P. Koch, M. Lemeshko, and D. Sugny, "Quantum control of molecular rotation," *Reviews of Modern Physics*, vol. 91, no. 3, p. 035005, 2019.

[44] K. Mølhave and M. Drewsen, "Formation of translationally cold MgH^+ and MgD^+ molecules in an ion trap," *Physical Review A*, vol. 62, no. 1, p. 011401, 2000.

[45] S. Willitsch, M. T. Bell, A. D. Gingell, and T. P. Softley, "Chemical applications of laser- and sympathetically-cooled ions in ion traps," *Physical Chemistry Chemical Physics*, vol. 10, pp. 7200–7210, 2008.

[46] B. Roth and S. Schiller, *Sympathetically cooled molecular ions: From principles to first applications*. 01 2009.

[47] A. K. Hansen, O. O. Versolato, L. Kłosowski, S. B. Kristensen, A. Gingell, M. Schwarz, A. Windberger, J. Ullrich, J. R. C. López-Urrutia, and M. Drewsen, "Efficient rotational cooling of Coulomb-crystallized molecular ions by a helium buffer gas," *Nature*, vol. 508, pp. 76–79, April 2014.

[48] P. F. Staanum, K. Højbjerre, P. S. Skyt, A. K. Hansen, and M. Drewsen, "Rotational laser cooling of vibrationally and translationally cold molecular ions," *Nature Physics*, vol. 6, no. 4, pp. 271–274, 2010.

[49] P. Bowe, L. Hornekær, C. Brodersen, M. Drewsen, J. Hangst, and J. Schiffer, "Sympathetic crystallization of trapped ions," *Physical Review Letters*, vol. 82, no. 10, p. 2071, 1999.

[50] I. S. Vogelius, L. B. Madsen, and M. Drewsen, "Rotational cooling of molecular ions through laser-induced coupling to the collective modes of a two-ion Coulomb crystal," *Journal of Physics B: Atomic, Molecular and Optical Physics*, vol. 39, pp. S1267–S1280, sep 2006.

[51] S. Schiller and V. Korobov, "Tests of time independence of the electron and nuclear masses with ultracold molecules," *Physical Review A*, vol. 71, p. 032505, Mar 2005.

[52] S. Alighanbari, G. Giri, F. L. Constantin, V. Korobov, and S. Schiller, "Precise test of quantum electrodynamics and determination of fundamental constants with HD^+ ions," *Nature*, vol. 581, no. 7807, pp. 152–158, 2020.

[53] D. Schuster, L. S. Bishop, I. Chuang, D. DeMille, and R. Schoelkopf, "Cavity QED in a molecular ion trap," *Physical Review A*, vol. 83, no. 1, p. 012311, 2011.

[54] F. Wolf, Y. Wan, J. C. Heip, F. Gebert, C. Shi, and P. O. Schmidt, "Non-destructive state detection for quantum logic spectroscopy of molecular ions," *Nature*, vol. 530, no. 7591, pp. 457–460, 2016.

[55] M. Shi, P. Herskind, M. Drewsen, and I. Chuang, "Microwave quantum logic spectroscopy and control of molecular ions," *New Journal of Physics*, vol. 15, no. 11, p. 113019, 2013.

[56] N. Aharon, M. Drewsen, and A. Retzker, "General scheme for the construction of a protected qubit subspace," *Physical Review Letters*, vol. 111, no. 23, p. 230507, 2013.

[57] M. Sinhal, Z. Meir, K. Najafian, G. Hegi, and S. Willitsch, "Quantum-nondemolition state detection and spectroscopy of single trapped molecules," *Science*, vol. 367, no. 6483, pp. 1213–1218, 2020.

[58] K. Najafian, Z. Meir, M. Sinhal, and S. Willitsch, "Identification of molecular quantum states using phase-sensitive forces," *Nature Communications*, vol. 11, no. 1, pp. 1–10, 2020.

[59] T. Schneider, B. Roth, H. Duncker, I. Ernsting, and S. Schiller, "All-optical preparation of molecular ions in the rovibrational ground state," *Nature Physics*, vol. 6, no. 4, pp. 275–278, 2010.

[60] X. Tong, A. H. Winney, and S. Willitsch, "Sympathetic cooling of molecular ions in selected rotational and vibrational states produced by threshold photoionization," *Physical Review Letters*, vol. 105, no. 14, p. 143001, 2010.

[61] D. Leibfried, "Quantum state preparation and control of single molecular ions," *New Journal of Physics*, vol. 14, no. 2, p. 023029, 2012.

[62] P. O. Schmidt, T. Rosenband, C. Langer, W. M. Itano, J. C. Bergquist, and D. J. Wineland, "Spectroscopy using quantum logic," *Science*, vol. 309, no. 5735, pp. 749–752, 2005.

[63] S. Ding and D. Matsukevich, "Quantum logic for the control and manipulation of molecular ions using a frequency comb," *New Journal of Physics*, vol. 14, no. 2, p. 023028, 2012.

[64] J. Mur-Petit, J. J. García-Ripoll, J. Pérez-Ríos, J. Campos-Martínez, M. I. Hernández, and S. Willitsch, "Temperature-independent quantum logic for molecular spectroscopy," *Physical Review A*, vol. 85, no. 2, p. 022308, 2012.

[65] Y. Lin, D. R. Leibrandt, D. Leibfried, and C.-w. Chou, "Quantum entanglement between an atom and a molecule," *Nature*, vol. 581, no. 7808, pp. 273–277, 2020.

[66] C.-w. Chou, C. Kurz, D. B. Hume, P. N. Plessow, D. R. Leibrandt, and D. Leibfried, "Preparation and coherent manipulation of pure quantum states of a single molecular ion," *Nature*, vol. 545, no. 7653, pp. 203–207, 2017.

[67] L. D. Carr, D. DeMille, R. V. Krems, and J. Ye, "Cold and ultracold molecules: science, technology and applications," *New Journal of Physics*, vol. 11, p. 055049, may 2009.

[68] I. S. Vogelius, L. B. Madsen, and M. Drewsen, "Blackbody-radiation–assisted laser cooling of molecular ions," *Physical Review Letters*, vol. 89, p. 173003, Oct 2002.

[69] I. Vogelius, L. Madsen, and M. Drewsen, "Rotational cooling of molecules using lamps," *Journal of Physics B: Atomic, Molecular and Optical Physics*, vol. 37, no. 22, p. 4571, 2004.

[70] A. Mokhberi and S. Willitsch, "Sympathetic cooling of molecular ions in a surface-electrode ion trap," *Physical Review A*, vol. 90, no. 2, p. 023402, 2014.

[71] E. S. Shuman, J. F. Barry, and D. DeMille, "Laser cooling of a diatomic molecule," *Nature*, vol. 467, no. 7317, pp. 820–823, 2010.

[72] J. Lim, J. R. Almond, M. A. Trigatzis, J. A. Devlin, N. J. Fitch, B. E. Sauer, M. R. Tarbutt, and E. A. Hinds, "Laser cooled YbF molecules for measuring the electron's electric dipole moment," *Physical Review Letters*, vol. 120, p. 123201, Mar 2018.

[73] R. Rugango, J. E. Goeders, T. H. Dixon, J. M. Gray, N. Khanyile, G. Shu, R. J. Clark, and K. R. Brown, "Sympathetic cooling of molecular ion motion to the ground state," *New Journal of Physics*, vol. 17, no. 3, p. 035009, 2015.

[74] Y. Wan, F. Gebert, F. Wolf, and P. O. Schmidt, "Efficient sympathetic motional-ground-state cooling of a molecular ion," *Physical Review A*, vol. 91, no. 4, p. 043425, 2015.

[75] H. G. Dehmelt, "Radiofrequency Spectroscopy of Stored Ions I: Storage," *Advances in Atomic and Molecular Physics*, vol. 3, pp. 53–72, Jan. 1968.

[76] H. G. Dehmelt, "Radiofrequency Spectroscopy of Stored Ions II: Spectroscopy," *Advances in Atomic and Molecular Physics*, vol. 5, pp. 109–154, Jan. 1969.

[77] F. M. Penning, "Die Glimmentladung bei niedrigem Druck zwischen koaxialen Zylindern in einem axialen Magnetfeld," *Physica*, vol. 3, pp. 873–894, Jan. 1936.

[78] P. K. Ghosh, *Ion Traps*. Oxford Univ. Press, 1995.

[79] R. Grimm, M. Weidemüller, and Y. B. Ovchinnikov, "Optical dipole traps for neutral atoms," in *Advances in atomic, molecular, and optical physics*, vol. 42, pp. 95–170, Elsevier, 2000.

[80] W. Smith, D. Goodman, I. Sivarajah, J. Wells, S. Banerjee, R. Côté, H. Michels, J. Mongtomery, and F. Narducci, "Experiments with an ion-neutral hybrid trap: cold charge-exchange collisions," *Applied Physics B*, vol. 114, no. 1, pp. 75–80, 2014.

[81] Z. Meir, T. Sikorsky, R. Ben-shlomi, N. Akerman, M. Pinkas, Y. Dallal, and R. Ozeri, "Experimental apparatus for overlapping a ground-state cooled ion with ultracold atoms," *Journal of Modern Optics*, vol. 65, no. 5-6, pp. 501–519, 2018.

[82] C. Schneider, M. Enderlein, T. Huber, and T. Schätz, "Optical trapping of an ion," *Nature Photonics*, vol. 4, no. 11, pp. 772–775, 2010.

[83] J. Schmidt, A. Lambrecht, P. Weckesser, M. Debatin, L. Karpa, and T. Schaetz, "Optical trapping of ion coulomb crystals," *Physical Review X*, vol. 8, no. 2, p. 021028, 2018.

[84] T. Schaetz, "Trapping ions and atoms optically," *Journal of Physics B: Atomic, Molecular and Optical Physics*, vol. 50, no. 10, p. 102001, 2017.

[85] M. Drewsen, "Ion coulomb crystals," *Physica B-Condensed Matter*, vol. 460, pp. 105–113, 2015.

[86] N. Aharon, M. Drewsen, and A. Retzker, "Enhanced quantum sensing with multi-level structures of trapped ions," *Quantum Science and Technology*, vol. 2, p. 034006, jul 2017.

[87] T. Rosenband, D. Hume, P. Schmidt, C.-W. Chou, A. Brusch, L. Lorini, W. Oskay, R. E. Drullinger, T. M. Fortier, J. E. Stalnaker, *et al.*, "Frequency ratio of Al^+ and Hg^+ single-ion optical clocks; metrology at the 17th decimal place," *Science*, vol. 319, no. 5871, pp. 1808–1812, 2008.

[88] S. Bize, S. A. Diddams, U. Tanaka, C. Tanner, W. Oskay, R. E. Drullinger, T. E. Parker, T. P. Heavner, S. R. Jefferts, L. Hollberg, *et al.*, "Testing the stability of fundamental constants with the Hg^+ 199 single-ion optical clock," *Physical Review Letters*, vol. 90, no. 15, p. 150802, 2003.

[89] L. Hollberg, C. W. Oates, G. Wilpers, C. Hoyt, Z. Barber, S. A. Diddams, W. Oskay, and J. C. Bergquist, "Optical frequency/wavelength references," *Journal of Physics B: Atomic, Molecular and Optical Physics*, vol. 38, no. 9, p. S469, 2005.

[90] P. Blythe, B. Roth, U. Fröhlich, H. Wenz, and S. Schiller, "Production of ultracold trapped molecular hydrogen ions," *Physical Review Letters*, vol. 95, no. 18, p. 183002, 2005.

[91] B. Roth, P. Blythe, H. Daerr, L. Patacchini, and S. Schiller, "Production of ultracold diatomic and triatomic molecular ions of spectroscopic and astrophysical interest," *Journal of Physics B: Atomic, Molecular and Optical Physics*, vol. 39, no. 19, p. S1241, 2006.

[92] S. Schiller and C. Lämmerzahl, "Molecular dynamics simulation of sympathetic crystallization of molecular ions," *Physical Review A*, vol. 68, no. 5, p. 053406, 2003.

[93] S. Schiller, D. Bakalov, A. K. Bekbaev, and V. I. Korobov, "Static and dynamic polarizability and the stark and blackbody-radiation frequency shifts of the molecular hydrogen ions H_2^+, HD^+, and D_2^+," *Physical Review A*, vol. 89, no. 5, p. 052521, 2014.

[94] C. Wellers, M. R. Schenkel, G. S. Giri, K. R. Brown, and S. Schiller, "Controlled preparation and vibrational excitation of single ultracold molecular hydrogen ions," *Molecular Physics*, p. e2001599, 2021.

[95] V. I. Korobov, P. Danev, D. Bakalov, and S. Schiller, "Laser-stimulated electric quadrupole transitions in the molecular hydrogen ion H_2^+," *Physical Review A*, vol. 97, no. 3, p. 032505, 2018.

[96] X. Tong, D. Wild, and S. Willitsch, "Collisional and radiative effects in the state-selective preparation of translationally cold molecular ions in ion traps," *Physical Review A*, vol. 83, no. 2, p. 023415, 2011.

[97] O. Versolato, M. Schwarz, A. Hansen, A. Gingell, A. Windberger, J. Ullrich, F. Jensen, J. C. López-Urrutia, M. Drewsen, *et al.*, "Decay rate measurement of the first vibrationally excited state of MgH^+ in a cryogenic Paul trap," *Physical Review Letters*, vol. 111, no. 5, p. 053002, 2013.

[98] A. Bertelsen, S. Jørgensen, and M. Drewsen, "The rotational temperature of polar molecular ions in coulomb crystals," *Journal of Physics B: Atomic, Molecular and Optical Physics*, vol. 39, pp. L83–L89, feb 2006.

[99] I. S. Vogelius, L. B. Madsen, and M. Drewsen, "Probabilistic state preparation of a single molecular ion by projection measurement," *Journal of Physics B: Atomic, Molecular and Optical Physics*, vol. 39, pp. S1259–S1265, sep 2006.

[100] S. Alighanbari, M. G. Hansen, V. Korobov, and S. Schiller, "Rotational spectroscopy of cold and trapped molecular ions in the lamb–dicke regime," *Nature Physics*, vol. 14, no. 6, pp. 555–559, 2018.

[101] S. Mackenzie, F. Merkt, E. Halse, and T. P. Softley, "Rotational state selectivity in N_2^+ X $^2\Sigma_g^+$ ($\nu^+ = 0$) by delayed pulsed field ionization spectroscopy via the a" $^1\Sigma_g^+$(ν= 0) state," *Molecular Physics*, vol. 86, no. 5, pp. 1283–1297, 1995.

[102] X. Tong, T. Nagy, J. Yosa Reyes, M. Germann, M. Meuwly, and S. Willitsch *Chemical Physics Letters*, vol. 547, 2012.

[103] F. H. Hall and S. Willitsch, "Millikelvin reactive collisions between sympathetically cooled molecular ions and laser-cooled atoms in an ion-atom hybrid trap," *Physical Review Letters*, vol. 109, no. 23, p. 233202, 2012.

[104] M. Sinhal and S. Willitsch, "Molecular-ion quantum technologies," 4 2022.

[105] S. Hoekstra, J. J. Gilijamse, B. Sartakov, N. Vanhaecke, L. Scharfenberg, S. Y. van de Meerakker, and G. Meijer, "Optical pumping of trapped neutral molecules by blackbody radiation," *Physical Review Letters*, vol. 98, no. 13, p. 133001, 2007.

[106] U. Hechtfischer, Z. Amitay, P. Forck, M. Lange, J. Linkemann, M. Schmitt, U. Schramm, D. Schwalm, R. Wester, D. Zajfman, *et al.*, "Near-threshold photodissociation of cold CH^+ in a storage ring," *Physical Review Letters*, vol. 80, no. 13, p. 2809, 1998.

[107] M. Drewsen. Private communications.

[108] P. F. Staanum, K. Højbjerre, R. Wester, and M. Drewsen, "Probing isotope effects in chemical reactions using single ions," *Physical Review Letters*, vol. 100, p. 243003, Jun 2008.

[109] https://qdyn-library.net/.

[110] G. P. Herbert Goldstein and J. Safko, *Classical Mechanics, Third Edition*. Addison Wesley, 2000.

[111] B. Brandsen and C. Joachain, *Physics of Atoms and Molecules*. Longman Scientific and Technical, 1983.

[112] J. J. Sakurai and E. D. Commins, "Modern quantum mechanics, revised edition," 1995.

[113] P. W. Atkins and R. S. Friedman, *Molecular Quantum Mechanics*. Oxford university press, 2011.

[114] A. Szabo and N. S. Ostlund, *Modern Quantum Chemistry: Introduction to Advanced Electronic Structure Theory*. Courier Corporation, 2012.

[115] A. Bertelsen, S. Jørgensen, and M. Drewsen, "The rotational temperature of polar molecular ions in coulomb crystals," *Journal of Physics B: Atomic, Molecular and Optical Physics*, vol. 39, p. L83, feb 2006.

[116] R. K. Wangsness, *Electromagnetic Fields, 2nd Edition*. 1986.

[117] M. Aymar, R. Guérout, M. Sahlaoui, and O. Dulieu, "Electronic structure of the Magnesium hydride molecular ion," *Journal of Physics B: Atomic, Molecular and Optical Physics*, vol. 42, no. 15, p. 154025, 2009.

[118] B. J. Sussman, "Five ways to the nonresonant dynamic stark effect," *American Journal of Physics*, vol. 79, no. 5, pp. 477–484, 2011.

[119] R. P. Feynman, "Forces in molecules," *Physical Review*, vol. 56, pp. 340–343, Aug 1939.

[120] R. González-Férez and P. Schmelcher, "Rovibrational spectra of diatomic molecules in strong electric fields: The adiabatic regime," *Physical Review A*, vol. 69, no. 2, p. 023402, 2004.

[121] M. Ndong, H. Tal-Ezer, R. Kosloff, and C. P. Koch, "A Chebychev propagator with iterative time ordering for explicitly time-dependent Hamiltonians," *The Journal of Chemical Physics*, vol. 132, no. 6, p. 064105, 2010.

[122] S. Patsch, D. M. Reich, J.-M. Raimond, M. Brune, S. Gleyzes, and C. P. Koch, "Fast and accurate circularization of a rydberg atom," *Physical Review A*, vol. 97, no. 5, p. 053418, 2018.

[123] S. Patsch, S. Maniscalco, and C. P. Koch, "Simulation of open-quantum-system dynamics using the quantum zeno effect," *Physical Review Research*, vol. 2, no. 2, p. 023133, 2020.

[124] M. H. Goerz, T. Calarco, and C. P. Koch, "The quantum speed limit of optimal controlled phasegates for trapped neutral atoms," *Journal of Physics B: Atomic, Molecular and Optical Physics*, vol. 44, no. 15, p. 154011, 2011.

[125] M. H. Goerz, E. J. Halperin, J. M. Aytac, C. P. Koch, and K. B. Whaley, "Robustness of high-fidelity rydberg gates with single-site addressability," *Physical Review A*, vol. 90, no. 3, p. 032329, 2014.

[126] M. W. Heger, C. P. Koch, and D. M. Reich, "Optimized sampling of mixed-state observables," *Physical Review E*, vol. 100, no. 5, p. 052105, 2019.

[127] S. Amaran, R. Kosloff, M. Tomza, W. Skomorowski, F. Pawłowski, R. Moszynski, L. Rybak, L. Levin, Z. Amitay, J. M. Berglund, *et al.*, "Femtosecond two-photon photoassociation of hot magnesium atoms: A quantum dynamical study using thermal random phase wavefunctions," *The Journal of Chemical Physics*, vol. 139, no. 16, p. 164124, 2013.

[128] D. J. Tannor, *Introduction to Quantum Mechanics: a Time-dependent Perspective*. University Science Books, 2007.

[129] D. Kosloff and R. Kosloff, "A Fourier method solution for the time dependent Schrödinger equation as a tool in molecular dynamics," *Journal of Computational Physics*, vol. 52, no. 1, pp. 35 – 53, 1983.

[130] G. B. Arfken and H. J. Weber, *Mathematical methods for physicists*. Elsevier, AP, 1999.

[131] J. C. Light and T. Carrington Jr, "Discrete-variable representations and their utilization," *Advances in Chemical Physics*, vol. 114, pp. 263–310, 2000.

[132] S. C. Chapra, R. P. Canale, *et al.*, *Numerical methods for engineers*. Boston: McGraw-Hill Higher Education,, 2010.

[133] R. Bisseling and R. Kosloff, "The fast Hankel transform as a tool in the solution of the time dependent Schrödinger equation," *Journal of Computational Physics*, vol. 59, no. 1, pp. 136–151, 1985.

[134] V. Kokoouline, O. Dulieu, and F. Masnou-Seeuws, "Theoretical treatment of channel mixing in excited Rb_2 and Cs_2 ultracold molecules: Perturbations in 0 u+ photoassociation and fluorescence spectra," *Physical Review A*, vol. 62, no. 2, p. 022504, 2000.

[135] H. Tal-Ezer and R. Kosloff, "An accurate and efficient scheme for propagating the time dependent schrödinger equation," *The Journal of Chemical Physics*, vol. 81, no. 9, pp. 3967–3971, 1984.

[136] M. Goerz, *Optimizing Robust Quantum Gates in Open Quantum Systems*. PhD thesis, Universität Kassel, 2015.

[137] R. Kosloff, "Time-dependent quantum-mechanical methods for molecular dynamics," *The Journal of Physical Chemistry*, vol. 92, no. 8, pp. 2087–2100, 1988.

[138] J. M. Berglund, M. Drewsen, and C. P. Koch, "State changes in single collisions between diatomic molecular ions and atomic ions. In preparation,"

[139] J. M. Berglund, M. Drewsen, and C. P. Koch, "Sympathetic cooling of diatomic molecular ions: Translational cooling dynamics and rotational state excitations. In preparation.,"

[140] D. Larson, J. C. Bergquist, J. J. Bollinger, W. M. Itano, and D. J. Wineland, "Sympathetic cooling of trapped ions: A laser-cooled two-species nonneutral ion plasma," *Physical Review Letters*, vol. 57, no. 1, p. 70, 1986.

[141] R. Drullinger, D. Wineland, and J. Bergquist, "High-resolution optical spectra of laser cooled ions," *Applied Physics*, vol. 22, no. 4, pp. 365–368, 1980.

[142] X. Tong, D. Wild, and S. Willitsch, "Collisional and radiative effects in the state-selective preparation of translationally cold molecular ions in ion traps," *Physical Review A*, vol. 83, no. 2, p. 023415, 2011.

[143] X. Tong, A. H. Winney, and S. Willitsch, "Sympathetic cooling of molecular ions in selected rotational and vibrational states produced by threshold photoionization," *Physical Review Letters*, vol. 105, p. 143001, Sep 2010.

[144] M. Drewsen, "Ion Coulomb crystals," *Physica B: Condensed Matter*, vol. 460, pp. 105–113, 2015.

[145] R. E. March and J. F. Todd, *Quadrupole ion trap mass spectrometry*, vol. 165. John Wiley & Sons, 2005.

[146] D. Berkeland, J. Miller, J. C. Bergquist, W. M. Itano, and D. J. Wineland, "Minimization of ion micromotion in a Paul trap," *Journal of Applied Physics*, vol. 83, no. 10, pp. 5025–5033, 1998.

[147] M. Drewsen and A. Brøner, "Harmonic linear Paul trap: Stability diagram and effective potentials," *Physical Review A*, vol. 62, no. 4, p. 045401, 2000.

[148] L. Hornekær, N. Kjærgaard, A. M. Thommesen, and M. Drewsen, "Structural properties of two-component Coulomb crystals in linear Paul traps," *Physical Review Letters*, vol. 86, pp. 1994–1997, Mar 2001.

[149] A. Hashemloo, C. M. Dion, and G. Rahali, "Wave packet dynamics of an atomic ion in a Paul trap," *International Journal of Modern Physics C*, vol. 27, no. 02, p. 1650014, 2016.

[150] A. Hashemloo and C. M. Dion, "Rotational dynamics of a diatomic molecular ion in a Paul trap," *Journal of Chemical Physics*, vol. 143, no. 20, p. 204308, 2015.

[151] J. Prestage, A. Williams, L. Maleki, M. Djomehri, and E. Harabetian, "Dynamics of charged particles in a Paul radio-frequency quadrupole trap," *Physical Review Letters*, vol. 66, no. 23, p. 2964, 1991.

[152] NIST, "Computational chemistry comparison and benchmark database, standard reference database number 101." https://cccbdb.nist.gov/, 2018.

[153] M. Bussmann, U. Schramm, D. Habs, V. Kolhinen, and J. Szerypo, "Stopping highly charged ions in a laser-cooled one component plasma of $^{24}Mg^{+}$ ions," *International Journal of Mass-Spectroscopy*, vol. 251, pp. 179–189, 2006.

[154] X. Tong, A. H. Winney, and S. Willitsch, "Sympathetic cooling of molecular ions in selected rotational and vibrational states produced by threshold photoionization," *Physical Review Letters*, vol. 105, p. 143001, Sep 2010.

[155] M. Germann, X. Tong, and S. Willitsch, "Observation of electric-dipole-forbidden infrared transitions in cold molecular ions," *Nature Physics*, vol. 10, p. 820, 2014.

[156] M. Germann and S. Willitsch, "Fine- and hyperfine-structure effects in molecular photoionization. I. General theory and direct photoionization," *Journal of Chemical Physics*, vol. 145, p. 044314, 2016.

[157] M. Germann and S. Willitsch, "Fine- and hyperfine-structure effects in molecular photoionization. II. Resonance-enhanced multiphoton ionization and hyperfine-selective generation of molecular cations," *Journal of Chemical Physics*, vol. 145, no. 4, p. 044315, 2016.

[158] J. M. Berglund, M. Drewsen, and C. P. Koch, "Femtosecond wavepacket interferometry using the rotational dynamics of a trapped cold molecular ion," *New Journal of Physics*, vol. 17, p. 025007, feb 2015.

[159] C. H. Townes and A. L. Schawlow, *Microwave Spectroscopy*. McGraw-Hill, New York, 1955.

[160] P. L. Jacobson, R. A. Komara, W. G. Sturrus, and S. R. Lundeen, "Microwave spectroscopy of heliumlike Rydberg states of H_2 and D_2: Determinations of the dipole polarizabilities of H_2^+ and D_2^+ ground states," *Physical Review A*, vol. 62, p. 012509, Jun 2000.

[161] R. González-Férez and P. Schmelcher, "Impact of electric fields on highly excited rovibrational states of polar dimers," *New Journal of Physics*, vol. 11, no. 5, p. 055013, 2009.

[162] W. Balfour, "Rotational analysis of the $A^1\Sigma^+ \rightarrow X^1\Sigma^+$ and $B^1\Pi \rightarrow X^1\Sigma^+$ systems of $^{24}MgH^+$, $^{25}MgH^+$, and $^{26}MgH^+$," *Canadian Journal of Physics*, vol. 50, no. 11, pp. 1082–1091, 1972.

[163] S. Haroche and J.-M. Raimond, *Exploring the Quantum*. Oxford Univ. Press, 2006.

ISBN 978-3-7376-1137-4